DOCTORAL THESIS

Stimulating vision: measuring and modelling transcranial direct current stimulation of the visual cortex

Author:

Sophie ESTERER

Supervised by:

Dr. David J. MCGONIGLE

A thesis submitted in fulfilment of the requirements
for the degree of Doctor of Philosophy

Cardiff University Brain Research Imaging Centre
School of Psychology
College of Biomedical and Life Sciences
Cardiff University

October 2019

Declaration of Authorship

I, Sophie ESTERER, declare that this thesis titled, "Stimulating vision: measuring and modelling transcranial direct current stimulation of the visual cortex" and the work presented in it are my own. I confirm that:

- This work has not been submitted in substance for any other degree or award at this or any other university or place of learning, nor is being submitted concurrently in candidature for any degree or other award.

- This thesis is being submitted in partial fulfilment of the requirements for the degree of PhD.

- This thesis is the result of my own independent work/investigation, except where otherwise stated, and the thesis has not been edited by a third party beyond what is permitted by Cardiff University's Policy on the Use of Third Party Editors by Research Degree Students. Other sources are acknowledged by explicit references. The views expressed are my own.

- I hereby give consent for my thesis, if accepted, to be available online in the University's Open Access repository for inter-library loans after expiry of a bar on access previously approved by the Academic Standards & Quality Committee.

Signed:

_____

Date:

_____

"Everything simple is false. Everything complex is unusable."

Paul Valéry

CARDIFF UNIVERSITY

Abstract

Stimulating vision: measuring and modelling transcranial direct current stimulation of the visual cortex

Transcranial direct current stimulation (tDCS) has enjoyed something of a renaissance in neuroscientific research, however, this has not been accompanied by a commensurate increase in our understanding of its neurobiological mechanisms. At present, there remains a large explanatory gap between the stimulation effects on cells in *in vivo* or *in vitro* studies and the wide variety of behavioural findings in human studies. Consequently, tDCS research is currently confronted with a wide variety of conceptual and methodological challenges that have hampered the development of mature rationales for its use in healthy and clinical populations.

This thesis aimed to address some of these challenges by combining data from behavioural and neuroimaging experiments with findings from individualised models of tDCS-induced electric fields. Experiments focused on the visual system, using relatively simple paradigms based on pattern-reversing checkerboards and the detection of achromatic dot stimuli to investigate stimulation effects on visual processing, The role of inter-individual variability — both in baseline sensory performance and in head anatomy — received particular attention in the design of studies.

In the second chapter of the thesis, the question of suitable current waveforms for double-blind, sham-controlled tDCS studies is discussed. The third chapter investigates the role of electrode montage in eliciting tDCS effects on contrast detection at central and peripheral visual field locations. In Chapters 4 and 5, inter-individual differences in anatomy are quantified using computational modelling of electric fields and neuroimaging methods. Work presented in Chapter 6 explores the feasibility of acquiring concurrent tDCS-NIRS-MEG data.

Together, results from these studies suggest that the large parameter space for designing and interpreting human tDCS experiments calls for a broad range of methodological advances in future tDCS research.

Acknowledgements

I would like to thank my supervisor, David McGonigle. After four years of working together, I am convinced that your commitment to rigorous science is only surpassed by your boundless enthusiasm for puns. I am extremely grateful for the opportunity you have given me to develop and explore my own ideas – and the patient advice you provided when I inevitably made my own mistakes.

I am also deeply indebted to many lovely and talented friends and colleagues, in particular:

- Lorenzo Magazzini and Diana Dima, for so generously sharing cups of coffee, cheese fondues and MEG expertise. You made me feel welcome and supported at CUBRIC from the very first to (almost) the very last day.
- Katy Unwin, for keeping faith during the ups and downs of our PhD journeys.
- Sara Sportelli, Leigh Abbot, Hannah Johnston and Lauren Breakwell, for their hard work as interns and MSc students.
- Cyril Charron, Gavin Perry, Chris Allen and Adam Partridge, for their crucial assistance with IT and lab equipment.
- Tony Redmond and Lindsey Rountree, for their invaluable advice on all things perimetric and extended loan of CRS equipment. I will return it soon, I swear!
- Leandro Beltracchini, for helping me make sense of FEM in the early days.
- Rachael Stickland, for sharing her insights on designing MEG-fMRI experiments.
- Dom Dwyer, for his reliably insightful questions over the years.
- Cariad Sealey and Zainab Hassan, for their unfazed guidance through all administrative hurdles (not to mention their support of my love affair with the label maker).
- Tom Marshall, for getting me into this tDCS malarkey in the first place.

I would also like to thank my family for their unwavering encouragement to follow my curiosity from the first time I ever asked, "But why...?".

Finally, Dominik, I could not wish for a more caring or supportive accomplice in my endeavours – scientific or otherwise. I can't wait to start the next big adventure with you!

List of Abbreviations

AAL	Automated Anatomical Labelling
ANOVA	Analysis of variance
AP	Action potential
ASL	Arterial spin labelling
BDNF	Brain-derived neurotrophic factor
BOLD	Blood oxygen level dependent
bpm	Beats per minute
CBF	Cerebral blood flow
CBV	Cerebral blood volume
CI	Confidence interval
CMRO2	Cerebral metabolic rate of oxygen
CNS	Central nervous system
CSF	Cerebro-spinal fluid
cw	Continuous-wave
DC	Direct current
deg	Degrees of visual angle
DLPFC	Dorsolateral prefrontal cortex
DPF	Differential pathlength factor
DTI	Diffusion tensor imaging
ECT	Electroconvulsive therapy
EEG	Electroencephalography
E-field	Electric field
EPSP	Excitatory postsynaptic potential
fd	Frequency-domain
FDR	False discovery rate
FEM	Finite element method/model
fMRI	Functional magnetic resonance imaging
FOS	Frequency-of-seeing
FSF	Fade-in — short stimulation — fade-out
GABA	Gamma-aminobutyric acid
GLM	General linear model
GM	Grey matter

HbO	Oxyhemoglobin
HbR	Deoxyhemoglobin
HD-tDCS	High-definition transcranial direct current stimulation
HRF	Hemodynamic response function
IPSP	Inhibitory postsynaptic potential
IQR	Interquartile range
JND	Just noticeable difference
LGN	lateral geniculate nucleus
LTD	Long-term depression
LTP	Long-term potentiation
M1	Primary motor cortex
MBLL	Modified Beer-Lambert law
MEG	Magnetoencephalography
MEP	Motor-evoked potential
MOCS	Method of constant stimuli
MRI	Magnetic resonance imaging
MRS	Magnetic resonance spectroscopy
MSR	Magnetically shielded room
n-AFC	n-alternative forced choice
NIRS	Near infra-red spectroscopy
NMDA	N-methyl-D-aspartate
NMR	Nuclear magnetic resonance
NVC	Neuro-vascular coulpling
OD	Optical density
OPM	Optically pumped magnetometers
PPF	Partial pathlength factor
PSF	Point-spread function
PSP	Post-synaptic potential
rCBF	Regional cerebral blood flow
RF	Receptive field
RMT	Resting motor threshold
ROI	Region-of-interest
SC	Superior colliculus
SD	Standard deviation
SE	Standard error
SNR	Signal-to-noise ratio
SQUID	Superconducting quantum interference device
tACS	Transcranial alternating current stimulation

tES	Transcranial electrical stimulation
td	Time-domain
tDCS	Transcranial direct current stimulation
TMS	Transcranial magnetic stimulation
tRNS	Transcranial random noise stimulation
V1	Primary visual cortex
VEP	Visual evoked potential

Contents

List of Figures

List of Tables

xxvi

Chapter 1

General Introduction

Transcranial direct current stimulation (tDCS) is a non-invasive brain stimulation technique that delivers weak electrical currents to the human cortex via scalp electrodes. While first re-introduced to mainstream neuroscience nearly two decades ago (Nitsche and Paulus, 2000; Priori et al., 1998), the technique has its roots in therapeutic applications that use electrical stimulation with high frequencies and intensities to directly cause neuronal activation in the brain, such as electroconvulsive therapy and electroanaesthesia (Priori, 2003). In contrast, current use of tDCS focuses on modulating brain activity in a targeted manner without directly eliciting neuronal action potentials. As a neuromodulatory approach, tDCS has been used to investigate and improve brain function in both healthy and patient populations.

However, the widespread use of tDCS is in stark contrast to our current understanding of its effects across different levels of description. At a neurophysiological level the mechanisms of action of tDCS are incompletely understood and it is still unclear how they relate to behavioural outcomes. Consequently, there remains a large explanatory gap between the cellular stimulation effects observed in animal studies and the wide variety of behavioural findings in human tDCS studies.

To date, the vast majority of tDCS studies have focused on evaluating its effects on measures from typical psychological experiments, where the dependent variable is behavioural performance (Coffman et al., 2014; Horvath et al., 2015; Kuo and Nitsche, 2012). In parallel, there have been a number of research groups exploring the use of passively applied experimental procedures to obtain objective values of physiological thresholds, such as motor-evoked potentials induced by transcranial magnetic pulses (TMS). At present, these studies are hampered in their conclusions by the unknown mappings between electrical stimulation parameters, neuronal polarisation changes in the brain and their subsequent effects on behaviour.

In addition, the importance of both between- and within-participant variability for stimulation outcomes has not been fully determined. These issues — combined with the growing appreciation of individual differences in basic cognitive tasks — have

meant that a wide range of tDCS studies have yielded heterogeneous results and criticism of the technique has become more vocal.

To tease apart the true effects of tDCS on behaviour, we must describe not only the spread of the induced electric field and its impact on cells in a given target brain region, but also how this effect subsequently influences the specific computations carried out by this region and their effect on participant behaviour.

In developing such a model, less complex experimental paradigms that employ elementary stimuli and simple behavioural demands are likely to be more useful than the ethologically implausible paradigms used to evoke MEPs and visual phosphenes. Thus, studying behaviour in a sensory system such as vision seems a logical place to begin to explore the underlying neurobiology of tDCS. The neural correlates of visual stimulus processing, in particular, are better understood than those underlying other sensory systems or higher-order cognitive functions.

1.1   Transcranial Direct Current Stimulation

1.1.1   From fish to firing rates

The use of electric currents in medicine dates back to classical antiquity, when the Roman physician Scribonius Largus (1–50 AD) recommended the use of electric discharges from live torpedo fish to alleviate headache and gout in his medical treatise *Compositiones medicae* (Scribonius Largus, 1529).

Over the following centuries, the medicinal use of torpedo fish was passed on through the works of Ancient Greek and Roman physicians. Persian physician Avicenna (980–1037) considered treatment with torpedo fish effective for headache, melancholy and epileptic seizures in his *Canon of Medicine* — a standard medical text at universities throughout Medieval Europe and the Islamic world, which remained in use well into the 17th century (Leibowitz, 1957; McGinnis, 2010).

In the 18th century, torpedo fish were once again used in a series of experiments that laid the groundwork for modern electrophysiology (Walsh and Seignette, 1773). In a controversial but seminal scientific exchange, Italian physician Luigi Galvani and physicist Alessandro Volta debated the nature of the electric force observed to cause muscle contraction in animal experiments. To disprove Galvani's concept of an "animal electric fluid" secreted by the brain and carried to the muscles via the nerves, Volta invented the first electrical battery, the "voltaic cell", and coined the term "galvanism" for a direct current of electricity produced by chemical reaction (Galvani, 1791, 1797; Volta, 1918, 1923). In 1804, Galvani's nephew Giovanni Aldini presented a series of lectures on the successful treatment of psychiatric patients through the application of "galvanic currents" over the head (Aldini, 1804; Figure 1.1).
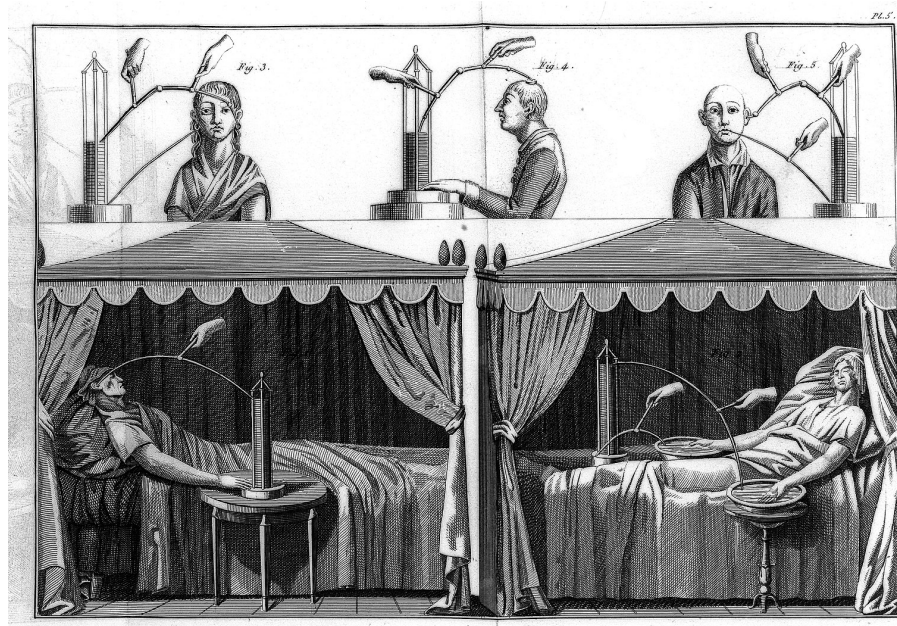
Figure 1.1: *Top panel:* Psychiatric patients receiving galvanic stimulation at different scalp locations via electrodes connected to a voltaic cell (Aldini, 1804). Middle figure shows Luigi Lanzarini, a 27-year-old farmer suffering from "melancholy madness", being treated at Santo Orsola Hospital in Bologna in 1801. *Lower panel:* Two recently deceased patients connected to voltaic cells; reproduced from the Wellcome Images collection at the Wellcome Library, London, under CC BY 4.0 license).

Less than a century later, Gustav Fritsch and Eduard Hitzig discovered that electrical stimulation of the cerebral cortex produced discrete movements in dogs (Fritsch and Hitzig, 1870; Hitzig, 1867, 1870). Their experiments in the motor cortex addressed several controversies amongst neurophysiologists of the time. Not only could they show that the cortex was electrically excitable, they also demonstrated that, far from being an insignificant "rind", the cortex was functionally relevant and that functions were topographically organised in the brain. Their findings were subsequently replicated and strengthened the idea of the brain as a potential target for manipulation with electrical currents.

In the following decades, evidence from different fields of research converged to confirm that information transfer between peripheral and central components of the nervous system was an electrochemical process. Neurons were conventionally considered to be the main component of the nervous tissue and information processing in the brain was viewed to rely on neuronal activity. Although a second group of cells was identified in the brain, which appeared to greatly outnumber neurons (Remak, 1844; Schwann, 1839; Virchow, 1860), these "neuroglia" were relegated to a largely non-functional role as the cellular "glue" surrounding and supporting neurons. This view has only recently been challenged by a wealth of new evidence pointing to an equal ratio of glia and neurons in the brain (Bartheld et al., 2016), and a much more
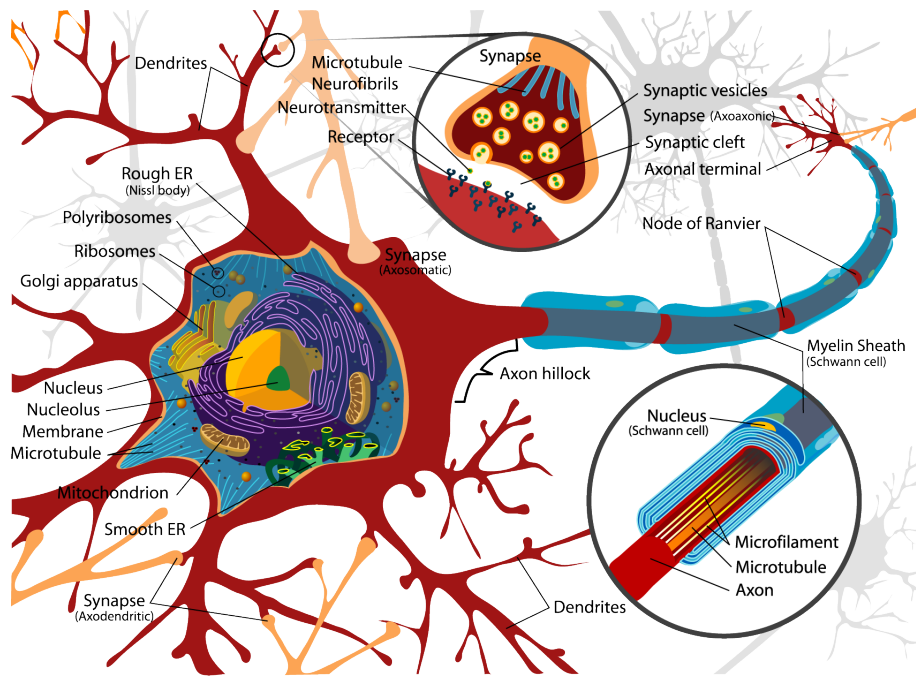
Figure 1.2: Diagram of a typical nerve cell with its characteristic organelles. The entire cell is enclosed by a plasma membrane, which acts as an electrical insulator. Neuronal signalling relies on the controlled movement of ions across the plasma membrane. If signals exceed a critical voltage threshold, an action potential is generated at the axon hillock and propagated along the axon via saltatory conduction; most post-synaptic elements are dendrites; image released to the public domain by the creator.

active participation of glial cells in information processing and neuroplasticity (e.g., Allen and Eroglu, 2017; Fields and Stevens-Graham, 2002; Halassa and Haydon, 2010; Perea et al., 2014; Stogsdill and Eroglu, 2017; Volterra and Meldolesi, 2005). However, in spite of recent interest in glial cells, the structure and function of neuronal cells has been much more thoroughly characterised over the last century.

Neurons receive and transmit electrochemical impulses via neurotransmitter-dependent, ionic and molecular interactions across their cell membranes (Figure 1.2). The lipid bilayer of the neuronal plasma membrane acts as an electrical insulator and is largely impermeable to the small inorganic ions that carry electrical charges, such as sodium (Na^+), calcium (Ca^{2+}), potassium (K^+) or chloride (Cl^-). Specialised pore-forming proteins are present in the plasma membrane, which selectively allow ions to pass through. Many different types of such "ion channels" have been identified and their activities combine to generate the complex patterns of neuronal firing.

When a neuron is at rest, its interior is negatively charged relative to its exterior by a small margin, i.e., the neuron is *polarised.* This polarisation is due to two factors: First, the neuron's cellular membrane is selectively permeable, allowing only certain molecules to pass into or out of the cell but not others. Second, membrane-bound molecular pumps release sodium ions and retrieve potassium ions at a different rate. At rest, a concentration gradient develops across the cell membrane due to the much
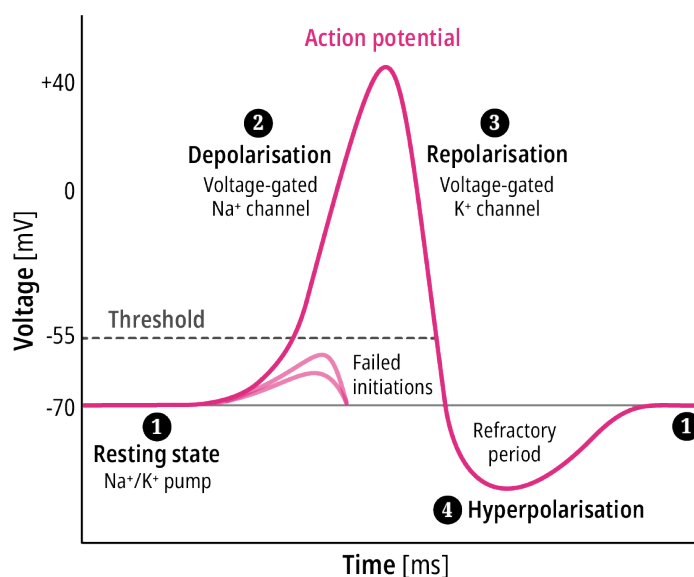
Figure 1.3: Schematic illustration of the typical phases of an action potential. (1) At rest, there is a net negative membrane potential of approximately 70 mV. (2) As the strength of a polarising stimulus is increased, a threshold is reached. Sodium-gated (Na$^+$) channels open and Na$^+$ flows into the cell, causing depolarisation. (3) Repolarisation occurs when the potassium-gated (K$^+$) channels open and K$^+$ flows out of the cell. (4) Hyperpolarisation is caused by an efflux K$^+$ or an influx of chloride (Cl$^-$) ions. While hyperpolarised, the neuron is in a refractory period (approx. 2 ms), during which it cannot generate further action potentials.

larger number of sodium ions outside the cell, increasingly forcing sodium into the cell. Similarly, inside the cell, a concentration gradient develops that pushes potassium ions out of the cell. The resulting charge difference between the immediate interior and exterior of the neuron amounts to approximately -70 mV and is referred to as the "resting membrane potential" (Figure 1.3-1).

If membrane permeability increases for any reason, an influx of Na$^+$ influx and efflux of K$^+$ results. As the ions seek to equalise their distribution, the neuron's interior temporarily becomes positive relative to its exterior, i.e., the neuron depolarises (Figure 1.3-2). Certain neurotransmitter-receptor interactions increase membrane permeability, producing a partial depolarisation due to an inward rush of sodium ions. Such an excitatory postsynaptic potential (EPSP) tends to push the neuron toward firing. Other interactions further decrease permeability, leading to an increase in polarisation (hyperpolarisation; Figure 1.3-4) that inhibits the neuron from firing (inhibitory postsynaptic potential, or IPSP).

For a signal to be propagated, the strength of the input must be sufficient to alter the membrane potential. A neuron usually integrates many different excitatory and inhibitory signals from other neurons at any given time. When the amount of excitation from incoming EPSPs crosses a critical threshold, the neuron will fire an action potential.
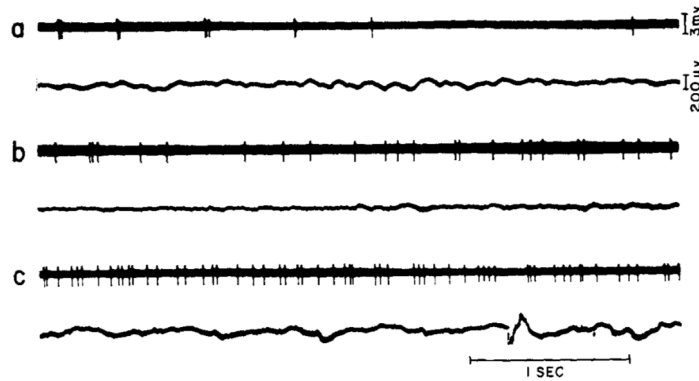
Figure 1.4: Effect of transcortical DC stimulation on spontaneous firing (top) and EEG (bottom) of neurons in cat visual cortex. (a) Surface-negative (cathodal) current; (b) Baseline resting activity; (c) Surface-positive (anodal) current; reproduced from Creutzfeldt et al., 1962.

Thus, altering the voltage difference across the cell membrane directly affects neuronal excitability and influences the neuron's firing behaviour. Accordingly, transcranial brain stimulation rests on the idea that applying an *exogenous* electrical field to the cortex will affect neuronal excitability — and eventually firing rate — by modulating the transmembrane potential.

Based on these principles, transcranial brain stimulation with direct currents received renewed attention from researchers in the 1960s. An *in vitro* experiment by Terzuolo and Bullock, 1956 demonstrated that an imposed voltage gradient in the range of 0.1 mV/100μ was sufficient to modulate spontaneous neuronal firing in slice preparations from crayfish and lobsters. Their work was followed by several *in vivo* studies, in which DC stimulation was applied directly to the cortex of anaesthetised animals.

Creutzfeldt et al., 1962 investigated stimulation effects on the spontaneous and evoked activity of neurons in the visual and motor cortices of cats and found that a minimum input current of 200 μA was required to elicit effects on neuronal discharge patterns. Importantly, net activity change was dependent on the surface polarity of the applied current: most neurons showed an increase in firing rate for surface-positive ("anodal") currents and a decrease in firing rate for surface-negative ("cathodal") currents (Figure 1.4).

Subsequent experiments by Bindman and colleagues replicated the polarity-specific findings of Creutzfeldt et al. and also highlighted the effect of stimulation duration on neuronal firing patterns (Bindman et al., 1962, 1964). Potentials evoked in the somatosensory cortex of rats through the stimulation of the contralateral forepaw were enhanced by surface-positive currents in the range of 5–50 μA. Notably, this response change typically peaked only after stimulation was applied for several minutes. Moreover, if the duration of stimulation exceeded 5 minutes, this activity enhancement was

maintained for up to 4 hours *after* stimulation offset. Surface-negative polarisation similarly elicited a long-lasting reduction in the size of evoked potentials.

An *in vivo* study in the cat motor cortex by Purpura and McMurtry, 1965 compared the responsiveness of both pyramidal tract (PT) and non-pyramidal tract cells to weak (30–80 μA/mm^2) and strong (100-400 μA/mm^2) DC stimulation applied for periods of 5–10 or 30–40 s. In agreement with previous findings, they found that strong anodal stimulation depolarised, whereas cathodal stimulation hyperpolarised deep-lying PT and non-PT cells. However, superficially located non-PT cells showed opposite effects — they were typically hyperpolarised by anodal currents and depolarised by cathodal currents. Weak current densities modulated evoked responses but failed to affect the membrane potential or EPSPs of PT neurons. In comparison, non-PT cells were more responsive to weak polarisation. After-effects of DC stimulation were observed in the form of prolonged potentiation of evoked activity and increased spike rates, although their duration was shorter than effects reported by Bindman et al., 1964. This confirmed that the duration of stimulation played an important role in the formation of prolonged stimulation outcomes. Most critically, results from this study emphasised that different cell types and cells at different cortical locations or with different orientations may be differentially affected by surface polarising currents.

Hence, these animal studies demonstrated that even weak direct currents applied at the scalp could reach cortical cells and induce a sufficiently large potential difference to modulate neuronal firing. Their collective findings formed the foundation for modern transcranial direct current stimulation (tDCS) as discussed in this thesis. However, although several early clinical studies reported beneficial effects of DC stimulation for the treatment of psychiatric patients (Carney et al., 1970; Costain et al., 1964; Herjanic and Moss-Herjanic, 1967; Ramsay and Schlagenauf, 1966; Redfearn et al., 1964), stimulation results in humans proved difficult to replicate and the approach was gradually abandoned (Hall et al., 1970; Lolas, 1977; Nias, 1976; Sheffield and Mowbray, 1968).

1.1.2 Contemporary methodology and conceptual models for tDCS

Interest in using weak electrical currents to non-invasively modify brain activity was rekindled at the turn of the 20th century by work from Priori et al., 1998 and Nitsche and Paulus, 2000, 2001. These studies were the first to investigate tDCS effects on cortical excitability using transcranial magnetic stimulation (TMS) and demonstrated that tDCS could induce prolonged and polarity-dependent, excitability changes in the human motor cortex.

Priori et al., 1998 used motor evoked potentials (MEPs) as a measure of cortical excitability to evaluate the impact of anodal or cathodal surface stimulation in humans.

In a series of experiments, weak DC stimulation (<0.5 mA) was applied for 7 seconds via two scalp electrodes positioned over the primary motor cortex (M1) and the chin. Motor thresholds were measured using single pulse TMS before and after stimulation. In a sample of 14 participants, cathodal tDCS at 0.3 mA did not affect motor thresholds, but anodal tDCS was associated with an average decrease in MEP amplitude of 8%. The authors interpreted this suppression as a hyperpolarising effect on superficial excitatory neurons, in line with the *in vitro* findings from Purpura and McMurtry, 1965. Moreover, a second experiment in five participants found that MEP depression following anodal tDCS increased with input current intensity (0.075–0.5 mA). However, in these initial experiments, cathodal stimulation preceded anodal stimulation within the same trial. A third experiment therefore assessed motor thresholds after anodal tDCS at 0.3 mA without prior cathodal stimulation and found no modulation of MEP size. In response, Priori et al. speculated that motor neurons might adapt to and compensate for DC stimulation and that the alternating anodal-cathodal stimulation protocol may have restrained such adaptation.

In contrast, Nitsche and Paulus, 2000 found evidence for polarity-dependent effects on excitability that followed the opposite pattern of results reported by Priori et al., 1998: anodal tDCS delivered to M1 *increased* MEP amplitude by 40%, whereas cathodal tDCS *decreased* MEPs by 30%. However, a number of methodological differences in the two studies were taken to explain their divergent findings. Firstly, the distribution of induced electric fields likely differed due to the different electrode montages (left M1 and contralateral orbita vs. M1 and chin). Secondly, the timing of tDCS delivery differed greatly: Priori et al. applied both anodal and cathodal tDCS within the same experimental session whereas Nitsche et al. tested the effects of each polarity on separate days. This approach for avoiding potential carry-over effects of stimulation has since become standard practice in the field. Stimulation sessions are commonly separated by at least 24–48 hours to allow neuronal excitability to return to baseline. Finally, Nitsche et al. varied current intensity from 0.2 to 1.0 mA and — in accordance with Priori et al., 1998 — found no after-effects for stimulation at intensities below 0.6 mA. By varying both current intensity and duration (4 s and 1–5 min), Nitsche and colleagues could show that stimulation after-effects were only elicited by sufficiently strong (1 mA, 3 min) or sufficiently long (0.6 mA, 5 min) stimulation. They concluded that excitability changes observed during 4 s of tDCS at 1.0 mA were likely due to shifts in neuronal resting membrane potentials, but that prolonged after-effects of tDCS must be produced by a different neurophysiological mechanism following on from changes in spontaneous firing.

Further support for tDCS effects on neuroplasticity was provided by a follow-up study, in which tDCS at 1.0 mA was applied to M1 for 5–13 min in steps of 2 minutes

(Nitsche and Paulus, 2001). While stimulation for 5 and 7 minutes increased MEP amplitude for up to 5 minutes post-offset, stimulation for 9, 11 or 13 minutes resulted in excitability changes for up to 90 minutes. Some inter-individual variability in effect size was observed, but, overall, results from this study were regarded as strong evidence for the ability of tDCS to non-invasively and reversibly induce lasting neuronal excitability changes.

The findings and methodology of these three studies had a seminal influence on tDCS research in the subsequent two decades. As a result, neuroscientists have once again begun to use tDCS in the hope of enhancing healthy cognitive function or alleviating neuro-psychiatric disorders. In comparison to other neuromodulatory techniques, such as TMS or deep brain stimulation, tDCS is easy-to-use, low-cost and portable, making it ideally suitable for clinical studies (Brunoni et al., 2012). The number of publications based on tDCS has been steadily rising (Santarnecchi et al., 2015), but a lack of standardisation has meant that most contemporary tDCS studies vary widely in their methodological approaches.

The effects of tDCS are thought to be primarily determined by the current dose applied at the scalp, the resulting effective polarisation of cells in the cortical area of interest, the neurophysiological response to it and the manner in which this response is measured. However, many of the factors influencing tDCS outcomes, such as trait- or state-dependent individual differences, are difficult to quantify and frequently neglected in the design and reporting of experiments.

Nonetheless, there are some basic similarities to most experimental protocols reported in the literature. Commonly, low-intensity electrical currents are applied via two large scalp electrodes placed over cortical areas considered relevant to the sensory or cognitive process of interest (see Figure 1.5 for an example of a widely used electrode montage for tDCS of the visual cortex). Electrode size typically ranges from 25–35 cm^2 and current intensity varies between 0.5–2.0 mA, resulting in current densities that fall within currently accepted safety limits (Grossman et al., 2019; Nitsche and Paulus, 2001). Stimulation is applied using carbon-filled silicone rubber electrodes which are either placed in saline-soaked sponge envelopes or prepared with a layer of conductive paste. Electrodes are most frequently positioned on the scalp according to the International 10-20 system for EEG. Alternatively, electrode placement can be guided by neuronavigation systems using participant-specific anatomical MRI data — an approach that is gaining traction, but is not yet widely used in the field.

A constant current is applied between the two electrodes, typically after gradually increasing the current over 5-30 s to minimise unpleasant skin sensations (Fertonani et al., 2015). Verum tDCS is generally applied for 5–30 minutes. Sham tDCS is most commonly achieved by briefly fading current in and out to mimic the peripheral sensations that often accompany verum stimulation (Gandiga et al., 2006). The question
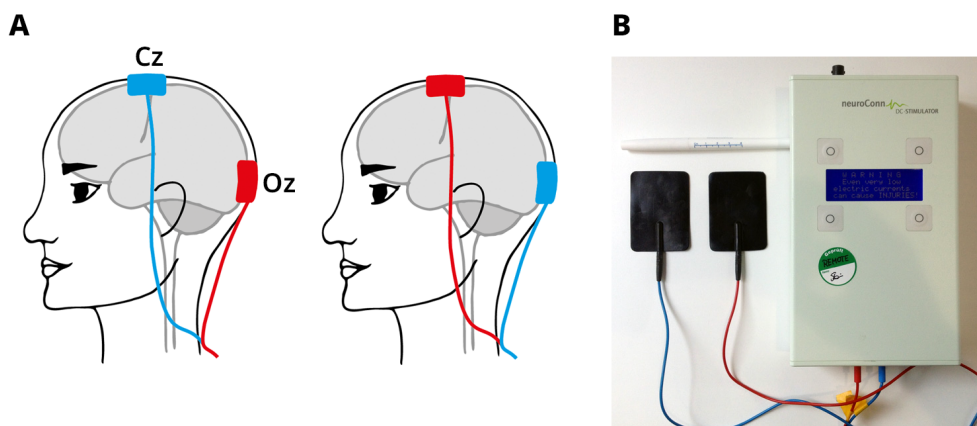
Figure 1.5: (A) Typical montage for tDCS of the visual cortex with electrodes placed over EEG positions Cz and Oz. At the scalp surface over the cortical target area, the applied current polarity is either anodal (left) or cathodal (right). (B) Stimulation device with two 5x7 cm silicone rubber scalp electrodes.

of appropriate stimulation protocols for double-blind, sham-controlled tDCS studies is discussed in further detail in Chapter 2.

Outcomes of tDCS are measured either *during* stimulation ("online") or *after* stimulation offset ("offline") and different neurophysiological mechanism of action have been proposed for online vs. offline tDCS. As discussed above, online stimulation with direct currents is widely — but perhaps simplistically — assumed to affect cortical excitability by transiently altering neuronal resting potential, thereby modulating the likelihood of neuronal firing without directly eliciting an action potential. In contrast, offline tDCS effects are now thought to involve long-term potentiation and depression-like neuroplasticity via modulated NMDA receptor-efficacy and altered intracellular Ca^{2+} levels (Stagg and Nitsche, 2011; Stagg et al., 2018). All tDCS experiments carried out as part of this thesis were based on online stimulation protocols.

Conceptual models of tDCS

The tDCS mechanisms proposed to date each attempt to describe stimulation effects at a different level of analysis. Therefore, it is unrealistic to look to any one of these mechanisms to fully explain tDCS outcomes. Without a doubt, the brain is a dynamic system whose behaviour emerges from the interactions of many minor entities of the system. Hence, we must develop suitable transfer functions for the different levels of description to gain a global perspective of tDCS in the human brain. Conceptual models of tDCS that attempt to link multiple levels of description have only recently begun to be formulated explicitly by tDCS researchers. While they all aim to conceptualise the same issue, they do so from different perspectives and make different simplifications of the brain's complexity.
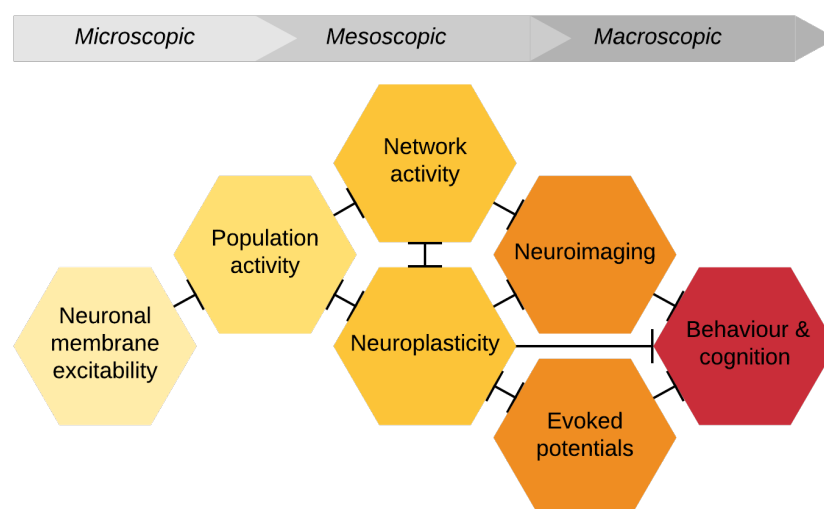
Figure 1.6: Levels of description for outcomes of direct current stimulation. To date, the transfer functions between stimulation effects spanning from the cellular level to human behaviour remain largely underdetermined; modified from Bestmann et al., 2015.

The starting point of the recent resurgence in tDCS research was the *anodal-excitation cathodal-inhibition (AeCi) model*, which assumes that the brain is a "passive" recipient of tDCS and that stimulation effects can be "dialled-up or down" by either increasing cortical excitability with anodal currents or decreasing excitability with cathodal currents. Outcomes at the neuronal level are then believed to directly relate to behaviour, e.g., stimulation with anodal tDCS depolarises the membrane potential and boosts behavioural performance on a given task. Critically, the model does not account for any of the intermediate levels involved in the mediation of stimulation effects. Such coarse simplification might be appropriate for comparatively clearly delimited phenomena such as the MEP in motor physiology, but fails to adequately explain the diverse and inconsistent findings of behavioural tDCS studies. Evidence from several recent reports has challenged the direct, linear relationship between current polarity and intensity and final stimulation outcome posited by the AeCi model (Esmaeilpour et al., 2019).

In contrast to the "static" AeCi model, the *activity-dependent model* proposes that tDCS effects depend on the state of the brain, i.e., the activity levels of neurons at the time of current stimulation. It is generally assumed that tDCS primarily targets neurons near to their firing threshold and thus only affects neurons relevant to and engaged in task execution (Bikson and Rahman, 2013; Miniussi et al., 2013). While this model expands to describing excitability increases or decreases in groups of neurons, it neglects the network-level dynamics involved in sensory and cognitive processes in the brain.

In principle, it is plausible that a *network activity-dependent model* is better-suited

to characterising high-level behavioural outcomes achieved with tDCS and could at least partially address the issue of the technique's low spatial resolution. Such a model assumes that electrical stimulation not only leads to activity-dependent modulation in the targeted cortical region but also in related networks (Luft et al., 2014). Indeed, it has been shown that neuronal networks are more affected by changes in electrical currents than the average single neuron (Francis et al., 2003). For instance, in the probable case that two functional networks overlap in a cortical region, tDCS would be expected to primarily affect the network most strongly activated by the task. A number of recent studies have supported the notion that behavioural tDCS effects depend on task-induced neural activity (e.g., Bortoletto et al., 2015; Furuya et al., 2014; Hsu et al., 2014; Tseng et al., 2012.

An alternative model proposed by Krause et al., 2013 focuses on the balance between excitatory and inhibitory cortical inputs for the maintenance of optimal brain function. Their *excitation-inhibition balance model* is based on findings from magnetic resonance spectroscopy (MRS) studies showing that anodal and cathodal tDCS affects local concentrations of inhibitory (GABA) and excitatory (glutamate) levels, respectively (Clark et al., 2011; Stagg et al., 2009; Stagg and Johansen-Berg, 2013). The authors argue that the direction of regional excitation/inhibition (E/I) imbalances, as measured by glutamate/GABA ratios, determines behavioural tDCS effects and that tDCS can be used to restore an optimal E/I balance for task performance. This model corresponds to the principles proposed by the AeCi model at a higher level and promises to explain individual differences in tDCS outcomes both in healthy and clinical populations. However, at the current stage of research, the effects of tDCS on neurotransmitter concentrations are poorly understood and the model is perhaps too general to elucidate specific tDCS outcomes. Furthermore, to fully understand the mechanism underlying E/I balance, factors such as levels of BDNF or cortical adenosine must likely also be taken into account.

More recently, the concept of limited resources in the brain, as widely used in cognitive models in psychology, has also been discussed in the context of tDCS mechanisms (Brem et al., 2014; Luber, 2014). The *zero-sum model* rests on the idea that it is impossible to boost cognitive functioning with tDCS without introducing a concurrent "loss" in another cognitive aspect. However, the validity of this model cannot easily be tested since it is difficult to measure multiple cognitive functions simultaneously. So far, only one experiment by Iuculano and Cohen Kadosh, 2013 has reported supporting evidence for the model. Moreover, the zero-sum model might easily be subsumed by network activity-dependent models.

Collectively, conceptual models of tDCS that aim to span different levels of description struggle to reduce the brain's complexity and frequently rely on overlapping or analogous conceptualisations that are difficult to test directly. While they might offer

useful *post hoc* explanations of observed outcomes, their physiological or psychological validity must be called into question. Consequently, many authors of empirical studies base their approach primarily on previously reported tDCS experiments and the development of theoretical frameworks is at risk of stagnation. If our goal is using electrical stimulation to effectively "coach" the brain in a broad range of healthy and clinical populations, the task ahead is not a trivial one.

1.1.3 You will, you won't, you do, you don't: open questions and challenges in tDCS research

The diversity of both stimulation protocols and conceptual models for tDCS is mirrored by the heterogeneity of empirical findings in the field. Recent meta-analyses across several sensory and cognitive domains indicate that there is a large variability in the results of reported studies (Dedoncker et al., 2016; Hashemirad et al., 2016; Hill et al., 2016; Horvath et al., 2014, 2015; Jacobson et al., 2011; Mancuso et al., 2016; Marquez et al., 2015; Medina and Cason, 2017; Price et al., 2015; Vaseghi et al., 2014).

Stimulation outcomes vary strongly not only in effect size but also in the direction of stimulation effects. In part, this heterogeneity can be attributed to differences in methodology. For example, the doses applied in sensory and cognitive tDCS studies are not adequately standardised, which hinders direct comparison of outcomes. Furthermore, a lack of rigorous reporting of experimental protocols impedes the collation and interpretation of published studies. However, apart from questions of methodology, researchers in the field are confronted with a variety of additional issues that contribute to the disparate findings reported in the literature.

First and foremost, both theoretical considerations and recent empirical findings suggest that the classic assumption of "anodal = excitatory" and "cathodal = inhibitory" is grossly oversimplified. As discussed above, this concept originated from a series of landmark animal studies in the 1960s, which demonstrated that anodal DC stimulation enhanced firing rates whereas cathodal DC stimulation reduced firing rates (Bindman et al., 1962; Creutzfeldt et al., 1962; Purpura and McMurtry, 1965). It is now well established that this form of DC stimulation concurrently affects both synaptic input and spiking output. Animal studies have shown that measures of synaptic input, such as pre-synaptic activation and synaptic transmission, as well as output response measures, such as firing rate or network oscillations, are modulated by exogenous direct currents (e.g., Baczyk and Jankowska, 2014; Bolzoni et al., 2013; Jefferys, 1981; Márquez-Ruiz et al., 2012; Rahman et al., 2013; Reato et al., 2010), This, however, has raised the question of how much changes in firing behaviour are caused by synaptic currents entering the neuron as opposed to changes in the neuron's responsiveness. A recent study integrated results from an *in vitro* experiment and computational models

to show that DC stimulation leads to opposing polarisation of the neuronal soma and dendrites (Lafon et al., 2017). Results suggested that, for anodal stimulation, these effects combine to simultaneously increase the driving force of synaptic activity and the probability of spiking at the soma. In contrast, for cathodal stimulation, the opposing effects on soma and dendrites tend to cancel out. Consequently, an asymmetry in the strength of anodal and cathodal stimulation is to be expected.

However, the validity of these findings for transcranial stimulation in humans is still unclear. Not only do human behavioural studies test a limited range of current intensities (0.5–2 mA), which translate to lower polarisation than that of corresponding fields in animal studies, but it has also proven difficult to extrapolate from rigorously controlled *in vitro* or *in vivo* animal studies to the much more complex morphology of functionally cohesive cortical areas in humans.

This is perhaps exemplified by a meta-analysis of tDCS studies by Jacobson et al., 2011, which showed that the likelihood of achieving the classic AeCi effect was 67% for motor tDCS studies, but only 16% for cognitive tDCS studies. Moreover, this difference was primarily driven by the difficulty of achieving cathodal-inhibitory effects in the cognitive (0.48) vs. motor domain (0.87). Unfortunately, we presently lack critical insights on so many intermediary levels of description that it is unclear if these findings are due to (1) cathodal effects being more difficult to achieve at the cellular level, as suggested by Lafon et al., 2017, (2) motor tDCS studies having primarily relied on MEPs to assess motor cortex stimulation — a comparatively well-constrained outcome measure for tDCS in humans, (3) cortical and/or cell morphology in the motor cortex being more amenable to exogenous polarisation or (4) a combination of all of these factors.

Laminar structure and cell morphology differ to some degree both between species and cortical regions. Radman et al., 2009 examined neuronal morphology in rat motor cortex slices and concluded that larger, more asymmetric cells have higher maximum somatic polarisation length. Therefore, they predicted that the soma of layer V pyramidal neurons is most sensitive to polarisation by optimally oriented, subthreshold electric fields. A distinguishing feature of the motor cortex is the existence of Betz cells in layer Vb. These giant pyramidal neurons can have a diameter up to 100 μm and display a great number of primary dendritic shafts branching out from the soma at many different points (Braak and Braak, 1976; Meyer, 1987; Rivara et al., 2003). Due to their unique morphology, Betz cells could thus constitute a critical factor in the divergent stimulation outcomes of tDCS in the motor cortex vs. other cortical areas (see Horvath et al., 2014, for a review).

In addition, the effects of tDCS are also determined by the orientation of neurons relative to the electrical field (Purpura and McMurtry, 1965; Ranck, 1975). It has been proposed that a radial current flow along the axon is most effective at eliciting somatic

polarisation, whereas tangential currents are most effective at causing terminal polarisation (Rahman et al., 2013). Consequently, cortical folding is a key factor for the overall outcome of stimulation. The uniform currents applied in most animal studies are unlikely to occur in human electrical stimulation where much larger cortical areas are targeted and induced electric fields are much more diffuse. This difference is likely to significantly confound any meaningful comparison of animal and human findings.

Based on these considerations, it seems highly implausible that an electrical field applied via large scalp electrodes would be globally depolarising or hyperpolarising, as has commonly been assumed in human tDCS studies based on the AeCi model. Indeed, numerous recent studies have highlighted that tDCS effects are complex and can become non-linear under certain conditions. For instance, contrary to findings reported in the seminal paper by Nitsche and Paulus, 2000, increasing stimulation intensity does not necessarily increase stimulation efficacy (Bastani and Jaberzadeh, 2013; Kidgell et al., 2013) and might instead change the direction of excitability alterations (Batsikadze et al., 2013). Esmaeilpour et al., 2019 recently concluded that while physical models predict electric fields in the brain to increase with the applied current intensity at the scalp, current empirical evidence is insufficient to support the assumption of a simple, monotonic relationship between electric field intensity in a given brain region and the effect size of neurophysiological or behavioural changes. Beyond stimulation intensity, the timing of stimulation also potentially contributes to non-linear effects of tDCS. Contradicting outcomes of online vs. offline tDCS have been established in the context of motor (Sriraman et al., 2014; Stagg et al., 2011a) and cognitive performance (Martin et al., 2014; Ohn et al., 2008).

However, perhaps the most significant methodological challenge in tDCS research today is posed by the considerable number of inter- and intra-individual factors that are involved in determining stimulation outcomes but are difficult to adequately quantify and control for. On the one hand, trait-dependent differences between participants, e.g., in neuroanatomy, neurochemistry or baseline level of function, undoubtedly shape tDCS effects. On the other hand, experiments are additionally confounded by a variety of state-dependent aspects, such as the participant's levels of satiation, fatigue, metabolism or hormonal balance at the time of data collection. In turn, both trait- and state-dependent factors interact with the large variability in methodological protocols.

In recent years, several empirical studies have attempted to quantify intra- and inter-individual variability in response to non-invasive brain stimulation protocols in general, and to tDCS in particular (e.g., Ammann et al., 2017; Chew et al., 2015; Dyke et al., 2016b; Li et al., 2015; López-Alonso et al., 2014, 2015; Strube et al., 2015; Tremblay et al., 2016; Wiethoff et al., 2014). Once more, differences in the precise

methodology impede a clear comparison, but the emerging consensus appears to be that a considerable proportion of participants do not respond as expected.

A review by Li et al., 2015 identified that factors resulting in differences in the direction of tDCS-induced change are likely to introduce more variability at the group level of analysis than factors that only affect the size of the induced change. The authors propose that best practice may be to homogenise participants in the factors that are easiest to control, such as age and baseline ability. Furthermore, they argue that the impact of inter-individual differences depends on experimental design: while data collected in crossover designs is more affected by order or learning effects, cross-section studies are particularly vulnerable to the effects of inter-individual variability since tDCS intervention (anodal, cathodal or sham) becomes a between-subject factor.

López-Alonso et al., 2015 acquired data from 45 participants and reported that, across two sessions separated by at least six months, intra-individual variability is lower than inter-individual variability. In their sample, 53% and 58% of participants responded to anodal tDCS with the expected excitatory effect in the first and second session, respectively, and 78% of the "responders" in the first session showed a consistent response in the second session. In addition, their findings suggest that a change in cortical excitability during the first 30 min after stimulation offset is a predictor of the response in a subsequent session.

In a related experiment, Chew et al., 2015 explored inter-individual differences at a range of current intensities (0.2, 0.5, 1.0 and 2.0 mA) as well as intra-individual reliability across two identical anodal tDCS sessions in 29 participants. They found that stimulation at 0.5 mA was less effective at eliciting a response compared to 0.2 or 2.0 mA. At a group level, none of the different current intensities induced a significant increase in excitability compared to baseline. However, further analysis revealed distinct clusters for the 0.2 and 2.0 mA conditions and identified different groups of responders within each condition. Test-retest reliability was also evaluated for two sessions at 0.5 mA, but found to be very low at an individual level.

Another study by Wiethoff et al., 2014 compared 10 min of anodal and cathodal tDCS at 2.0 mA in 53 participants and found that anodal stimulation facilitated MEPs, whereas cathodal stimulation elicited no significant effect. A cluster analysis revealed that roughly 50% of participants in the sample had no or only a small response and the remaining half of participants showed an excitatory effect for both current polarities.

Strube and colleagues, 2015 compared responders and non-responders for 13 min of 1.0 mA anodal tDCS and paired-associative stimulation (PAS25) protocols in a sample of 30 participants. Contrary to other recent results, both protocols lead to significant group-level effects. Overall, for a >150% cut-off relative to baseline MEP values, 17% of their participants responded to both stimulation types, 33% responded only to PAS and 7% only to tDCS, whereas 46% of participants showed no effects. For tDCS

stimulation, they also found that responders showed higher intracortical facilitation at baseline.

Reflecting the field's general bias towards the motor domain, most studies on the variability of tDCS effects have focused on the motor cortex. It is therefore crucial to note that MEPs — the current "gold standard" measure of tDCS outcomes in the motor cortex — are subject to similar, but critically independent, inter- and intra-individual variability as tDCS (Li et al., 2015).

At present, no consensus on the most appropriate techniques and criteria to further categorise experimental participants as "responders" or "non-responders" has been reached amongst researchers in the field (Pellegrini et al., 2018). However, collectively, these studies provide compelling evidence for the need for the development of predictive markers for individualising or "titrating" the amount of current delivered by tDCS.

An obvious starting point to address this issue is the computational modelling of anatomical and functional cortical differences between participants. Both commercial and open-source software packages have recently started to become available to researchers interested in simulating tDCS-induced electric fields in the brain (Dannhauer et al., 2012; Dougherty and Turner, 2016; Huang et al., 2019; Lee et al., 2017; Saturnino et al., 2018). These finite-element modelling (FEM) pipelines are based on individual anatomical MR images and have provided support for the notion that anatomical heterogeneity across participants poses a significant confound, with electric fields in cortical target regions varying by up to 100% across individuals (Datta et al., 2012; Laakso et al., 2015; Opitz et al., 2015).

While the literature on simulation studies of tDCS is growing quickly, many model parameters are not yet well-established (Ruffini et al., 2013; Saturnino et al., 2019). For instance, the precise values and impact of different brain tissue properties and of tissue anisotropy are still a matter of debate. Moreover, by and large, the empirical validation of electric field stimulations yet remains to be tackled (Bestmann and Ward, 2017). Currently, the literature of studies combining FEM with behavioural or neurophysiological data on tDCS effects is extremely sparse. Chapter 4 of this thesis explores this issue in further detail.

Nonetheless, electric field modelling can not only inform behavioural studies but can also be fruitfully integrated with neuroimaging. After all, even if anatomical variability was perfectly captured by FEM based on anatomical MRI data, functional variability might not relate to the exact same anatomical features across individuals (Amunts et al., 2007; Roland and Zilles, 1998). Thus, electric field modelling and neuroimaging can be mutually informative.

The integration of tDCS with neuroimaging offers a promising opportunity to shed light on the physiological mechanisms of tDCS in humans and to optimise stimulation

protocols. Interactions between behavioural stimulation effects and neural activity can be characterised, linking different levels of description for stimulation outcomes. Therefore, in spite of inherent technical challenges (*cf.* Chapters 5 and 6), a growing body of work has explored the feasibility of combining electrical brain stimulation with neuroimaging (Bergmann et al., 2016).

The effects of tDCS have been investigated using functional magnetic resonance imaging (fMRI) and magnetic resonance spectroscopy (MRS; Turi et al., 2012), arterial spin labelling (ASL; Stagg et al., 2013; Zheng et al., 2011) and near-infrared spectroscopy (NIRS; Dutta, 2015; McKendrick et al., 2015), as well as electrophysiological techniques such as magnetoencephalography (MEG; Hanley et al., 2015; Marshall et al., 2015; Noury et al., 2016; Soekadar et al., 2013) and electroencephalography (EEG; Faria et al., 2012; Gebodh et al., 2019).

Depending on the imaging modality, a host of practical concerns arise when combining tDCS with neuroimaging, but common to all approaches is the question of whether to acquire data sequentially or simultaneously. The latter approach, where electrical stimulation is applied *during* neuroimaging, offers several advantages. First, both during and after tDCS it is preferable to limit the participant's movement and uncontrolled sensory stimulation to avoid confounding effects. It is therefore more practical for the participant to already be situated in the scanner when tDCS is applied. Secondly, concurrent acquisition provides a context-specific baseline for comparing neural activity pre-, peri- and post-tDCS. Finally, while many tDCS studies in humans have focused on tDCS after-effects, concurrent data acquisition allows to read out immediate effects arising during or just seconds after stimulation is applied.

Thus, such multimodal approaches pose certain constraints, but can be valuable in bridging the gap between neuronal and behavioural stimulation effects if current technical and conceptual limitations are carefully considered in the experimental design.

1.2   Aims and structure of this thesis

In summary, tDCS research is currently confronted with a wide variety of conceptual and methodological challenges that have hampered the development of mature rationales for its use in healthy and clinical populations. Consequently, criticism of transcranial electrical stimulation has recently become more vocal. It is incumbent upon researchers to now direct the field toward a more unified conceptual framework and well-characterised, reliable stimulation protocols.

To understand the true effects of tDCS on human behaviour, we must not only characterise the electric fields induced in the brain and how they affect cells in a given

target region but also the consequences of altered cellular activity for computations carried out by this region and the subsequent effects on participant behaviour (*cf.* Figure 1.6).

In developing such a comprehensive description, less complex experimental paradigms based on simple sensory stimuli and behavioural demands are likely more useful than paradigms that are ethologically much less plausible, such as TMS-induced MEPs and visual phosphenes, or paradigms investigating higher-order cognitive functions. Studying tDCS effects in a sensory system such as vision seems a fruitful place to begin to explore their underlying mechanisms. The neural correlates of visual stimulus processing have been extensively investigated and are currently better understood than those underlying other sensory systems. In particular, low-level stimulus processing in the early visual cortex, such as the integration of information on stimulus contrast and orientation, is comparatively well-described.

This thesis aimed to address several current methodological challenges in tDCS research by bringing together behavioural and neuroimaging data on tDCS outcomes, as well as findings from participant-specific models of induced electric fields. Experiments focused on the visual system, using relatively simple paradigms based on pattern-reversing checkerboards or the detection of achromatic dot stimuli to investigate tDCS effects on visual processing. The role of inter-individual variability — both in baseline sensory performance and in head anatomy — received particular attention in the study designs.

In Chapter 2, the question of suitable stimulation protocols for double-blind, sham-controlled tDCS studies of the visual cortex is discussed. Chapter 3 investigates the role of electrode montage in eliciting tDCS effects on contrast detection. In Chapters 4, 5 and 6 the role of inter-individual differences in anatomy is explored using computational modelling and neuroimaging methods. Chapter 7 provides a summary of the thesis, discusses the main findings in relation to each other and highlights points for future research. The remainder of the present chapter gives a brief overview of the structure and function of the visual system and introduces the methodological background of psychophysical, neuroimaging and modelling work presented in this thesis.

1.3 Structure and function of the visual system

Humans, like all primates, rely heavily on visual information for both basic adaptive behaviours (e.g., finding food or shelter) and more complex social behaviours (e.g., nursing offspring). Consequently, brains have adapted to absorb, integrate and react to visual information in increasingly effective ways throughout the course of evolution.
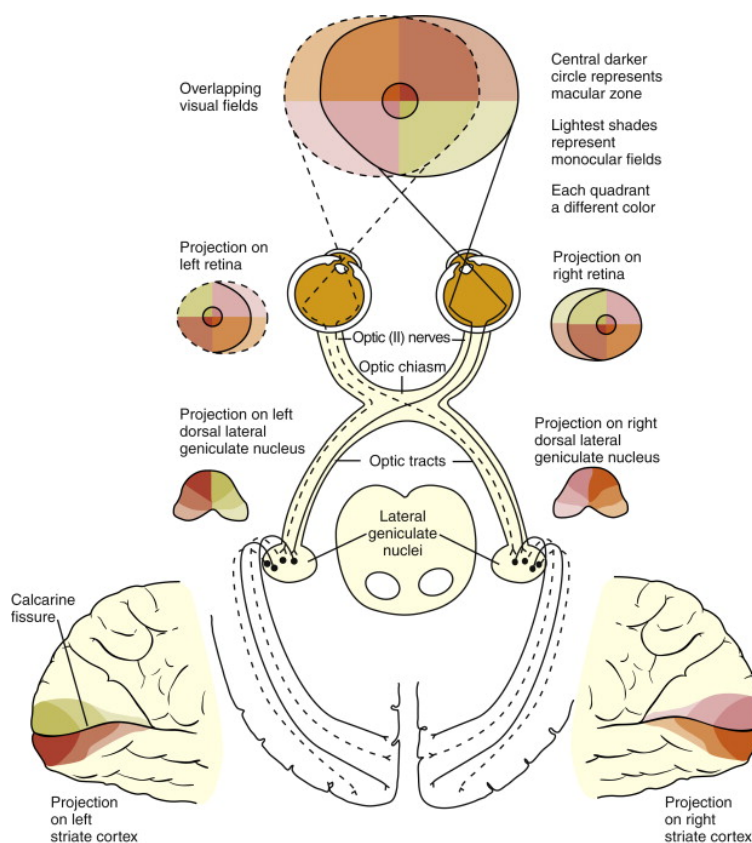
Figure 1.7: Diagram of the visual pathway from the eye to the primary visual cortex; reproduced from Remington, 2012.

In primates, a large proportion of the brain subserves vision. Visual perception emerges from an interaction of cellular activity in the retina, thalamic nuclei and multiple areas of the cerebral cortex (Kandel et al., 2013). The pathway carrying visual information from the environment to the brain includes the retina, optic nerve, optic chiasm, optic tract, lateral geniculate nuclei (LGN), optic radiations, primary visual cortex (also referred to as striate cortex or V1) and extrastriate cortex (Figure 1.7).

Hubel and Wiesel first proposed that receptive fields (RFs) of cells at one level of the visual system are effectively shaped by the input from cells at a lower level of the system (1962). Their theory was subsequently adapted to include "top-down" feedback loops, allowing cells at a higher level to modulate the activity of cells at a lower level. Over the past century, receptive fields have been mapped for cells at all levels of the visual system, from retinal photoreceptors to extrastriate cortical cells. Due to the existence of feedback loops across the whole system, any "local" description of a given receptive field is, however, inevitably incomplete.

The first step in the visual pathway is the transformation of energy from reflected light into bioelectric signals by photoreceptor cells in the retina. The retina adapts flexibly to changing conditions for vision, such as the large diurnal variations in illumination. There are two different types of photoreceptors encoding the visual image

in different intensity ranges — rods and cones. Cones are highly concentrated in the fovea at the centre of the visual field. They respond rapidly to light, confer colour vision and serve photopic vision (i.e., under high or day light conditions). In contrast, rods respond to light more slowly, confer achromatic vision and underlie scotopic vision (i.e., under low light or night-time conditions). They are much more numerous than cones and are primarily located in the periphery and absent in the fovea.

Both photoreceptors types signal the absorption of photons via a decrease in glutamate release to bipolar cells. Cones connect directly to bipolar cells, which subsequently excite retinal ganglion cells, whereas rods synapse onto specialised rod bipolar cells whose signals are linked via amacrine cells to the cone bipolar cells. These vertical, excitatory pathways are modulated by primarily inhibitory, horizontal connections. The organisation of ganglion cell receptive fields enables the detection of contrast, for example in the perception of object edges. Each RF is organised into a central region, the "centre", and a concentric ring around it, the "surround". The two areas respond oppositely to light and are mutually inhibiting. For instance, light in the RF centre might increase the firing rate of a ganglion cell, whereas light in the surround would decrease its firing. Uniform stimulation of both centre and surround would elicit a response corresponding to stimulation of the centre, but with a much smaller amplitude.

To date, about 20 different types of ganglion cells selectively tuned to detect different stimulus aspects have been identified. Cells cover the retina in an interleaved fashion such that any point on the retina lies within the RF centre of at least one ganglion cell. If one conceptualises each cell population as transmitting a distinct neural representation of the visual field, the firing behaviour of a single ganglion cell can be interpreted as one pixel. Thus, about 20 neural representations of visual input are conveyed to the brain, differing in polarity (ON vs. OFF), temporal responsiveness (sustained vs. transient), spatial resolution (fine vs. coarse), spectral filtering (broadband vs. dominated by R/G/B colour) and selectivity for other stimulus features, such as motion. Interestingly, recent work has uncovered the presence of an additional photoreceptive mechanism in the form of ganglion cells that are intrinsically light-sensitive based on the expression of melanopsin. Zaidi et al., 2007 found that blind patients without functional rods and cones retained circadian, neuroendocrine and neurobehavioral responses to light and even displayed visual awareness of light. These findings challenge the conventional assumption that "visual" responses to light are exclusively mediated by rod- and cone-based photoreception.

All primates share two main pathways from the eye to the brain. The extrastriate pathway is formed by retinal ganglion cells that project to the superior colliculus (SC) in the midbrain. The geniculostriate pathway begins with an overlapping group of retinal ganglion cells whose axons exit the retina via the optic nerve, cross the optic

chiasm and terminate at the dorsal lateral geniculate nuclei (LGN), from where cells project to the primary visual cortex.

In each hemisphere, the LGN receives a retinal signal from both eyes but only one half of the visual field. Within the LGN, information about the eye of origin is preserved since fibres from each eye connect to different LGN layers. The interleaved magnocellular, parvocellular, and koniocellular layers of the LGN receive signals from correspondingly-named types of retinal ganglion cells — "P" ganglion cells transmit information from rods and synapse onto the parvocellular layer, "M" ganglion cells transmit information from cones and connect to the magnocellular layer, and "K" ganglion cells send axons to the koniocellular layer. The role of koniocellular cells remains unclear, but is hypothesised to involve the processing of information from short-wavelength "blue" ON-cells (Martin et al., 1997).

The lateral geniculate nuclei have commonly been characterised as passive "relay" stations between retina and cerebral cortex. However, new evidence suggests that the LGN receive strong feedback connections from V1 and numerous other brain structures (Cudeiro and Sillito, 2006; Guillery and Sherman, 2002). Moreover, neuroimaging studies have demonstrated that directed attention to a spatial location can modulate neural activity in the LGN (Kastner et al., 2006).

The spatial position of ganglion cells within the retina is maintained in the spatial organisation of cells within the LGN layers. This retinotopic organisation is also preserved in the primary visual cortex. However, the visual field image is rotated both horizontally and vertically within V1 (e.g., cells in the upper right bank of the calcarine sulcus respond strongly to the lower left visual field, *cf.* Figure 1.7).

Visual performance crucially depends on the amount of cells dedicated to a task, and the same "cortical magnification" between the peripheral receptor density and cortical areal representation seen in primate auditory and somatosensory cortices is also found in vision. Among primates, a large portion of V1 is mapped to the small, central portion of the visual field — cells processing input from the fovea are about 30-100 times more prevalent than cells processing stimuli from the visual periphery (Daniel and Whitteridge, 1961; Strasburger et al., 2011). The cortical magnification factor M was originally defined by Daniel and Whitteridge, 1961 as the diameter in V1 (i.e., mm of cortical surface) onto which 1 degree of the visual field projects. The inverse of M increases linearly with eccentricity in the visual field. If a large number of cells are devoted to a small visual angle, high processing capacity is assigned to a small area of the visual field. A consequence of this organisation is that visual acuity is best in the centre of the visual field and poorest in the far periphery. In psychophysical experiments on vision, performance variations across the visual field are therefore often equalised by increasing the stimulus diameter depending on eccentricity. For example, this is typically done in automated threshold perimetry protocols used to
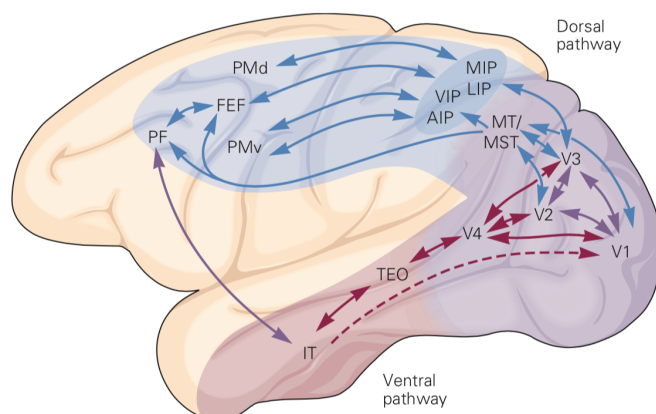
Figure 1.8: Cortical areas involved in visual processing. In the macaque monkey, areas V1, V2, V3, V4 and MT integrate local stimulus features to construct contours and surfaces, and to segregate foreground from background. (AIP, anterior intraparietal cortex; FEF, frontal eye fields; IT, inferior temporal cortex; LIP, lateral intraparietal cortex; MIP, medial intraparietal cortex; MST, medial superior temporal cortex; MT, middle temporal cortex; PF, prefrontal cortex; PMd, dorsal premotor cortex; PMv, ventral premotor cortex; TEO, occipito-temporal cortex; VIP, ventral intraparietal cortex; V1, V2, V3, V4, primary, secondary, third and fourth visual areas; reproduced from Kandel et al., 2013.

determine contrast detection thresholds. It is worth noting here that in the perimetric experiments presented in this thesis (*cf.* Chapter 3) stimulus size was *not* adjusted to compensate for cortical magnification. However, differences in visual performance across the visual field varies widely between different visual functions, such as spatial acuity, pattern recognition or motion perception, and cortical magnification is only one of many factors that determine visual performance.

The primary visual cortex is organised in columns of neurons tuned to specific stimulus characteristics. Hubel and Wiesel, 1962 described two different types of cells in V1, "simple" and "complex" cells, which are selective to stimuli of different spatial orientations. Simple cells are found mainly in layers 4 and 6 of V1 and have distinct excitatory and inhibitory regions within their receptive fields. Complex cells are found mainly in layers 2, 3 and 5 and have overlapping ON and OFF regions, i.e., they respond continuously as a line or edge crosses the RF along an axis perpendicular to the RF orientation.

Signals from the retina representing stimulus contrast and movement are processed in V1 to analyse the shape of objects. In two distinct stages, the cortex first identifies object boundaries, which are represented by multiple fragmented lines with a specific orientation (low-level processing), and then integrates this information into a prototypical object representation (intermediate-level processing).

A typical visual scene encompasses a large number of line segments and surfaces. Consequently, the task of determining which elements belong to the same object is a highly complex problem. To overcome this ambiguity, neuronal response in the visual

cortex is strongly context-dependent. In addition, multiple feed-forward, as well as horizontal and feedback connections exist between V1 and extrastriate regions of the visual cortex (Figure 1.8). Moreover, intermediate-level vision is not just a "bottom-up" process but is also influenced by "top-down" feedback information from higher-order cortical areas. The functional properties of neurons in the visual cortex can therefore be modulated by visual experience, perceptual learning, attention or expectation.

1.4   Psychophysics

1.4.1   Measurement of detection thresholds

The term *psychophysics* was first introduced by Gustav Theodor Fechner, a German philosopher, physicist and early experimental psychologist. In his seminal work *Elemente der Psychophysik* (1860; *Elements of Psychophysics*), Fechner proposed that mind and body, while seemingly separate entities, were, in fact, different aspects of the same reality. In his view, the mind was amenable to measurement and mathematical description, and therefore psychology had the potential to become a quantifiable science.

In 1824, the German philosopher J. F. Herbart had expressed the idea that mental events had to cross a limen between the conscious and unconscious — they had to be stronger than some critical threshold to be consciously experienced (Herbart, 1824). Fechner applied Herbart's concept to the measurement of the human sensory system and developed experimental methods for relating subjective sensation to the physical magnitude of stimuli. Importantly, he expanded on the principle of the *just-noticeable difference* (JND), previously proposed by Ernst Heinrich Weber (1834). The JND, or *difference threshold*, is the minimal difference between two stimuli that leads to a change in conscious experience.

Fechner conceived of the JND as a basic unit of measurement for sensation magnitude — the "atom" of psychological experience. Critically, he made two assumptions: (1) that the JND is a constant fraction of the stimulus, and (2) regardless of its size in physical units, the JND constitutes the smallest detectable increment in sensation and is therefore always subjectively the same size, i.e., one JND is perceptually equal to another JND. Based on these assumptions, he developed a scale of sensation magnitude by counting JNDs, where the zero point on the scale was represented by the intensity in physical units of a stimulus at the boundary between sensation and no sensation (i.e., the *absolute threshold*).

The non-linear relationship between psychological sensation and the physical intensity of a stimulus is formalised by the Weber–Fechner law given in Equation 1.1:

as stimulus intensity increases, greater and greater changes in intensity (ϕ; in units above absolute threshold) are required to change the magnitude of sensation (ψ) by a constant amount. The value of the constant multiplier k depends on the particular sensory dimension and modality.

$$\psi = k \, log \, \phi \qquad (1.1)$$

For over a century, Fechner's work was widely accepted in psychology and the concept of a *sensory threshold* became central to psychophysics. However, later research showed that the law proposed by Fechner applied only within the midrange of stimulus intensity but not at the extremes. Moreover, contrary to the notion that all JNDs are subjectively equal, studies aiming to measure JNDs suggested that the difference threshold was not a fixed quantity for some sensory modalities, such as the duration of sound or the intensity of electric shocks (e.g., Durup and Piéron, 1932; Stevens, 1936; Stevens et al., 1958). Stevens re-formulated the relationship between stimulus intensity and sensory magnitude as the power law given in Equation 1.2 (Stevens, 1960).

$$\psi = k \, \phi^n \qquad (1.2)$$

If the power represented by n is less than 1, this equation roughly corresponds to Fechner's law; if $n = 1$, the equation represents stimuli that are subjectively judged to be very similar to their objective intensity, such as the duration of sound; and if the exponent is greater than 1, the equation describes stimuli whose subjective magnitude exponentially increases with their physical intensity, such as electric shocks. Just as Fechner's law, Steven's law is an approximation that is primarily accurate for the midrange of stimulus intensities and varies across repeated measurements and individuals.

In modern psychophysics, the JND has therefore been redefined as the stimulus difference that can be discriminated with a certain probability, such as 50% or 75%. For example, a contrast detection threshold is defined as the minimum amount of contrast required for a visual stimulus to be just detectable. In the context of this thesis, detection thresholds were determined at the 50% performance level.

1.4.2 Automated threshold perimetry

The term *perimetry* refers to the systematic measurement of visual field function. References to the evaluation of the visual field date back to Archaic Greece, when Hippocrates described hemianopsia in the 5th century B.C. (Johnson et al., 2011; Lascaratos and Marketos, 1988). However, until the mid-19th century, visual field testing was mostly qualitative. The introduction of quantitative visual field measurements to

clinical ophthalmology is widely attributed to Albrecht von Graefe and his work on glaucoma (Graefe, 1856).

Over the past 150 years, a multitude of quantitative perimetric methods has been developed. An early example is the tangent screen procedure popularised by Danish ophthalmologists Jannik Peterson Bjerrum and Henning Rønne (Bjerrum, 1889). Using this approach, small targets (typically white, grey or coloured beads) were presented on the tip of a wand in front of a uniformly dark, flat screen. However, this method was limited to measuring the central 30° radius of the visual field. To overcome this, Aubert and Förster introduced the arc perimeter, which could be used to evaluate the full visual field but failed to provide a consistent background adaptation level (Johnson et al., 2011). To address this problem, Hans Goldmann developed the bowl perimeter in the 1940s (Goldmann, 1945, 1946). With the Goldmann perimeter, uniform background illumination could be achieved for the whole visual field and stimuli could be projected onto the background to measure the difference threshold. In his work, Goldmann systematically explored the relationship between stimulus intensity, stimulus size and background luminance and his contributions were hugely influential in standardising perimetry.

However, the Goldmann perimeter did not eliminate all sources of variability — stemming from the instrumental hardware, examiner and patient. In the 1970s, the issue of error and variability in perimetry was widely recognised and discussed (Fankhauser et al., 1977a; Heijl and Krakau, 1975; Lynn, 1969; Portney and Krohn, 1978). It was proposed that, while patient-related variability was difficult to minimise, examiner-related error could be reduced by automating the measurement procedure. Initial attempts to automate the kinetic aspects of the Goldmann perimeter were hampered by technical difficulties and failed to improve on manual kinetic perimetry (Fankhauser et al., 1977a; Gloor, 2009; Portney and Krohn, 1978). Consequently, subsequent efforts focused on developing automated methods for *static* perimetry. Frank Frankhauser and his team were successful in developing the first truly automated visual field device, the Octopus perimeter, which is still commercially available nearly five decades later (Bebie et al., 1976; Fankhauser et al., 1977b). Numerous other automated and semi-automated perimeters have been introduced since and the Octopus has been superseded by the Humphrey Field Analyzer as the reference standard for perimetry (Johnson et al., 2011; NICE, 2017).

Visual stimulus parameters

Today, Goldmann kinetic perimetry and threshold static automated perimetry continue to be the most widely used methods of perimetry. In kinetic perimetry, a stimulus is moved from a subthreshold area to a suprathreshold area at a standardised speed

and the location where the stimulus is first detected is recorded. In static perimetry, stationary stimuli are presented at fixed points in the visual field.

Due to the spatial summation of visual information, larger stimuli are more likely to be seen (Jonson et al., 1978). Modern perimeters frequently follow Goldmann's convention for stimulus size, which defines six different stimulus sizes denoted by 0 and Roman numerals I through V (Goldmann, 1945, 1999). Each stimulus covers a four-fold larger area, ranging from 0.002 deg^2 to 2.32 deg^2. Static and kinetic perimetry typically rely on different stimulus sizes: kinetic procedures use Goldmann I stimuli (0.01 deg^2) of fixed luminance, whereas static procedures most commonly use Goldmann III stimuli (0.15 deg^2) with varying luminance.

The human brain is sensitive to very fast temporal changes in visual input, but under certain conditions, the visual system also integrates information for substantial periods of time, for instance, in low contrast settings. For stimuli up to several hundred milliseconds in duration, temporal integration in the visual system follows Bloch's law (Bloch, 1885): the visibility of otherwise identical stimuli is determined only by the product of their luminance and duration (i.e., their energy). If the luminance of a stimulus is reduced by 50%, the stimulus can still be detected if its duration is doubled. Equally, a static stimulus presented for 2 ms will be roughly twice as visible as one presented for 1 ms. Beyond a certain stimulus duration, further exposure to the stimulus will not lead to higher detectability. Temporal summation is considered largely complete by 100 ms and automated perimeters typically employ stimulus durations of 100 or 200 ms (Haag-Streit AG, 2014; Zeiss, 2014a,b).

The contrast detection experiments reported in this thesis were based on a static automated perimetry procedure, in which Goldmann III-equivalent stimuli were presented for 200 ms on a standard Goldmann background of 10 cd/m^2.

1.4.3 Psychometric functions and the method of constant stimuli

Psychometric functions relate the observer's behaviour on a given psychophysical task (e.g., proportion of correct responses on a detection task) to a physical property of the stimulus (e.g., its luminance contrast). Typically, psychometric functions are measured with the aim of summarising behaviour using one or more parameters, i.e., a threshold contrast in the case of automated threshold perimetry. An in-depth discussion of psychometric function fitting is beyond the scope of this thesis, but the general rationale is briefly summarised here.

The key aspects of measuring and estimating psychometric functions are: (1) selecting appropriate stimulus levels; (2) choosing a function to fit the data; (3) fitting the function; (4) estimating the errors associated with the function's parameters estimates; (5) evaluating the function's goodness-of-fit.

Method of constant stimuli

The first step in using forced-choice procedures such as static threshold perimetry is to select stimulus intensities that will optimally sample observer response. A common approach is the method of constant stimuli (MOCS), which was taken in the psychophysical experiments presented in Chapters 3 and 4. With this non-adaptive technique, the stimulus intensity in each trial is randomly selected from a pre-determined set of values. The range of luminance values is chosen to span the expected perceptual threshold such that observer performance ranges from never detected (i.e., 0% seen) to always detected (i.e., 100% seen). Each stimulus intensity is randomly presented to the observer many times over the course of the procedure. For each stimulus value, the number of trials where the observer responded correctly is calculated and used to construct a frequency-of-seeing (FOS) curve. If an appropriate psychometric function is fitted to the data, this method provides accurate estimates of the perceptual threshold (α) as well as other parameters, such as the function's slope (β).

Some pilot data is usually acquired to obtain a first, rough estimate of α — often using an adaptive staircase procedure, where the stimulus intensity in each trial is determined based on the response in the previous trial. This pilot data is then used to select an appropriate range of stimulus values for the method of constant stimuli procedure. In addition, the number of presentations per stimulus level and their position on the FOS curve have been shown to affect the threshold and slope parameter estimates. Hill (2001) investigated the effect of different sampling schemes for Yes/No and 2-AFC psychophysical procedures and found that a given sampling procedure may be optimal for theshold estimation but sub-optimal for estimating the slope, and vice versa. While not completely identical, the Yes/No design described by Hill (2001) closely approximates the contrast detection task used in this thesis and informed our sampling strategy, which comprised of eight stimulus intensities and 15 presentations per intensity value. This approach represented a compromise to ensure that both threshold and slope of the psychometric function could be estimated with sufficient accuracy. A detailed description of our sampling procedure is provided in Chapter 3 and illustrated in Figure 3.4.

Psychometric function fitting

Equation 1.3 gives the generic form of the psychometric function $\psi(x)$ specifying the relationship between the probability of a correct response and the stimulus strength x (Wichmann and Hill, 2001).

$$\psi(x; \alpha, \beta, \gamma, \lambda) = \gamma + (1 - \gamma - \lambda)F(x; \alpha, \beta) \qquad (1.3)$$
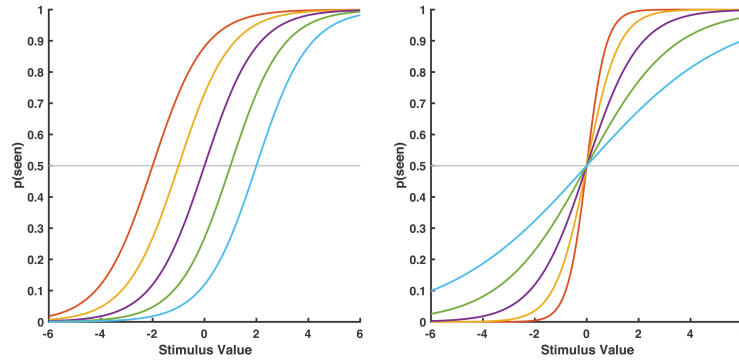
Figure 1.9: *Left:* Examples of psychometric functions with different thresholds (50% seen) but the same slope; *Right:* Psychometric functions with the same threshold but different slopes (MATLAB code courtesy of https://davehunter.wp.st-andrews.ac.uk/2015/04/12/fitting-a-psychometric-function, accessed on 07/11/17).

As illustrated in Figure 1.9, the FOS curve typically takes a sigmoidal shape with asymptotes at sub- and supra-threshold stimulus levels. The shape of the curve is determined by the parameters α (threshold), β (slope), γ (guess rate), λ (lapse rate) and *F*, which is usually a sigmoid function such as the logistic, cumulative normal, Weibull or Gumbel distribution. Based on the findings reported by Rountree (2018), the psychometric functions presented in this thesis were fitted using a logistic distribution. The lateral position of the FOS curve indicates the observer's sensitivity to the stimulus (i.e., α), whereas the slope of the curve (β) describes the relationship between change in observer response and stimulus change (i.e., between contrast sensitivity and stimulus strength). The parameters α and β are characteristics of the observer; their exact values can only be estimated and they are therefore typically denoted $\hat{\alpha}$ and $\hat{\beta}$.

For the purpose of the contrast detection experiments presented in this thesis, $\hat{\alpha}$ was determined as the point on the psychometric function where the stimulus was perceived 50% of the time, i.e., where p(seen) = 0.5.

The expression of $\hat{\beta}$ varies between different types of psychometric functions, but two approaches are commonly taken in vision research: the first is to express $\hat{\beta}$ as the FOS curve's gradient at the location of threshold (Wichmann and Hill, 2001). The second is to express the response variability as the spread of the data, i.e., the range between two non-asymptotic points along the curve, either as the interquartile range (Chauhan et al., 1993; Strasburger, 2001) or the standard deviation (Prins and Kingdom, 2016; Turpin et al., 2010).

Unlike $\hat{\alpha}$ and $\hat{\beta}$, the parameters γ and λ do not estimate properties of the underlying sensory mechanism, but rather aim to describe the behaviour of a non-idealised observer. The guess rate (γ) describes chance-level performance, i.e., the probability of a correct response despite the stimulus not being detected by the underlying

sensory mechanism. The guess rate is generally assumed to be determined by the experimental procedure (for example, for an m-AFS task $\gamma = 1/m$). In turn, the lapse rate (λ) characterises observer vigilance or motivation and the probability of an incorrect response despite the stimulus being sufficiently supra-threshold to be detectable by the underlying sensory mechanism.

If no allowance is given for guess and lapse rates, or if inappropriate rates are chosen during function fitting, the threshold and slope estimates of a psychometric function may be severely biased (Prins, 2012; Treutwein and Strasburger, 1999; Wichmann and Hill, 2001). To avoid this issue, the frequency-of-seeing curves presented in this thesis were fitted using the Bayesian psychometric inference method described by Schutt et al. (2016), with guess and lapse rates constrained between 0% and 10%.

The goodness-of-fit for a given psychometric model is described by the deviance residuals, i.e., the residual difference between the data and the fitted psychometric function.

1.5   Neuroimaging

1.5.1   Magnetoencephalography (MEG)

The use of magnetoencephalography (MEG) as a technique for measuring the magnetic fields produced by brain activity was pioneered by David Cohen, 1968.

Neuronal signal generation in MEG

Neural activity generates time-varying electrical currents through two cellular mechanisms: rapid depolarisation of the neuronal membrane resulting in action potentials (APs) and slower post-synaptic potentials (PSPs) mediated by various neurotransmitter systems. While the slower components of the PSPs are much smaller in amplitude than APs, at the scale of cell populations, the combined effect of PSPs is stronger than that of APs (Figure 1.10). Therefore, the intracellular PSPs produced at the apical dendrites of pyramidal neurons are thought to be the primary source of MEG signals (Baillet, 2017; Da Silva et al., 2010). Both theoretical models and empirical evidence have shown that the synchronous firing of at least 10,000–50,000 cells is necessary to generate a signal detectable with MEG (Murakami and Okada, 2006).

Pyramidal neurons in the cortical sheet are arranged in palisades with their apical dendrites aligned orthogonally to the cortical surface. Due to this spatial organisation, they form "open fields" and effectively act as current dipoles, where — following Fleming's right-hand rule — a weak magnetic field is generated orthogonal to the neuronal dendrite (De No, 1947; Hansen et al., 2010). Since the cortex is folded, forming
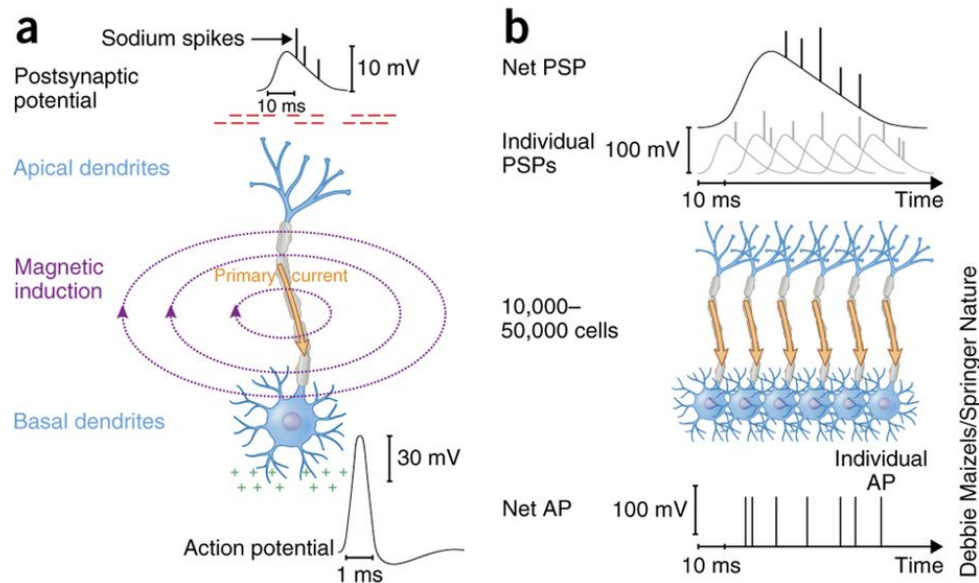
Figure 1.10: Cellular origins of MEG signals. (a) The morphology of the pyramidal neurons results in greater induced magnetic field strength than fields from more stellate cellular morphologies; (b) At the population level, the combined effect of slower PSPs is stronger than that of APs if firing behaviour is synchronised in a group of cells; reproduced from Baillet, 2017.

gyri and sulci, some cell assemblies have dendrites that are perpendicular to the skull surface, whereas those of other populations are parallel to the skull. This is a crucial consideration for MEG measurements, as MEG sensors are primarily sensitive to magnetic fields with components that are normal to the skull, i.e., fields that are generated by neuronal currents oriented tangentially to the skull.

MEG instrumentation

The extracranial magnetic fields produced by neuronal currents are extraordinarily weak and typically measured on a scale of femtoteslas (10^{-15} T; Hämäläinen et al., 1993). Accordingly, sensor technology for MEG must be sensitive to magnetic fields about 10–100 million times smaller than the earth's magnetic field. To achieve such extreme sensitivity, superconducting quantum interference devices (SQUIDS) are used (Zimmerman et al., 1970). If these small coils are cooled to approximately -270°C and coupled with flux transformers (also referred to as pick-up coils), they can detect the small electrical currents induced by neuronal magnetic fields (Singh, 2006).

As magnetic induction travels freely through both biological tissues and air, MEG sensors — unlike EEG electrodes — do not need to attach directly to the head. In most current MEG systems, arrays of about 300 sensors are embedded in a thermally insulated dewar filled with liquid helium. The participant's head is inserted in this "helmet", resulting in a typical sensor-scalp distance of approximately 20 mm (Baillet,
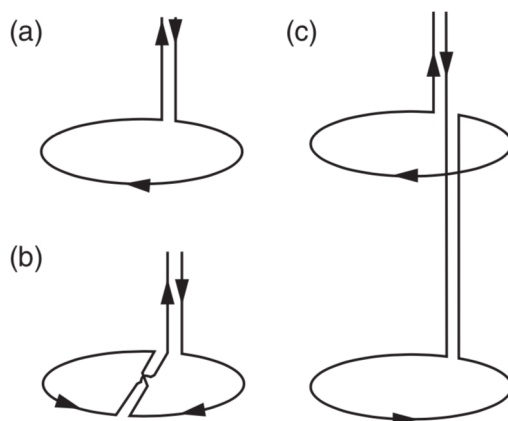
Figure 1.11: Flux transformer geometries for MEG. (a) magnetometer; (b) planar gradiometer; (c) axial gradiometer; reproduced from Hansen et al., 2010.

2017). MEG signals depend on the location and orientation of the pick-up coils in relation to the neuronal current sources. Consequently, the participant's head position inside the dewar is critical for localising measured signals in the cortex. Therefore, the monitoring of head movements during data acquisition is an important factor for data quality. With the recent advent of a new MEG sensor technology in the form of optically pumped magnetometers (OPMs), an alternative to cryogenic, superconducting MEG systems has emerged, where sensors are directly attached to the scalp and measured signals are less sensitive to head motion (Tierney et al., 2019).

Due to their acute sensitivity, SQUID sensors are subject to many electromagnetic nuisance sources. Moving objects — ranging from car traffic to metal items on a participant's clothing — or electrically powered instruments generate magnetic fields that are several orders of magnitude stronger than neuronal signals. The issue of electromagnetic noise is particular pertinent when MEG is combined with tDCS, as discussed in Chapter 6 of this thesis.

To some degree, external noise can be reduced by the design of pick-up coils. The simplest configuration is single pick-up coil (*magnetometer*, see Figure 1.11a). This is set-up is very sensitive to nearby sources, but is also to far-away nuisance sources. The sensitivity to distance sources can be decreased by adding a compensation coil, which mostly measures noise (*gradiometer*, see Figures 1.11b,c). Axial gradiometers combine a pick-up coil with a compensation coil that is wound in the opposite direction and shifted by about 50 mm. For nearby sources, they are maximally sensitive at the rim of the sensor. In contrast, planar gradiometers place the two coils side-by-side, resulting in peak sensitivity directly underneath the sensor.

The MEG system (CTF MEG International Services LP, Coquitlam, Canada) used for MEG recordings described in Chapter 6 comprises 275 1st-order axial gradiometers and 29 reference magnetometers, which are used to regress out additional noise in data post-processing and to implement synthetic 3rd-order gradiometers (Vrba and

Robinson, 2001a).

In addition, MEG instrumentation is typically housed in rooms with multilayered, electromagnetic shielding (commonly referred to as "MSR").

Functional imaging with MEG

Although electromagnetic noise from extracranial sources poses a confound, MEG measures brain activity as an absolute physical quantity in a highly time-resolved manner. The frequency band of MEG signals is approximately 0.5–1,000 Hz, allowing to measure neuronal dynamics with a millisecond temporal resolution (Baillet, 2017). In comparison to EEG, which offers a similarly high temporal resolution, MEG is less susceptible to muscle artefacts, as volume conductor effects are reduced (Claus et al., 2012).

However, the anatomical localisation of measured signals constitutes a fundamental problem in MEG. The sensitivity of MEG is not equally distributed across the brain (Irimia et al., 2014). It has been shown that cortical sources at superficial locations produce signals up to 100 times stronger than subcortical sources (Attal and Schwartz, 2013; Hillebrand and Barnes, 2002). It is therefore commonly believed that imaging of deeper-lying structures, such as the thalamus or amygdala, is not feasible with MEG. Recent evidence from empirical and modelling work, however, suggests that deep structure can be sucessfully localised if appropriate signal processing techniques are used (e.g., Attal and Schwartz, 2013; Cornwell et al., 2008).

Source localisation in MEG is an ill-posed inverse modelling problem: a given magnetic field measured at the sensor level could have been generated by an infinite number of underlying neuronal source distributions (Sarvas, 1987). There are several mathematical approaches for addressing the inverse problem by imposing prior constraints. Source analyses presented in this thesis were based on a linearly constrained minimum-variance beamforming (LCMV) approach (Hillebrand and Barnes, 2005; Van Veen et al., 1997). The LCMV method is a spatially adaptive filter, which allows to estimate the amount of neuronal activity at any given location in the brain. Forward models for MEG source localisation are typically based on high-resolution scans of the participant's head obtained using MRI. The brain is then divided into a 3D grid, and the source strength at each grid point is computed. LCMV beamforming is based on minimising the source signal (or variance) at a given location under the assumption that sources in different parts of the brain are not temporally correlated. The LCMV approach relies on estimates that are calculated in the time domain and produces a three-dimensional spatial distribution of the power of neuronal sources, which can be overlaid on the brain.

Beamforming can attenuate noise sources without requiring *a priori* specification of the number of active sources (Vrba and Robinson, 2001b). While beamformer images may have non-uniform spatial resolutions, they can resolve active sources with a resolution of approximately 2-20 mm (Barnes et al., 2004; Hillebrand and Barnes, 2011). The feasibility of using beamforming approaches to attenuate noise induced by tDCS is discussed in Chapter 6.

1.5.2   Near-infrared spectroscopy (NIRS)

Near-infrared spectroscopy (NIRS) is a non-invasive, optical technique for measuring the hemodynamic changes associated with brain activity. The use of NIRS as a functional imaging method relies on the principle of neuro-vascular coupling, also known as the hemodynamic response. This principle also forms the basis of functional magnetic resonance imaging (fMRI), which measures brain activity as a blood-oxygen-level dependent (BOLD) signal. Through neuro-vascular coupling, neuronal activity in a brain region of interest is linked to related changes in the local cerebral blood flow (Figure 1.14b).

Optical properties of biological tissues

The use of continuous light to non-invasively investigate human tissues dates back to the 19th century. When light enters tissue, photons are either absorbed by pigmented compounds (chromophores) or scattered on their trajectory through the material. The proportions of absorption and scattering depend on the optical properties of the material. In the brain, the hemoglobin in blood vessels acts as the principal chromophore. It is mainly present in two forms: one saturated with oxygen (oxyhemoglobin; HbO), and one without oxygen (deoxyhemoglobin; HbR). In the 1860s, German physiologist Felix Hoppe-Seyler and Anglo-Irish physicist George Gabriel Stokes first recognised the oxygen transport function of hemoglobin and described the optical absorption spectra of oxygenated and deoxygenated hemoglobin (Perutz, 1995).

The discovery of the Beer-Lambert law by French mathematician Pierre Bouguer was a further essential step towards quantifying hemoglobin concentration. Bouguer characterised the logarithmic relationship between the decrease in light intensity and the thickness of the material it traverses (i.e., photon path length) (Bouguer, 1729). The law is often erroneously attributed to Swiss scientist Johann Heinrich Lambert. However, in his publications, Lambert directly quoted from Bouguer's work (Lambert, 1760). In 1852, German physicist August Beer extended the law to reflect that not only was light absorbance proportional to material thickness but also to the concentration of the attenuating chromophores in the material (Beer, 1852).

However, the Beer-Lambert law only applies in non-scattering media and thus does not hold for photon propagation in biological tissues. In the 1980s, the Modified Beer-Lambert law (MBLL) was introduced, which incorporates a differential pathlength factor (DPF) (Delpy et al., 1988). Scattering significantly increases the optical path length travelled by photons and therefore increases the probability of absorption occurring. Adding a dimensionless DFP accounts for this increase in path length. The DFP depends on wavelength as well as the tissue absorption coefficient (μ_a) and scattering coefficient (μ_s). The factor is either measured experimentally or — more commonly — based on previous publications reporting the DPF for different conditions and wavelengths (e.g., Duncan et al., 1996b; Scholkmann and Wolf, 2013; Van der Zee et al., 1992). Furthermore, since chromophore concentrations are time-dependent, Delpy and colleagues proposed to calculate concentration changes by comparing measurements at two different time points (t_0 and t_1), such that the MBLL was reformulated as Equation 1.4 (1988).

$$\Delta A(\Delta t, \lambda) = -log_{10}(\frac{I(t_1, \lambda)}{I(t_0, \lambda)}) = \sum_{i=1}^{n} \epsilon_{i\lambda} \Delta c_i(t) DPF(\lambda) d \tag{1.4}$$

where

A ... attenuation of light

I ... light intensity

λ ... wavelength of incident light

ϵ ... molar extinction coefficient

c ... chromophore concentration

d ... optical path length

DPF ... differential pathlength factor

Brain volume sampling with NIRS

Frans Jöbsis is widely credited with the early development of NIRS — or, as he initially called it, niroscopy — as a neuroimaging technique. In a seminal article in *Science*, he demonstrated that the high transparency of brain tissues to near-infrared light (NIR) light could be exploited to continuously monitor blood oxygenation levels in neonates (Jöbsis, 1977).

The use of NIRS for functional brain imaging takes advantage of the "optical window" in which skin, skull and brain tissues are mostly transparent to near-infrared light (approximately 650–950 nm, *cf.* Figure 1.12). The oxygenated and deoxygenated hemoglobin present in the brain's blood vessels absorbs light more strongly than the surrounding tissues. The differing absorption spectra of HbO and HbR allow the measurement of changes in hemoglobin concentration by comparing light attenuation at multiple NIR wavelengths.
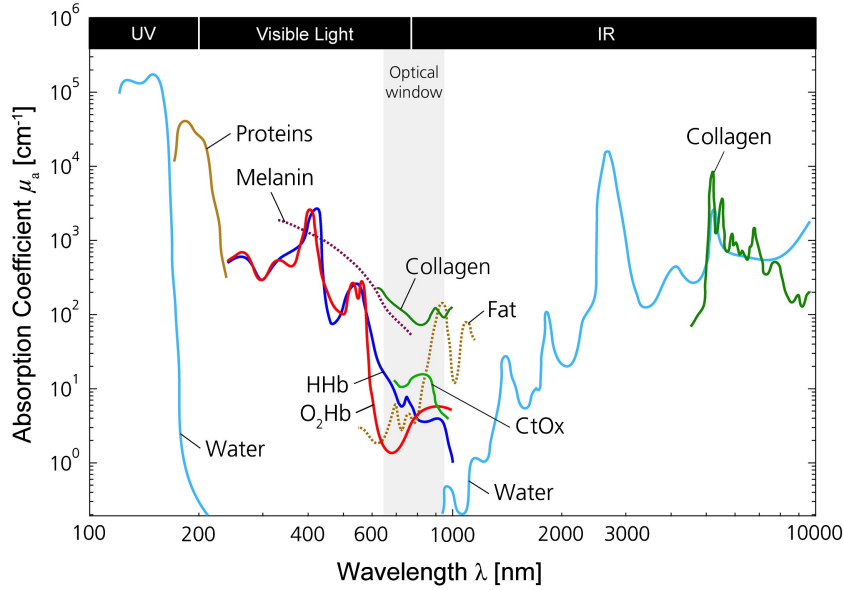
Figure 1.12: Absorption spectra (logarithmic base) for oxyhemoglobin (O_2Hb), deoxyhemoglobin (HHb), proteins, water, collagen, fat and cytochrome oxidase (CtOx) present in human tissues. The isosbestic point within the optical window, at which oxyhemoglobin and deoxyhemoglobin have the same absorption coefficient, lies at approximately 810 nm; reproduced from Scholkmann et al., 2014.

Typically, at least two different NIR wavelengths are used, with one wavelength above and one below the isosbestic point (810 nm) at which oxy- and deoxyhemoglobin have the same absorption coefficient. The selection of wavelengths optimally suited to measure [HbO] and [HbR] depends on a complex interplay of factors, including the tissue types, the chromophores, the homogeneity of tissues and the mathematical approach taken to solve this optimisation problem. A number of different methods based on theoretical or experimental approaches have been proposed for wavelength selection and are summarised in Scholkmann et al. (2014). The data presented in this thesis was acquired using continuous light with wavelengths of 685 and 830 nm.

If oxyhemoglobin and deoxyhemoglobin are evaluated at multiple wavelengths and time points, their relative concentration changes Δc_i can be calculated by solving the Modified Beer-Lambert law as:

$$\begin{bmatrix} \Delta[HbR] \\ \Delta[HbO] \end{bmatrix} = \frac{1}{d} \cdot \begin{bmatrix} \epsilon_{HbR,\lambda_1} & \epsilon_{HbO,\lambda_1} \\ \epsilon_{HbR,\lambda_2} & \epsilon_{HbO,\lambda_2} \end{bmatrix}^{-1} \begin{bmatrix} \frac{\Delta A(\Delta t,\lambda_1)}{DPF(\lambda_1)} \\ \frac{\Delta A(\Delta t,\lambda_2)}{DPF(\lambda_2)} \end{bmatrix} \tag{1.5}$$

NIRS instrumentation

NIRS data can be acquired using three different optical techniques to deliver light into the brain: (i) *continuous-wave* (cw) NIRS, which is based on constant tissue illumination and simply measures light attenuation; (ii) *frequency-domain* (fd) NIRS, which
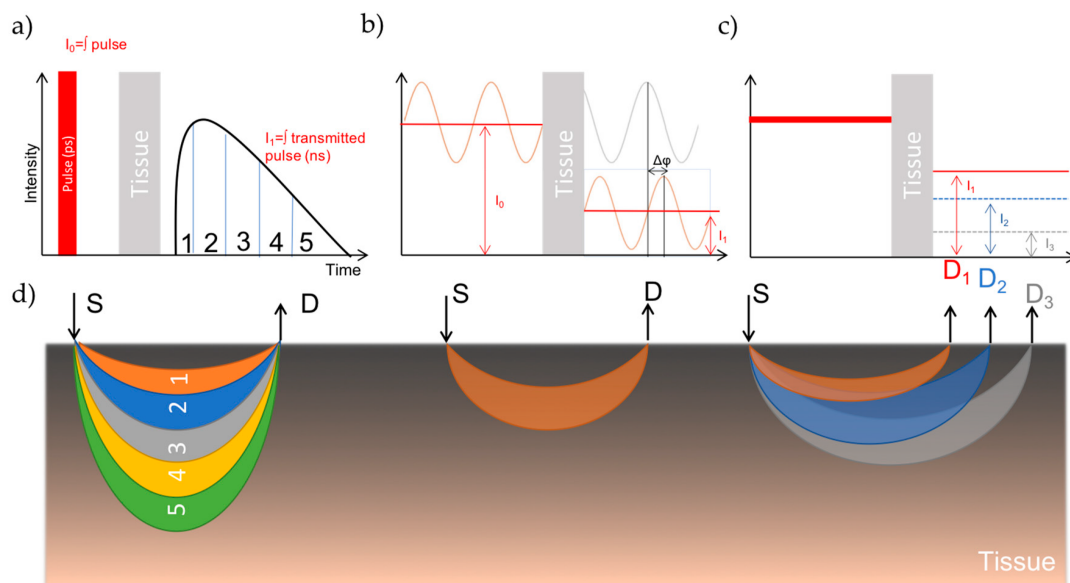
Figure 1.13: Schematic of the three NIRS techniques. (a) Time-domain NIRS; (b) Frequency-domain NIRS; (c) Continuous-wave NIRS; (d) Illustration of the resulting net photon path; reproduced from Lange and Tachtsidis, 2019.

illuminates brain tissues with intensity-modulated light and measures both the attenuation and phase delay of re-emitted light; and (iii) *time-domain* (td) NIRS, where ultrashort pulses of light are used to illuminate tissues and the shape and attenuation of the pulse after tissue propagation is measured. A schematic overview of these techniques is given in Figure 1.13; a more detailed discussion can be found in Contini et al., 2012.

Importantly, only fd- and td-NIRS allow to characterise the optical tissue properties such that *absolute* HbO and HbR concentrations can be calculated. In contrast, the data presented in Chapter 6 of this thesis was acquired using a cw-NIRS system — at present the simplest and most widely used approach. As illustrated in Figure 1.13a, with cw-NIRS, light at a constant incident intensity is compared to the re-emitted, attenuated light, providing *relative* estimates of HbO and HbR concentration. In comparison to frequency- and time-domain systems, cw-NIRS devices are low in cost and the vast majority of commercially available NIRS systems are based on this technique (for an overview see Scholkmann et al., 2014).

To measure from the brain, an array of NIR light emitters (source optodes) and detectors (detector optodes) is placed on the skull (Figure 1.14). Most commonly, source optodes are laser diodes or light emitting diodes (LEDs), while detectors are avalanche photodiodes (APDs).

Due to the complex effect of photon scattering across different tissues, the optical path length is longer than the physical distance between the source and detector. The resulting spatial distribution of NIR light across the different brain tissue layers is often described as a "banana-shaped" region (see Figure 1.14). The depth sensitivity of NIRS depends on multiple factors, including source–detector distance, source
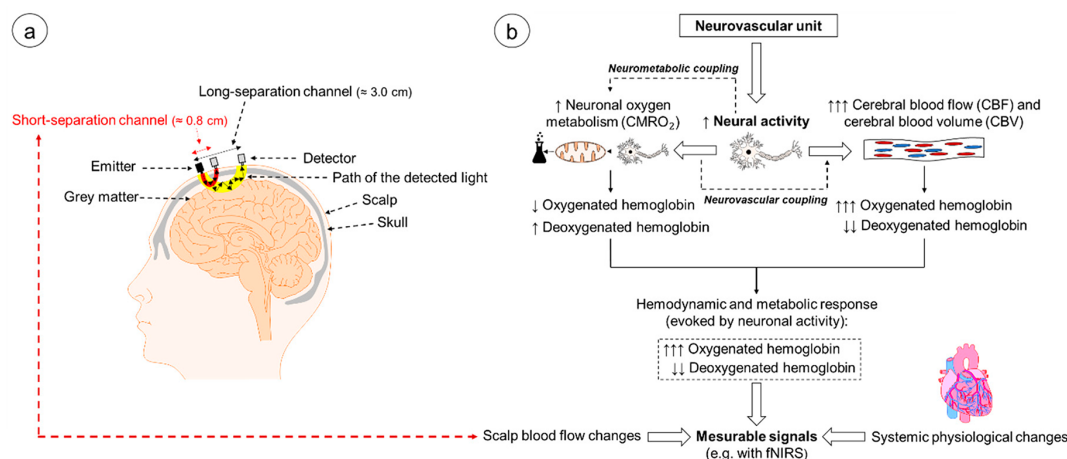
Figure 1.14: (a) Schematic illustration of a NIRS montage using short-separation channels to measure from the scalp and long-separation channels to measure from the brain; the assumed "banana-shaped" photon path through brain tissues is also illustrated. (b) Schematic illustration of the neurovascular unit and the changes in cerebral hemodynamics and oxygenation induced by neuronal activity; reproduced from Herold et al., 2018 under CC BY 4.0 license.

power, detector sensitivity, optical properties of the scalp and skull, adipose tissue thickness and the degree of white matter myelination. For measuring neuronal activity, adequate depth sensitivity (approximately 30–50% of source-detector distance) can be achieved with a S-D separation of approximately 2–3 cm for infants, and 3–5 cm for adults (Brigadoi and Cooper, 2015; Strangman et al., 2014).

Several practical aspects of setting up a NIRS system can compromise or benefit the quality of acquired data. First, stable optode-scalp coupling is critical for reliable light transmission. Mechanical strain on the optode or hair under the optode can interfere with coupling. NIRS optode arrays are usually held in place by head straps or caps, and care must be taken to assure that optodes are placed accurately in relation to the cortical target and coupled to the scalp. Second, both incident and re-emitted light can be attenuated by darkly-pigmented hair or skin. While some studies have excluded participants based on these criteria (e.g., Wijeakumar et al., 2012), this is not an advisable practice if the aim is to generalise findings. Third, ambient light can confound the measurement of light intensity at detector optodes. Stray light should therefore be prevented from reaching the detector, for example, by covering the optode array with a black cloth (Coyle, Ward, and Markham 2004; Chenier and Sawan, 2007). Finally, the signal is contaminated by fluctuations in hemoglobin concentrations in the superficial tissues of the brain related to cardiac activity, respiration, blood pressure changes and task-evoked vasoconstriction. To address this, so-called "short-separation" or "proximity detectors" are placed approximately 10 mm from the light-emitting sources. At this spatial separation, signal changes hemoglobin fluctuations in the blood vessels of the scalp can be captured and used in data analysis (Brigadoi and Cooper, 2015; Kirilina et al., 2012).
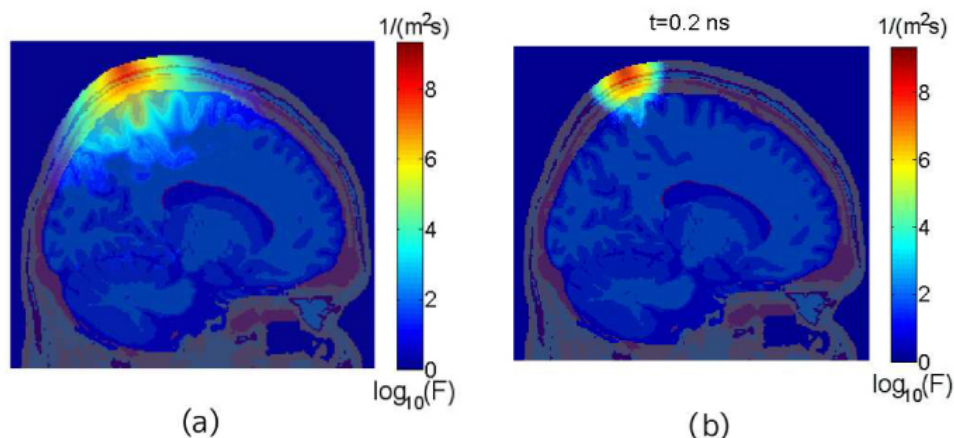
Figure 1.15: (a) Continuous-wave and (b) time-resolved solutions of photon migration in an MRI-based head model (colour map depicts the logarithmic fluence); reproduced from Fang and Boas, 2009a.

Photon migration modelling

The spatial sensitivity profile of a source-detector pair is defined by the spatial probability distribution of photons entering brain tissues at a given source location, scattering in the tissues, and being emitted at a particular detector location. Over the past decades, analytical solutions to quantitatively describe this photon transport in tissues have been refined (e.g., Arridge et al., 1992).

The probabilistic path of photons through brain tissues can be modelled using the photon transport software tMCimg, which is integrated in the open-source package AtlasViewer (Boas et al., 2002). Based on Monte Carlo simulation, the photon migration forward problem can be solved accurately for a complex 3D head model constructed from an anatomical MRI scan, such as the standard Colin27 model (Collins et al., 1998).

Photon migration through tissues with spatially varying optical properties (i.e., different absorption and scattering coefficients) is computed by representing the optical properties within volumetric elements on a cubic grid (1 mm^3 voxel size). The tissue types are specified as input to the Monte Carlo simulation in the form of voxel groups with identical optical properties.

The initial position and direction of the photon at the surface under the source optode is defined. As the photon is propagated from one scattering event to the next, scattering or absorption coefficients are checked for change at every 1 grid spacing. This process is continued until the photon exits the brain or has travelled longer than a predefined time (10 ns), as the likelihood of photon detection after this period is exceedingly low. If the photon exits at a detector location, the detector and path length of the photon in each tissue type prior to being detected are recorded.

The resulting forward model represents the spatial sensitivity to cortical absorption changes of each measurement channel. This information can later be used in the

analysis of functional NIRS data to calculate the effect of absorption changes within different tissue types.

1.5.3   Structural magnetic resonance imaging (MRI)

In common with other human functional neuroimaging methods, the point-spread function (PSF) of NIRS and, to a lesser extent, MEG data can make the anatomical localisation of functional results problematic. To address this, researchers typically collect a *structural* MR image in tandem with any functional data, and the functional data with lower spatial resolution is then co-registered to the structural data.

MRI relies on the principle of nuclear magnetic resonance (NMR), discovered independently by Bloch and Purcell in the 1940s (Bloch et al., 1946; Purcell et al., 1946). The first application of NMR as a topographic imaging modality came in 1973, using NMR of hydrogen atoms in the human body (Lauterbur, 1973). Subatomic particles, such as protons, electrons and neutrons, all possess a property known as spin, which describes the amount of angular momentum associated with a particle. Spin is typically described in multiples of $\frac{1}{2}$, and can be either positive or negative. It is possible for particles with opposite spin values (i.e. $\frac{1}{2}$ and $-\frac{1}{2}$) to combine or pair — this negates the physical properties of spin. In this brief review, we will concentrate on particles which are unpaired, in particular the hydrogen nucleus, 1H (the proton). This is important for life: in organisms, the most abundant atom with spin is the hydrogen atom, typically in the form of water (the human body is roughly 63% hydrogen atoms; Tanzi et al., 2019).

When elements with an odd atomic weight (an odd number of protons) are placed within an external magnetic field they will align themselves with the direction of the field. If protons are placed within a strong external magnetic field, they will occupy one of two possible energy levels. The difference in energy levels is related to the frequency of the two states by Planck's constant (*h*):

$$E = h\nu, \tag{1.6}$$

where is *E* is the energy (J), ν is the frequency (Hz), and *h* = 6.626 x 10^{-34} (Js). The lower energy level is preferred, although the number of protons occupying either level is very similar (as a rough example, for every 1 x 10^7 protons in the higher energy state, there will be 1.0000007 x 10^7 protons in the lower state). Nevertheless, this difference means that the population magnetic vector (the vector sum of all individual nuclei) points in the direction of the external field. This is called "longitudinal magnetisation" as it is "along" the direction of the external magnetic field.

However, while within the field, the protons are not stationary but spin or precess around the magnetisation vector (in the direction of the external field) with a certain
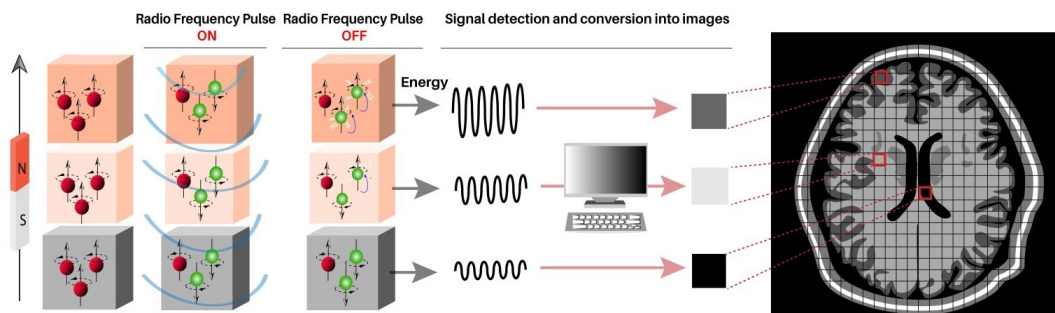
Figure 1.16: Schematic of MRI signal generation. Depending on which tissue a hydrogen proton lies within (e.g., grey matter, CSF, etc.) its spin is disrupted in a characteristic way by the RF pulse, and its return to baseline is distinct from that of nearby tissues. The resulting electrical current is detected by the MRI hardware and forms the basis of the MRI signal; illustration by Huixuan Liang adapted from https://knowingneurons.com/2017/09/27/mri-voxels/ (accessed on 08/10/19).

frequency. This *precession frequency* is proportional to the magnetic field strength, and to the type of nuclei within the field. The relationship of precession frequency and magnetic field strength is described by the Larmor equation:

$$\omega_0 = \gamma B_0, \tag{1.7}$$

where ω_0 is the precession frequency (Hz), B_0 is the strength of the external magnetic field (T), and γ is a constant, the gyromagnetic ratio, which varies depending on the nuclei within the field. From the above, it is clear that placing a source with a high water content (such as a human) within a static magnetic field will cause the sample to become magnetised after a certain period of time. The rate constant that governs the time for a sample to reach magnetic equilibrium is known as *T1*. While in the field, the hydrogen nuclei within the water precess with their Larmor frequency. However, the net magnetic vector ($\vec{M}$) of the source is still in the direction of the static field. As MRI relies upon measuring the signal that is produced when precessing atoms are perturbed from magnetic equilibrium, the protons must be somehow "shifted" from this state in order to use them as a signal source. Although $\vec{M}$ is in the direction of the static B_0 field, each individual proton has a component of magnetisation that is orthogonal to the B_0 field. This component is caused by precession, and because each individual proton will precess with a slightly different phase, there is no net transverse magnetisation. It is possible to change this arrangement by exposing the protons to radio frequency (RF) pulses of a particular frequency. Only when the RF pulse matches the frequency of precession (which happens to be the Larmor frequency) can energy be transferred between the pulse and the protons. This phenomenon is known as *resonance*.

The energy from the RF pulse is absorbed by the protons, causing some of them to occupy the higher energy state. This reduces the net magnetisation vector in the B_0

direction (the longitudinal magnetisation) — in effect, disrupting the magnetic equilibrium of the sample. This RF pulse is referred to as the B_1 or RF field. In addition to its effects on the longitudinal magnetisation, the RF pulse works to focus the phases of the precessing photons. This means that it induces a component of transverse magnetisation at the same time as the longitudinal magnetisation decreases in magnitude. The resulting transverse magnetisation is essential for fMRI studies — and, as noted below, for the contrast between certain tissue compartments in the head — and its kinetics are described by the *T2* time constant. Whereas before, the moving electrical charge of the proton induced the magnetic field of the proton, after the RF pulse, the precessing transverse magnetisation vector produces a changing magnetic field. This in turn induces an electrical current. This electrical current is the basis of the MRI signal and causes a signal current to be induced in an antenna in the MRI instrumentation (Figure 1.16).

Once the RF pulse is turned off, protons gradually decay or relax back to their original energy levels. This causes the longitudinal magnetisation vector to return to its original value. This process is called T1 or spin-lattice relaxation, as the energy emitted from the protons as they return to the lower energy state is transferred to their local tissue environment. The exact composition of that environment will affect T1. For example, the protons in water have a longer T1 than those in fat, since the carbon bonds in fat resonate near the Larmor frequency, facilitating the transfer of energy. In the human brain, the different water content of grey and white matter (71% and 84%, respectively) means that T1 contrasts can be used to provide contrast between these tissues — although this does not mean that it is possible to unambiguously differentiate them. For most functional imaging studies, ensuring good quality contrast between grey and white matter is sufficient. However, as will become plain in the next section, both T1- and T2-weighted images are required to accurately segment the separate tissue compartments of the brain and associated tissues (e.g., skull, CSF, etc.) to allow experimenters to explore the modelling of tDCS-induced electrical fields in the head.

1.6   Finite-element-modelling of tDCS

The dose of tDCS is defined by parameters that affect the electromagnetic field induced in the body and includes factors such as electrode size, shape, position, orientation and number, the intensity and polarity of current at each electrode, the skin preparation at the electrode-scalp interface, the duration of the applied current and the duration of current fade-in/out periods.

However, as discussed previously, using the same dose parameters across a group of participants does not necessarily ensure that the resulting polarisation in the cortex — or indeed participants' behavioural or neurophysiological responses — will be the same. One factor is that the distribution of the electric field ($\vec{E}$ or E-field) within the brain is substantially affected by differences in head geometry. As it is generally not possible to acquire direct, *in vivo* measurements of $\vec{E}$, computational modelling is currently our best means to estimate tDCS-induced electric fields in the human brain.

The majority of modelling studies to date have used the finite element method (FEM) to solve the governing physical equations that describe the induced *E*-field (see Salvador et al., 2019 for a tabulated review of computational tDCS studies). This approach was also taken in constructing the models presented in this thesis (*cf.* Chapters 4, 5 and 6).

Key steps in creating and solving FEM of tDCS include: (1) acquiring a participant-specific, anatomical MRI scan; (2) segmenting the MR image into different tissue compartments; (3) assigning conductivity values to each tissue to create a volume conductor model; (4) placing virtual electrodes on the volume conductor model; (5) tessellating the volume conductor model into a 3D mesh; (6) numerically solving the Laplace equation for the electric potential distribution; and (7) visualising and evaluating the estimated E-field.

1.6.1 MRI segmentation & volume conductor modelling

The first modelling studies of transcranial electrical stimulation used simple three-sphere models to approximate the geometry of the head (Miranda et al., 2006; Rush and Driscoll, 1968). Studies carried out over the past ten years have been based on more sophisticated head models constructed from anatomical MRI data.

After structural MR images have been acquired (*cf.* section on structural MRI above), they must be segmented into the different brain tissues (Figure 1.17A and B). Typically skin, skull, white matter, grey matter and cerebrospinal fluid are segmented to create tissue masks for the volume conductor model. Accurate segmentation of the skull is particularly important due to its low conductivity. Windhoff et al., 2013 therefore recommend that both T1- and T2-weighted images with and without fat-supression are acquired.

Strategies for MRI segmentation differ significantly between software pipelines and toolboxes for FEM. However, they commonly involve a multi-step approach, where MR images are first segmented automatically, inspected manually and subsequently touched up using simple morphological operations to fix local defects. Nielsen et al., 2018 provide a recent review on the state-of-the-art for automatic skull segmentation.
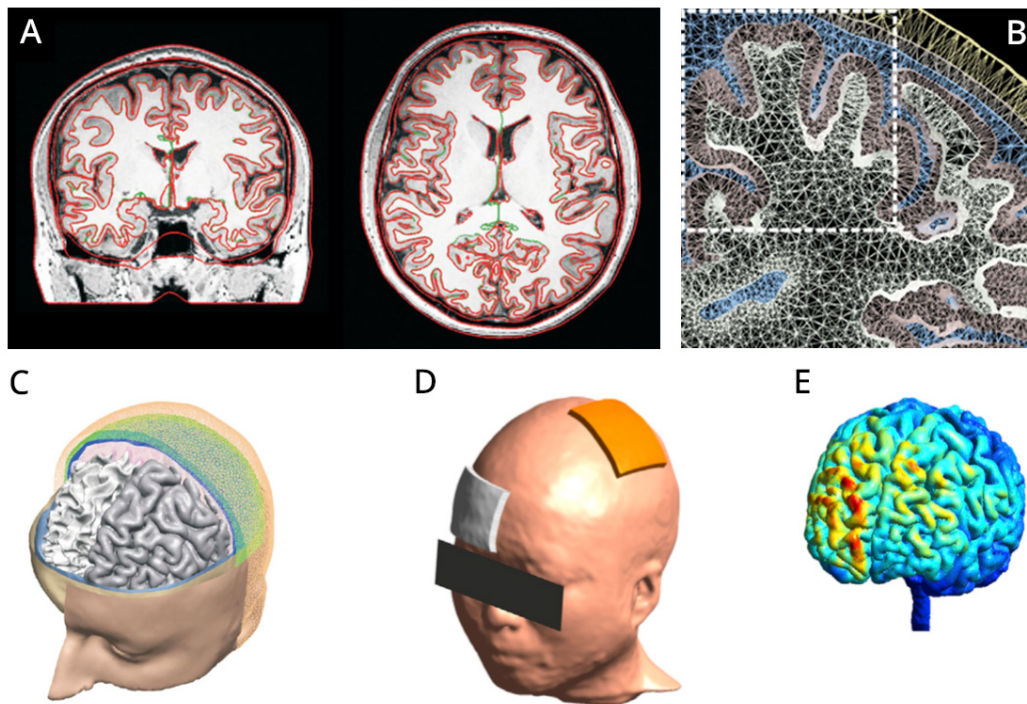
Figure 1.17: Steps in creating a volume conductor model for FEM of tDCS. (A) Segmented tissue boundaries overlaid on a structural T1-weighted MR image (coronal and horizontal slices); (B) Coronal slice through the motor cortex showing tetrahedral volume mesh elements; (C) Cut-away view of the resulting mesh surfaces for different brain tissues (skin, skull, CSF, GM and WM); (D) Extended volume conductor model including the neck and a typical electrode montage for left motor cortex stimulation; (E) The estimated E-field in GM is visualised; images adapted from Nielsen et al., 2018 and Windhoff et al., 2013.
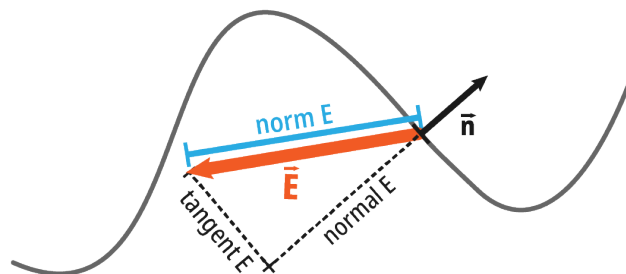
Figure 1.18: Decomposition of the electric field vector $\vec{E}$ in relation to the GM surface. Given the normal vector $\vec{n}$, $\vec{E}$ can be decomposed into a normal and tangent component. The length of $\vec{E}$ (i.e., norm E) describes the strength of the induced electric field.

For work reported in this thesis, details regarding MRI segmentation are provided in the relevant thesis chapters.

The volume conductor model is a model of the head as a passive conducting medium. It describes its geometry and electromagnetic properties. The partial differential equations that define the electromagnetic fields in such a conductive medium, together with the prevailing boundary conditions, can then be solved numerically.

Electromagnetic fields

The equations[1] describing the electric and magnetic fields arising from distributions of electric charges and currents, and their change in time were formulated by Maxwell, 1861 as

$$\nabla \cdot \vec{E} = \frac{\rho}{\epsilon_0} \tag{1.8}$$

$$\nabla \times \vec{E} = -\frac{\partial \vec{B}}{\partial t} \tag{1.9}$$

$$\nabla \cdot \vec{B} = 0 \tag{1.10}$$

$$\nabla \times \vec{B} = \mu_0 \left(\vec{J} + \epsilon_0 \frac{\partial \vec{E}}{\partial t} \right) \tag{1.11}$$

where $\vec{E}$ [V/m] is the electric field, $\vec{B}$ [T] the magnetic field, $\vec{J}$ [A/m^2] the current density, ρ [C/m^2] the charge density, ϵ_0 [F/m] the permittivity, and μ_0 [N/A^2] the permeability of free space. The divergence ($\nabla \cdot \vec{f}$) and curl ($\nabla \times \vec{f}$) of a vector field $\vec{f}$ are described by $\nabla = \left(\frac{\partial}{\partial x}, \frac{\partial}{\partial y}, \frac{\partial}{\partial z} \right)$.

As described by Maxwell's equations, an electric field is generated if a charge density distribution (Eq. 1.8) or a time-varying magnetic field (Eq. 1.9) is present. Conversely, a magnetic field is generated if a current density distribution or time-varying electric field (Eq. 1.11) is present. (Equation 1.10 describes the non-existence of magnetic monopoles).

The relationship between an electric field and the resulting current density in a material with conductivity σ [S/m] is described by

$$\nabla \cdot \vec{J} = \sigma \vec{E} \tag{1.12}$$

---

[1]Polarisation and magnetisation fields have been omitted from the formulation of Maxwell's equations here, as dielectric or magnetic materials are assumed to be absent.

Equation 1.12 is the equivalent of Ohm's law for volumetric current distributions. In isotropic materials, the direction of $\vec{J}$ follows the direction of $\vec{E}$. In FEM of tDCS-induced fields in the brain, white matter is sometimes assumed to be anisotropic, in which case σ is expressed as a 3 x 3 tensor.

Quasi-static approximation & boundary conditions

If electromagnetic fields are time-varying within the low frequency range, Maxwell's equations can be simplified under the assumption that fields do not change over time. For frequencies under 1 kHz, *in vivo* capacitance measurements in dogs (Schwan and Kay, 1957) and impedance measurements in monkey primary visual cortex (Logothetis et al., 2007) have shown that the electrical properties of biological tissues are primarily resistive (Plonsey and Heppner, 1967). Therefore, the effects of propagation, capacitance and induction are neglected in simulations of fields induced by constant currents, as are applied with tDCS, i.e.,

$$\frac{\partial \vec{E}}{\partial t} = \frac{\partial \vec{B}}{\partial t} = 0, \tag{1.13}$$

such that the electric field has zero curl and can be expressed as

$$\vec{E} = -\nabla\phi, \tag{1.14}$$

where ϕ is the scalar electric potential. The above equations can then be reformulated to give the Laplace equation

$$\nabla \cdot \sigma \nabla \phi = 0, \tag{1.15}$$

which provides a description of the potential field in an infinite, homogenously conductive medium. For volume conduction models of the human head, boundary conditions must be applied to describe a volume conductor domain with a boundary surface $\delta\Omega$ (i.e., the head) and a surrounding non-conductive medium (i.e., the air around the head). A potential ϕ_0 is applied to parts of the surface $\delta\Omega_e$ (i.e., the scalp electrodes), such that current can flow into/out of the domain at $\delta\Omega_e$ but not elsewhere on the surface $\delta\Omega_{\sim e}$. Thus, boundary conditions are set as

$$\phi \mid \delta\Omega_e = \phi_0 \tag{1.16}$$

and

$$\sigma \nabla \phi \cdot \hat{n} \mid \delta\Omega_{\sim e} = 0. \tag{1.17}$$

At the locations of the scalp electrodes, the electric potential ϕ is determined by the Dirichlet boundary condition (Eq. 1.16); the potential at all other locations on the head surface is determined by the Neumann boundary condition (Eq. 1.17).

1.6.2 The finite element method

The Laplace equation (Eq. 1.15) is then solved to obtain the distribution of ϕ in the head model. Using the finite element method, numerical approximations of the solutions to the partial differential equation are found based on a principle of discretisation. Since the volume conduction domain is too complex for the equation to be solved analytically, the head model is divided into many small sub-domains. A solution can then be approximated by solving the equation for each element.

Most commonly, tetrahedral or hexahedral elements are used, each offering specific advantages. Hexahedral elements can be created directly from the segmented MRI by converting each voxel into a cubic element. In contrast, tetrahedral elements can vary in size and therefore conform better to complex curved geometries — however, tetrahedral meshes typically take longer to construct. Indahlastari and Sadleir, 2015 compared models based on both types of elements and found no clear relationship between the element type and percentage differences of both estimated mean and median current density. For the sake of computational efficiency, a trade-off must be established between the number of elements and the accuracy of the approximation (Figure 1.17C). Numerous commercial and open-source software tools exist to tesselate a volume conductor models into 3D element meshes, but the influence of mesh size and quality on tDCS simulations has not yet been adequately characterised (Nielsen et al., 2018; Windhoff et al., 2013).

Before the model can be solved, the material properties must be defined for all mesh elements (i.e., values for σ must be assigned for elements belonging to the same biological tissue type, as well as for materials belonging to the electrodes and electrode-scalp interface). As discussed in Chapter 4, the question of appropriate tissue conductivity values — particularly for the skull — is still a matter of debate (Ruffini et al., 2013; Saturnino et al., 2019).

When all information about the geometry of the volume conductor model, the conductivities and the boundary conditions is available (Figure 1.17D and B), elements are combined into a single matrix equation, which is solved iteratively until an error limit is reached. This is done automatically using FEM software. For example, all FEM presented in this thesis were solved using the GetDP toolbox (Geuzaine, 2007).

1.6.3   Evaluating E-field estimates from FEM

As illustrated in Figure 1.17E, once the finite element model is solved, the estimated electric field can be visualised using toolboxes for mesh visualisation, such as Gmsh (Geuzaine and Remacle, 2009). For the purpose of work presented in this thesis, the terms electric field "magnitude", "strength" and "intensity" all refer to the vector norm of the electric field, i.e., of $\vec{E}$ (Figure 1.18). This measure is visualised and used in our analyses of tDCS-induced fields in Chapters 4–6.

Chapter 2

Single vs. double current ramp protocols for double-blind tDCS

2.1 Introduction

Rigour and repeatability are two essential concepts in ensuring unbiased and well-controlled experimental designs in psychology. Appropriate control groups, randomised experimental conditions, placebo interventions and related methods are often combined to reduce the risk of drawing inaccurate conclusions from a given experiment. But while these procedures can assist in ensuring the validity of the study design, they can do little to control for bias effects, where the experimenter or the participant's knowledge of the expected outcomes of an experiment can modify their behaviour and, potentially, the experiment's outcomes.

Typically, bias is addressed by adopting a double-blind experimental design, and, over the past two decades, researchers in the field of transcranial direct current stimulation (tDCS) have increasingly embraced this approach (Bikson et al., 2018; Brunoni et al., 2011; Woods et al., 2016). Most tDCS experiments compare the modulation of a behavioural measure, such as reaction time or verbal fluency, during "verum" (i.e., active) and "sham" (i.e., placebo) stimulation. As many tDCS studies use within-subject designs, it is essential that both participant and experimenter are unaware of the stimulation condition as it is delivered. For tDCS, the effectiveness of a given blinding strategy will depend on a combination of factors, spanning the spectrum from the psychological (demand characteristics of experimenter/participant) to the physiological (the ability of the "sham"/placebo to recreate the subjective sensation of electrical stimulation) (Benedetti, 2014b; Benedetti et al., 2016; Nichols and Maner, 2008). Robust blinding is, however, particularly difficult to achieve for device-based interventions such as transcranial electrical stimulation — in part due to participants' perceptions and expectations around the concept of "high technology", and the elaborate procedures of application (Boutron and Ravaud, 2011; Hróbjartsson and Gøtzsche, 2010).

To date, most placebo-controlled tDCS studies have relied on "active sham" tDCS for participant blinding. These sham stimulation protocols aim to mimic the cutaneous sensations commonly observed during verum tDCS, such as itching or tingling under the electrodes. Typically, these sham protocols are based on a "fade-in, short-stimulation, fade-out" (FSF) waveform, where current is gradually ramped up over several seconds and briefly held constant before being ramped down again (Fonteneau et al., 2019; Gandiga et al., 2006). This approach is widely used. For example, the popular NeuroConn DC-STIMULATOR (NeuroCare Group GmbH, Ilmenau, Germany) uses an FSF waveform with a constant current period fixed at 1/30th of the total length of the stimulation period (see Figure 2.3, *Middle*). In this manner, a FSF sham protocol for 15 minutes of verum stimulation at 1.0 mA might consist of a 15 s linear current fade-in, 30 s of constant stimulation at 1.0 mA, and a 15 s fade-out. These short periods of stimulation are designed to emulate the cutaneous effects of tDCS, and are believed to avoid any accompanying central neuromodulation (Nitsche et al., 2008; Woods et al., 2016). Most commercial tDCS devices support double blinding through the use of "blinding codes": multidigit codes that are linked to stimulation protocol parameters (duration, intensity, etc.) saved in the stimulator's memory. In a double-blind study, the experimenter enters one of these pre-set codes to select which stimulation protocol will be used, with each code specifying that either a "verum" or "sham" stimulation protocol will be delivered. In this manner, the exact details of the stimulation session are hidden from the experimenter, who can be given the codes and is unblinded only at the end of data acquisition.

This combination of techniques — the "active sham" to blind the participant and the use of pre-defined codes to blind the experimenter — is typically regarded as sufficient to reduce any potential sources of bias in tDCS studies. However, recent work has cast doubt on this assumption. While a meta-analysis by Bikson et al., 2018 found that 84% of tDCS studies were sham-controlled, a wide variety of current waveforms was used for both verum and sham conditions, and the reporting of sham protocol parameters in particular was inconsistent across studies. Contrary to best-practice guidelines (Woods et al., 2016), blinding effectiveness was assessed in only 25% (for participants) and 1.2% (for experimenters) of the reviewed studies. Bikson and colleagues (2018) also noted that, as two thirds of the studies examined failed to record sensory side effects, the effectiveness of the "active sham" to reproduce the peripheral sensations of the verum protocol could not be confirmed.

Moreover, several studies have indicated that blinding using "active sham" tDCS is compromised under certain circumstances. The intensity of the current used in stimulation can play a role: for instance, participants may be successfully blinded for stimulation at 1 mA (Ambrus et al., 2012; Gandiga et al., 2006) but not at 2 mA (O'Connell et al., 2012; Wallace et al., 2016). A study by Kessler and colleagues found that rates

of sensory side effects were significantly higher for verum vs. sham stimulation at 1.5 mA (2012). Another study similarly reported that while participants could not reliably distinguish between the stimulation conditions for tDCS at 2 mA, they did experience significantly higher comfort levels for sham vs. verum tDCS (Russo et al., 2013). The intensity and quality of sensory sensations experienced can, therefore, affect participant blinding.

However, even if experimenters employ low stimulation currents to reduce levels of sensory side-effects, the basic design of the typical "active sham" waveform may in itself be poorly suited to act as an active placebo. For example, the FSF waveform, by far the most widely used method for sham tDCS, does not include a final "ramp down" of current (Figure 2.3, *Middle*). As skin sensations during stimulation tend to be more pronounced while current is ramped (Fertonani et al., 2015), sensory side effects are therefore commonly experienced at the beginnings and ends of stimulation. However, the FSF sham protocol uses only a single ramp up and down at the beginning of the stimulation, as noted above (*cf.* Figure 2.3, *Top & Middle*). As the intention of using the active sham is to mimic the sensory side-effects of verum stimulation as closely as possible, a "double ramp" sham protocol — containing current ramps both at the beginning and end of the session — may be a better choice to ensure robust participant blinding while also minimising active stimulation time.

As multiple factors influence blinding in tDCS, researchers aiming to design effective tDCS experiments face multiple challenges. To begin with, extracting useful guidelines from sham protocols previously published in the literature is difficult due to the varying methodological approaches and lack of sufficient detail in reporting (Fonteneau et al., 2019). Furthermore, factors such as participant experience, stimulation intensity or duration can undermine masking, but previous findings do not provide clear guidance for experimental design. While some of these factors have been explored previously, there have been few attempts to formally assess in a single study how sensory experiences, differing protocols for an "active sham" condition and explicit knowledge of the experiment may act both individually and in concert to unblind *both* participants and experimenters.

In the current chapter we chose to address this issue by using separate between-groups experiments based on a simple visual detection task to evaluate the relative efficacies of different "active sham" protocols, i.e. a "single ramp"/FSF and a "double ramp" protocol for controlling both experimenter and participant blinding. We also tested the robustness of investigator blinding in both sham protocols before and after electrodes were removed from the scalp.

2.2   Methods

2.2.1   Study design and participants

This study comprised two between-groups experiments, each consisting of multiple, within-subject sessions (see Figure 2.1 for an overview). In all sessions, participants performed a simple visual detection task (*cf.* Chapter 3) while receiving verum or sham tDCS.

All participants were naive to transcranial electrical brain stimulation. They were not made aware that the study included a sham condition. Participants were healthy and had no contraindications to tDCS, as assessed by self-report. Ethical approval for the study was obtained from the School of Psychology Research and Audit Ethics Committee at Cardiff University. All procedures were carried out in accordance with the Declaration of Helsinki. Informed consent was obtained from each participant prior to the experiment and all volunteers were reimbursed for their time.

Forty-eight right-handed participants under the age of 35 years were recruited. Twenty-four participants (M = 22.8$\pm$4.11 years; 19 female) completed *Experiment A* ("double ramp" sham protocol). A second set of twenty-four participants (M = 21.7$\pm$3.06 years; 14 female) completed *Experiment B* ("single ramp" sham protocol).

In Experiment A, participants received anodal and sham tDCS (2 sessions in total). In Experiment B, participants received anodal, cathodal and sham tDCS (3 sessions in total). Session order was counterbalanced between participants and each session was scheduled at least 48 hours apart to avoid any potential carry-over effects of electrical stimulation (Monte-Silva et al., 2013).

2.2.2   Transcranial direct current stimulation

Transcranial direct current stimulation was delivered using a NeuroConn DC-STIMULATOR PLUS (NeuroCare Group GmbH, Ilmenau, Germany), with two electrodes placed at Oz and Cz (International 10-20 EEG system). This electrode montage is commonly used in tDCS studies of the visual system (Costa et al., 2015b).

Current was applied at 1.5 mA via two 5x5 cm^2 silicone-rubber electrodes, resulting in a nominal current density of 0.06 mA/cm^2. The scalp areas covered by the electrodes were prepared with alcohol and Nuprep skin prep gel (Weaver and Company, Aurora, CO, USA). Electrodes were attached to the scalp with a thin layer of ten20 conductive paste (Weaver and Company, Aurora, CO, USA), see Figure 2.2. The stimulator's maximum impedance limit was set to 20 kΩ during the experiment.

At the beginning of each experimental session a short impedance test protocol was run, consisting of a linear 10 s current fade-in, followed by 15 s of constant stimulation at 1.5 mA and a 10 s fade-out. Impedance levels were recorded by the experimenter
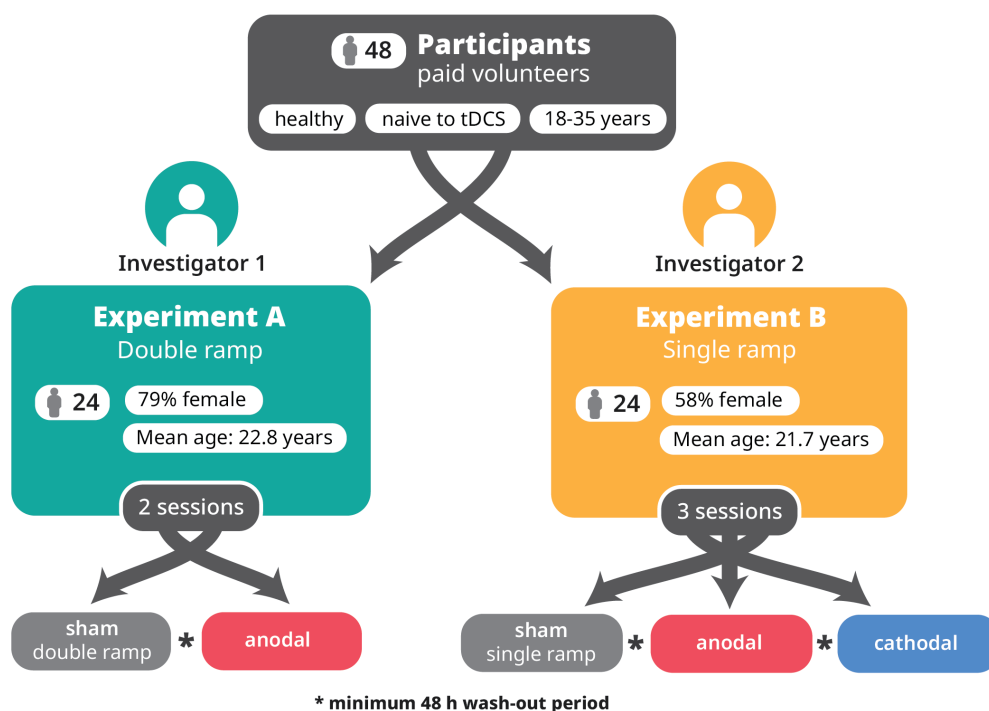
Figure 2.1: Visual summary of the study design. The order of tDCS sessions was counterbalanced.

at the 25 s mark (just before the fade-out). Mean test impedance was 2.03 ± 0.77 kΩ for sessions in Experiment A, and 2.69 ± 1.07 kΩ for sessions in Experiment B.

Stimulation waveforms for participant blinding

To explore the effects of different sham waveforms on bias and blinding, we used three different current waveforms for tDCS: one for verum, and two for sham stimulation. In the verum tDCS condition was based on a typical FSF protocol, where current was applied for 30 minutes with a 10 s ramp-up/down (Figure 2.3 *Top*). For sham tDCS, the first protocol *("double ramp" sham, Experiment A)* consisted of a half-wave sinus waveform with 20 s duration triggered once at the beginning and once at end of the experiment (Figure 2.3 *Bottom*). This waveform aimed to mimic a linear 10 s current fade-in to 1.5 mA followed by an immediate 10 s fade-out. The second protocol *("single ramp" sham, Experiment B)* employed the built-in sham mode (i.e., the FSF waveform) used by the NeuroConn DC-STIMULATOR PLUS device, where current was ramped-up over 10 s, held constant at 1.5 mA for 60 s and ramped-down over 10 s (Figure 2.3 *Middle*).

Figure 2.2: Steps for preparing the scalp-electrode interface on a participant's head. Electrodes are covered with a thin layer of ten20 conductive paste. After the scalp is prepared with alcohol and Nuprep skin gel, consecutive thin layers paste are applied between strands of hair. Finally, the scalp electrode is attached.
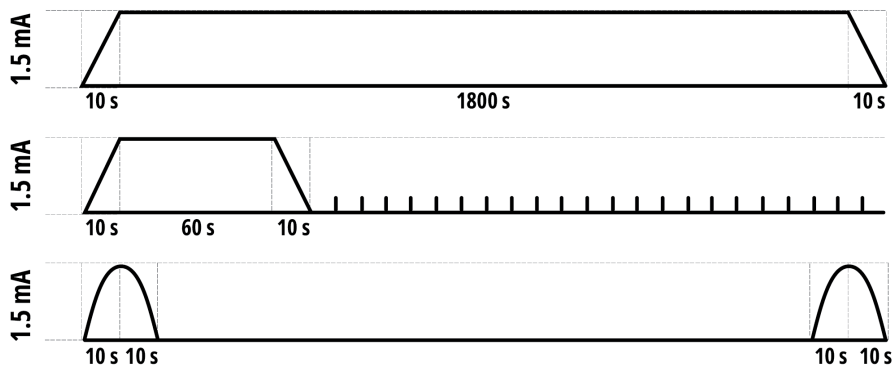
Figure 2.3: Illustration not to scale. *Top:* Current waveform for verum tDCS with linear current ramp up to 1.5 mA over 10 s and constant current stimulation for 30 minutes. *Middle:* "Single ramp" waveform for sham tDCS using the NeuroConn device in "study" mode. For impedance control, a small current pulse occurs every 500 ms (110 μA over 15 ms). *Bottom:* "Double ramp" waveform for sham tDCS using the NeuroConn device in "sinus (hw)" mode with a remote trigger.

Experimenter blinding

In Experiment B ("single ramp"), the NeuroConn DC-STIMULATOR PLUS was used in "study mode", which delivers an FSF waveform for sham tDCS. It does not allow the experimenter any flexibility in deciding the duration of the FSF waveform, or the ability to change its basic shape (as noted in Turi et al., 2019). This meant that, in order to use a "double ramp" protocol (Figure 2.3 *Middle*) in Experiment A, the stimulator was programmed in "sinus (hw)" mode. The resulting half-cycle sine wave of current — essentially a minimally smoothed version of a typical ramp — was twice triggered remotely by the experimental computer, thus delivering the "double ramp". Triggering was performed via a custom PsychoPy script (Version 1.85, Peirce and MacAskill, 2018) without intervention from the experimenter.

Six-digit "blinding codes" which determined the stimulation condition were preselected and randomised by one of the experimenters (DJmcG), who was not involved in data collection. At the beginning of each session, experimenters only entered the assigned blinding code into the device. The display of the stimulator was covered after this step to ensure that the experimenter could not be unblinded by accident (Figure 2.4).
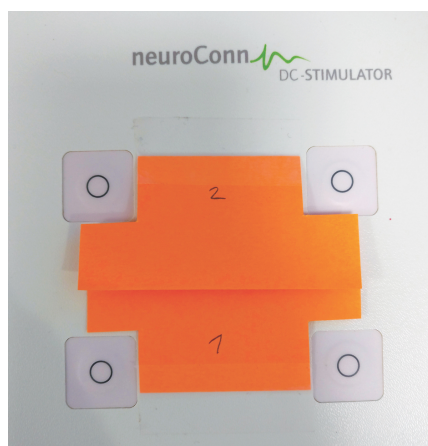
Figure 2.4: The screen of the NeuroConn DC-STIMULATOR PLUS device was covered after entering the blinding code.

2.2.3 Experimental task

While we did not wish to evaluate the effects of blinding on participant performance or stimulation effects, we required participants to carry out an active, attention-demanding task during the experiment to recreate the typical context of a tDCS experiment. To this end, participants performed a visual contrast detection experiment while receiving verum or sham tDCS. Visual stimuli were presented on an OLED display (25" Sony PVM-A250 Trimaster EL, 1920 x 1080 px resolution, 60 Hz frame rate, 120 Hz refresh

rate). Participants were seated in a dark room at a viewing distance of 50 cm. Achromatic circular stimuli at randomly varying luminance levels were displayed for 200 ms at locations extending 20° or 4° from fixation. Participants were instructed to fixate the screen centre and to press a button when they detected a stimulus. Each block of 120 stimulus presentations was separated from the subsequent block by a 60 s rest interval, to allow participants to rest their eyes. Though in the current study we were not focused on analysing participants' behavioural responses, we used the same basic protocol as our subsequent empirical studies (*cf.* Chapters 3 and 6), wherein we commenced brain stimulation 180 s before the onset of the experimental task to ensure that participants were not distracted by any transient sensory symptoms caused by stimulation onset.

2.2.4   Assessment of participant experiences and blinding

Participant blinding and sensory perceptions were assessed using questionnaires and verbal report to the experimenters.

The **strength of sensations** experienced by the participant during tDCS, such as itching or heat, was queried at three time points during the protocol (Figure 2.5): (1) after the first 10 seconds of tDCS; (2) during the first break in the task (i.e., after approx. 10 minutes); and (3) immediately after tDCS offset. Participants were asked to verbally rate their sensations on a scale from 0 ("no sensation at all") to 5 ("very strong sensations").

Sleepiness was assessed pre- and post-task using the Stanford Sleepiness Scale, which required participants to choose one of seven statements best representing their level of perceived sleepiness (Hoddes et al., 1973).

Participants' sensory experiences during the experimental protocol were evaluated using a questionnaire directly after tDCS offset. Similar to the adverse effects questionnaire published by Brunoni et al., 2011, nine specific sensations, such as "itching", "burning" or "nausea", were rated on a scale from 0–3 (0, absent; 1, mild; 2, moderate; 3, severe; *cf.* Table 2.5).

Participants' ability to correctly identify the tDCS condition was assessed using a debriefing questionnaire at the end of the study. Participants were asked to indicate whether they believed they had been receiving "real or placebo stimulation" for each session, and to rate the confidence level of this assessment on a scale from 1–10. None of the participant documentation provided (e.g., study advertisements, information or consent forms) had mentioned the possibility that sham stimulation would be delivered.
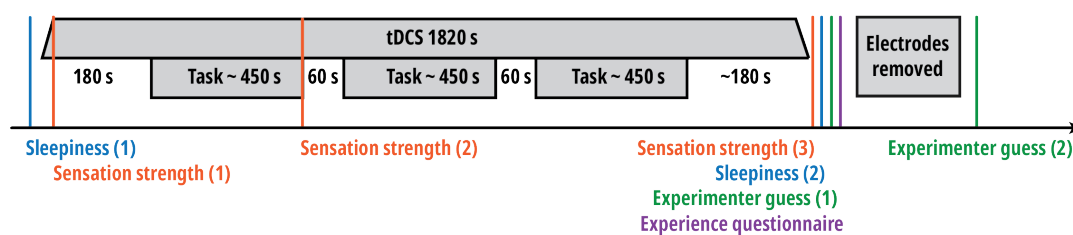
Figure 2.5: Experimental protocol for assessing participant experiences and investigator blinding in each tDCS session. During the protocol, participants verbally reported the strength of sensations. Before and after the task, participants were asked to remain still with their head in a headrest.

2.2.5 Assessment of experimenter blinding

Anecdotally, experimenters have noted that in some participants verum stimulation may produce transient skin reddening under the electrode. This prompted us to investiage experimenter blinding twice in each session: (1) immediately after tDCS offset and before further interaction with the participant and (2) after removing the tDCS electrodes from the scalp and assessing the participant's sensory experiences (Figure 2.5). Each time, experimenters were required to guess whether the participant had received "real or placebo stimulation" in the current session, and to rate the confidence level of their assessment on a scale from 1–10.

2.2.6 Data analysis

Investigators were unblinded after data acquisition was completed. Statistical analyses were performed on unblinded data using RStudio (Version 1.1.463, RStudio Team, 2016).

2.3 Results

2.3.1 Wash-out periods

To avoid any potential carry-over effects of tDCS, sessions were scheduled at least 48 hours apart. The median length of the wash-out period in *Experiment A* was 8.0 days (range: 2–69). In *Experiment B*, median wash-out was 7.5 days (range: 2–61) between the first and second session and 8.5 days (range: 2–99) between the second and third session.

2.3.2 Strength of sensation

Participants verbally reported the strength of sensations they experienced (1) after tDCS ramp-up; (2) during the first break and (3) after tDCS offset, see Figure 2.6.

In *Experiment A*, a two-factor repeated-measures ANOVA showed a significant main effect for *Time* ($F(2,46) = 21.27$, $p = .000$, $\eta_G^2 = .158$), but not *Stimulation condition* ($F(1,23) = 1.37$, $p = .253$, $\eta_G^2 = .008$). The interaction between *Time* and *Stimulation condition* was significant, $F(2,46) = 9.85$, $p = .000$, $\eta_G^2 = .063$.

For *Experiment B*, the equivalent analysis showed significant main effects for both *Time*, $F(2,46) = 35.44$, $p = .000$, $\eta_G^2 = .397$ and *Stimulation condition*, $F(2,46) = 8.67$, $p = .000$, $\eta_G^2 = .09$. The *Time* x *Stimulation condition* interaction was not significant, $F(4,92) = 1.54$, $p = .198$, $\eta_G^2 = .017$.
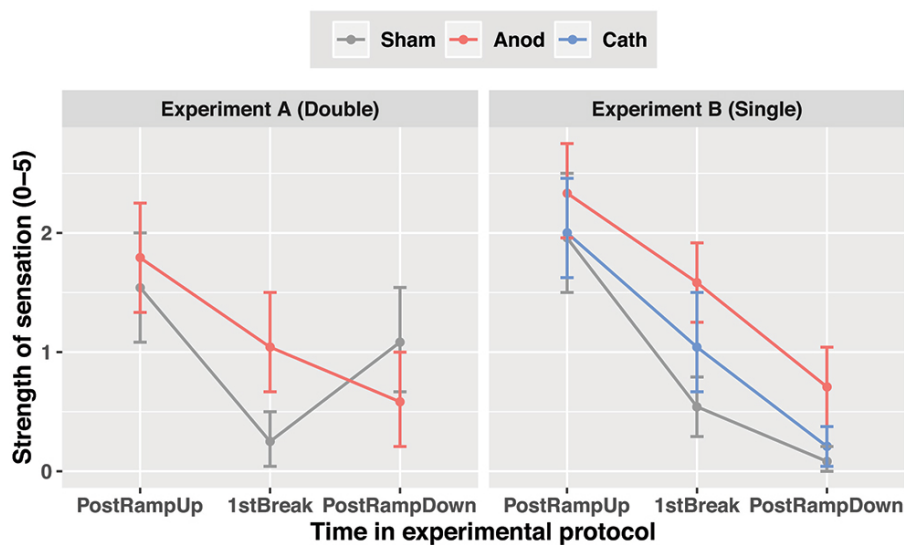
Figure 2.6: Strength of sensations (mean, 95% CI) experienced by participants during tDCS (0 = "no sensation" to 5 = "very strong sensation").

A Wilcoxon signed-rank test indicated no significant difference in the *Mean strength of sensations* experienced across the three measurement times in the sham condition of Experiment A (*Mdn* = 0.67) compared to Experiment B (*Mdn* = 0.83), *W* = 281, *p* = .892, *r* = -0.03.

In addition, to explore the relationship between subjective sensory sensations and blinding, we evaluated whether the mean strength of sensation experienced by participants throughout a given session correlated with their ability to correctly identify the stimulation type for that session. We used logistic regression in these analyses to avoid any potential issues arising from treating ordinal scale data as continuous. For *Experiment A*, logistic regression analysis indicated that *Stimulation* but not *Mean strength of sensation* significantly influenced participants' accuracy in distinguishing verum from sham tDCS (see Table 2.1).

A similar analysis for *Experiment B* showed that neither *Mean strength of sensation* nor *Stimulation* (anodal or cathodal) affected the odds of participants correctly guessing the stimulation condition (see Table 2.2).

	Beta (SE)	95% CI for odds ratio		
		Lower	Odds ratio	Upper
Mean strength of sensation	-0.64 (0.46)	0.20	0.53	1.27
Stimulation (anodal)	2.98 (0.80)***	4.69	19.73	116.42

Table 2.1: Experiment A. Note: ***p = .000. R^2 = .30 (Hosmer-Lemeshow), .34 (Cox-Snell), .44 (Nagelkerke). Model χ^2(2) = 19.6, p = .000. Model AIC = 52.62.

	Beta (SE)	95% CI for odds ratio		
		Lower	Odds ratio	Upper
Mean strength of sensation	0.37 (0.38)	0.69	1.44	3.09
Stimulation (anodal)	-0.25 (0.66)	0.21	0.78	2.80
Stimulation (cathodal)	-0.08 (0.61)	0.28	0.93	3.04

Table 2.2: Experiment B. Note: R^2 = .01 (Hosmer-Lemeshow), .01 (Cox-Snell), .02 (Nagelkerke). Model χ^2(3) = 0.96, p = .812. Model AIC = 102.3.

2.3.3 Sleepiness

Participants rated their perceived level of alertness before and after the experimental protocol (Figure 2.7). Mean sleepiness *pre-protocol* was 2.06±0.67 in *Experiment A* and 1.76±0.80 in *Experiment B*. Mean sleepiness *post-protocol* was 3.02±1.26 in Experiment A and 2.76±1.23 in Experiment B.

Two-factor repeated-measures ANOVAs showed a significant main effect for *Time* (pre- vs. post-protocol) in both experiments (*Experiment A*: F(1,23) = 28.23, p = .000, η_G^2 = .189; *Experiment B*: F(1,23) = 42.10, p = .000, η_G^2 = .192). *Stimulation condition* did not significantly affect sleepiness (Experiment A: F(1,23) = 1.00, p = .328, η_G^2 = .007; Experiment B: F(2,46) = 0.012, p = .988, η_G^2 = .000). In both experiments, the *Time* x *Stimulation condition* interaction was not significant (*Experiment A*: F(1,23) = 0.812, p = .377, η_G^2 = .004; *Experiment B*: F(2,46) = 1.417, p = .253, η_G^2 = .004).
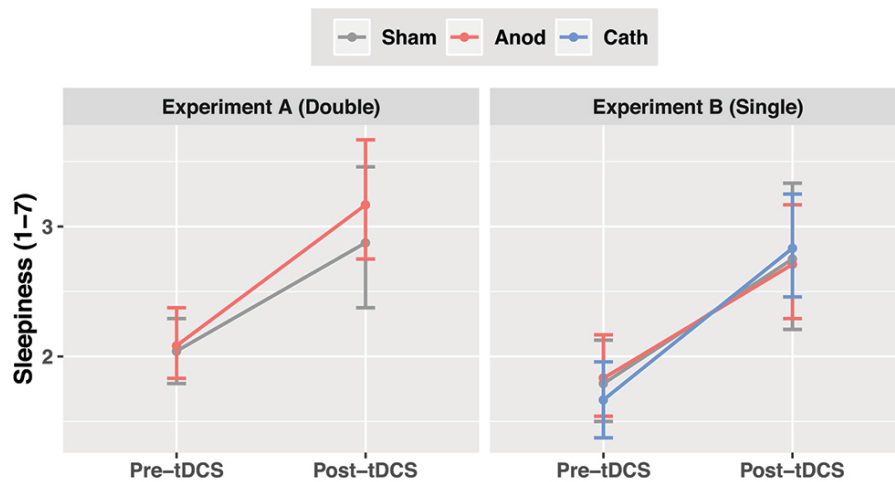
Figure 2.7: Participant alertness (mean, 95% CI) was assessed before and after the experimental protocol using the Stanford Sleepiness Scale (1–7). For both experiments, participants reported significantly lower alertness after the protocol in all stimulation conditions.

2.3.4 Participant blinding

Participant blinding was assessed at the end of the study. In *Experiment A* (2 sessions), 25% of participants (6 of 24) correctly identified the stimulation type for both sessions. An exact binomial test indicated that participants did not guess correctly more often than would be expected by chance (i.e., 25%), *p* = .578 (1-sided). Alternatively, we assumed that participants may have anticipated that at least one session was a placebo intervention. Under the more conservative assumption that participants had a 50% chance of guessing correctly, participants also did not perform above chance level, exact binomial *p* = .997 (1-sided).

In *Experiment B* (3 sessions), 33% of participants (8 of 24) correctly identified the stimulation type for all three sessions. Participants performed above chance level, exact binomial, *p* = .007 (1-sided), if a 12.5% chance of guessing correctly was assumed. However, an exact binomial test also showed that participants did not guess correctly more often than would be expected by chance under the more conservative assumption of a 33% chance level, *p* = .563 (1-sided).

We also explored whether participants' confidence in their assessment of the stimulation type related to the accuracy of their guess. *Rating confidence* did not differ significantly in the two experiments, (*M* = 5.42±2.21 in *Experiment A*; *M* = 5.71±2.58 in *Experiment B*), *W* = 300, *p* = 0.5). For both experiments, logistic regression analyses indicated that participants' *Rating confidence* did not significantly affect the odds of correctly guessing the stimulation condition (see Table 2.3 for *Experiment A* and Table 2.4 for *Experiment B*).

	Beta (SE)	95% CI for odds ratio		
		Lower	Odds ratio	Upper
Rating confidence	-0.28 (0.24)	0.46	0.76	3.09

Table 2.3: Experiment A. Note: R^2 = .06 (Hosmer-Lemeshow), .06 (Cox-Snell), .09 (Nagelkerke). Model $\chi^2(1)$ = 1.49, *p* = .222. Model AIC = 29.5.

	Beta (SE)	95% CI for odds ratio		
		Lower	Odds ratio	Upper
Rating confidence	-0.29 (0.18)	0.50	0.75	1.05

Table 2.4: Experiment B. Note: R^2 = .09 (Hosmer-Lemeshow), .11 (Cox-Snell), .15 (Nagelkerke). Model $\chi^2(1)$ = 2.75, *p* = .097. Model AIC = 32.8.

Sensory experiences of participants during tDCS

An tabular overview of the mean strength (0–3) of specific sensory perceptions participants reported to have experienced during tDCS is provided in Table 2.5.

	Experiment A		Experiment B		
	Sham	**Anodal**	**Sham**	**Anodal**	**Cathodal**
Burning	0.96 (0.77)	0.32 (0.48)	0.29 (0.62)	0.75 (0.74)	0.29 (0.46)
Difficulty concentrating	0.27 (0.72)	0.50 (0.60)	0.71 (0.75)	0.62 (0.82)	0.88 (0.85)
Head pain	0.00 (0.00)	0.00 (0.00)	0.00 (0.00)	0.04 (0.20)	0.04 (0.20)
Itching	0.77 (0.71)	0.36 (0.49)	0.46 (0.72)	0.92 (0.72)	0.75 (0.79)
Nausea	0.04 (0.20)	0.00 (0.00)	0.00 (0.00)	0.04 (0.20)	0.00 (0.00)
Neck pain	0.00 (0.00)	0.05 (0.21)	0.08 (0.28)	0.04 (0.20)	0.08 (0.28)
Scalp pain	0.04 (0.20)	0.14 (0.35)	0.21 (0.59)	0.25 (0.68)	0.08 (0.41)
Tingling	0.88 (0.65)	0.82 (0.66)	0.96 (0.81)	0.92 (0.78)	0.79 (0.59)
Change in visual perception	0.20 (0.50)	0.36 (0.66)	0.29 (0.46)	0.12 (0.34)	0.29 (0.55)

Table 2.5: Mean (SD) (0–3) of sensory perceptions reported by participants after tDCS offset.

2.3.5 Experimenter blinding

To explore how bias may affect experimenter blinding, the experimenters were asked to identify the stimulation condition twice in each session: (1) immediately after tDCS offset (*"pre-removal"*) and (2) after electrodes were removed from the scalp and participant's sensory experiences were assessed (*"post-removal"*). We evaluated the robustness of investigator blinding separately for each experimental session.

For *Experiment A* (2 sessions), exact binomial tests showed that Investigator 1 did not correctly guess the stimulation type above chance level either before or after electrodes were removed (see exact p-values provided in Table 2.6). In *Experiment B* (3 sessions), Investigator 2 did correctly identify the tDCS condition above chance level only *before* electrodes were removed in the first session. After electrodes were removed in the first session and in all subsequent sessions she did not guess above chance level, see Table 2.7. These results suggest that experimenter blinding was generally robust for both sham protocols, with the exception of the first tDCS session in *Experiment B*.

	Pre-removal		Post-removal	
	Correct	p (1-sided)	**Correct**	p (1-sided)
Session 1	50%	.581	45.8%	.729
Session 2	66.6%	.076	62.5%	.154

Table 2.6: Investigator blinding before and after electrode removal in Experiment A ("double ramp"). The percentage of correct guesses of stimulation condition by the experimenter (Investigator 2) is shown for each session. One-tailed p-values from exact binomial tests are reported.

While removing scalp electrodes and assessing the participant's experiences did not appear to affect investigator blinding, paired Wilcoxon signed-rank tests found a significant difference in experimenters' *Rating confidence* before and after electrodes were removed (M_{pre} = 4.27±1.75 and M_{post} = 4.65±2.05 in *Experiment A*; M_{pre} = 6.21±2.34 and M_{post} = 5.85±2.30 in *Experiment B*), W = 159, p = .040, r = -0.296 for *Experiment A*; W = 663 , p = .047, r = -0.252 for *Experiment B*. Investigator 1 (*Experiment A*) was significantly more confident *after* electrode removal, whereas Investigator 2 (*Experiment B*)

	Pre-removal		Post-removal	
	Correct	p (1-sided)	**Correct**	p (1-sided)
Session 1	75%	.011	61.9%	.192
Session 2	45.8%	.857	40.9%	.857
Session 3	58.3%	.271	40%	.868

Table 2.7: Investigator blinding before and after electrode removal in Experiment B ("single ramp"). The percentage of correct guesses of stimulation condition by the experimenter (Investigator 1) is shown for each session. One-tailed *p*-values from exact binomial tests are reported.

was more confident *before* she removed electrodes and assessed participants' experiences.

Furthermore, we investigated whether experimenters' confidence in their assessment of stimulation type related to the accuracy of their guess. Logistic regression analyses showed that *Rating confidence* did not significantly affect the odds of correctly identifying the stimulation condition before or after electrode removal in *Experiment A* (see Table 2.8). In contrast, in *Experiment B*, the investigator's confidence did relate to her odds of guessing the stimulation type *after* but not before electrodes were removed (see Table 2.9).

	Beta (SE)	95% CI for odds ratio		
		Lower	**Odds ratio**	**Upper**
Rating confidence *(pre)*	0.13 (0.17)	0.82	1.14	1.63
Rating confidence *(post)*	0.29 (0.16)	0.10	1.33	1.86

Table 2.8: Experiment A. *Pre-removal:* R^2 = .00 (Hosmer-Lemeshow), .01 (Cox-Snell), .02 (Nagelkerke). Model $\chi^2(1)$ = 0.57, *p* = .452. Model AIC = 68.64. *Post-removal:* R^2 = .06 (Hosmer-Lemeshow), .07 (Cox-Snell), .10 (Nagelkerke). Model $\chi^2(1)$ = 3.69, *p* = .055. Model AIC = 62.52.

	Beta (SE)	95% CI for odds ratio		
		Lower	**Odds ratio**	**Upper**
Rating confidence *(pre)*	0.19 (0.11)	0.98	1.21	1.50
Rating confidence *(post)*	0.37 (0.13)**	1.13	1.44	1.91

Table 2.9: Experiment B. *Pre-removal:* R^2 = .03 (Hosmer-Lemeshow), .04 (Cox-Snell), .06 (Nagelkerke). Model $\chi^2(1)$ = 3.14, *p* = .076. Model AIC = 97.93. *Post-removal:* **p = .001. R^2 = .11 (Hosmer-Lemeshow), .14 (Cox-Snell), .18 (Nagelkerke). Model $\chi^2(1)$ = 9.08, *p* = .003. Model AIC = 80.8.

2.4   Discussion

The "fade-in, short-stimulation, fade-out" (FSF) protocol for sham tDCS (Gandiga et al., 2006) has been widely used in tDCS research, and is generally assumed to be indistinguishable from real stimulation. However, recent studies have begun to cast doubt on its efficacy for participant blinding (Fonteneau et al., 2019).

The work presented in this chapter focused on the relationship between participant blinding and the use of different current waveforms for "active sham" tDCS protocols which aim to mimic the peripheral — but not central — neural correlates of neurostimulation. Participant blinding in tDCS has frequently been upheld as superior to comparable attempts in TMS paradigms (Brunoni and Fregni, 2011). The combination of auditory and muscular activation artefacts in TMS — caused in part by its short and focal central activation of brain tissue — stands in contrast to the silent, longer stimulation periods in tDCS experiments. However, as discussed above, there are numerous aspects of a typical tDCS study, including the expectations of participants and experimenters, that can undermine blinding robustness even in carefully designed tDCS paradigms. Here we present work that attempts to explore a number of these influences, including the peripheral sensory experiences of participants and the use of different "active sham" protocols.

Some previous tDCS studies have explored blinding by requiring participants to give moment-by-moment reports of their subjective experience of tDCS (e.g., Ambrus et al., 2012; Greinacher et al., 2019). In these experiments, participants were idle while stimulation was applied. It can, however, reasonably be assumed that the execution of a task would divert attention and thereby facilitate any habituation to or distraction of the participant from tDCS-related sensations. Other studies tend to be task-based, but assessed blinding only at the end of the session or study (e.g., Brunoni et al., 2014; O'Connell et al., 2012; Palm et al., 2013). In our current work, we aimed to find a useful balance between, on one hand, meeting the attentional conditions of a task-based tDCS experiment, and, on the other hand, capturing participants' experiences both during and after stimulation (similar to the approach taken by Russo et al., 2013, for example). Our intention was to explore participant blinding in the context of a typical tDCS experiment — a more pressing question for empirical tDCS work, arguably, than the experiences of participants in a study that focuses on recording sham experiences to the detriment of the study's ethological validity. To this end, we used a simple, attention-demanding task (i.e., visual contrast detection) and queried participants during a short break in the experiment. As our study design comprised tDCS sessions across several days, participants were asked to indicate whether they believed they had received verum or sham tDCS only at the end of the last experimental session.

We compared two types of waveforms for "active sham" tDCS — a "single ramp"/FSF protocol, where current was only ramped up/down at the beginning of the session, and a "double ramp" protocol, where the same current ramp was included twice, once at the beginning, and once at the end of the session. Overall, our results indicate that participant blinding was effective for the "double ramp" sham protocol, as participants did not correctly identify the stimulation condition above chance level. However, for

the FSF protocol, blinding efficacy depended on our assumption in regard to participants' expectations about the study design. The experiment included three stimulation sessions in total (anodal, cathodal, sham; counterbalanced). We first assumed that participants had no prior expectations regarding the experimental design (i.e., they had a 12.5% chance of correctly guessing the stimulation condition) and found that participants *did* guess above chance level, suggesting that blinding was compromised. However, although they were not made aware that they would receive sham tDCS, the majority of our participants were students of medicine, optometry and psychology and may have anticipated that our study design included a placebo session (i.e., a 33% chance guessing correctly). Under these assumptions, we found that participants failed to perform above chance, indicating that blinding for the FSF protocol was effective.

It is also important to note that, in the present study, a participant had to identify the stimulation type correctly for *all* experimental sessions in order to be considered "unblinded". In that sense, our criterion for rating the blinding of an individual participant as compromised was comparatively strict, since the incorrect identification of just one session was sufficient for the participant be counted as successfully blinded. This is a crucial difference to previous single-session or between-subjects studies in which participant blinding was assessed as a "correct guess/incorrect guess" about the received stimulation (e.g., the recent large cohort study by Turi et al., 2019).

However, our ability to make definite conclusions about the blinding efficacy of the two different ramp protocols is limited by the differences in experimental design: in *Experiment A* ("double ramp" sham), participants attended two sessions of tDCS, while in *Experiment B* ("single ramp"/FSF sham), they attended three sessions of tDCS.

It is also worth pointing out again that our participants had no previous experience of tDCS and were not informed that the study included a sham stimulation condition. As part of our informed consent procedure, participants were merely informed that they "may or may not" experience sensory side-effects of stimulation, such as itching or tingling on the scalp. Blinding may be more difficult to achieve if participants have to be made aware of placebo conditions or of details regarding the sham stimulation (e.g., due to informed consent requirements by the local ethics committee). On the other hand, one must also consider that larger placebo effects have been reported in clinical trials that did *not* inform patients about the possible placebo intervention (Hróbjartsson and Gøtzsche, 2010).

Outside of any conclusions to be drawn from comparing our two different ramp protocols, we found that, overall, participants' accuracy in identifying the stimulation condition was not related to the average level of sensations they experienced during or immediately after tDCS. As participants reported their experiences of tDCS directly

to the experimenter, we cannot exclude the possibility that so-called "Hawthorne effects" may have biased our findings — although it is unclear if the presence of the experimenter would be likely to increase or decrease the level of reported sensations. Moreover, the concept itself has recently come under scrutiny (McCambridge et al., 2014). Furthermore, we found that participants' confidence in assessing the stimulation condition at the end of the study also had no significant association with the accuracy with which they identified the tDCS condition

It has previously been argued that tDCS effects may be mediated via unspecific changes in global arousal due to the stimulation of peripheral (cranial and spinal) nerves as opposed to central neuromodulation (Tyler et al., 2015). In our study, participants consistently reported higher sleepiness at the end of the session compared to the beginning of the session. However, as this relationship was similar for both sham and verum tDCS, it most likely reflects task demands rather than biological effects of electrical stimulation.

Overall, our findings on participants blinding underline the complexity of designing and evaluating sham protocols for tDCS. The issue is complicated further by the potential influence of the experimenters' knowledge, expectations and behaviour. We therefore also assessed experimenter blinding in each tDCS session. Our results suggest that experimenter blinding was robust for both sham protocols. The experimenters did not guess correctly above chance level either before or after electrodes were removed from the scalp. Contrary to expectations, one of the two investigators was *less* confident in her assessment of the stimulation condition *after* electrode removal. This may be due to the use of conductive paste for attaching the scalp electrodes, as typically some paste remained on the hair and scalp after electrode removal, which may have obstructed the assessment of skin redness, especially for participants with dark or dense hair.

This study does not address the potential issue that particularly realistic "active sham" protocols may also elicit particularly large placebo effects (i.e., the issue of differential placebo effects). Indeed, meta-analyses have indicated that larger effects of placebo interventions are associated with physical placebo interventions. Moreover, studies based on participant-involved outcomes (i.e., participant-reported outcomes or experimenter-reported outcomes involving participant cooperation), as well as studies with small sample sizes and studies with the explicit purpose of studying placebo are also more likely to elicit larger placebo effects (Hróbjartsson and Gøtzsche, 2010). All of the above characteristics are fulfilled to varying degrees by the majority of current tDCS studies. In a future study, it may therefore be useful to compare verum tDCS both to a "no treatment"/"zero stimulation" condition as well as an "active sham" condition — ideally as part of a large, task-based study.

There remain numerous open questions in regard to the methodology for double-blind, sham-controlled tDCS studies. For example, it has been suggested that participant blinding may be improved through the use of HD-tDCS. A multi-electrode set-up informed by models of the induced electric field may allow to create a sham condition where skin sensations are elicited without cortical polarisation. Multiple smaller electrodes likely activate fewer receptive cells and may therefore reduce skin sensations (Bikson et al., 2018; Turi et al., 2014). However, to our knowledge, no direct comparison of sham efficacy in two-electrode vs. multi-electrode tDCS experiments has been carried out.

As an alternative approach, experimenters may consider the topical pre-treatment of electrode scalp areas with analgesic gels. Safety parameters for electrical stimulation in humans are now well-established (Grossman et al., 2019) and analgesic preparation of the scalp would render "active sham" stimulation unnecessary without risking skin lesions during verum tDCS.

In conclusion, our evaluation of current waveforms for "active sham" tDCS indicates that a double-ramp waveform reliably blinded participants to tDCS at 1.5 mA. In contrast, results on the efficacy of the widely-used FSF sham protocol partially depended our underlying assumptions about participants' chance level of guessing. We found that both sham protocols were effective for blinding the experimenters. While investigators felt more confident, they were not, in fact, more accurate in identifying the stimulation condition after electrodes were removed from the scalp (i.e., based on skin redness). The limitations of our present findings should be considered carefully in the design of future studies. To avoid difficulties in comparing results across studies, the field would benefit greatly from more detailed descriptions of sham protocol parameters in future reports. Finally, without a doubt, the robustness of protocols for participant and experimenter blinding should be explicitly evaluated as a matter of routine. However, both the brain stimulation field and the wider clinical research community have yet to converge on an agreement regarding the best methods for doing so.

Chapter 3

Modulating contrast sensitivity with tDCS

3.1 Introduction

Transcranial direct current stimulation is thought to transiently alter the transmembrane potential of neurons, inducing changes in neuronal excitability (Nitsche and Paulus, 2000) and ultimately affecting behaviour. Studies of the motor cortex have shown that tDCS can induce excitability changes in the amplitude of TMS-induced motor-evoked potentials (MEP) (Nitsche and Paulus, 2000, 2001; Nitsche et al., 2007). Similarly, electrical stimulation of the visual cortex has been found to modulate TMS-induced phosphene thresholds (Antal et al., 2003). Both of these approaches use a passive experimental procedure to obtain objective values of physiological thresholds. However, the vast majority of tDCS studies have focused on typical psychological experimental designs, where the dependent variable is behavioural performance (Coffman et al., 2014; Horvath et al., 2015; Kuo and Nitsche, 2012). These studies are thus hampered in their conclusions by the unknown mappings between electrical stimulation, neuronal polarisation changes, and their subsequent effects on behaviour.

To tease apart the true effects of tDCS on behaviour, we must establish something akin to a "reciprocal computational model", describing not only the spread of the electrical field and its effect in a cortical target region, but also how this effect subsequently influences the specific computations carried out by the target region, and how these ultimately produce behaviour. In developing such a model, less complex experimental paradigms that employ elementary stimuli and simple behavioural demands are likely to be more useful than the paradigms used to evoke MEPs and visual phosphenes, as these tend to lack ethological validity. Primary cortical sensory regions are perhaps some of the most extensively studied and best understood areas of the human brain. Thus, using a sensory system such as vision seems a logical place to begin to explore the underlying neurobiology of tDCS. The neural correlates of visual stimulus processing, in particular, are better understood than those underlying other sensory systems

or higher-order cognitive functions such as memory, emotion, or decison-making.

However, compared to direct current stimulation of the motor cortex, few studies have investigated tDCS effects in other sensory areas and outcomes have proven less reliable (Horvath et al., 2014; Jacobson et al., 2011). Several early tDCS studies explored the application of direct current stimulation to the visual cortex. For example, a study by Antal and colleagues showed that cathodal tDCS increased perceptual thresholds in a grating contrast sensitivity task (Antal et al., 2001). Consistent with an anodal-excitatory and cathodal-inhibitory interpretation, Antal et al. (2004) then demonstrated that anodal tDCS elevated the amplitude of the N70 visual evoked potential, while cathodal tDCS reduced N70 amplitude. Using the same sinusoidal luminance gratings, Antal et al. could also show a reduction of gamma and beta power for the N70 component after cathodal stimulation. While results from these early studies suggested that tDCS could affect visual processing in healthy populations with some degree of specificity, it is important to note that these experiments were neither double-blinded nor placebo-controlled. Using within-subject designs, these studies evaluated tDCS effects by directly comparing anodal and cathodal tDCS without a "sham" tDCS control condition (*cf.* Chapter 2). Furthermore, the sample sizes in these studies were particularly small, varying from 9–16 participants. A recent sham-controlled study by Brückner and Kammer (2016), in contrast, failed to find effects of tDCS on TMS-induced phosphene thresholds.

More recently, several double-blind tDCS studies in healthy participants have evaluated stimulation effects on vision. Typically, these studies have focused on experimental tasks thought to preferentially engage hierarchically lower visual areas (i.e., V1, V2 and related areas), such as detection and discrimination tasks.

In general, tDCS studies of visual function have relied on the rich literature of lesion studies in humans to justify why a certain electrode montage would modulate a given behavioural function. In both humans and animals, lesion experiments have established the causal role of the primary visual cortex in the detection and discrimination of visual stimuli (Lashley, 1943; Weiskrantz et al., 1974; Weiskrantz, 1996). Recently, more sophisticated *in vivo* experiments have come to similar conclusions, for example, optogentic studies that allow the reversible inhibition of V1 in mice (Glickfeld et al., 2013). The detection of luminance differences, in particular, is a task well-suited for studies aiming to primarily engage visual cortical areas; it is considered to be a pre-attentive, parallel process with comparatively little involvement of higher fronto-parietal areas. It has been suggested that contrast detection is comparatively little affected by complex cognitive confounds, such as working memory, task comprehension or left/right errors (Hanck et al., 2012).

In the context of probing the basic effects of electrical stimulation on a simple sensory task, several studies have therefore employed contrast detection tasks to evaluate tDCS outcomes in the visual system. However, the heterogeneity of the employed stimulation and behavioural paradigms makes it difficult to draw definite conclusions about the observed effects.

For example, Kraft et al. (2010) used automated threshold perimetry to measure the effect of anodal and cathodal tDCS at 1 mA on contrast sensitivity and found an increase in detection performance in anodal compared to sham stimulation when stimuli were presented in the central 8° of the visual field. Compared to baseline, anodal tDCS only enhanced contrast sensitivity for eccentricities below 2°. In contrast, cathodal stimulation did not affect detection performance at any eccentricities within 10°. In addition, perceptual learning effects were measured, but only observed for threshold perimetry *before* tDCS.

In contrast, a study by Costa et al. (2015a) compared the effects of tDCS on central (<10°) vs. peripheral (30-60°) visual fields and also attempted to replicate the findings from Kraft and colleagues. Participants received 1.5 mA anodal, cathodal and sham stimulation while performing 10-2 and 60-4 automated perimetry protocols. Results showed that anodal tDCS decreased thresholds only for the peripheral regions of the visual field (60°). The excitatory tDCS effects on the central visual field reported by Kraft et al. were not replicated. Instead of the expected facilitation, the results indicated a trend towards an inhibitory effect of anodal tDCS on the central field.

More recently, in a comprehensive, sham-controlled study, Reinhart et al. (2016) found that 20 minutes of anodal tDCS at 2.0 mA improved vernier acuity and increased the amplitude of visually-evoked potentials (VEPs), whereas cathodal stimulation had a detrimental effect on visual acuity and attenuated VEPs. Moreover, their results suggested that tDCS-induced improvements in visual acuity co-occurred with increased contrast sensitivity as measured in an adaptive two-alternative forced choice task. Interestingly, tDCS effects on visual acuity were largest in the participants with the poorest baseline acuity, suggesting that participants' initial performance on a given task may directly affect the amount that brain stimulation can modulate their abilities.

The effects of tDCS on contrast sensitivity may also depend on stimulation timing. Behrens et al. (2017) recently investigated whether 20 minutes of tDCS at 1.5 mA repeated over five consecutive days could affect contrast sensitivity in healthy participants. Their findings showed that anodal tDCS led to a significantly greater immediate enhancement of contrast perception only from the second day onward. Furthermore, long-term tDCS effects up to four weeks were only observed for the central 2-4° of visual field.

Findings from these studies provide further evidence that tDCS can affect visual processing. However, differences in experimental designs and tDCS protocols make

a direct comparison of their results difficult and hamper a clear interpretation. For example, Kraft et al. applied tDCS to the electrode positions O1 or O2, with the "reference" electrode at Cz. In contrast, Costa and colleagues delivered tDCS via the more common Oz-Cz montage. However, Reinhart et al. used a novel montage with the target electrode on P1 or P2 and the "reference" electrode on the contralateral cheek. Behrens and collagues, in turn, relied on anatomical MRI data to place the target electrode over the striate area of V1 of the left hemisphere and placed the "reference" electrode at position Cz. Furthermore, electrode size and current intensity differed in the four studies (25 cm^2 and 70 cm^2 at 1.0 mA *vs.* 25 cm^2 at 1.5 mA *vs.* 19.25 cm^2 and 52 cm^2 at 2.0 mA *vs.* 35 cm^2 at 1.5 mA). In combination, these methodological differences can be expected to produce both different effective current densities and different electric field directions in the targeted cortical regions.

Overall, the relative influence of stimulation parameters, such as current intensity, electrode size, electrode position and current polarity and duration, has not yet been sufficiently or systematically reviewed. Moreover, performance on even "simple" visual tasks such as contrast detection is modulated by multiple factors, e.g., attention, fatigue or response bias. We lack a clear explanatory framework for how tDCS-induced neurophysiological changes affect typical psychophysical parameters such as response time, detection sensitivity or error rates.

Moving beyond the choice of task and stimulation parameters, the confounding effect of inter- and intra-individual factors is also problematic. Trait-dependent differences between participants can span a number of variables, including the neuroanatomical, neurochemical or even participants' baseline ability on a given task — all of which will play some role in modulating tDCS effects on behaviour. Several recent studies have attempted to define such inter- and intra-individual sources of variability in non-invasive brain stimulation in general, and to tDCS in particular (Ammann et al., 2017; Chew et al., 2015; Dyke et al., 2016a,b; Laakso et al., 2015; Li et al., 2015; López-Alonso et al., 2014, 2015).

Results from these studies all point to a considerable proportion of "non-responders" to tDCS, highlighting the need to develop predictive markers for targeted tDCS approaches. A review by Li et al., 2015 proposes that best practice may be to focus on inter-individual factors that are easiest to control, such as age and baseline ability, and to avoid between-subjects experimental designs. In addition to non-responders, some participants may only show tDCS effects for the most difficult classes of stimuli. It is therefore crucial to measure participant performance at a range of difficulties and to avoid using only a single measure of performance.

With these issues in mind, our present work seeks to build on the previous contrast detection studies exploring tDCS effects in humans. In the work described here, we used a forced-choice threshold perimetry procedure to investigate the effects of verum

and sham tDCS on luminance detection thresholds at central (4°) vs. peripheral (20°) visual field positions in young, healthy participants. This behavioural task, though, has been selected primarily for its simplicity: we were not *per se* interested in mapping the visual field of our participants; rather we designed this study as a "probe" of the relationship between simple sensory processing and tDCS effects across a randomly sampled population.

We have sought to remove some of the less desirable sources of variance: for example, the current report is a double-blind, sham-controlled study to address an obvious weakness of earlier work. However, to maintain the generalisability of our findings we have also tried to ensure that our study encompasses "ethologically valid" sources of variance, such as inter-individual differences in brain structure and function, variation in electrode placement across sessions and training/expertise effects on the task.

For the visual cortex, we currently lack definitive empirical evidence on (1) the minimum magnitude of tDCS-induced fields required to directly modulate the activity of visual neurons, (2) which electrode montage induces the strongest electric field in the early visual cortex, and (3) whether there is a simple linear relationship between the magnitude of tDCS-induced fields and the magnitude — or presence — of behavioural change.

We therefore acquired anatomical MRI scans for a subset of participants in this study. These participant-specific MRIs — described in more detail in Chapter 4 — were used to retrospectively examine any inter-individual differences in performance and induced electric field strength in our sample.

To further explore the relationship between electrode montage, behaviour and induced electrical field strength, we used two different scalp electrode montages to modulate visual function. The first montage places electrodes at EEG positions Oz and Cz, and is commonly used to target the visual system. The second montage places electrodes bilaterally at PO7 and P08. Preliminary finite-element-models of the electric fields induced by these montages are illustrated for the MNI152 template brain in Figure 3.1.

We applied tDCS at the same current intensity (1.5 mA) via each electrode montage and assessed stimulation effects in two groups of participants (see Figure 3.2 for an overview). For both groups (i.e., electrode montages), we compared the effects of sham and verum tDCS in a within-subjects design. While receiving tDCS, participants performed an automated threshold perimetry task to measure contrast sensitivity across four central and peripheral visual field eccentricities. Based on previous reports in the literature, we set out to explore the following questions in this chapter: i) Can verum tDCS modulate performance on a visual contrast task when compared to sham tDCS? ii) Does this putative modulation show differential effects between central and peripheral visual field locations?
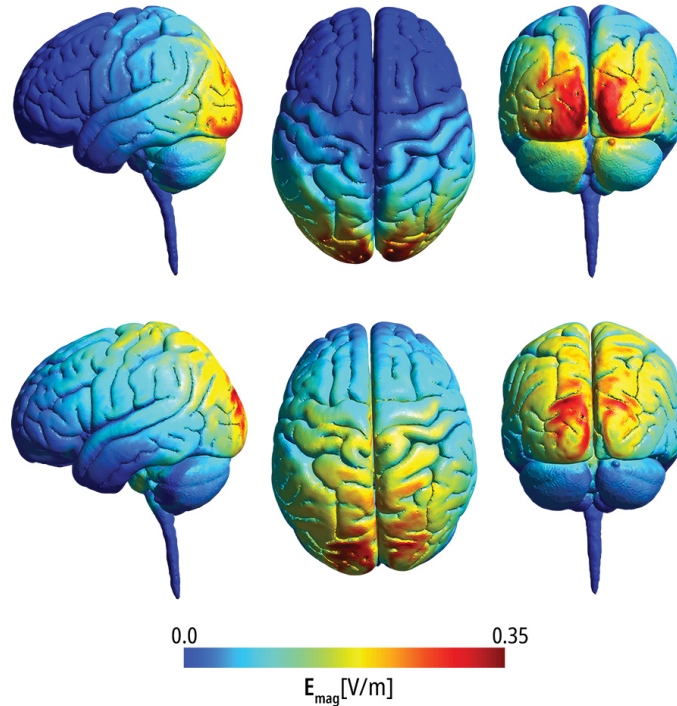
Figure 3.1: Finite-element-models of electric field magnitude [V/m] in the MNI152 template brain. Models for tDCS at 1.5 mA were constructed using the open-source software SimNIBS v3.0.5 (Thielscher et al., 2015). *Top:* PO7-PO8 electrode montage with anode at PO8 (Experiment 2). *Bottom:* Oz-Cz electrode montage with anode at Oz (Experiment 1).

3.2 Methods

3.2.1 Study design and participants

Forty-four right-handed participants under the age of 35 years were recruited for this study. Ethical approval for the study was obtained from the School of Psychology Research and Audit Ethics Committee at Cardiff University. Research was carried out in accordance with the Declaration of Helsinki. Informed consent was obtained from each participant prior to data collection and all participants were paid for participation.

This study used a double-blind, sham-controlled design (see Figure 3.2 for visual overview). All participants took part in an intake session and multiple tDCS sessions (within-subject). Twenty-two participants (M = 22.06±0.69 years; 13 female) completed *Experiment 1* (Oz-Cz electrode montage). A second group of twenty-two participants (M = 22.09±0.44 years; 18 female) completed *Experiment 2* (PO7-PO8 electrode montage).

In *Experiment 1*, participants received anodal and cathodal verum stimulation as well as sham tDCS (3 sessions in total). In *Experiment 2*, participants received verum and sham tDCS (2 sessions in total). Participants were not made aware that the study

included a sham condition. Session order was counterbalanced between participants and each session was scheduled at least 48 hours apart to avoid potential carry-over effects of tDCS (Monte-Silva et al., 2013). Each participant completed his/her sessions at the same time of day to minimise potential circadian variation in contrast sensitivity (Andrade et al., 2018).

In each tDCS session, participants performed an automated threshold perimetry task while verum or sham tDCS was applied to the occipito-parietal cortex. Participants were tested using both eyes. All participants had an uncorrected visual acuity of ≥6/9.5 as measured with a reduced Snellen chart at a viewing distance of 6 feet. Spherical refractive error was limited to +6.00 DS and -2.5 DS, if under 30 years or +1.00 DS and -2.5 DS, if over 30 years. Astigmatism was restricted to <±3.00 DC. Participants reported to be free of any neurological, ocular or systemic disease and any medications affecting visual performance.
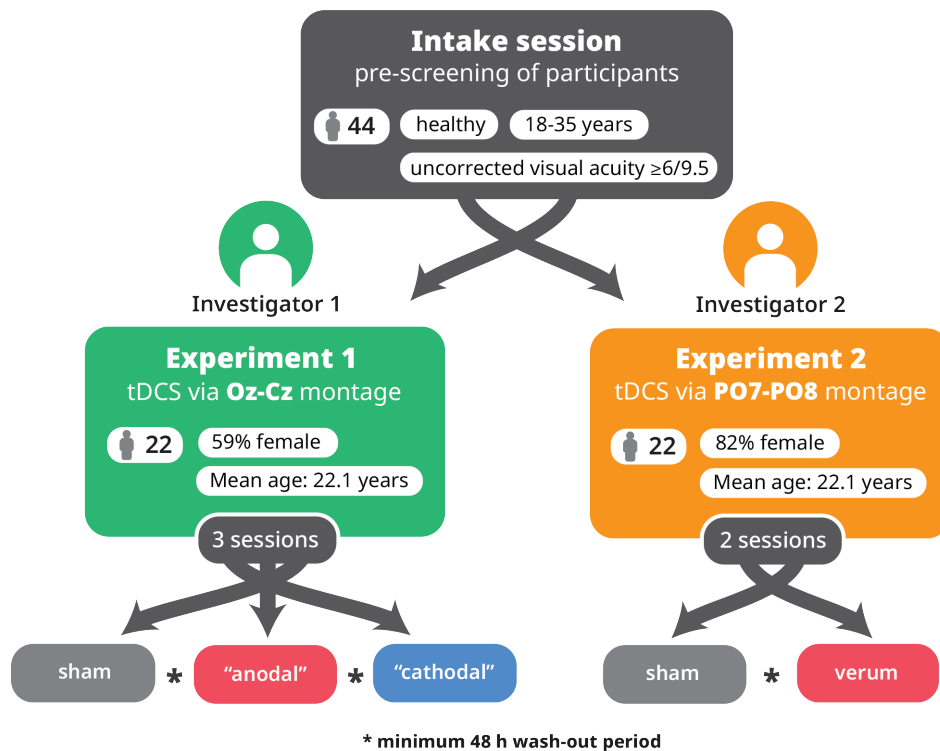
Figure 3.2: Visual summary of study design. The order of tDCS sessions was counterbalanced with a minimum wash-out period of 48 hours.

3.2.2 Transcranial direct current stimulation

Transcranial direct current stimulation was delivered using a NeuroConn DC-STIMULATOR PLUS (NeuroCare Group GmbH, Ilmenau, Germany) and two scalp electrodes. In *Experiment 1*, electrodes were placed at Oz and Cz (International 10-20 EEG system). We chose this electrode position based on previous tDCS studies on the visual system (for

review see Costa et al., 2015b). In *Experiment 2,* we used a bilateral montage, with electrodes at EEG positions PO7 and PO8. As illustrated in Figure 3.1, finite-element-models of electric field patterns in the MNI152 template brain suggested that the peak electric field magnitude induced by the Oz-Cz was located near the parieto-occipital junction and further away from the occipital pole when compared to the PO7-PO8 montage.

Current was applied at 1.5 mA via 5x5 cm^2 silicone-rubber electrodes, resulting in a nominal current density of 0.06 mA/cm^2. The scalp areas covered by the electrodes were prepared with alcohol and Nuprep skin prep gel (Weaver and Company, Aurora, CO, USA). Electrodes were attached to the scalp with a thin layer of ten20 conductive paste (Weaver and Company, Aurora, CO, USA).

At the beginning of each tDCS session, a short impedance test protocol was executed, which consisted of an automatic 10 s fade-in, followed by 15 s of constant stimulation at 1.5 mA and a 10 s fade-out. Impedance levels were recorded at the 25 s mark. Test impedance levels were $\leq$5.4 kΩ (M = 2.7 $\pm$ 0.13 kΩ) in *Experiment 1* and $\leq$7.8 kΩ (M = 3.7 $\pm$ 0.31 kΩ) in *Experiment 2*.

During verum tDCS, current was applied for 30 min with a 10 s fade-in/out at the beginning and the end of the protocol. During sham tDCS, current was applied for the first 60 s of the protocol with a 10 s fade-in/out to mimic the peripheral sensations induced by verum tDCS (*cf.* Figure 2.3 in Chapter 2.). The NeuroConn DC-STIMULATOR was used in "study" mode and during stimulation the lower half of the device screen was hidden from view — effectively removing any cues as to the stimulator's performance — to fully blind the experimenter.

3.2.3   Apparatus and stimuli

Visual stimuli were presented on a gamma-corrected OLED display (25" Sony PVM-A250 Trimaster EL, 1920 x 1080 px resolution, 60 Hz frame rate, 120 Hz refresh rate) driven by a ViSaGe MKII Stimulus Generator (Cambridge Research Systems, Rochester, UK). Participants were seated in a dark room at a viewing distance of 50 cm. The stimulus presentation routine was programmed in MATLAB (Version 2014b; The Math-Works, Inc., Natick, MA) using the CRS toolbox (Version 1.27; Cambridge Research Systems, Rochester, UK).

Achromatic, circular stimuli with a diameter of 0.43° (Goldmann III equivalent) were displayed for 200 ms at locations extending 20° or 4° from fixation in the upper left or lower right quadrants (four test locations in total, see Figure 3.3). A uniform background luminance of 10 cd/m^2 was maintained, in keeping with most current models of automated perimeters. Throughout all tests, participants were instructed to fixate a cross at the screen centre. Failure to keep fixation was monitored using a

LiveTrack eyetracker (Cambridge Research Systems, Rochester, UK). The participants' task was to press a button when they saw a stimulus at any of the four locations. Responses to detected stimuli were recorded by a button press (Cedrus RB-530; Cedrus, USA). Participants were not instructed to respond rapidly and no feedback about response accuracy was given.
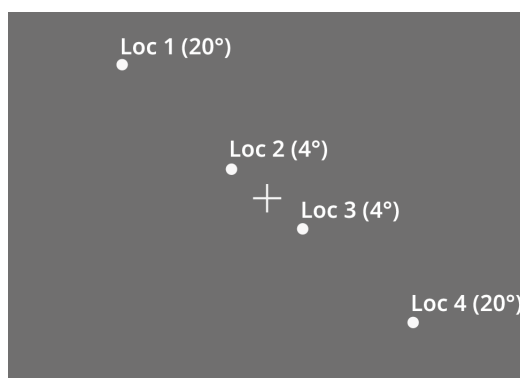
Figure 3.3: Illustration of the four stimulus locations at central (4°) and peripheral (20°) visual field eccentricities (stimulus diameter not to scale). Data from Locations 1 and 4, and Locations 2 and 3 were pooled for analysis.

3.2.4   Psychophysical procedure

Luminance detection thresholds during tDCS were measured with a method of constant stimuli (MOCS) in which the psychometric function was densely sampled around the expected p(seen) = 0.5 value (i.e., the energy threshold where 50% of stimuli are seen). Frequency-of-seeing (FOS) curves were constructed in a three-stage approach adapted from Rountree et al. (2018), as illustrated in Figure 3.4. Sub- and supra-threshold stimuli were presented at energy levels on the asymptotes of the expected frequency-of-seeing (FOS) curve (*cf.* Hill, 2001).

Stage 1

In an initial intake session, each participant completed an adaptive 1up-1down staircase procedure to determine an approximate energy threshold for each of the four visual field locations. This threshold was then used to construct an efficient sampling protocol for the MOCS in the subsequent stages. Stimulus energy increased/decreased by 0.5 log energy following the first reversal, with proportionally smaller step sizes following each subsequent reversal. Stimulus energy was modulated in steps of 0.05 log unit (i.e., the minimum possible step size) following the fourth and fifth reversals. The staircase terminated after six reversals. The threshold at each test location was taken as the mean of the final four reversals.
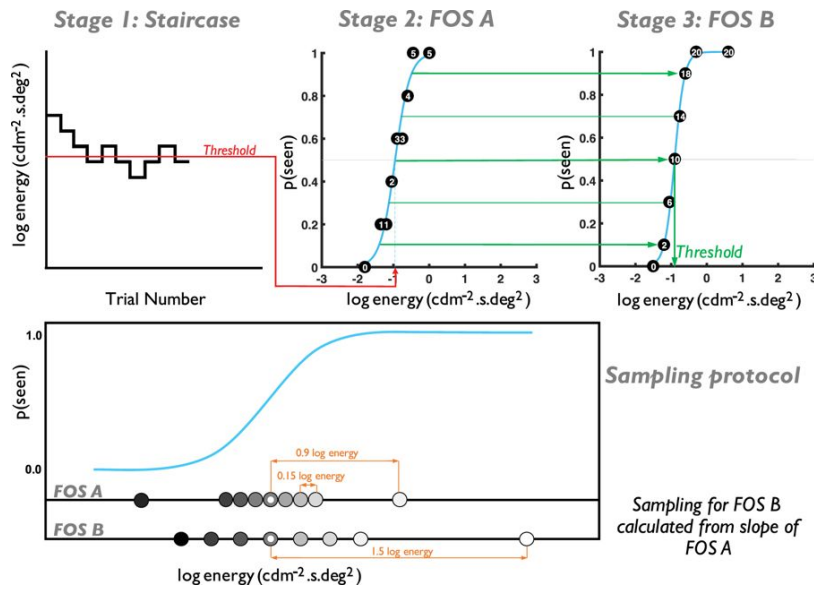
Figure 3.4: Illustration of the three-stage process for determining threshold variability, adapted from Rountree et al., 2018. *Stage 1:* short 1:1 staircase procedure. *Stage 2:* short MOCS (5 presentations per stimulus level), using the threshold from Stage 1 to select presented energy values. *Stage 3:* standard MOCS (15 presentations per level), using the FOS slope from Stage 2 to inform the presented energy values.

To monitor observer attention, no stimulus was presented at eight random instances throughout the procedure and a button press from the participant was recorded as a false positive. False positive rates were <25% for all participants. In addition, at eight random instances throughout the test, a stimulus was presented at 1.5 log energy higher than the first reversal at that test location and failure to respond was recorded as a false negative. The staircase procedure was run once to allow participants to familiarise themselves with the stimuli presentation and was then repeated after a 60 s rest break. Perceptual threshold values from the second staircase run were then used in the non-adaptive stimulus presentation routine in Stage 2. No tDCS was applied during these staircase procedures.

Stage 2

In each tDCS session, we first conducted a short MOCS procedure to estimate an approximate FOS curve position and to optimise curve sampling for the full MOCS procedure in Stage 3.

This short MOCS procedure used nine stimulus energy levels, each presented five times at each of the four test locations (180 presentations in total). The nine energy bins were based on the threshold measured with the staircase procedure in Stage 1, including three bins above and three bins below this threshold level, each separated by 0.15 log energy, as well as two more values at 0.9 log energy above and below the

staircase threshold level. Energy levels and test locations were randomised during stimulus presentation and a 30 s rest break was taken halfway through the procedure.

Based on the measured responses, a FOS curve was constructed for each of the four test locations and a psychometric function was fitted. Energy values at p(seen) = 0.1, 0.3, 0.5, 0.7, and 0.9 were estimated from the curve and used to sample the psychometric function in the next stage.

Stage 3

Participants received tDCS at 1.5 mA for 180 s before stimulus presentation started (see Figure 3.5). Fifteen repetitions of eight energy levels at each of the four test locations were presented in random order. A 60 s rest break was taken after every 120 presentations. Five of the energy levels were determined from the FOS curve measured during the initial short MOCS (Stage 2), i.e., levels for p(seen) = 0.1, 0.3, 0.5, 0.7, and 0.9. Three additional energy levels were used: two levels were determined as p(seen) = ± 2 standard deviations from the psychometric function fitted in the previous stage, and a further level high above threshold, determined as p(seen) = 0.5 + 1.5 log energy, to boost observer attention by presenting a greater number of supra- than sub-threshold stimuli.

Figure 3.5: (Illustration not to scale.) Protocol for Stage 3 of the test procedure. Current was faded in 190 s before visual stimulus presentation began. Sampling of FOS B curves was completed across three task blocks with 60 s breaks. Total tDCS duration was limited to 1800 s.

3.2.5 Data analysis

Investigators were unblinded after data acquisition was completed. Data analysis was conducted on the unblinded FOS data collected in Stage 3 of the test procedure. Trials in which a stimulus was detected were excluded from analysis if the response time was ≥ 2 standard deviations.

Psychometric functions were fitted in MATLAB (Version 2015b; The MathWorks, Inc., Natick, MA, USA) using the Psignifit toolbox (Version 4), which implements the Bayesian psychometric inference method described by Schutt et al. (2016). Frequency-of-seeing curves were fitted using a logistic psychometric function where guess and lapse rates were constrained between 0% and 10%. Increment energy (ΔE, in cd/m^2.s.deg^2) was calculated as the product of increment luminance (cd/m^2), stimulus duration (s)

and stimulus area (deg^2). The energy threshold was defined as the log energy value at p(seen) = 0.5. Psychometric function slope was determined at the 50% performance level. Subsequent data analyses were based on these values.

Statistical analyses were performed with RStudio (Version 1.1.463, RStudio Team, 2016). As threshold perimetry was carried out under binocular viewing conditions, data from Locations 2 and 3, and Locations 1 and 4 were grouped into *central* (4°) and *peripheral* (20°) eccentricities by calculating their mean threshold energy, psychometric function slopes and response times.

3.3   Results

3.3.1   Wash-out periods

Sessions were scheduled at least 48 hours apart to avoid any potential carry-over effects of tDCS. In *Experiment 1*, median wash-out was 7 days (range: 2–61) between the first and second session and 8.5 days (range: 2–99) between the second and third session. The median length of the wash-out period in *Experiment 2* was 7 days (range: 3–123).

3.3.2   Effects on contrast detection threshold

In *Experiment 1* (Oz-Cz, Table 3.1), mean detection thresholds at the 50% performance level ($\hat{\alpha}$) were analysed in a repeated-measures ANOVA with factors *Stimulation condition* (anodal, cathodal, sham) and *Eccentricity* (central, peripheral). A significant main effect was found for *Eccentricity* ($F(21) = 664.68$, $p < .001$), but not for *Stimulation condition* ($F(42) = 2.22$, $p = .121$).

Mauchly's test indicated that the assumption of sphericity was violated for the *Stimulation condition* x *Eccentricity* interaction ($W = 0.673$, $p = .019$, $\varepsilon = .75$). We therefore report Greenhouse-Geisser corrected values here. The analysis failed to show a significant main effect for the interaction ($F(42) = 1.47$, $p = .242$), see Figure 3.6 *Left*.

An equivalent analysis for *Experiment 2* (PO7-PO8, Table 3.2) similarly showed a significant main effect only for *Eccentricity* ($F(21) = 867$, $p < .001$) but not for *Stimulation condition* ($F(21) = 0.178$, $p = .678$). The interaction effect between the two factors was also non-significant ($F(21) = 0.03$, $p = .872$), see Figure 3.6 *Right*.

Eccentricity	Condition	Mean±SE
Central	*Sham*	-1.922±0.022
	Anodal	-1.920±0.024
	Cathodal	-1.902±0.021
Peripheral	*Sham*	-1.474±0.023
	Anodal	-1.449±0.030
	Cathodal	-1.427±0.040

Table 3.1: *Experiment 1*: Mean log energy threshold $\hat{\alpha}$ (cd/m^2.s.deg^2) at central and peripheral visual field locations for sham, anodal and cathodal tDCS.

Eccentricity	Condition	Mean±SE
Central	*Sham*	-1.968±0.017
	Verum	-1.975±0.017
Peripheral	*Sham*	-1.540±0.024
	Verum	-1.544±0.019

Table 3.2: *Experiment 2*: Mean log energy threshold $\hat{\alpha}$ (cd/m^2.s.deg^2) at central and peripheral visual field locations for sham and verum tDCS.
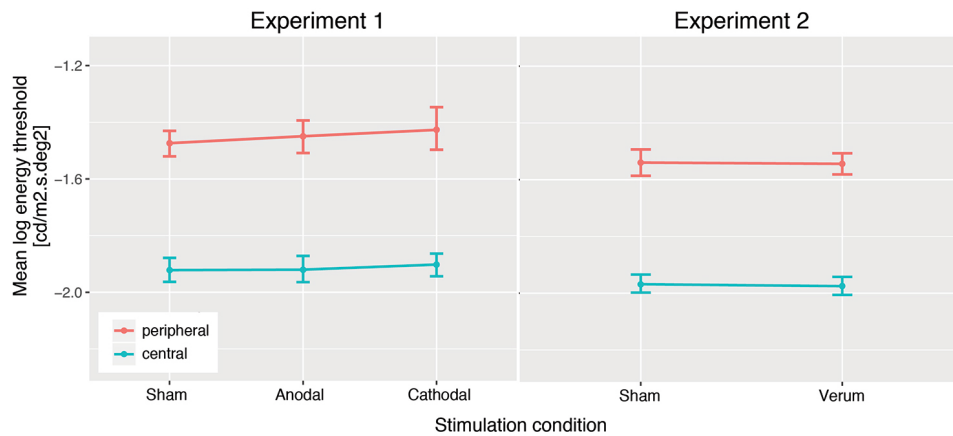
Figure 3.6: Interaction graph for $\hat{\alpha}$ (mean, 95% CI) for stimulus detection as measured by automated threshold perimetry during tDCS. In both experiments and all tDCS conditions, detection thresholds were significantly higher at peripheral (20°) vs. central (4°) visual field locations.

3.3.3 Effects on the slope of the psychometric function

To explore if tDCS had differential effects on the relationship between task performance and stimulus signal strength, we also assessed the slope of the psychometric function ($\hat{\beta}$) at the 50% performance level.

In *Experiment 1* (Oz-Cz, Table 3.3), slope values of the psychometric function were analysed in a repeated-measures ANOVA with factors *Stimulation condition* (anodal, cathodal, sham) and *Eccentricity* (central, peripheral). We found significant main effects for both *Eccentricity* ($F(21) = 4.62$, $p = .043$) and *Stimulation condition* ($F(42) = 4.03$, $p = .025$). However, the interaction between *Stimulation condition* and *Eccentricity* was not significant ($F(42) = 0.51$, $p = .606$), see Figure 3.7 *Left*.

For *Experiment 2* (PO7-PO8, Table 3.4), a two-way repeated-measures ANOVA showed a significant main effect for *Eccentricity* ($F(21) = 17.10$, $p < .001$) but not *Stimulation condition* ($F(21) = 2.37$, $p = .138$). The interaction effect between the two factors was also non-significant ($F(21) = 0.035$, $p = .853$) see Figure 3.7 *Right*.

Eccentricity	Condition	Mean±SE
Central	*Sham*	4.671±0.307
	Anodal	4.255±0.247
	Cathodal	4.147±0.333
Peripheral	*Sham*	4.213±0.281
	Anodal	4.038±0.364
	Cathodal	3.380±0.248

Table 3.3: *Experiment 1*: Mean $\hat{\beta}$ at central and peripheral visual field locations for sham, anodal and cathodal tDCS.

Eccentricity	Condition	Mean±SE
Central	*Sham*	4.953±0.438
	Verum	5.465±0.421
Peripheral	*Sham*	3.802±0.210
	Verum	4.180±0.283

Table 3.4: *Experiment 2*: Mean $\hat{\beta}$ at central and peripheral visual field locations for sham and verum tDCS.
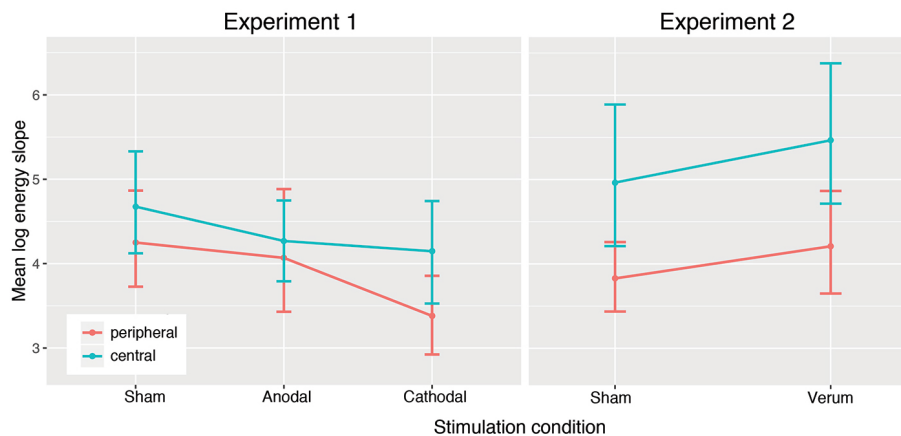
Figure 3.7: Interaction graph for $\hat{\beta}$ (mean, 95% CI) as measured by automated threshold perimetry during tDCS. In both experiments psychometric function slopes were shallower at peripheral (20°) vs. central (4°) locatiosn.

3.3.4 Effects on response times

For both experiments, response times for visual stimulus detection were analysed in repeated-measures ANOVAs with factors *Stimulation condition* and *Eccentricity*.

For *Experiment 1* (Oz-Cz, Table 3.5), we found a significant main effect for *Eccentricity* ($F(21) = 1000.3$, $p < .001$). Mauchly's test indicated that the assumption of sphericity was violated for the factor *Stimulation condition* ($W = 0.637$, $p = .011$, $\varepsilon = .73$) and the interaction between the factors ($W = 0.568$, $p = .004$, $\varepsilon = .70$), therefore Greenhouse-Geisser corrected degrees of freedom are reported. There was a significant main effect for *Stimulation condition* ($F(42) = 20$, $p < .001$). The *Stimulation condition* x *Eccentricity* interaction was also significant ($F(42) = 17.7$, $p < .001$), see Figure 3.8 *Left*). This suggests that the effects of tDCS differed for stimuli presented at central vs. peripheral visual field locations. Bonferroni-corrected *post hoc* tests showed significant differences between response times at central vs. peripheral locations in all tDCS conditions ($p < .001$ for sham, anodal and cathodal tDCS). We found differing patterns of significance, however, when examining stimulation effects within the centre and periphery in isolation. For central locations, there was no significant difference for sham compared to either anodal ($p = .804$) or cathodal stimulation ($p = .999$). In contrast, for peripheral locations, sham vs anodal ($p < .001$) or sham vs cathodal stimulation ($p < .001$) were both significant.

Exploring whether response times were significantly different between the two stimulation conditions gave contrasting results again: RTs for anodal vs. cathodal stimulation differed significantly at peripheral locations ($p = .002$), but not at central locations ($p = .999$). Comparing verum tDCS, we also found significant differences for response times to peripheral stimuli in the anodal condition vs. central stimuli in the cathodal condition ($p < .001$), as well as for central stimuli in the anodal condition vs. peripheral stimuli in the cathodal condition ($p < .001$).

For *Experiment 2* (PO7-PO8, Table 3.6), we similarly found significant main effects for *Eccentricity* ($F(21) = 538.47$, $p < .001$) and *Stimulation condition* ($F(21) = 6.28$, $p = .021$). The interaction effect between the two factors was significant, $F(21) = 18.32$, $p < .001$, indicating that tDCS effects differed for central vs. peripheral visual field locations (see Figure 3.8 *Right*). Bonferroni-corrected *post hoc* tests revealed significant differences for response times at central vs. peripheral locations for both sham ($p < .001$) and verum tDCS ($p < .001$). Response times also differed significantly at peripheral locations for sham vs. verum stimulation ($p = .007$) but not at central locations ($p = .999$).

3.3.5 Goodness-of-fit of psychometric functions

We evaluated the effect of different stimulation conditions on response variability (i.e., internal noise) by comparing the respective psychometric function slopes. However, it is also possible that tDCS affected neural noise. To address this possibility, we tested

Eccentricity	Condition	Mean$\pm$SE
Central	*Sham*	0.495$\pm$0.008
	Anodal	0.508$\pm$0.008
	Cathodal	0.504$\pm$0.008
Peripheral	*Sham*	0.732$\pm$0.018
	Anodal	0.830$\pm$0.004
	Cathodal	0.758$\pm$0.013

Table 3.5: *Experiment 1*: Response times for contrast detection during tDCS.

Eccentricity	Condition	Mean$\pm$SE
Central	*Sham*	0.492$\pm$0.010
	Anodal	0.487$\pm$0.008
Peripheral	*Sham*	0.728$\pm$0.012
	Anodal	0.772$\pm$0.007

Table 3.6: *Experiment 2*: Response times for contrast detection during tDCS.
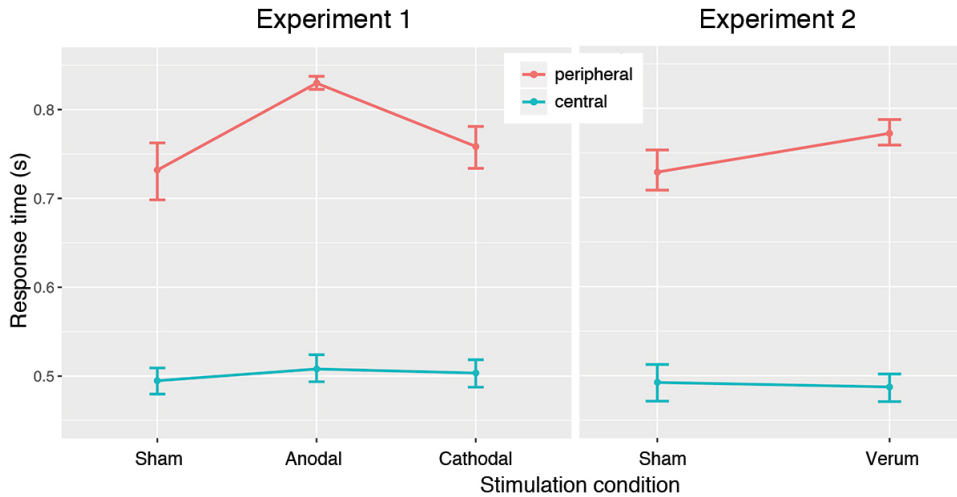
Figure 3.8: Interaction graph for response times (mean, 95% CI) for visual stimulus detection during tDCS. In both experiments and across all tDCS conditions, response times were significantly higher for peripheral (20°) vs. central (4°) visual field locations.

for systematic differences in model fit for the different tDCS conditions and stimulus luminance levels.

For each of the fitted psychometric functions, we calculated deviance residuals for all data points, where residuals were negative for data points falling below the psychometric function and positive for data points above the psychometric function. Thus, a psychometric function closely fitting the data would result in deviance residuals with a mean close to zero and a minimal standard deviation. Using the sum of the squared deviations between our model and the data, Deviance *D*, as a metric, we then assessed the GOF for each tDCS condition. For both experiments, Deviance *D* was compared in repeated-measures ANOVAs with factors *Stimulation condition* and *Eccentricity*.

For *Experiment 1,* we found no significant main effect for either *Stimulation condition* ($F(42) = 0.06$, $p = .939$) or *Eccentricity* ($F(63) = 2.52$, $p = .663$). The interaction effect between the factors was also non-significant ($F(126) = 0.686$, $p = .662$), see Figure 3.9.

An equivalent analysis for *Experiment 2* similarly showed no significant main effect for either *Stimulation condition* ($F(21) = 01.47$, $p = .239$) or *Eccentricity* ($F(63) = 2.21$, $p = .957$). The *Stimulation condition* x *Eccentricity* interaction was also not significant ($F(63) = 1.08$, $p = .364$), see Figure 3.10.

These results indicate that, for both experiments, the goodness-of-fit was similar across all stimulation conditions and eccentricities.
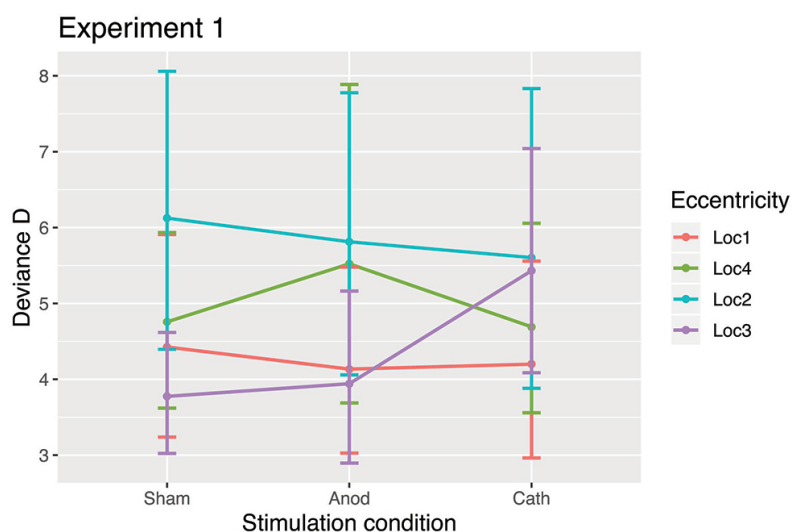
Figure 3.9: *Experiment 1:* Deviance *D* for peripheral (20°) vs. central (4°) visual field locations. Goodness-of-fit was similar across all stimulation conditions and eccentricities.
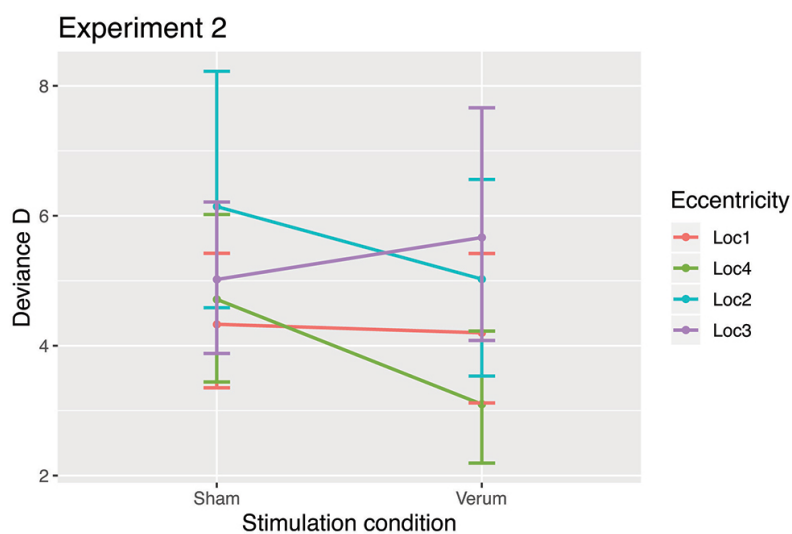
Figure 3.10: *Experiment 2:* Deviance *D* for peripheral (20°) vs. central (4°) visual field locations. Goodness-of-fit was similar across all stimulation conditions and eccentricities.

For each tDCS condition, we also visualised the deviance residuals for the eight luminance bins of our visual stimuli at all four eccentricities. Figures 3.11 and 3.12 suggest that the goodness-of-fit did not differ systematically across luminance bins.

3.3.6   Participant blinding

We assessed the robustness of participant blinding using a debriefing questionnaire at the end of the study. After data collection was completed, participants were asked to guess if they had been receiving "real or placebo stimulation" for each session.

In *Experiment 1* (3 sessions), 32% of participants (7 of 22) correctly guessed the stimulation type for all three sessions. Assuming that participants had a 12.5% chance of guessing correctly, they correctly guessed the stimulation condition above chance level, exact binomial, p = .015 (1-sided), indicating that participant blinding was compromised for Experiment 1. Alternatively, under the more conservative assumption that participants may have expected at least one session to be a placebo intervention (i.e., a 33% chance of guessing correctly), an exact binomial test showed that participants did *not* guess correctly above chance level, p = .626 (1-sided).

In *Experiment 2* (2 sessions), 27% of participants (6 of 22) correctly guessed the stimulation type for both sessions. An exact binomial test indicated that participants did not guess correctly more often than would be expected by chance (i.e., 25%), p = .483 (1-sided). Alternatively, under the more conservative assumption that participants had a 50% chance of guessing correctly, participants also did not perform above chance level, exact binomial p = .992 (1-sided).

3.4   Discussion

In this double-blind study, we investigated the effect of tDCS on contrast sensitivity at central and peripheral visual field locations in young, healthy participants. In two separate groups of participants, we targeted the visual cortex using two different electrode montages (Oz-Cz vs. PO7-PO8). Stimulation effects on luminance detection thresholds at the 50% performance level, on psychometric function slope and on response times were assessed for each group.

For both electrode montages, as well as both verum and sham tDCS, results showed that contrast detection thresholds were higher at peripheral (20°) compared to central (4°) eccentricities. This difference in contrast sensitivity is expected for the measurement conditions in our study (Johnson et al., 1978; Pöppel and Harvey, 1973). However, contrary to previous findings in the literature (Costa et al., 2015a; Kraft et al., 2010; Reinhart et al., 2016), verum tDCS failed to modulate contrast detection thresholds when compared to sham stimulation for both electrode montages.
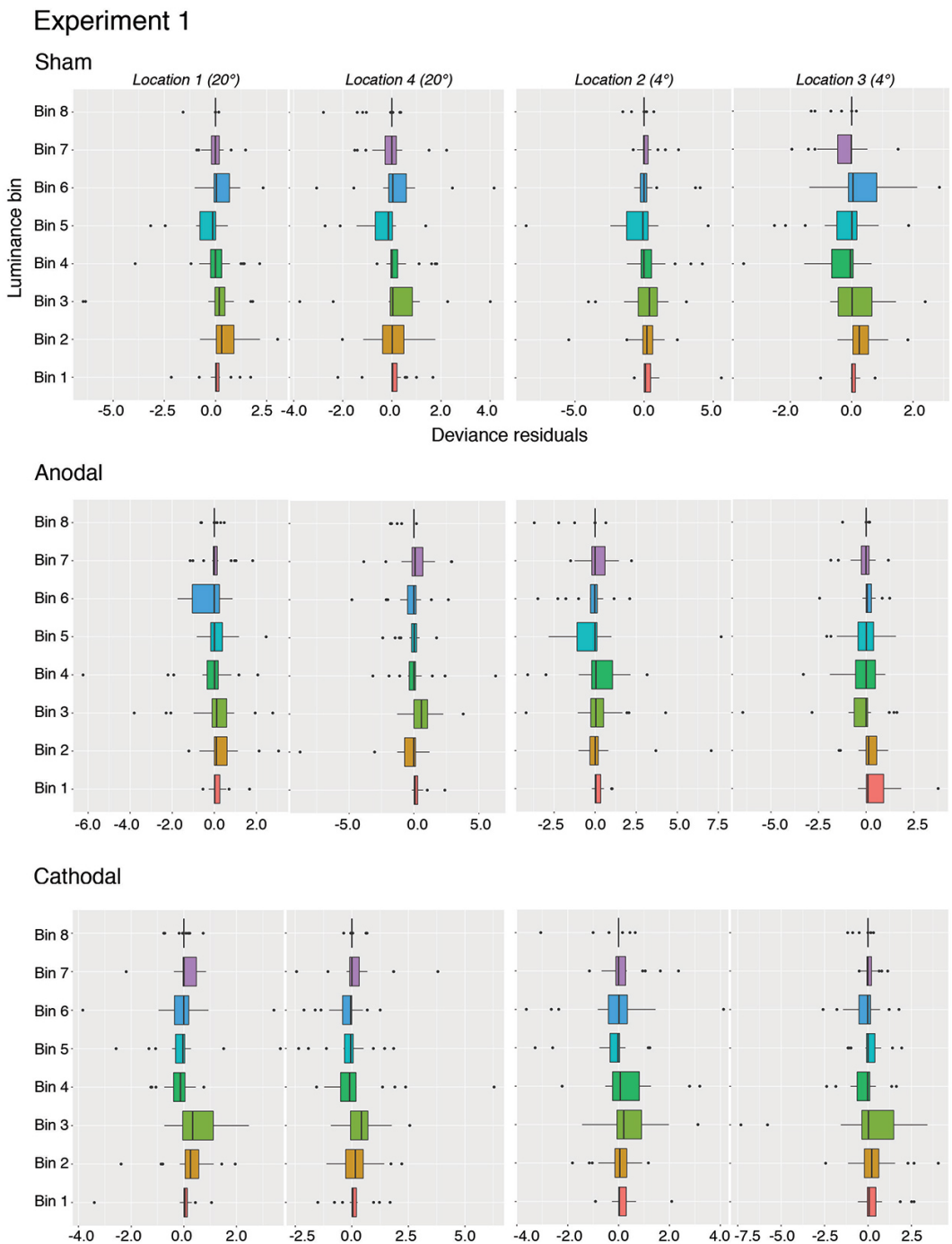
Figure 3.11: *Experiment 1:* Deviance residuals across the eight visual stimulus luminance bins at peripheral (20°) and central (4°) visual field locations.
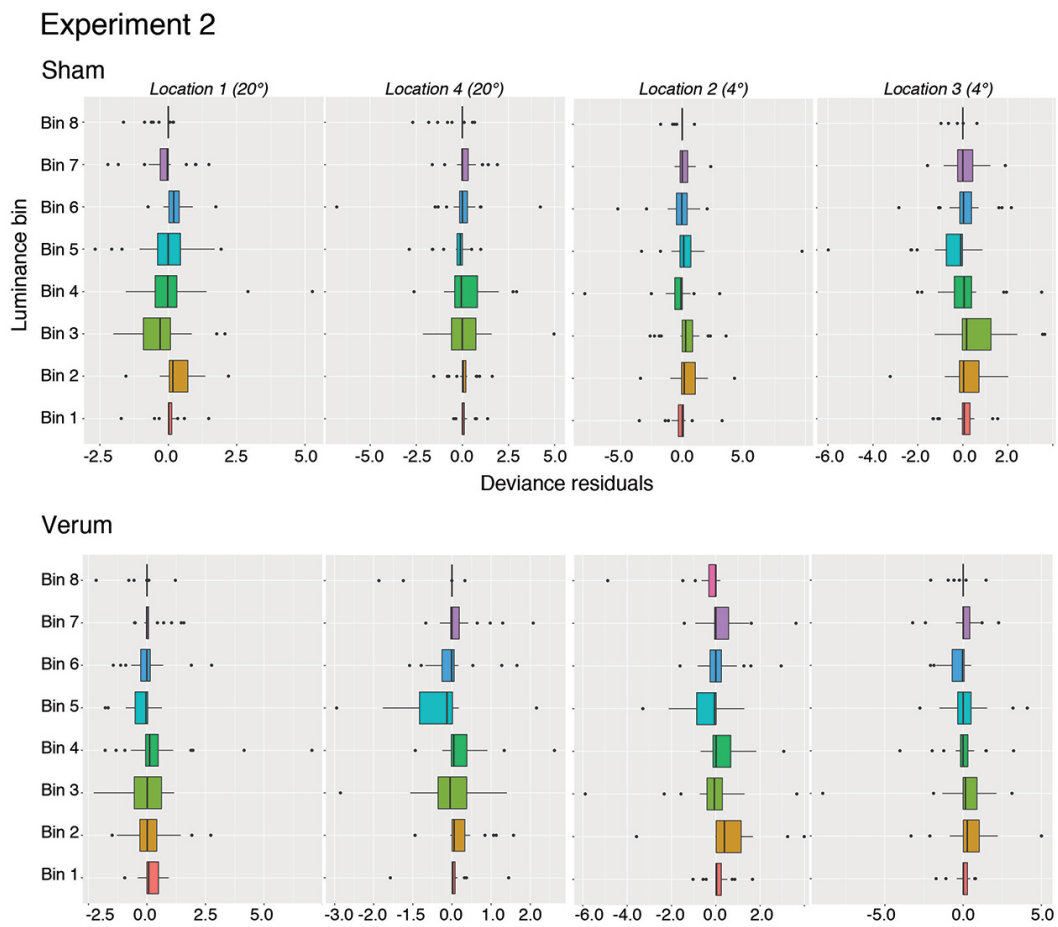
Figure 3.12: *Experiment 2:* Deviance residuals across the eight visual stimulus luminance bins at peripheral (20°) and central (4°) visual field locations.

As an alternative metric of participants' sensitivity to stimulus change, we also evaluated tDCS effects on psychometric function slope. We found that slopes were consistently shallower at peripheral eccentricities, suggesting that the degree of uncertainty in the response to stimulus luminance change differed between visual field locations. As stimulus size was the same at central and peripheral locations, stimuli presented at 20° likely were harder to perceive, resulting in higher observer uncertainty. However, our results also indicated that tDCS affected psychometric function slope only when delivered via the Oz-Cz electrode montage but not via the PO7-PO8 montage.

Several factors may have contributed to the lack of tDCS effects. As discussed previously, the question of inter-individual variability in response to tDCS is a particularly pertinent issue. Previous work suggests that tDCS outcomes in an initial screening session are predictive of participants' chances of responding to tDCS in future sessions: for tDCS in the motor system, 60–69% of individuals who respond to anodal tDCS once are likely to consistently show effects from tDCS in the future (López-Alonso et al., 2015). Some authors have suggested that including only such "good responders" in experiments can significantly reduce the sample size needed to find significant results (López-Alonso et al., 2014).

While adopting this approach may be advantageous for some experiments, we have deliberately chosen not to do so. Firstly, it is not clear that findings on inter- or intra-individual differences in the motor system can or should easily be generalised to other cortical regions. For example, Brückner and Kammer (2016) failed to find a modulation of phosphene thresholds after both anodal or cathodal tDCS of the visual cortex. Rather, their study identified high inter-individual variability in tDCS response and found moderate intra-individual reliability in the direction of modulation only for cathodal tDCS. More recently, He et al. (2019) also reported a lack of offline tDCS effects on the contrast sensitivity function in healthy adults. They observed no significant correlation between contrast sensitivity changes in two anodal tDCS sessions and a sham session, arguing against a "responder/non-responder" approach to tDCS effects on visual processing.

Secondly, we were interested in sampling the true variability of participant responses across a sample of the population. The pre-selection of good responders is likely to preclude any real generalisability to such a population. One likely source of this variance is the varying anatomical conditions across different cortical areas, which can strongly influence tDCS outcomes. Because skull thickness determines the flow of current through the brain, and thus the effective electric field strength in the grey matter (Datta et al., 2011; Giordano et al., 2017), one plausible reason for smaller tDCS effects over V1 compared to the primary motor cortex can be seen in the relatively greater skull thickness and density of the occipital bone compared to the parietal

bone (Voie et al., 2014; Zarghooni et al., 2016). The effects of tDCS are also dependent on the distance and orientation of neuronal axons in the electric field: the drift of membrane potential is higher when current flow is oriented in parallel to the neuronal axons rather than orthogonally (Lafon et al., 2017; Rahman et al., 2013). In contrast to M1, cells in V1 are mainly horizontally orientated and located deep in the occipital cortex (Dougherty et al., 2003). This anatomical aspect may be another reason for relatively weaker tDCS effects in the early visual cortex.

In addition, tDCS-induced electric field strength likely differs across the early visual areas (V1, V2, V3) that preferentially process central vs. peripheral stimuli. Central and peripheral portions of the visual field are mapped to neurons in different spatial locations (Wang et al., 2013), with the central field being processed by more superficial cells located in the occipital pole. Thus, for an Oz-Cz electrode montage, neurons processing central stimuli lie closer to the polarising scalp electrode than more peripheral regions processed by cells in the calcarine fissure. Accepting this fact, one would still expect to see *some* effect of tDCS in our study — at least on the central visual field for the Oz-Cz electrode montage. However, preliminary finite-element-models of the electric field spread of our electrode montages (Figure 3.1) have suggested that the focal point of the electric field induced by the widely-used Oz-Cz montage lies *not* in the early visual cortices, but is instead located nearer to the parieto-occipital junction, with diminished field strengths found in the occipital pole. This issue is explored in more detail in Chapter 4.

Moreover, it is possible that the current intensity we used was simply too low to effectively polarise the relevant neuronal populations in the early visual cortices — at least for a subset of our participants. While the same or lower current intensities have led to effects in previous tDCS studies of contrast sensitivity (Costa et al., 2015a; Kraft et al., 2010), several recent studies have highlighted that tDCS effects can become non-linear under certain conditions. For instance, in a study on the primary motor cortex by Batsikadze and colleagues (2013), the application of cathodal tDCS for 20 min at 2 mA resulted in cortical excitability enhancement instead of inhibition. Their findings suggest that increasing current intensity does not necessarily increase stimulation efficacy but might instead change the *direction* of excitability alterations. In another tDCS study, Bastani and Jaberzadeh (2013) compared the effects of different current intensities (0.3, 0.7, 1.4 and 2 mA) on corticospinal excitability. Counterintuitively, they found that after 10 min of continuous stimulation, anodal tDCS at 0.3 mA induced significantly larger excitability changes than stimulation at 0.7 mA. It is currently unclear, how these findings translate to the visual system, but given its morphological complexity, similar non-linearities can likely be expected.

The observed lack of modulation of detection thresholds in both experimental groups may also be due to variance in the placement of electrodes across participants. In this

study, electrodes were placed based on head measurements following the EEG 10-10 system – a widely used approach likely leading to small placement errors across repeated sessions. We do not, however, have data allowing us to quantify this placement variation for our current sample of participants. The use of a functional localiser MRI protocol in combination with a neuronavigation system could mitigate this source of variance in future studies — at the cost of an increased burden on participants and resources.

Additional inter-individual variance may also stem from gender differences in tDCS effects. Sex differences in the response to anodal tDCS of the visual cortex have been reported in a study that evaluated VEPs, phosphene thresholds and contrast sensitivity in 46 participants (Chaieb et al., 2008). In women, anodal tDCS increased cortical excitability significantly when compared to an age-matched male participant group. Notably, no significant difference between male and female participants was observed immediately after stimulation. As our samples were not fully balanced in regard to gender, such sex differences might constitute a confounding factor. However, the findings from Chaieb and colleagues primarily concern *offline* effects of tDCS. Further studies are required to clarify if gender-specific differences also occur for online tDCS.

Furthermore, the effects of tDCS on cortical regions – and ultimately behaviour – may be governed by participants' abilities on a given task. For instance, Reinhart et al. (2016) found that tDCS effects on visual acuity were greatest for participants with poorest baseline acuity. "Floor" and "ceiling" effects (where participants are extremely poor or extremely skilful in their abilities on a given task) are common in psychological paradigms. In the present study, we have tried to avoid floor and ceiling effects by individually tailoring the stimulus energy levels in the task to each participants' threshold for each particular session. The method of constant stimuli (MOCS) ensures that participants judge stimuli across the entirety of their perceptual abilities. Here, we have focused on a single estimate of their ability, the widely used 50% threshold measure. However, it is possible that the effects of tDCS are more obviously manifest *at* the ceiling and floor levels.

While the factors discussed above do not, *per se*, explain why we observed no systematic tDCS effect on contrast sensitivity, they have all likely increased the variance in our sample. A subset of these factors can be explored by electric field models of tDCS. While we do not present the data here, we acquired anatomical MRI scans for all participants in Experiment 1 with the aim of modelling individual electric field spread. Combined insight from these participant-specific models and our behavioural data allowed us to explore the issue of inter-individual variance in Chapter 4.

It also worthwhile to note that, for samples with high variance, significant differences between verum and sham tDCS may only be achievable with repetitive application. This notion is supported by a recent study from Behrens et al. (2017), which

found significant effects of anodal tDCS on contrast sensitivity in the central visual field only after the second day of application.

Finally, we had no hypothesis regarding tDCS effects on response times and, in keeping with established practice for automated threshold perimetry, had not instructed participants to respond rapidly. Response time to luminance stimuli is determined by stimulus strength (i.e., size, intensity and duration), background illumination, noise from spontaneous neuronal activity and degree of uncertainty of stimulus perception. In this study, background illumination as well as stimulus duration, intensity and – importantly – size were the same at central and peripheral eccentricities. We would therefore expect stimuli closer to fixation to be perceived more easily and response times to be lower at central eccentricities (Ando et al., 2001; Rains, 1963; Wall et al., 2002). Indeed, we observed lower response times for stimuli presented at central vs. peripheral visual field locations across all experimental conditions. Additionally, our results show that verum tDCS modulated response times for peripheral but not central stimuli when compared to sham tDCS. This finding was consistent in both groups of participants. Contrary to expectations based on the classic "anodal-excitatory/cathodal-inhibitory" paradigm of tDCS, anodal verum stimulation via the Oz-Cz electrode montage *negatively* affected performance. Verum tDCS similarly had a deleterious effect on response time for tDCS delivered via the bilateral PO7-PO8 montage.

In conclusion, in contrast to previous reports, we failed to observe significant effects of tDCS on contrast detection thresholds regardless of electrode montage. On the basis of our behavioural findings, it remains unclear whether differences in methodology or inter/intra-individual variance in tDCS response is the primary cause of this discrepancy. This question is explored further in Chapter 4.

Chapter 4

Variability of tDCS effects: relating behaviour to electric field models

4.1 Introduction

Transcranial direct current stimulation has transitioned into clinical use, for example in trials applying tDCS to treat depression or chronic pain (David et al., 2018; Palm et al., 2016). Our lack of a deeper understanding of tDCS's underlying mechanisms may be acceptable if the clinical benefits outweigh the possible concerns arising from this missing insight. The parameter space for electrical stimulation of the brain is extremely large and the effective selection of stimulation parameters is challenging. As a result, most studies to date have been based on a "one-dose-fits-all" approach to transcranial stimulation.

However, outcomes in both basic research studies and clinical trials have been inconsistent and criticism of tDCS has highlighted the technique's poor repeatability (e.g., Horvath et al., 2014, 2015; Learmonth et al., 2017). Recent studies on inter- and intra-individual differences in electric brain stimulation outcomes emphasise this, pointing to a considerable proportion of non-responders, and highlighting the need to develop predictive markers for dose-dependent tDCS approaches (Ammann et al., 2017; Chew et al., 2015; Dyke et al., 2016b; Li et al., 2015; López-Alonso et al., 2015; Strube et al., 2015; Tremblay et al., 2016; Wiethoff et al., 2014). In recent years, computational neurostimulation efforts have therefore aimed to develop quantitative models linking stimulation dose to changes in neurophysiology, behaviour and cognition.

A major concern in human tDCS studies — at least for experiments aiming to target a specific brain region — is inter-participant differences in functional neuroanatomy. This can be extremely difficult if only scalp locations are used to determine electrode positioning for participants. Even if we ignore the inherent problems arising from using locations on the scalp to infer the locations of underlying cortical regions, detailed cytoarchitectonic atlases have shown that anatomically defined gyri and sulci do not always subserve the same functions between individuals. Moreover, the transcranial

induction of currents in the brain is complex, and encompasses numerous internal (e.g., state- and trait-dependent anatomical and functional characteristics of the participant) and external (e.g., stimulation parameters or experimental design) factors.

A starting point for the development of individually targeted tDCS is the modelling of anatomical differences between participants. For example, Opitz and colleagues simulated tDCS-induced electric fields and found that roughly 50% of the variation of the field in the region-of-interest below the stimulation electrode is determined by anatomical factors, such as the thickness of skull and CSF, the depth of sulci, as well as the distance to the electrode edge and the distance between anode and cathode (Opitz et al., 2015). In a similar effort, Laakso et al., 2015 combined the structural MRI scans of 24 participants with finite-element modelling (FEM) to calculate electric field estimates for tDCS to the motor cortex. They found that, at a group level, the average fields did indeed concentrate near the primary motor cortex. Nonetheless, consistent with several smaller modelling studies (Datta et al., 2012; Truong et al., 2013), their models showed substantial differences in both the magnitude and location of individual electric fields.

Finite-element models of tDCS that aim to provide participant-specific results rely on magnetic resonance imaging (MRI) to capture the details of individuals' head anatomy. Key steps in modelling the induced electric fields are the accurate segmentation of MRIs, the creation of a volume conductor model and the numerical solution of the FEM. A number of different open-source software tools are available for each of these steps. Recently, several software packages combining these into automated or semi-automated pipelines have been made available to the tES research community. Examples of "out-of-the-box" packages include SCIRun BrainStimulator (Dannhauer et al., 2012), SimNIBS (Saturnino et al., 2018) and ROAST (Huang et al., 2019). However, while these integrated pipelines facilitate access to modelling tools for tDCS, it is currently unclear how accurately the electric field models they produce reflect *in-vivo* truths and, thus, to which degree they can meaningfully inform experimental designs or assist in the interpretation of behavioural results. To date, very few studies have attempted to combine FEM simulations of tDCS with empirical data. An early exception is a study by Kim et al., 2014, which investigated the relationship between behavioural performance in a verbal working memory (VWM) task and patterns of induced electric fields in participants' brains simulated using FEM. Seventeen participants were tested before and after tDCS of the dorsolateral prefrontal cortex (DLPFC). Individuals who displayed enhanced VWM task performance after stimulation had a significantly larger current density at the DLPFC than other participants, supporting the notion that the variable behavioral effects of tDCS might, in part, be explained by the varying anatomical differences between participants.

More recently, Mikkonen et al., 2018 measured the resting motor threshold (RMT)

— an indicator of transcranial magnetic stimulation (TMS) sensitivity previously shown to relate to motor cortical tDCS after-effects — in 28 participants. Using FEM on participant-specific MRI data, they simulated both tDCS- and TMS-induced electric fields. They found that RMT correlated with the tDCS-induced electric field magnitude in the hand area of the primary motor cortex (M1) — but not in areas outside M1. Participants with low RMTs tended to have higher estimates of electric field strength in hand M1 than participants with high RMTs. In addition, there was a positive correlation between electric field magnitudes estimated for TMS and tDCS, indicating that participants receiving high TMS-induced electric fields may also experience high tDCS-induced fields.

Antonenko et al., 2019 similarly aimed to investigate the neurophysiological correlates of tDCS' effects, relating the results of magnetic resonance spectroscopy (MRS) and resting-state functional resonance imaging (rsfMRI) to simulations of electric field distributions. In a sample of 24 participants, they targeted the left sensorimotor cortex with tDCS to quantify stimulation effects on the resting state sensorimotor network (SMN) strength, seeking to relate their results to GABA and glutamate concentrations measured with MRS. In line with previous studies (Filmer et al., 2019; Stagg et al., 2009; Stagg et al., 2011b), they observed a decrease of GABA concentrations and an increase in SMN strength for verum compared to sham tDCS. Importantly, the magnitudes of tDCS-induced neurophysiological modulations were significantly associated with SimNIBS-based estimates of electric field strengths in the left precentral gyrus.

Thus, findings from these studies combining FEM with empirical data suggest that inter-individual differences in head anatomy likely contribute to the variability of tDCS-effects in paradigms targeting the motor cortex, sensorimotor cortex or DLPFC. However, to our knowledge, no previous study has investigated the association of behavioural or neurophysiological outcomes and electric field distribution for the visual cortex. As previously discussed, the visual cortex may be a particularly challenging brain region to target with tDCS for a number of anatomical reasons, in particular the region's complex patterns of cortical folding. Individually-tailored stimulation approaches may therefore be especially important to achieve consistent tDCS effects in visual experiments.

In Chapter 3, we evaluated tDCS effects on visual function by applying tDCS via the "classic" Oz-Cz electrode montage while participants performed a contrast detection task. At a group level, we failed to find significant modulations of behaviour for verum compared to sham tDCS. Here, we investigated if inter-individual differences in simulated electric field strengths in the visual cortex relate to inter-individual differences in behavioural modulation. Participant-specific MR images were used to estimate electric field distributions using two different open-source pipelines (i.e., SimNIBS and ROAST) and the agreement of the resulting estimates was assessed.

4.2   Methods

4.2.1   Participants

Twenty-two right-handed participants under 35 years of age (M = 22.06±0.69 years; 13 female) were recruited for this study. Ethical approval for the study was obtained from the School of Psychology Research and Audit Ethics Committee at Cardiff University and research was carried out in accordance with the Declaration of Helsinki. Informed consent was obtained from each participant prior to data collection and all participants were paid for participation. Participants reported to be free of any neurological, ocular or systemic disease and any medications affecting visual performance.

4.2.2   Behavioural data acquisition & tDCS

The behavioural data acquired as part of Experiment 1 described in Chapter 3 was used in this study. A brief summary of the data acquisition and analysis is given below; all further details are provided in Chapter 3.

Participants took part in three tDCS sessions (sham, anodal and cathodal stimulation; session order was counterbalanced). Participants completed all sessions at the same time of day to reduce intra-individual variance due to circadian variation in contrast sensitivity (Andrade et al., 2018). Direct current stimulation was delivered at 1.5 mA via an Oz-Cz electrode montage while participants performed an automated contrast detection task. The luminance range of visual stimuli was pre-tailored to span each participant's individual detection range (0-100%).

To evaluate behavioural performance, detection thresholds ($\hat{\alpha}$) and psychometric function slopes ($\hat{\beta}$) at the 50% performance level were estimated for stimuli presented at central (4°) and peripheral (20°) positions of the visual field. Importantly, for the analyses in the present study, the *difference* of thresholds and slopes in sham and anodal tDCS sessions were used as the behavioural outcome measures (i.e., $\Delta\hat{\alpha}$ and $\Delta\hat{\beta}$).

4.2.3   MRI acquisition

Sequence parameters for the acquisition of structural MR images were based on the recommendations in Windhoff et al., 2013. Two T1-weighted and two T2-weighted contrasts were collected for each participant using a Siemens 3T Prisma scanner with a 64-channel head coil (Siemens Healthcare GmbH, Erlangen, Germany). The FOV of the sequences was specifically chosen to include regions of the neck, as studies have suggested this may result in more accurate models of current distribution (Nielsen et al., 2018; Saturnino et al., 2018). Both T1- and T2-weighted images were collected to ensure good contrast between different brain and tissue compartments for subsequent

segmentation; both fat-suppressed and non-fat suppressed versions of the T1 and T2 scans were acquired. The T1 sequence was a 3D TurboFLASH sequence (sagittal acquisition; FOV 192 x 320 x 320; voxel size 1 mm isotropic), and the T2 a 3D Turbospin Echo (axial acquisition; FOV 256 x 256 x 96; voxel size 1 x 1 x 2 mm, with a 1 mm gap to decrease the amount of fat shift in the slice selection direction).

4.2.4 Head digitisation

Head locations were digitised based on individual structural MRI data using a Brainsight neuronavigation system (Rogue Research Inc., Montreal, Canada). Anatomical landmarks (Nz, LPA, RPA, tip of the nose) were digitised. The locations of the centre of each scalp electrode were similarly recorded in the anodal tDCS session of *Experiment 1* (*cf.* Chapter 3) and used in all subsequent modelling of electric fields.

4.2.5 Finite-element-modelling

At present, there are a number of options available for investigators wishing to model the electric fields arising from tDCS in individual participants. We chose to employ two of the most widely used open-source software packages available, ROAST v2.7.1 (Huang et al., 2019) and SimNIBS v3.0.5 (Saturnino et al., 2018). Both follow a broadly similar workflow from the acquisition of MR images to the visualisation of electric fields, but there are also significant differences between their approaches. A schematic overview of the two modelling pipelines is given in Figure 4.1.

Volume conductor models

For each participant, tissues including white matter, grey matter, CSF, skin and skull were segmented automatically to generate a volume conductor model of the head. While we had originally collected four MR images for each participant, we followed the current recommendations of the authors of each package and used only two of these, a T1 and a T2-weighted image.

For our implementation of SimNIBS, we used the *headreco* option, which calls SPM12 (Penny et al., 2011), to segment extra-cerebral structures and brain tissues, including the neck region. Surface reconstructions of the grey matter were created using the computational anatomy toolbox CAT12 (Dahnke et al., 2013). As part of the standard SimNIBS workflow, the segmentation results were touched-up by the automatic application of simple morphological operations. The segmentation outputs were then inspected manually, with particular attention paid to tissue boundaries. These volume masks were converted into surface format for the mesh generation, and used to generate tetrahedral volume meshes with Gmsh (Geuzaine and Remacle, 2009).
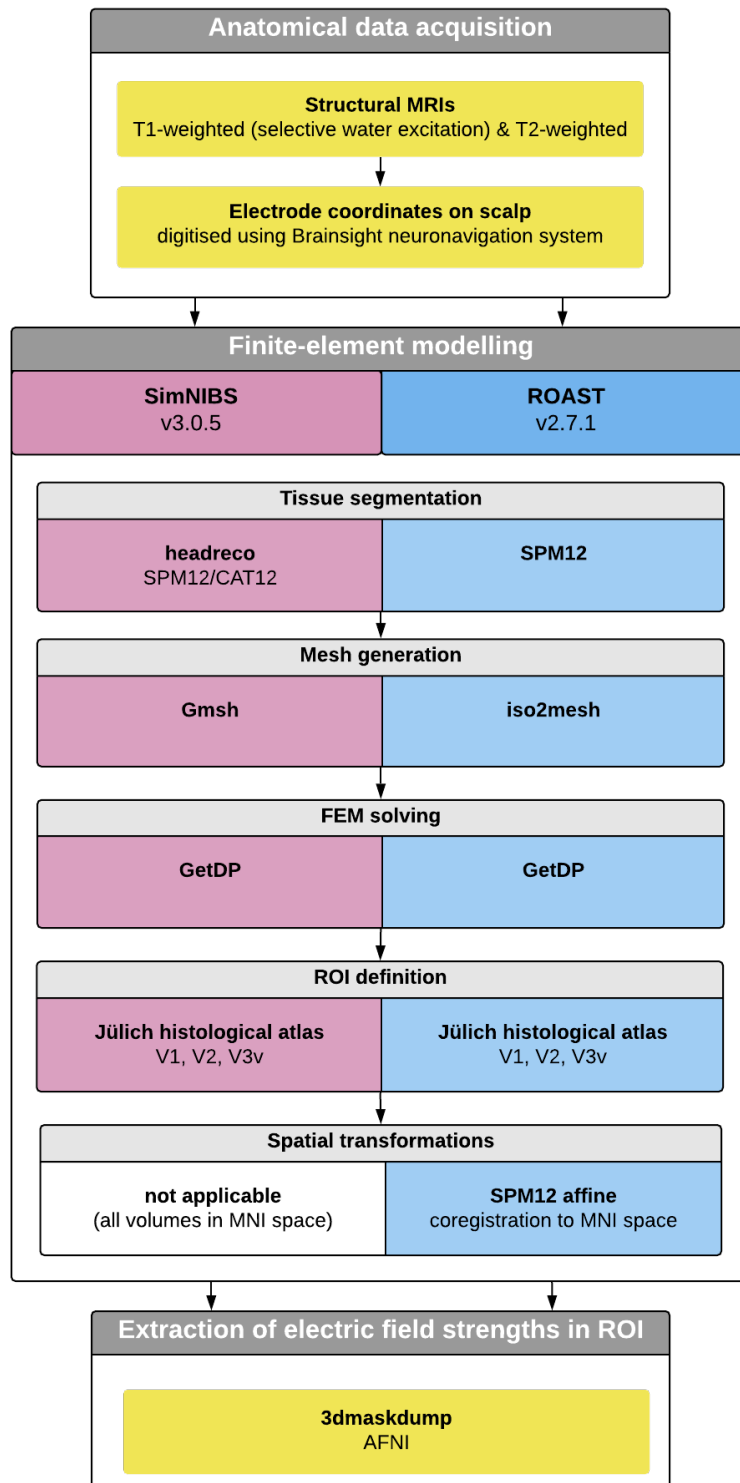
Figure 4.1: Schematic of workflow for constructing and solving finite-element models of tDCS-induced field strengths using SimNIBS and ROAST.

Tissue conductivity	σ (S/m)
White matter	0.126
Grey matter	0.275
CSF	1.654
Skull	0.010
Skin	0.465
Electrode	0.100
Conductive paste	1.000

Table 4.1: Tissue conductivities for FEM.

For our ROAST pipeline, we used v2.0.7, which calls SPM12's segmentation routines, similar to SimNIBS. Subsequently, the segmentation results undergo an automatic post-processing step specific to ROAST, presumably performing a similar touch-up of the outputs (Huang et al., 2013). After this point, the pipelines diverge, with ROAST using the *cgalv2m* function from the MATLAB toolbox iso2mesh (Fang and Boas, 2009b) to generate a volumetric mesh. Notably, in contrast to SimNIBS, meshes created with ROAST are based on hexahedral elements.

FEM set-up and solving

Conductivity values (Table 4.1) were assigned to the segmented tissues based on the parameters recommended by Windhoff et al., 2013. For finite-element models constructed with ROAST, scalp electrodes were modelled using the default value of 3 mm for electrode thickness and 2 mm for the gel layer. For FEMs constructed with SimNIBS, the thickness of the electrodes and conductive gel layer was set to the default values of 1 mm and 5mm, respectively. For both pipelines, the whole surface of the electrode was treated as the connector. For both pipelines, the open-source software GetDP (Geuzaine, 2007) was used to solve the finite-element models for voltage and electric field distribution. The resulting mesh files of electric field distribution were then transformed to volumetric NIFTI (*.nii) images via pipeline-specific interpolation algorithms.

Region-of-interest definition and field magnitude extraction

Region-of-interest masks were constructed based on the JuBrain Cytoarchitectonic Atlas (Amunts and Zilles, 2015; Amunts et al., 2007). Masks for visual regions V1, V2 and V3v in the left and right hemispheres were identified using each participant's MR images. An ROI for the early visual cortex was defined as the combination of voxels assigned to V1, V2 and V3v (Figure 4.2). As ROAST's volumetric results are displayed in native (i.e.,"participant") space, an additional affine transformation was used per participant (SPM12's coregistration function) to transform the *.nii volumes to MNI space. For both pipelines, the electric field magnitude (i.e., the vector norm of the electric

field, *cf.* Figure 1.18) was then extracted for each voxel identified as grey matter that lay within a given visual ROI using the *3dmaskdump* tool in AFNI (Cox, 1996).
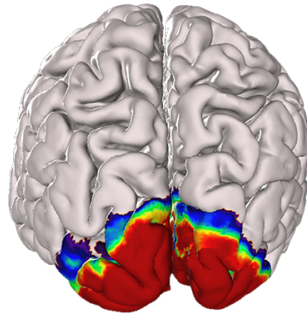
Figure 4.2: Participant-specific early visual cortex ROIs were defined as a combination of regions V1, V2 and V3v as identified by the JuBrain Cytoarchitectonic Atlas. The ROI is illustrated in the Colin27 template brain here (Collins et al., 1998).

4.2.6   Data analysis

Details regarding the analysis of behavioural data are provided in Chapter 3. All additional statistical analyses were performed using MATLAB v2017b (The MathWorks Inc., Natick, MA, USA) and R v3.6.1/RStudio v1.1.463 (RStudio Team, 2016).

Within each ROI, voxels with electric field magnitudes of exactly zero were omitted from analysis, because they were misidentified as belonging to the GM. Across participants and ROIs, an average of 0.3±1.7% of voxels were omitted for estimates based on ROAST, and 63.7±6.6% for estimates based on SimNIBS. In addition, for SimNIBS, an averge of 0.5±0.3% voxels had estimated field magnitudes below zero, likely due to an interpolation error. These voxels were also omitted from analysis. Furthermore, voxels with values above 0.8 V/m were rejected as physiologically unrealistic. Field magnitudes of 0.8 V/m have only been observed for 2.0 mA current input, so we chose this arbitrary cut-off to threshold our ROIs (Huang et al., 2017). An average of 13.4±15.2% of voxels were rejected for estimates from ROAST, and 0.1±0.1% for estimates from SimNIBS. An overview of the total percentage of excluded voxels for each ROI and participant is provided in Figures 4.3 and 4.4.

For each visual ROI, the mean electric field magnitude of voxels within the ROI was calculated. We then assessed the correlation between the estimated mean field magnitude and behavioural outcomes ($\Delta\hat{\alpha}$, $\Delta\hat{\beta}$).

Furthermore, due to current controversies over their differing approaches for simulating tDCS effects, we investigated the agreement among electric field strength simulations based on the ROAST and SimNIBS pipelines. However, the appropriate statistical approach to assess the degree of agreement of two methods is not immediately obvious. While correlation quantifies the degree to which two variables are related,

	ROAST			SimNIBS		
	Mean(SD)	Min	Max	Mean(SD)	Min	Max
Early visual	0.173(0.028)	0.128	0.240	0.205(0.030)	0.152	0.269
V1	0.171(0.028)	0.119	0.236	0.204(0.029)	0.153	0.266
V2	0.175(0.026)	0.135	0.239	0.213(0.033)	0.156	0.280
V3	0.173(0.038)	0.116	0.281	0.177(0.029)	0.131	0.238

Table 4.2: Mean(SD) and range of estimated mean electric field magnitude in the visual ROIs of 22 participants. Results from FEM constructed with ROAST and SimNIBS are given.

it does not necessarily imply that there is good agreement between the two methods. An alternative approach — taken here — is to quantify the agreement between two measurements by constructing limits-of-agreement based on the mean and standard deviation of the *differences* between two methods (Bland and Altman, 1986). This approach is commonly used to directly compare differences between two techniques designed to measure the same parameter.

4.3 Results

4.3.1 Mean electric field strength in visual ROI

Mean electric field strengths in the grey matter of visual ROIs were extracted for head models created with ROAST and SimNIBS (Table 4.2). For models constructed with ROAST, the group average of mean electric field strength in the early visual cortex was 0.17±0.02 V/m, varying by up to 53.3% between participants (Figure 4.5). In comparison, for models constructed with SimNIBS, the group average was 0.20±0.03 V/m, varying by up to 54.2% between participants (Figure 4.6).

4.3.2 Electric field distribution in the whole brain

Visualisations of the electric field distribution in our sample of participants suggest that, using an Oz-Cz montage, the electric field may spread widely through the brain, certainly beyond the areas directly underneath each electrode. While the highest field strengths generally lie in the parieto-occipital cortex, our simulations suggest that a subset of participants likely experienced significant field strengths in cortical regions lying anterior to the vertex (see Figures 4.7–4.9 for ROAST results and Figures 4.11–4.14 for SimNIBS results).
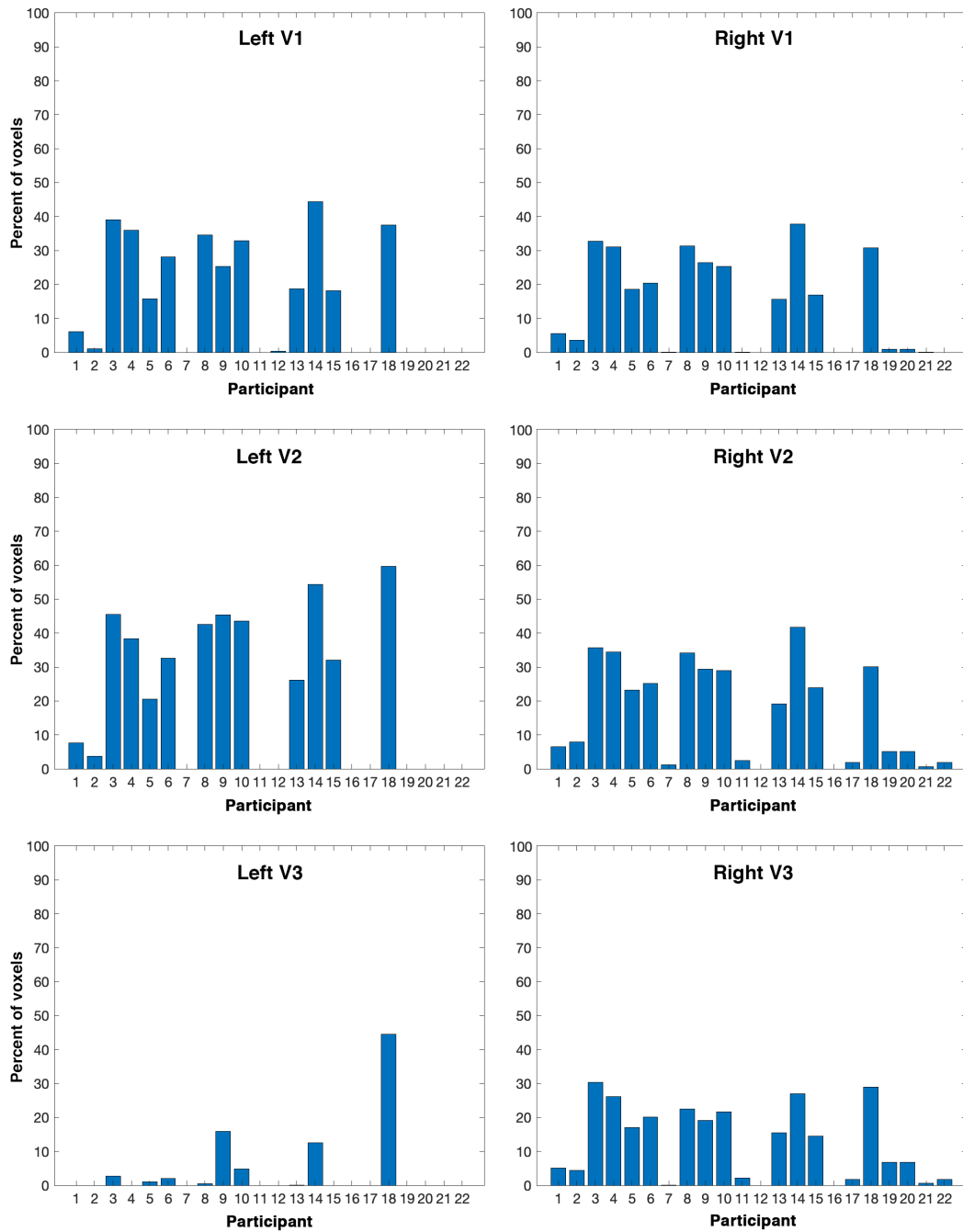
Figure 4.3: Percentage of ROI voxels omitted from analysis for FEM constructed with ROAST.
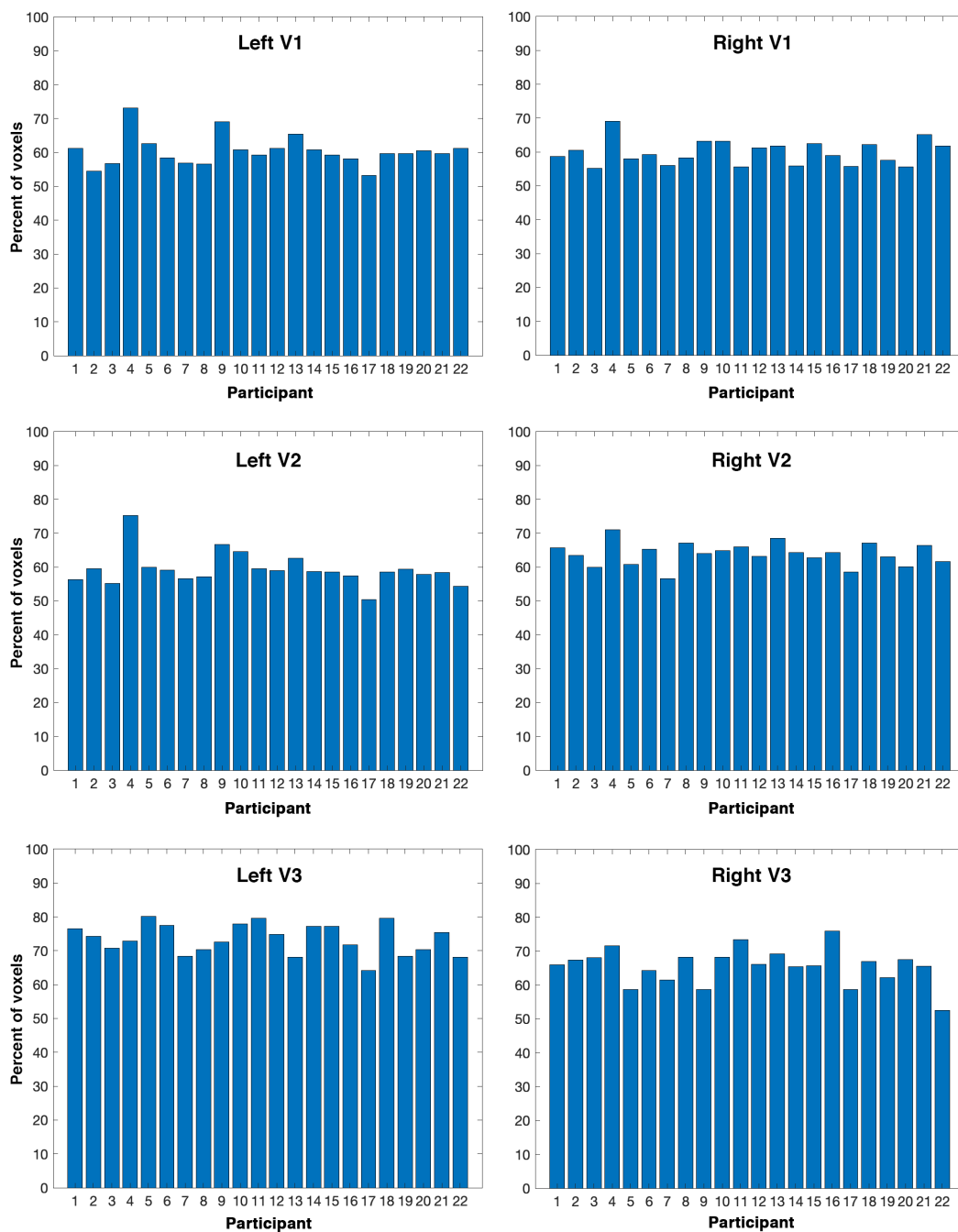
Figure 4.4: Percentage of ROI voxels omitted from analysis for FEM constructed with SimNIBS.
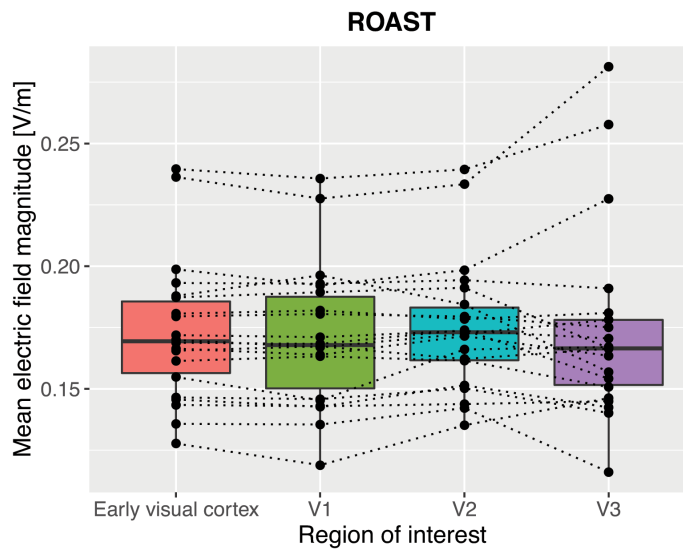
Figure 4.5: Variability of mean electric field strength [V/m] for grey matter in visual ROIs as modelled using ROAST. Early visual cortex was defined as areas V1, V2 and V3v.
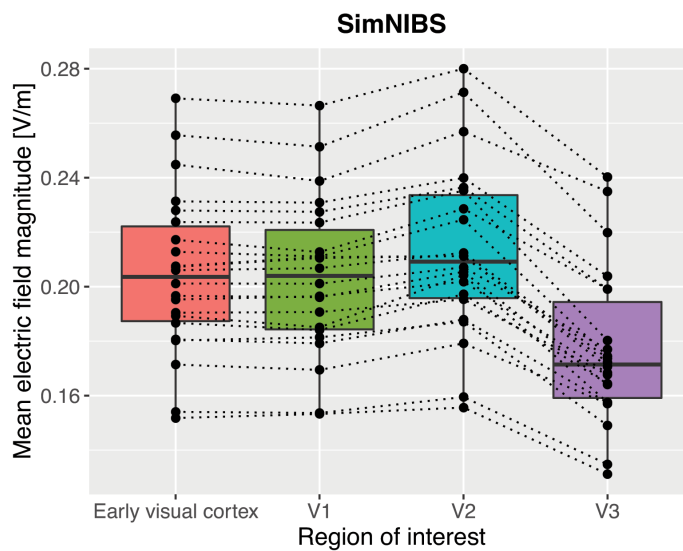
Figure 4.6: Variability of mean electric field strength [V/m] for grey matter in visual ROIs as modelled using SimNIBS. Early visual cortex was defined as areas V1, V2 and V3v.
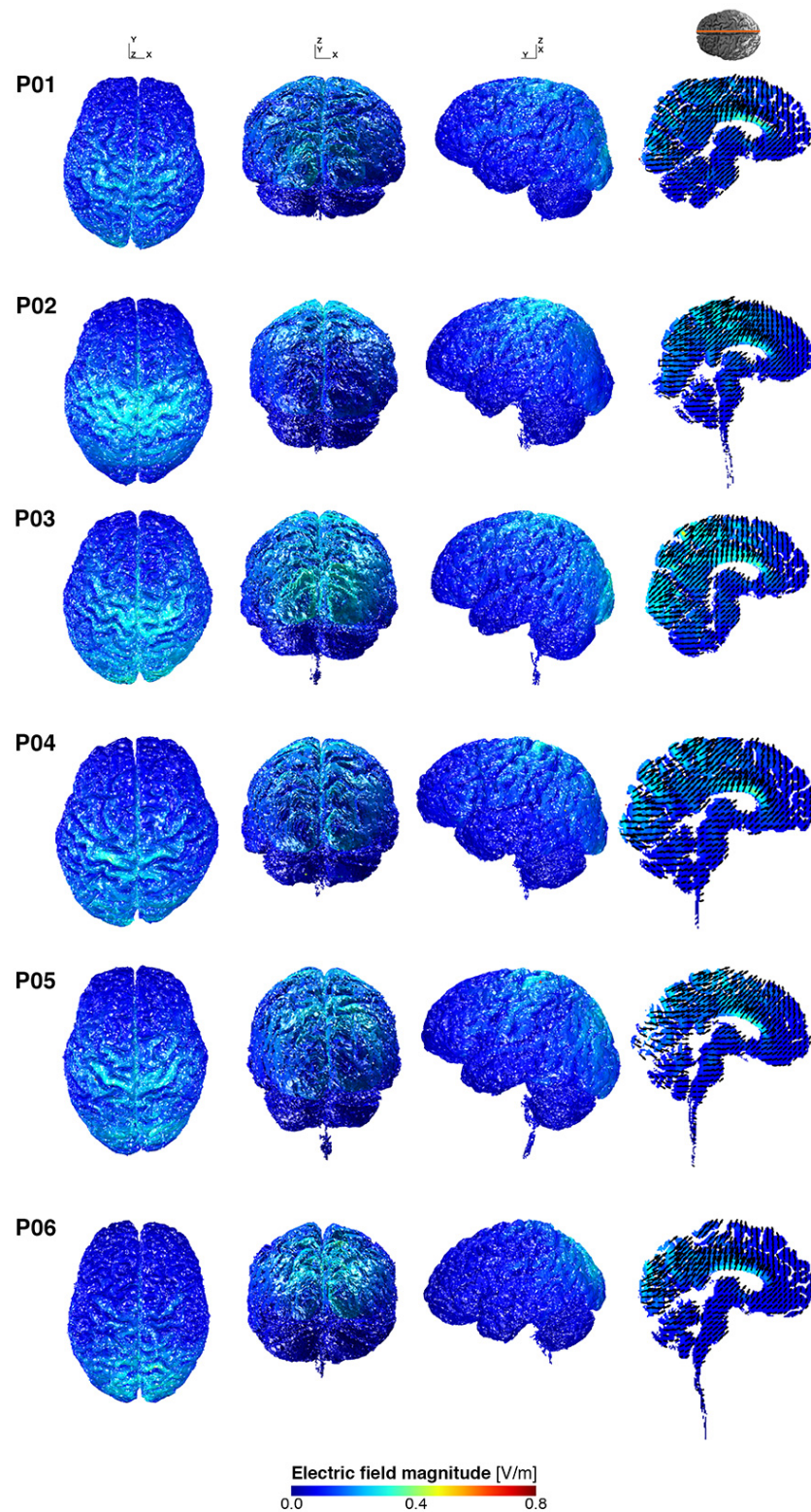
Figure 4.7: Distribution of electric field strength [V/m] as modelled with ROAST. Note that the scale of head sizes is constant within but not across participants due to variability in the length of brain stem captured in the MR image. Participants 1–6 are shown here; continued in Figures 4.8, 4.9 and 4.10.
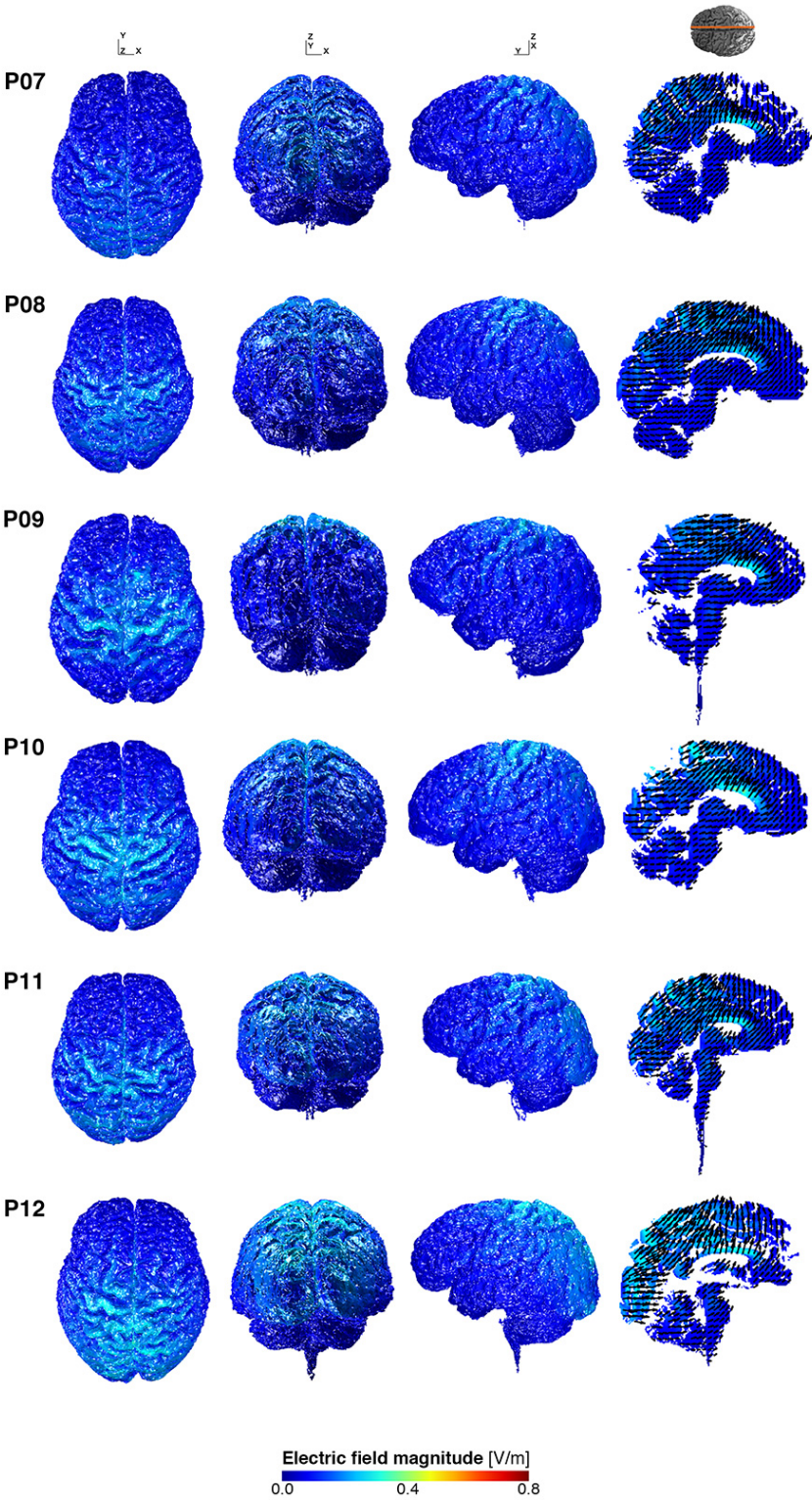
Figure 4.8: Distribution of electric field strength [V/m] as modelled with ROAST. Participants 7–12 are shown here; *cf.* Figures 4.7, 4.9 and 4.10.
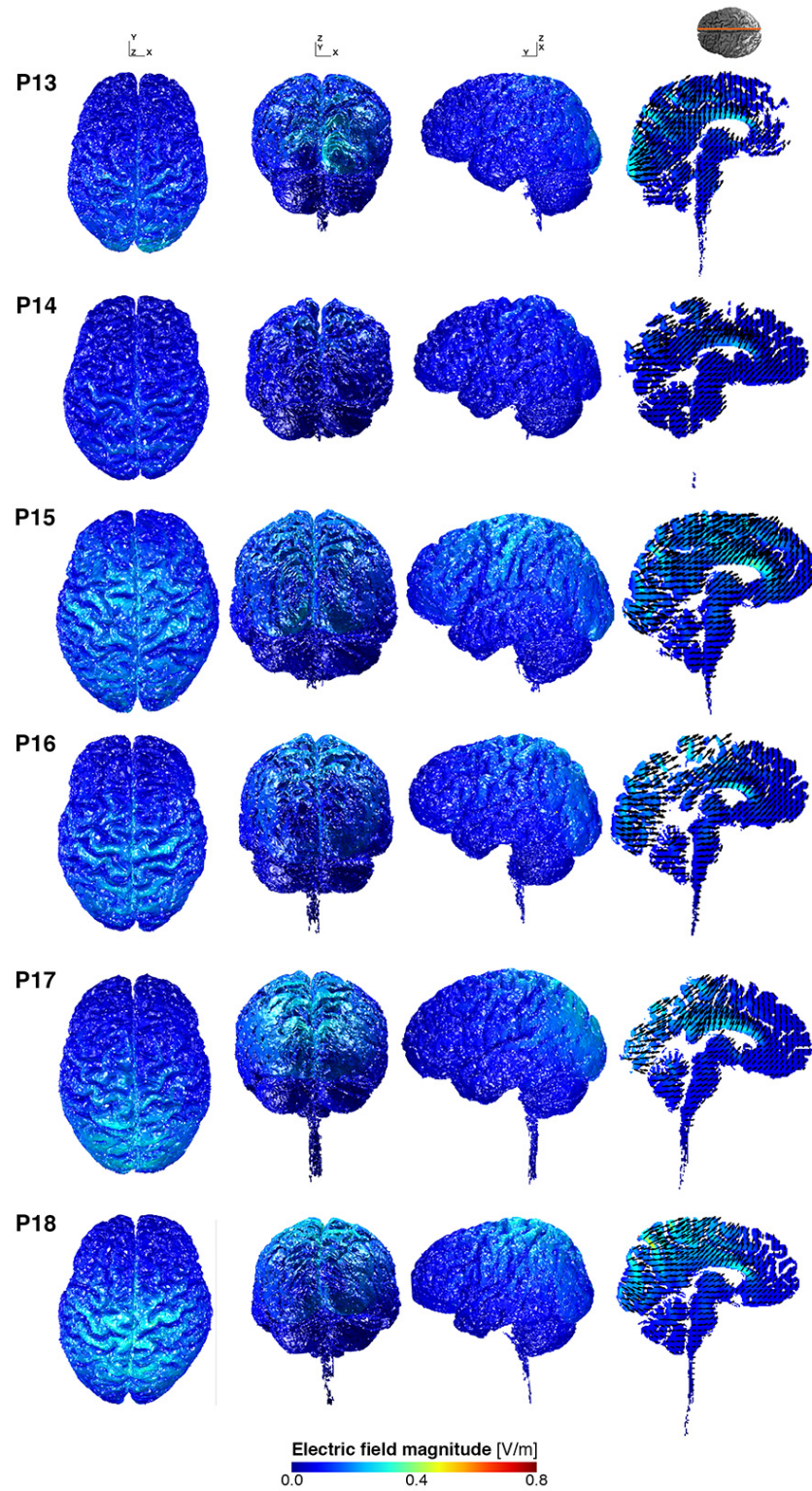
Figure 4.9: Distribution of electric field strength [V/m] as modelled with ROAST. Participants 13–18 are shown here; *cf.* Figures 4.7, 4.8 and 4.10.
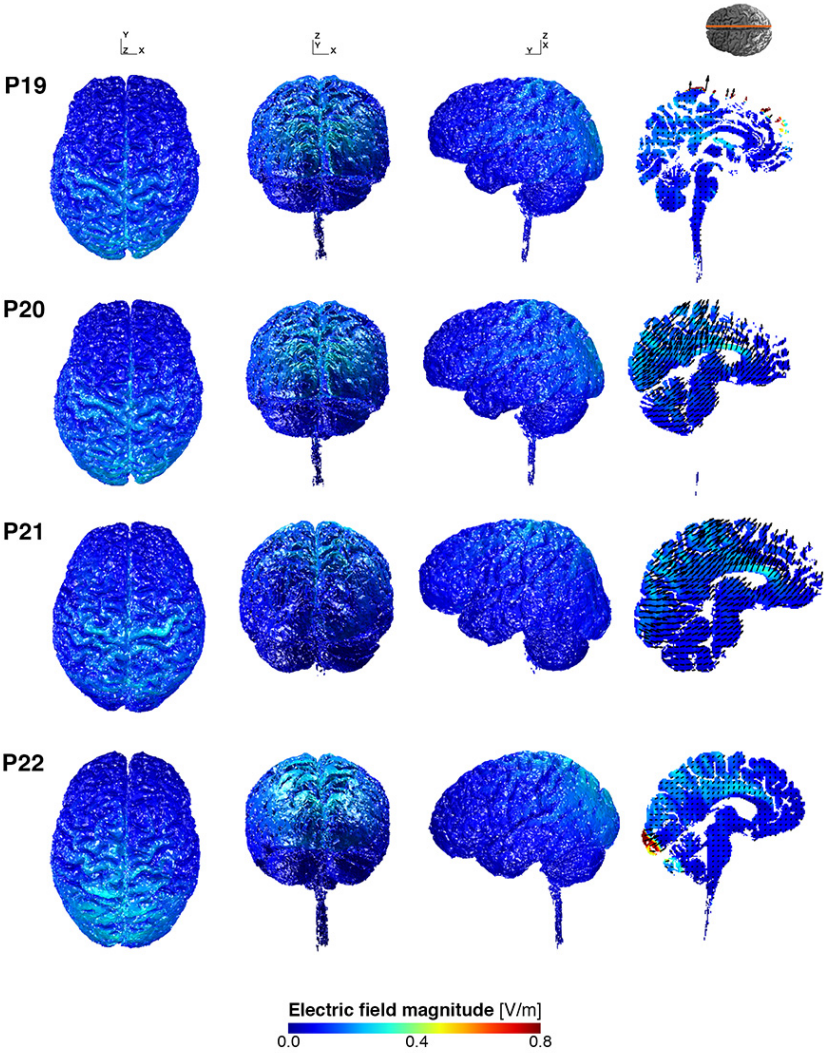
Figure 4.10: Distribution of electric field strength [V/m] as modelled with ROAST. Participants 19–22 are shown here; *cf.* Figures 4.7, 4.8 and 4.9.
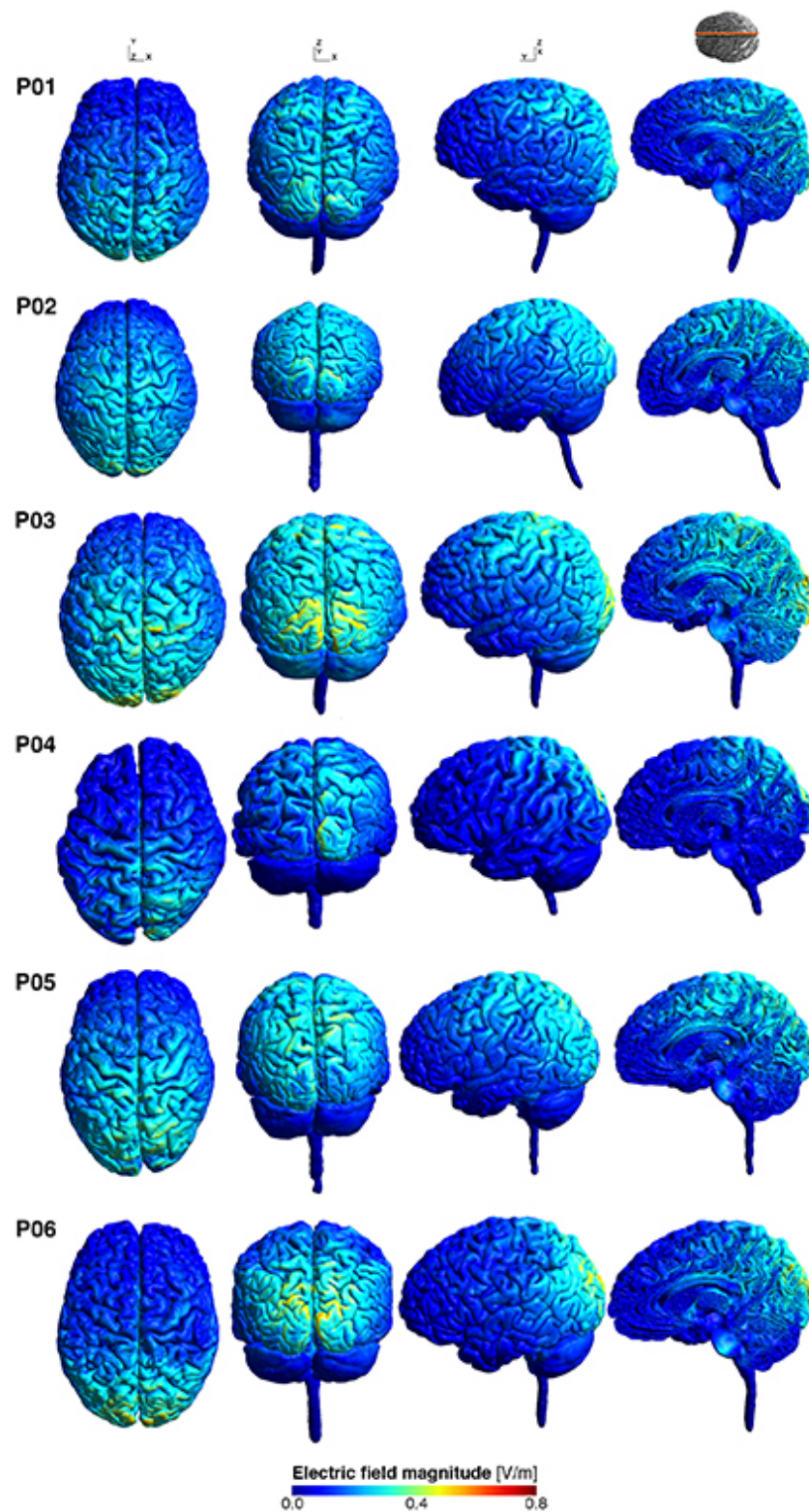
Figure 4.11: Distribution of electric field strength [V/m] as modelled with SimNIBS. Note that the scale of head sizes is constant within but not across participants, as each image has been scaled to include the entirety of the modelled brainstem and spinal cord, which varies between participants. Participants 1–6 are shown here; continued in Figures 4.12, 4.13 and 4.14.
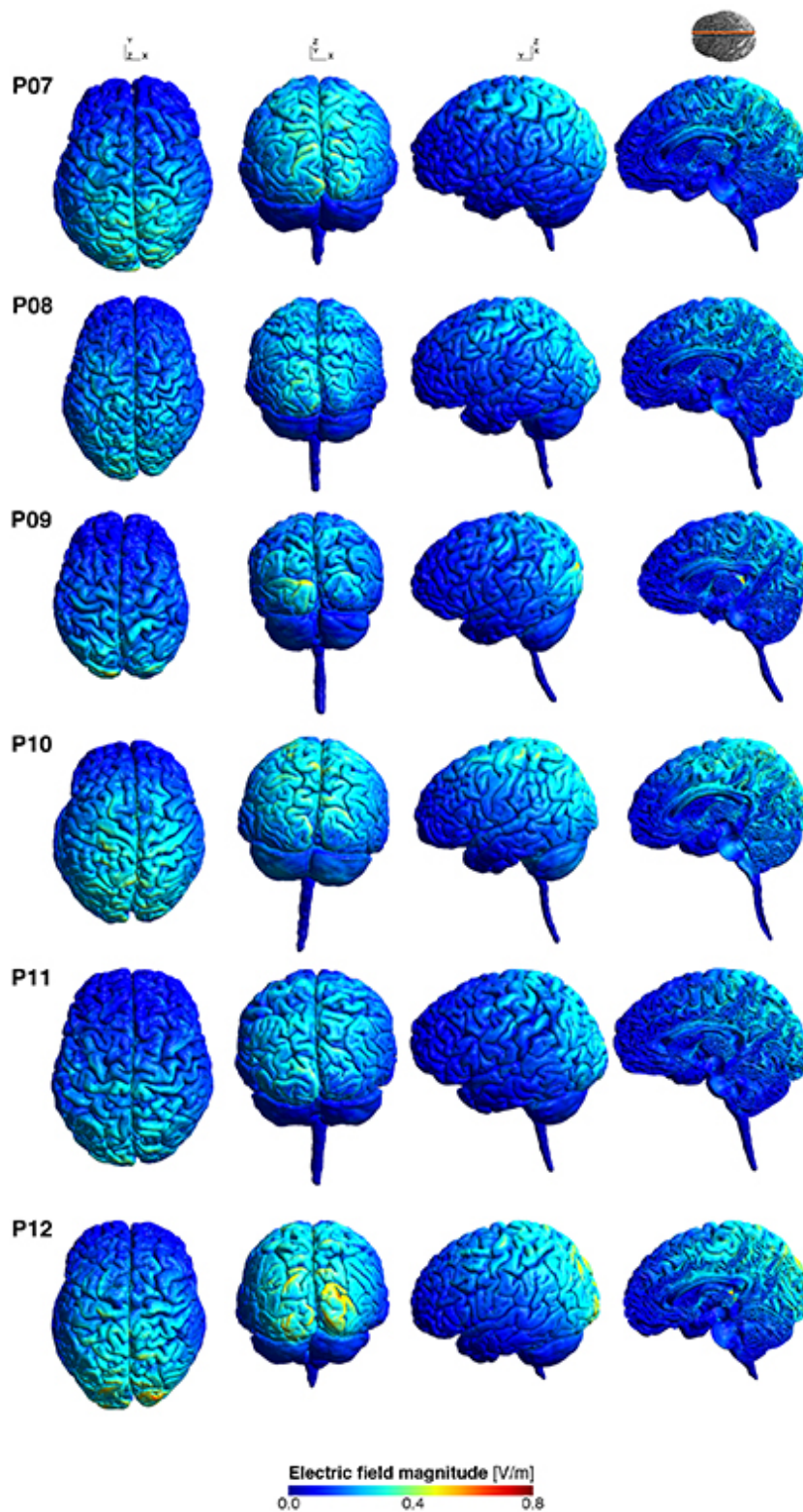
Figure 4.12: Distribution of electric field strength [V/m] as modelled with SimNIBS. Participants 7–12 are shown here; *cf.* Figures 4.11, 4.13 and 4.14.
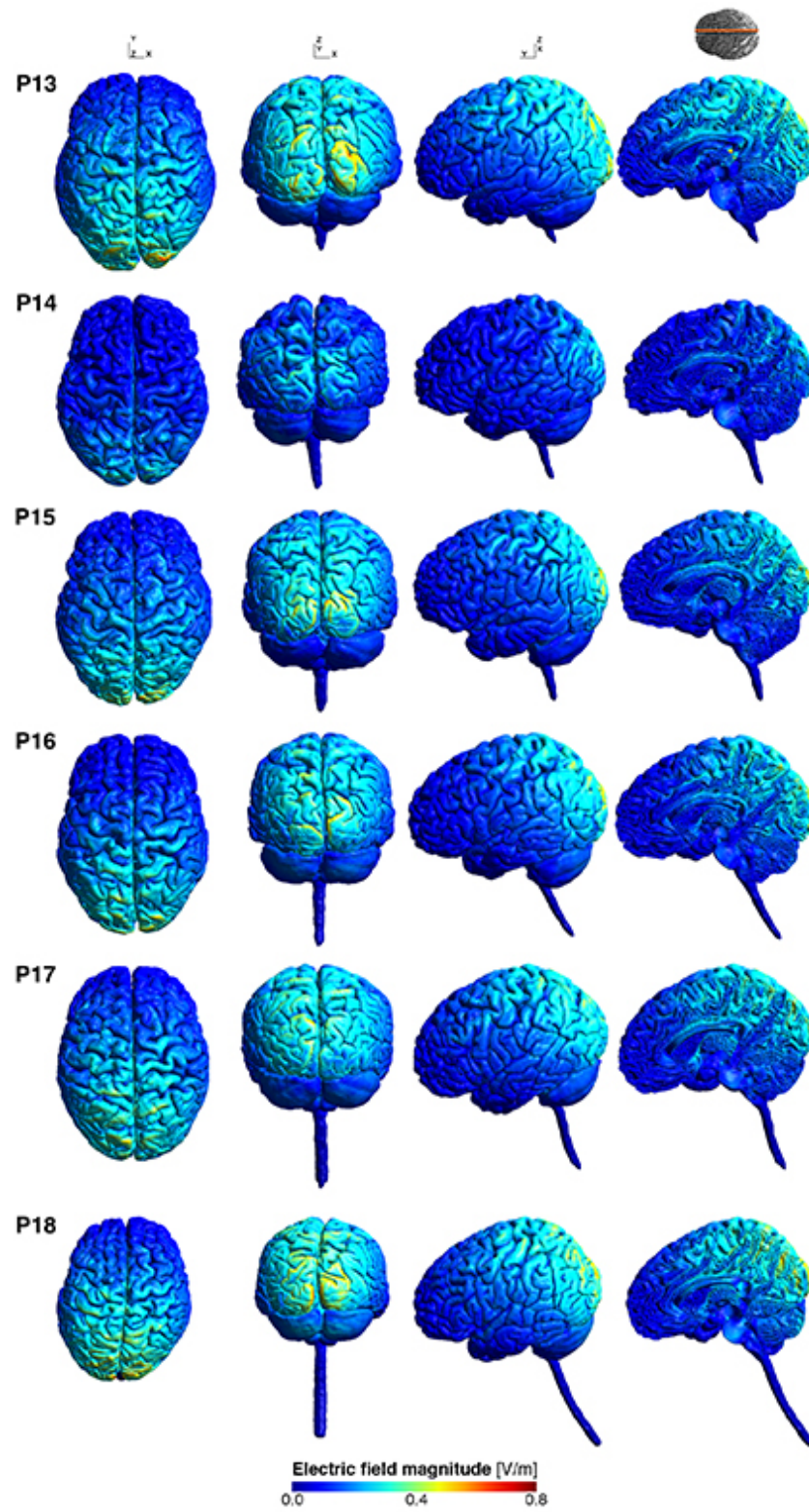
Figure 4.13: Distribution of electric field strength [V/m] as modelled with SimNIBS. Participants 13–18 are shown here; *cf.* Figures 4.11, 4.12 and 4.14.
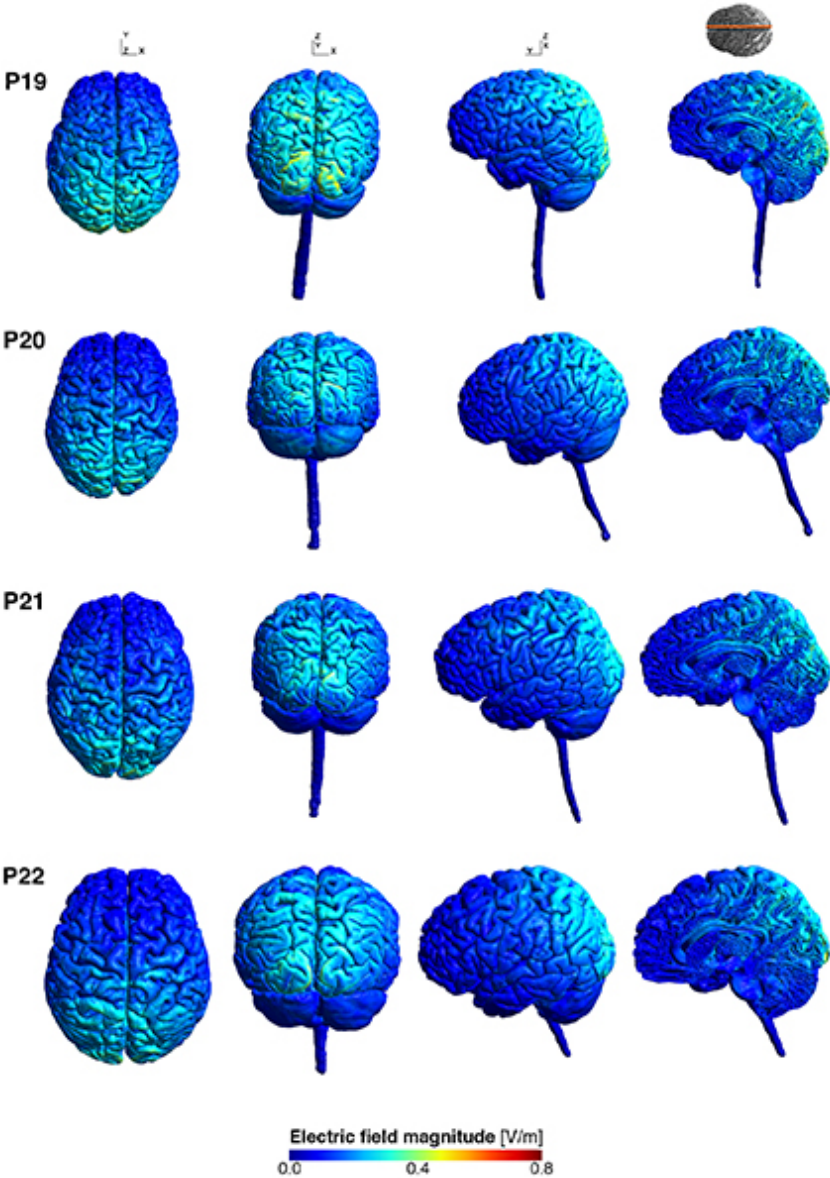
Figure 4.14: Distribution of electric field strength [V/m] as modelled with SimNIBS. Participants 19–22 are shown here; *cf.* Figures 4.11, 4.12 and 4.13.
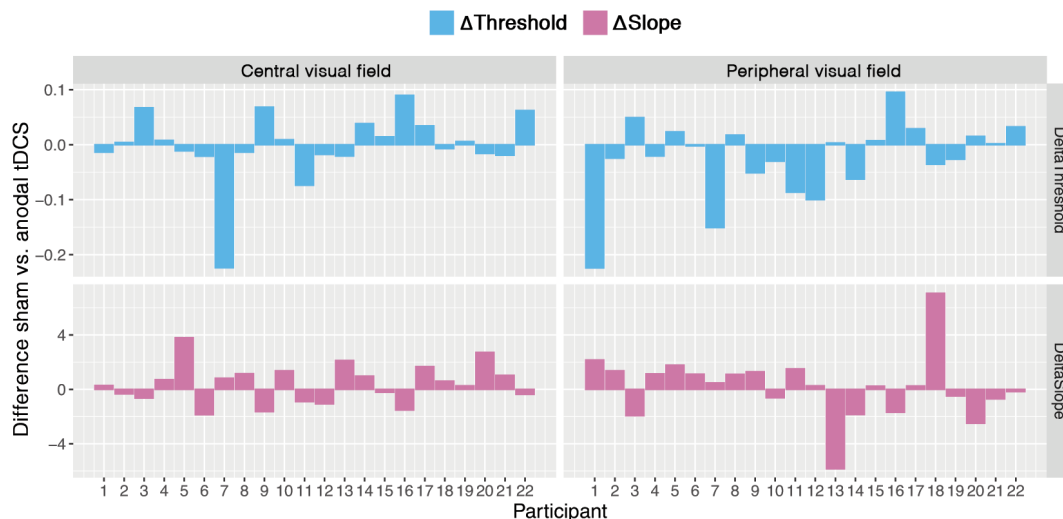
Figure 4.15: Differences of behavioural outcomes ($\Delta\hat{\alpha}$ and $\Delta\hat{\beta}$) measured at central (4°) and peripheral (20°) visual field locations during sham vs. anodal tDCS.

4.3.3 Correlation of tDCS-induced behavioural changes and modelled electric field strength

To evaluate the association between behavioural effects (Figure 4.15) and simulated electric field strengths, Spearman's rank correlation coefficients (ρ) were computed (α = .05, two-sided). For both modelling pipelines and all visual ROIs, correlations between mean electric field strength and contrast detection threshold or psychometric function slope were non-significant (p > .05). Correlation matrices are provided in Figures 4.16 and 4.17.

4.3.4 Agreement of ROAST and SimNIBS field strength estimates

Shapiro-Wilk tests of normality indicated that estimates of mean electric field strengths in the visual ROIs of 22 participants were normally distributed (p > .05), with the exception of ROAST estimates in V3v (W = 0.8, p = 0.002), see Figure 4.18.

We also evaluated the agreement among electric field strength simulations based on the ROAST and SimNIBS pipelines. In the early visual cortex ROI (i.e., combined V1, V2 and V3v), a Bland-Altman analysis of the agreement of electric field magnitudes simulated with ROAST and SimNIBS found a significant bias of -0.032±0.026 V/m, indicating that on average estimates based on SimNIBS were 0.032 V/m higher than estimates based on ROAST, see Figure 4.19.

Furthermore, to assess if there were systematic differences between the field strength estimates for the three separate visual regions-of-interest, we carried out a repeated-measures ANOVA with factors *Pipeline* (ROAST, SimNIBS) and *ROI* (V1, V2, V3v).
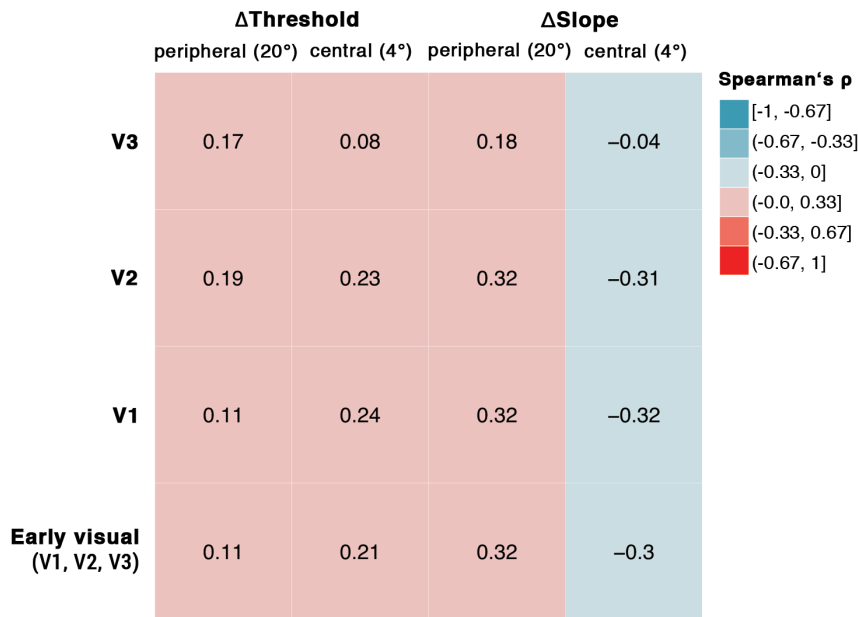
Figure 4.16: Correlation coefficients (Spearman's ρ) for behavioural outcomes and mean electric field strength modelled using ROAST. All correlations were non-significant, $p > .05$.
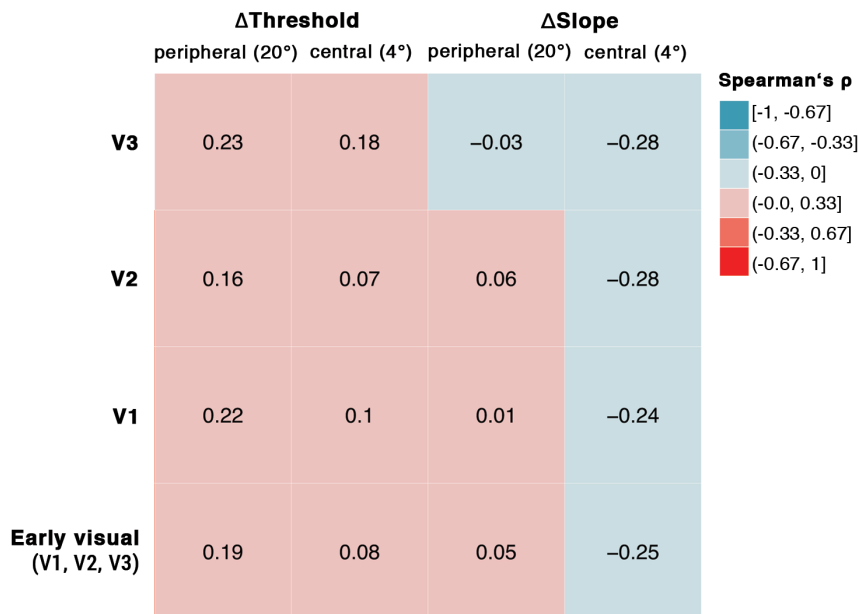
Figure 4.17: Correlation coefficients (Spearman's ρ) for behavioural outcomes and mean electric field strength modelled using SimNIBS. All correlations were non-significant, $p > .05$.
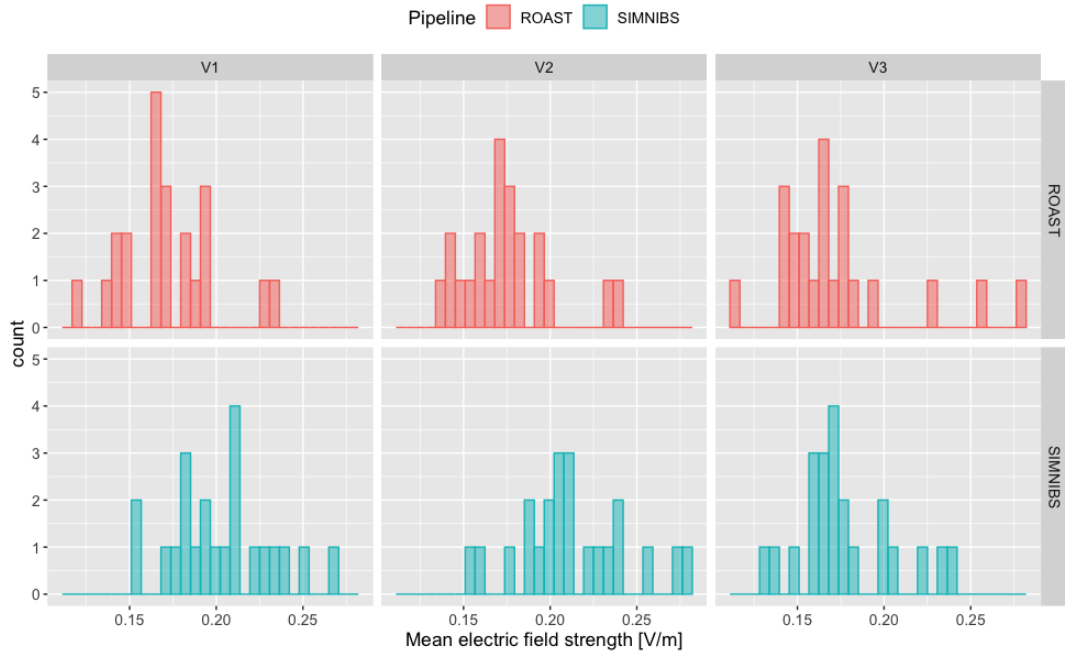
Figure 4.18: Histograms of mean electric field strengths estimated with ROAST and SimNIBS.
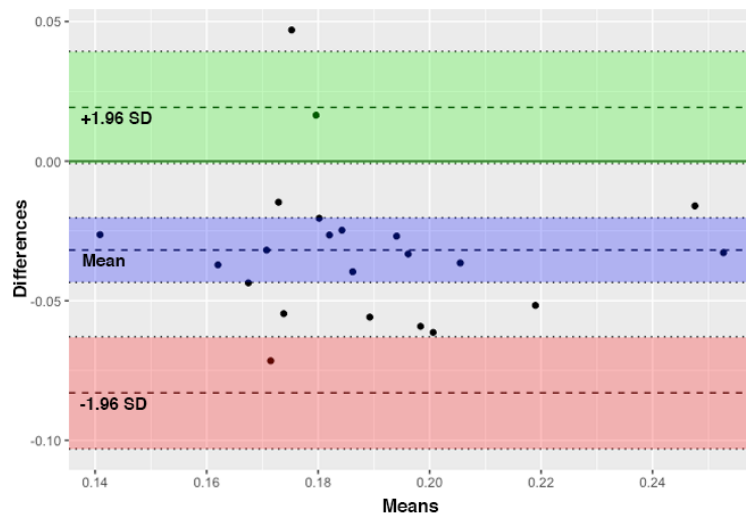
Figure 4.19: Bland-Altman plot of mean electric field strengths estimated with ROAST and SimNIBS (95% confidence intervals on the limits-of-agreement were calculated using two-sided tolerance factors).

We found a significant main effect for both *Pipeline* ($F(21) = 18.5$, $p < .001$) and *ROI* ($F(42) = 44.8$, $p < .001$). The interaction between the two factors was also significant ($F(42) = 46.9$, $p < .001$), see Figure 4.20. Mauchly's test indicated that the assumption of sphericity was violated for the factor *ROI* ($W = 0.351$, $p < .001$, $\varepsilon = .606$) and the interaction between the factors ($W = 0.403$, $p < .001$, $\varepsilon = .626$), therefore Greenhouse-Geisser corrected degrees of freedom are reported.

Bonferroni-corrected *post hoc* comparisons revealed that electric field magnitudes simulated with SimNIBS were significantly higher than those simulated with ROAST

for V1 (p < .001) and V2 (p < .001) but not V3 (p = 1.00). Field estimates created with SimNIBS were significantly lower in V3 compared to both V1 (p < .001) and V2 (p < .001). The difference of field magnitudes in V1 and V2 was also significant (p < .001). In contrast, there were no significant differences between estimates created with ROAST for any of the ROIs (V1–V2, p = .202; V1–V3 and V2–V3, p = 1.00).
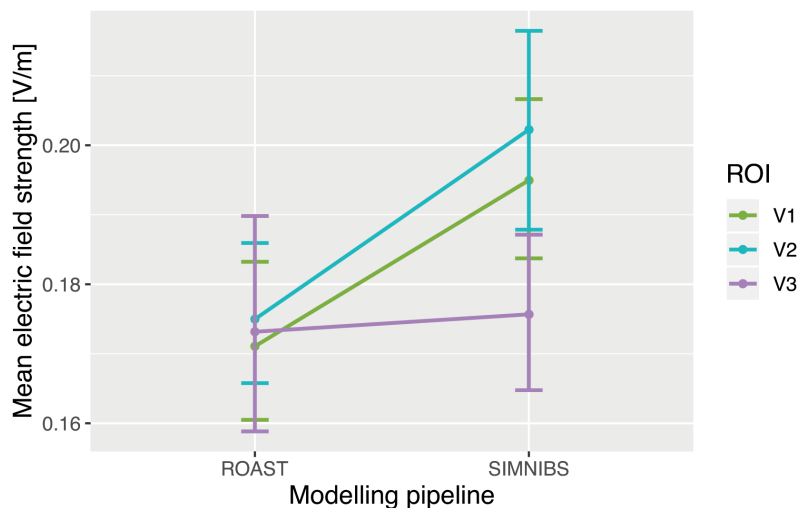
Figure 4.20: Interaction graph for mean electric field strengths (mean, 95% CI) in visual ROIs estimated using ROAST or SimNIBS.

4.4   Discussion

The present study aimed to relate behavioural changes induced by tDCS to finite-element simulations of tDCS-induced electric field strength. We assessed tDCS effects on behaviour using an automated threshold perimetry task measuring contrast sensitivity. Using the SimNIBS and ROAST software pipelines for FEM, we simulated electric field distribution based on participant-specific head models to evaluate whether inter-individual differences in behavioural tDCS effects were related to differences in field strengths in the early visual cortex. We also assessed the agreement of E-field magnitudes estimated using SimNIBS and ROAST.

As discussed in Chapter 3, in contrast to previous studies (Behrens et al., 2017; Costa et al., 2015a; Kraft et al., 2010; Reinhart et al., 2016), we did not find significant effects of anodal compared to sham tDCS on either detection threshold or psychometric function slope when stimulation was applied via an Oz-Cz electrode montage. We also found no significant correlation between simulated E-field strengths in the early visual cortex (V1, V2 and V3v) and behavioural changes for either modelling pipeline, despite using visual stimuli pre-tailored to each participant's perceptual range — to reduce any potential floor or ceiling effects on performance — and modelling electric fields based on participant-specific MRI data. Our initial hypothesis was that using

such a personalised, participant-focused approach would act to reduce the variability in tDCS outcomes. While this was not the case, there are a number of factors which may contribute to our non-significant findings, as we explore below.

To date, there have been few studies investigating how models of tDCS-induced electric field changes in the brain vary between participants. There have been fewer still that have attempted to use these results to explain individual differences in participant behaviour, and, of these, most have focused on the motor cortex, seeking to explain the variability in resting motor threshold (RMT; Mikkonen et al., 2018) or motor-evoked potentials (MEP; Laakso et al., 2019) between participants.

Using these two measures to index "motor cortex excitability" is a useful heuristic, but it remains controversial how useful either may be as a true index of actual real-world motor *behaviour*. Our intention in the current study was to use a task which would engage participants by requiring a volitional response to a simple visual stimulus. This choice of paradigm was informed by the frequent lack of significant results in tDCS studies designed to modulate complex behaviour, as studies employing simpler measures tend to be more successful. For example, MEP amplitude modulation was the only measure found by Horvath and colleagues to be significantly modulated by tDCS in their meta-analysis (Horvath et al., 2014). In this context, the significant relationships found by Mikkonen and Laakso's group are encouraging, but are difficult to relate directly to our paradigm.

Differences in definitions of what constitutes an "experimental task" are not the only way in which our work differs with much of the extant literature. Like many novel techniques in human neuroscience, there are currently a number of different, complementary, but also competing software packages that can be used to model patterns of electric field distributions induced by tDCS (Dannhauer et al., 2012; Huang et al., 2019; Jung et al., 2013; Saturnino et al., 2018). As a pluralistic approach to the analysis of data in neuroimaging and stimulation can prevent package or pipeline-specific biases (*cf.* Smith et al., 2005), we chose to use the two most widely-used open-source software packages, ROAST (Huang et al., 2019) and SimNIBS (Saturnino et al., 2018) to create our electric fields. The differences between the two software packages are discussed in detail in Huang et al., 2019; for reference, the implementations of the two packages used for our work are most similar to the "ROAST (1)" and "SimNIBS-hrE (6)" implementations described in Figure 1 of their paper.

Any discussions of the accuracy of simulation electric fields *in vivo* require some reference or "ground truth" for methods to be compared and for the magnitude and location of modelling results to be scrutinised. To date, modelling studies have relied upon data acquired from patients undergoing invasive neurosurgery, allowing neurophysiological recordings to be made from the brain (Huang et al., 2017; Opitz et al., 2016). By using tDCS on these patients, empirical recordings from the electrodes in

brain tissue can be compared directly to the results produced from simulations. Both SimNIBS and ROAST have been used in this manner. These studies allow us to make some broad comparisons of the magnitude distributions of our own modelling results.

The results from these studies, using 1.0 mA peak-to-peak stimulation, found that the maximum electric field magnitudes in the brain did not exceed 0.5 V/m *in vivo*. These results are broadly in line with our own findings. Overall, both our modelling pipelines estimated an average induced electric field magnitude of around 0.2 V/m in the early visual cortex (V1, V2, V3v), with inter-individual variations of up to 55% and maxima under 0.3 V/m.

Our intention in using both of these modelling pipelines was to allow for some comparison between them and to evaluate any systematic biases in a larger MR data set (while Huang et al., 2019 used a data set of 14 brains for some comparisons between SimNIBS and ROAST, the vast majority of comparisons have been made using the "NY Head" — a single, high-resolution MR (Huang et al., 2013). Again, our results are broadly in line with those of Huang et al., 2019, who found that SimNIBS produced field estimates that were on average 0.02–0.04 V/m higher than those created with ROAST (our own Bland-Altman analysis returned a similar bias of 0.032 V/m). The similarity of these results is all the more striking as our data and the data from Huang et al. were based on different electrode montages, current inputs and cortical ROIs. While we, like Huang and colleagues, are uncertain as to why SimNIBS would produce consistently higher magnitude results than ROAST, the differences are roughly an order of magnitude smaller than the typical maximum field changes found in tDCS modelling studies. Considered in tandem with the broad similarities in the range and maxima of the magnitudes of our modelled fields, our lack of significant findings here does not seem to be a direct result of an issue with either the quality of our MR data or our local implementations of SimNIBS or ROAST. The reason likely lies within the vast parameter space of possible analysis metrics that can be used when trying to relate the results of modelling results and tDCS-induced behavioural changes.

Unlike for DTI and MRI, there is currently no large, open-source repository of MR data and electric field modelling results available to the tDCS community. Such a repository could be useful in reducing the parameter space for analysis. Using data-mining approaches, the optimal use of the "raw" voxel-wise or node-wise voltage outputs from a given tDCS model could be evaluated according to whichever criteria the experimenter wishes.

The lack of a standard analysis method or pipeline may be why a number of tDCS papers utilising electric field models have been content in the past to present only cortical surface-rendered illustrations of their results (e.g. Hampstead et al., 2017), or to report only simple statistics such as the maximum field value across the entire brain of participants. To date, few studies have attempted quantitative analyses of

experimental and modelling data — in particular, analyses where cortical ROIs were defined based on cytoarchitectonic data from human post-mortem tissues, allowing to compare E-field strength in anatomically meaningful ROIs across participants.

Despite the involved complexities discussed above, two recent papers have shown impressive relationships between FEM and empirical results, although these studies focus on the use of neurophysiological data from the motor system (Laakso et al., 2019; Mikkonen et al., 2018). Direct comparisons between their analysis methods and our own are limited, as the authors relied upon their own in-house software for FEM. In addition, the approach chosen by the Mikkonen and Laakso group focused on estimating electric fields on a surface — an estimation of the cortical grey matter sheet, produced by segmentation of their MR data in FreeSurfer (Fischl, 2012). This approach has some similarities with early implementations of SimNIBS, which also relied upon FreeSurfer segmentation tools to construct separate surfaces for each tissue layer (GM, WM, CSF, etc.).

In contrast, from its earliest implementations, ROAST has relied upon FEM analyses based on volumetric segmentation. As we note above, we did not find large differences between ROAST and SimNIBS for our data set. While the results comparing SimNIBS and ROAST in the report by Huang et al., 2019 were broadly in line with ours, we took further steps to ensure that the results from both pipelines were comparable. To remove any obvious issues based on the comparison of voltages derived from surface estimates (SimNIBS) versus volume estimates (ROAST) of E-fields, we made use of on the fact that current versions of both packages allow to save their outputs as 3D NIFTI images. However, even though both packages can use somewhat similar segmentation tools [1], their post-segmentation touch-up routines are automatic and not accessible to users. Consequently, despite our attempts to minimise obvious differences between our local implementations of the two pipelines, some differences remain between the two approaches.

Trying to optimise these pipelines is not a trivial undertaking — as reported by Huang et al., 2019, estimates from earlier implementations of SimNIBS and ROAST could differ by an average of 67%. Again, these difference appear to have been driven by different tools and parameter choices for MRI segmentation and subsequent FEM solving: earlier versions of SimNIBS used FSL/FreeSurfer to produce a surface-based approach for MRI segmentation, giving good details of the gyri and sulci, but arguably worse results for other brain tissue compartments. Similarly, earlier versions of ROAST used the segmentation routines within SPM8, not 12. From our results here and those within Huang et al., 2019, the use of a common segmentation method (SPM12) seems to reduce the magnitude of differences between the two pipelines.

---

[1]The most recent version of ROAST uses SPM12's "universal segmentation" (Ashburner and Friston, 2005), and our implementation of SimNIBS used the CAT12 toolbox in SPM12.

In our present analysis, both modelling pipelines were based on the same conductivity values for tissue layers. However, in general, the exact values for tissue conductivity remain unclear and there is some variability in the reported literature (Windhoff et al., 2013). Moreover, it is an open question to which extent conductivity values vary across individuals (Ruffini et al., 2013). Addressing this issue is not trivial, as *in vivo* measurements of human tissues are difficult to obtain. Recently, promising efforts have been made to measure tissue conductivities directly during surgery (Koessler et al., 2017), or using intracranial electrodes (Huang et al., 2017) and — controversially — *ex vivo* in cadavers (Opitz et al., 2017; Underwood, 2016). Indirect measurements via non-invasive techniques have also been carried out by Chauhan et al., 2017, but a clear consensus on appropriate values has yet to reached.

Furthermore, our models have assumed isotropic conductivity for all tissue compartments. While this may be a sensible first approximation for the thinner tissue layers like grey matter, some authors have argued that using anisotropic assumptions for the white matter and skull may improve model accuracy (Dannhauer et al., 2011; Rampersad et al., 2014). Although modelling white matter anisotropy may only affect deeper WM tracts — perhaps too deep to be significantly modulated by typical tDCS currents — the skull is a different matter, as it is highly resistive and current applied at the scalp must pass through bone to reach the brain's surface. In most individuals, the skull is thicker over the occipital region, which may give more weight to conductivity differences between compact and spongy compartments. As spongiosa is more highly conductive than compacta, for an electrode closer to a skull region containing a larger proportion of spongy bone, more current is shunted through this compartment, thereby increasing current strength in the grey matter. In our current analysis of tDCS of the visual cortex, the assumption of isotropy may therefore have biased model estimates.

While a range of tissue conductivity values have been proposed in the literature (Windhoff et al., 2013), little work has been carried out on evaluating the influence of conductivity choices on subsequent FEM results. This has been explored in a recent paper from Saturnino et al., 2019, in which they present a new computational approach to quantify these effects of varying conductivity parameters. Their analysis relied on non-intrusive generalised polynomial chaos expansion to quantify the reliability of resulting field estimates and to determine the most influential tissue conductivities. Their findings indicate that "conductivity uncertainty" more strongly affects the electric field's magnitude than its direction or its overall spatial distribution. Furthermore, tDCS-induced fields were primarily influenced by the conductivity parameters for grey and white matter, as well as skull and scalp.

While choices of conductivity values and segmentation routines are important in any tDCS modelling study, it may be that the large, complex parameter space defining

the possible ways to extract and analyse results from tDCS models has a greater effect on the difference between significant and non-significant findings. It is interesting to note that of the two motor tDCS studies discussed above, Laakso et al., 2019 did not find any significant relationships between their empirical and modelling results *until* they attempted what was — to a first approximation — a search of part of the analysis parameter space. When using linear statistical tools similar to our own, they found similar, non-significant results.

Finally, our current analyses differ from those of Laakso et al. and Mikonen et al. in that we have only focused on the magnitude of the electric field (i.e., the vector norm of $\vec{E}$, *cf.* Figure 1.18), while their analyses were based on the normal component of $\vec{E}$. It is currently an empirical question whether electric field *magnitude* or field *direction* is more predictive of functional tDCS outcomes. Unfortunately, the physiological mechanisms of tDCS are not sufficiently well-understood to decide *a priori* which factor is more relevant. As tissue conductivity along the neuronal fibre is higher than in the direction perpendicular to fibres, pyramidal neurons oriented orthogonal to the GM surface are most likely to be effectively polarised by tDCS (Rahman et al., 2013). By comparing the normal component of the grey matter surface with the modelled electric field vectors, preferred field direction in a region-of-interest can be assessed. With technical advances of open-source FEM software packages, such analyses are becoming increasingly feasible. Interestingly, modelling work by Rampersad et al., 2013 suggests that the most widely used electrode configurations for visual cortex tDCS (typically Oz-Cz or O1/O2-Cz, *cf.* Costa et al., 2015b), which have been proven effective in empirical studies, more strongly resemble direction-optimised than strength-optimised montages. These findings suggest that field direction may be the more relevant factor for determining stimulation effects.

In summary, we have presented both qualitative and quantitative results on simulated electric fields from two open-source FEM pipelines, SimNIBS and ROAST. For tDCS at 1.5 mA applied via an Cz-Oz electrode montage, the results from the two pipelines are broadly similar in their spatial distribution and magnitudes. In general, surface-rendering suggests that the electric field is widely distributed in the parieto-occipital cortex, with the main focus extending towards more frontal areas in some participants. Our findings show that estimates based on SimNIBS were significantly higher than estimates based on ROAST, with this difference being on average around 0.03 V/m. Overall, estimated mean field magnitudes were in line with *in vivo* measurements obtained in previous studies. However, despite taking an individualised approach to both sensory stimulation and head model construction for FEM, we found no significant correlation between estimates of tDCS-induced E-field strength in the early visual cortex and behavioural performance in a contrast detection task. Our study highlights that researchers interested in modelling tDCS-induced electric fields

are currently confronted with numerous methodological and conceptual questions.

Chapter 5

Electrode-optode placement for tDCS-NIRS of the visual cortex

5.1 Introduction

Over the past two decades, investigations of tDCS effects in humans have highlighted the difficulty of extrapolating findings from *in-vitro* or *in-vivo* animal studies to the complex morphology of functionally cohesive brain regions in humans. Our understanding of how electrical stimulation affects brain activity and ultimately behaviour remains incomplete.

Two primarily neuronal mechanisms for tDCS effects on brain activity are currently most widely accepted: first, that electric fields modulate neuronal response thresholds by transiently altering resting membrane potentials without eliciting action potentials (Liebetanz et al., 2002; Nitsche and Paulus, 2001; Stagg and Nitsche, 2011); and second, that tDCS leads to synaptic changes similar to long-term potentiation (LTP) and long-term depression (LTD) via NMDA receptor changes and increases in postsynaptic Ca^{2+} levels (Fritsch et al., 2010; Liebetanz et al., 2002; Lisman, 2001).

However, the transcranial induction of an electric field in the brain may also produce extra-neuronal effects (Gellner et al., 2016). In a recent publication, Pulgar proposed that direct current stimulation may not only affect neurons but also other components of the neurovascular unit, such as glial and vascular cells (2015). While glia cannot generate action potentials, they do have a transmembrane potential. They are thought to play an important role in the functional control of oxygenated blood flow to target brain regions through the use of vasodilation and vasoconstriction (Gordon et al., 2008; Koehler et al., 2009; Metea and Newman, 2006).

Astrocytes, for instance, may mediate local blood flow through Ca^{2+} elevations induced by neuronal activity, as perivascular astrocytic end-feet lying in close proximity to neurons can secrete vasodilatory agents (Anderson and Nedergaard, 2003; Zonta et al., 2003). Large surges of Ca^{2+} have been observed during tDCS (Monai et al., 2016) and theoretical calculations suggest that tDCS-induced transmembrane potential changes

are similar in magnitude to those observed physiologically in astrocytes during neuronal activation (Ruohonen and Karhu, 2012). Therefore, it is possible that functional tDCS effects are ultimately mediated not through direct actions on neurons but via modulations of astrocytic function. However, this is unlikely to be the whole story: several *in-vitro* experiments have also demonstrated the effects of electrical stimulation on endothelial cells and pericytes (Hall et al., 2014a; Trivedi et al., 2013; Zhao et al., 2012).

These findings suggest that experiments aiming to uncover aspects of tDCS mechanisms in humans should also consider extra-neuronal pathways of DC stimulation. Along with the technique's purported effects on neuronal membrane potential, changes in regional cerebral blood flow (rCBF) may play a part in extra-neuronal tDCS effects. Indeed, recent evidence indicates that tDCS modulates cerebral perfusion in humans (Lang et al., 2005; Stagg et al., 2013). For example, Zheng and colleagues found that anodal tDCS induced a significant increase in rCBF during stimulation, whereas cathodal tDCS induced a small increase during stimulation and a decrease post-stimulation (Zheng et al., 2011).

The relative ease of application of tDCS is often held up as a positive aspect of the technique. However, the parameter space of tDCS experiments in humans is, in fact, complex and multidimensional: the behavioural task; electrode placement and stimulation parameters; the variance in functional neuroanatomy and traits/behaviour of the participants; and finally, the effects of stimulation on both neurophysiological and neurovascular activity. No one experiment can hope to fully capture or control for all of these. Nonetheless, focused investigations of the mechanisms underlying tDCS are not a waste of time. At present, using state-of-the-art neuroimaging techniques represents the best means to bridge the gap between cellular and behavioural effects of tDCS in humans.

Current neuroimaging methods provide windows into brain activity with varying degrees of spatial and temporal resolution. Combining different neuroimaging techniques to study the same cognitive or sensory processes can provide complimentary insights on their physiological underpinnings. In particular, acquiring data from multiple imaging modalities within a single study — while introducing certain design limitations — can provide insight above and beyond a given method in isolation.

Several recent studies have investigated the feasibility of using magnetoencephalography (MEG) to capture neuronal activity during tDCS (Hanley et al., 2015; Marshall et al., 2015; Neuling et al., 2015; Noury et al., 2016; Soekadar et al., 2013). However, as behavioural effects of tDCS may not be mediated exclusively through modulations of neuronal activity, we propose to integrate near-infrared spectroscopy (NIRS) with MEG and tDCS. This experimental approach is both complementary and advantageous to fMRI-EEG-tDCS studies (Dutta, 2015): MEG captures electrophysiological activity

from the whole brain with a high temporal resolution, whereas NIRS monitors changes in rCBF without perturbation from tDCS-related electrical currents — a unique advantage over other neuroimaging techniques. In addition, while having lower spatial resolution than fMRI, NIRS offers a roughly ten-fold increase in temporal resolution and allows to monitor both oxy- and deoxyhemoglobin activity independently.

However, studies combining online tDCS with NIRS-MEG face several conceptual and technical challenges: First, the magnetic fields induced by online tDCS introduce significant additional artefacts in the MEG signal — an issue which must be addressed by the experimental design and which is discussed in further detail in Chapter 6.

Secondly, NIRS optodes must be arranged on the scalp such that changes in the cortical region-of-interest can realistically be measured. This is a comparatively trivial issue in many NIRS studies, which often aim to measure prefrontal activation by placing optodes on the forehead. In contrast, visual cortex NIRS in adults must not only overcome the mechanical and light-absorbing interference from hair but also capture hemodynamic changes in a cortical structure that is folded deeply in the calcarine fissure. Previous work has suggested that during visual stimulus processing the greatest signal changes are captured by NIRS channels over the primary visual cortex, with a bias towards the left hemisphere (Toronov et al., 2007). A study by Wijeakumar et al. investigated the distribution of absolute HbO and HbR concentration changes in response to simple visual stimulation over occipital and posterior parietal regions (2012). Their findings showed that the largest hemodynamic changes occurred at EEG positions O1 and O2 and at locations vertically between O1, O2, PO3 and PO4. However, in concurrent tDCS-NIRS experiments, the positions of tDCS electrodes and NIRS optodes on the scalp are mutually restrictive. Trade-offs in NIRS signal strength and optimal electric stimulation are likely unavoidable and should be evaluated carefully.

Third, intra- and inter-individual variance has been discussed in the context of tDCS in previous chapters, but has also been explored specifically for NIRS of the visual cortex in a study by Kashou and Giacherio, 2016. In a sample of 10 participants, they showed that an appropriate level of sensitivity was achievable for measurements of the visual cortex, but that reliability was poor across sessions and participants. Intra- and inter-individual variance is a particularly pertinent issue for multimodal studies, where the additional burden to resources introduced by using several modalities tends to reduce sample sizes. To maximise study power, it is therefore desireable to optimise both stimulation and recording profiles prior to data acquisition.

Finally, for many experimental objectives there is no clear evidence for the optimal level of tDCS input current intensity. Finite-element-models of tDCS-induced electric fields can not only be used to select suitable electrode locations for tDCS but also to gauge the input current intensity required to induce sufficient field strengths across a sample of participants.
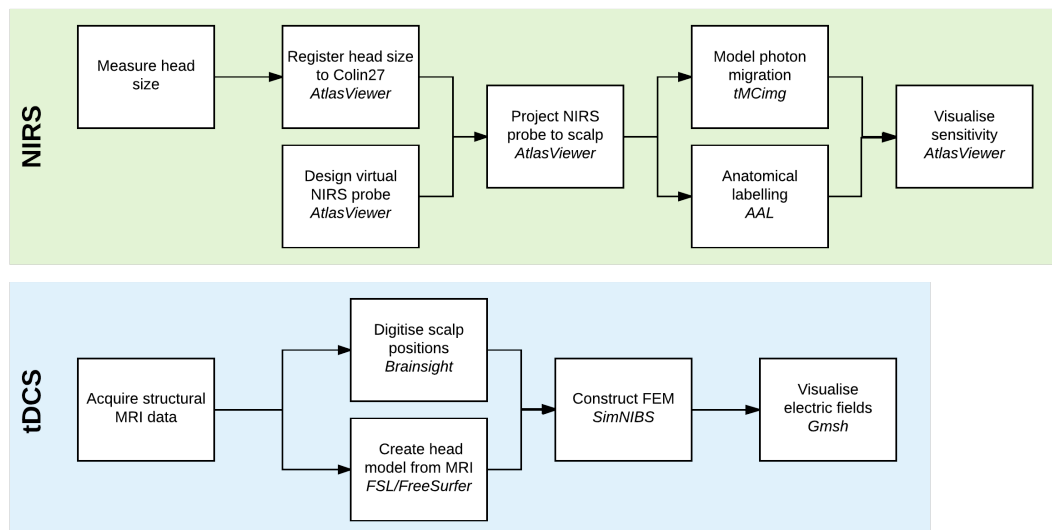
Figure 5.1: Schematic illustration of pipeline for the modelling of tDCS electrode and NIRS optode configurations.

Here, we present a software pipeline for creating sensitivity profiles for neuroimaging with NIRS and modelling tDCS-induced electrical fields based on participant-specific anatomical data. By accounting for inter-individual differences in anatomy, these models can inform the design of future concurrent visual tDCS-NIRS experiments, including the tDCS-NIRS-MEG pilot study described in Chapter 6.

5.2 Methods

Our analysis pipeline incorporated the freely available software package SimNIBS v2.0.1 (Windhoff et al., 2013) for simulating tDCS-induced electric fields, and the open-source package AtlasViewer for creating NIRS sensitivity profiles (Aasted et al., 2015); see Figure 5.1 . Finite element models (FEMs) of electric field strength were calculated for each participant based on individual anatomical MRI scans. The sensitivity of a NIRS probe designed to measure hemodynamic response in the visual cortex was evaluated by scaling an atlas brain to each participant's head size. As a proof-of-principle, we applied this software pipeline to the brains of three healthy pilot participants (2 male, 1 female; M = 33.7±7.0 years,).

5.2.1 MRI acquisition & segmentation

Sequence parameters for the acquisition of MR images were adapted from the specifications set out by Windhoff et al., 2013 using a 3T Siemens TIM Trio, adapted for use on CUBRIC's 3T Siemens Prisma (Siemens Healthcare GmbH, Erlangen, Germany) with a 32-channel head coil. Both T1 and T2 sequences were collected to ensure optimal acquisition of different tissues for subsequent segmentation, with both fat-suppressed

and non-fat suppressed versions acquired. The T1 sequence was a 3D TurboFLASH sequence (sagittal acquisition; FOV 240 x 256 x 192; voxel size 1 mm isotropic), and the T2 a TSE (TURBOSpin Echo; axial acquisition; FOV 256 x 256 x 96; voxel size 1 x 1 x 2 mm, with a 1 mm gap to decrease the amount of fat shift in the slice selection direction).

For each participant, tissues including white matter, grey matter, CSF, skin and skull were segmented automatically using the SimNIBS v2.0.1 pipeline (Windhoff et al., 2013). The fat-suppressed T1 images were used as input for FreeSurfer (Fischl, 2012), the fat-suppressed T1- and T2-weighted MR images were used to reconstruct the inner skull boundary with FSL BET/BETsurf, and the normal T1- and T2-weighted images were used to reconstruct the outer skull boundary and the skin surface with FSL. Segmentation results were inspected manually using FSLView and FreeSurfer with attention paid to tissue boundaries. The final volume masks were used to create triangle surfaces and tetrahedral volume meshes using the "mri2mesh" tool as described in Windhoff et al., 2013.

5.2.2 Head digitisation

Scalp positions were recorded based on participant-specific structural MRI scans (T1nfs) using a Brainsight Neuronavigation system (Rogue Research Inc., Montreal, Canada). Anatomical landmarks as defined by the International 10-10 EEG system (Nz, Cz, Iz, LPA, RPA, Oz) as well as the centre of each scalp electrode were digitised. In addition, we measured head circumference, as well as Nz-Iz and LPA-RPA distances with a tape measure (see Table 5.1).

Participant	Circumference	Nz–Iz	LPA–RPA
P01	61.0	35.0	37.0
P02	60.0	36.0	35.5
P03	52.0	31.0	30.0
Mean±SD	*57.67±4.93*	*34.00±2.65*	*34.17±3.69*

Table 5.1: Head measurements [cm] for participants based on the 10-10 EEG system.

5.2.3 Optode array modelling using AtlasViewer

Several parameters crucially influence the data quality that can be achieved with a given NIRS probe design. To ensure that a given NIRS probe montage will target a specific cortical region, the density of measurement channels must be weighed against the optimal source-detector separation (typically approximately 3 cm; see Brigadoi and Cooper, 2015; Strangman et al., 2014). The number of available source-detector

Figure 5.2: Combined optode-electrode montage for tDCS-NIRS of the visual cortex. The NIRS array is centred over EEG position Oz and held in place by three rubber head bands (spaced approximately 30 mm apart). tDCS electrodes are centred over PO7 and PO8 and attached to the head with a layer of ten20 conductive paste.

pairs (i.e., measurement channels) is usually limited by the NIRS hardware system. In the case of concurrent tDCS-NIRS designs, the probe geometry is further constrained by having to accommodate the large scalp electrodes for tDCS (Figure 5.2).

Probe design

To evaluate if our proposed 20-channel NIRS optode array successfully targeted the visual cortex, we first constructed a "virtual" optode probe using the AtlasViewer "SDgui" module (Aasted et al., 2015). Aspects of the probe design were constrained by the NIRS system: using the head straps supplied with the Brainsight NIRS system (Rogue Research Inc., Montreal, Canada), optodes can be spaced horizontally at 10 mm and vertically at 30 mm distances. To record from visual cortex in the current study, we used eight S-D pairs at 30 mm vertical and 10 mm horizontal separation (*cf.* Figures 5.2 and 5.3). The probe was centred on the Oz EEG position using head straps.

Accounting for individual head size

To account for inter-individual differences in head size, we scaled the standard Colin27 atlas brain (Collins et al., 1998) to each participant's head measurements (see Table 5.1). These measurements were used to construct an ellipsoid matching the head dimensions to calculate the coordinates of five 10-10 reference points (Iz, Nz, Cz, LPA, RPA). The atlas brain was then registered to these reference points using an affine transform in AtlasViewer.
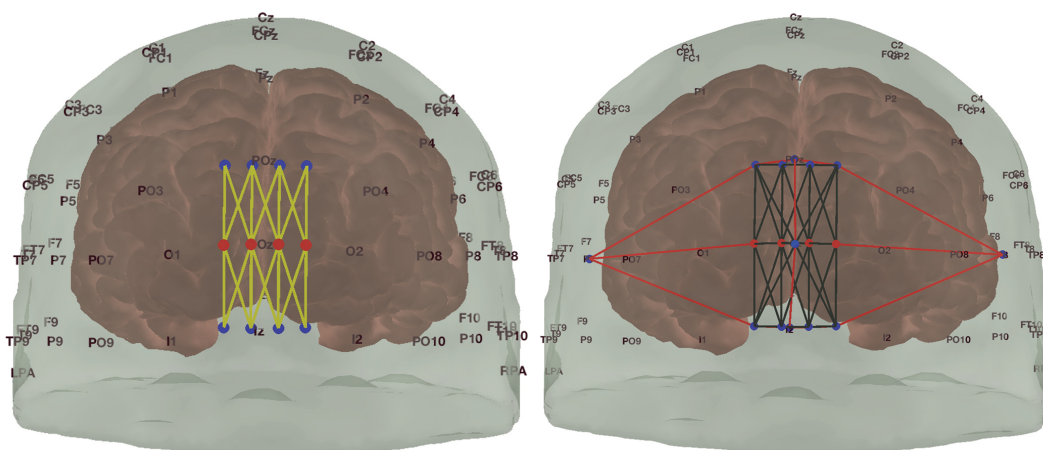
Figure 5.3: *Left:* NIRS probe geometry as defined in AtlasViewer. The array is centered on EEG position Oz. Measurement channels (yellow) are defined between four sources (red) and eight detectors (blue). *Right:* Spring and anchor point definitions determine source-detector spacing and registration of the probe to the head surface.

Projection to the cortical surface

AtlasViewer was used to register the "virtual" NIRS probe to the head surface based on the spatial registration tools described in Tsuzuki et al., 2007 and Tsuzuki et al., 2012. For each NIRS channel, we then projected a vector perpendicular to the head surface at the midpoint of the S-D pair onto the cortical surface. For each participant and channel, we report the resulting cortical projection points in MNI space as well as the corresponding anatomical region as defined by the Automated Anatomical Labelling atlas (AAL; Tzourio-Mazoyer et al., 2002).

Photon migration modelling of visual cortex NIRS

We computed spatial sensitivity profiles (i.e., forward models) for our NIRS probe array using the photon transport software tMCimg in AtlasViewer (Boas et al., 2002). Following the approach outlined in Chapter 1, we used a random walk Monte Carlo method evaluating the launch of 10^7 photons per source optode. The AtlasViewer/TM-Cimg default values were used for the optical properties of the tissue types defined in the Colin27 head model (see Table 5.2).

5.2.4 Electric field modelling of visual cortex tDCS

The NIRS optode array constrained the available electrode positions for tDCS of the visual cortex. This meant we were limited to evaluating a bilateral montage with electrodes on the left and right of the NIRS probe, i.e., at EEG positions PO7 and PO8.

Tissue	Scattering coefficient μ_s	Absorption coefficient μ_a
Skin	0.6600	0.0191
Skull	0.8600	0.0136
CSF	0.0100	0.0026
Grey matter	1.1000	0.0186
White matter	1.1000	0.0186

Table 5.2: Optical properties for scattering and absorption in brain tissues modelled using AtlasViewer/TMCimg.

Figure 5.4: *Left:* Silicone-rubber electrodes (5 x 5 cm) prepared for electrical stimulation with a thin layer of conductive paste. *Right:* Corresponding electrode definition, including connector plug, specified in SimNIBS for FEM of induced electrical fields.

Based on the SimNIBS software package, we modelled current inputs of 1.0, 1.5 and 2.0 mA via two 5 x 5 cm electrodes placed over PO7 (cathode) and PO8 (anode). Nominal current densities for the 35 cm^2 electrode surface area at different current intensities are given in Table 5.3. Using the individual head volume meshes, electrodes were centred on the participant-specific, digitised scalp positions in MNI space. For one pilot participant (P02), we also compared tDCS at 1.5 mA via a PO7-PO8 montage to the commonly used Oz-Cz montage for visual cortex tDCS.

All models used the default tissue conductivities from SimNIBS (see Table 4.1). SimNIBS v2.0.1 calls the open-source software GetDP (Geuzaine, 2007) to both form and solve the FEM model for tDCS effects on tissues in the head. We modelled two silicone-rubber electrodes (1.2 mm thickness), as currently used in our lab, with a layer of conductive paste (4 mm). Recent work from Saturnino and colleagues has indicated that electrode connector plug position may influence electric field distribution in FEM of tDCS (Saturnino et al., 2015). To mimic the 5 x 5 cm silicone-rubber electrodes used in our tDCS experiments, we therefore also modelled the connector plug (20 x 5 mm), oriented perpendicularly to the bottom edge of the electrode (Figure 5.4).

Current input	Current density
1.0 mA	0.0286 mA/cm^2
1.5 mA	0.0429 mA/cm^2
2.0 mA	0.0571 mA/cm^2

Table 5.3: Nominal current densities for an electrode with 35 cm^2 surface area.

Channel		Participant 01		Participant 02		Participant 03	
Scr	*Det*	*MNI*	*AAL*	*MNI*	*AAL*	*MNI*	*AAL*
1	1	-10 -75 22	Cuneus_L	-11 -81 25	Cuneus_L	-13 -77 28	Cuneus_L
1	2	-7 -91 31	Cuneus_L	-9 -88 29	Cuneus_L	-9 -82 29	Occipital_Sup_L
1	5	-10 -93 4	Occipital_Mid_L	-11 -98 5	Occipital_Sup_L	-12 -91 1	Calcarine_L
1	6	-8 -99 6	Occipital_Sup_L	-9 -91 4	Calcarine_L	-9 -92 2	Calcarine_L
2	1	-7 -91 31	Cuneus_L	-9 -88 29	Cuneus_L	-9 -87 33	Occipital_Sup_L
2	2	-1 -94 33	Cuneus_L	0 -95 32	Cuneus_L	-2 -93 34	Cuneus_L
2	3	3 -92 32	Cuneus_L	3 -92 32	Cuneus_L	3 -90 32	Cuneus_L
2	5	-8 -99 6	Occipital_Sup_L	-8 -99 6	Occipital_Sup_L	-10 -94 2	Calcarine_L
2	6	-6 -99 4	Occipital_Sup_L	-6 -102 5	Calcarine_L	-7 -97 3	Calcarine_L
2	7	-2 -88 7	Calcarine_L	0 -101 8	Calcarine_L	0 -103 2	Calcarine_L
3	2	3 -92 32	Cuneus_L	3 -92 32	Cuneus_L	3 -90 32	Cuneus_L
3	3	8 -72 21	Cuneus_R	7 -83 25	Cuneus_R	9 -88 33	Cuneus_R
3	4	12 -74 21	Calcarine_R	13 -82 23	Cuneus_R	16 -91 34	Occipital_Sup_R
3	6	-2 -88 7	Calcarine_L	0 -101 8	Calcarine_L	0 -103 2	Calcarine_L
3	7	4 -86 7	Calcarine_L	6 -103 6	Calcarine_L	5 -88 7	Calcarine_L
3	8	11 -94 7	Calcarine_R	12 -96 7	Calcarine_R	14 -101 2	Calcarine_R
4	3	12 -74 21	Calcarine_R	14 -93 30	Cuneus_R	16 -91 34	Occipital_Sup_R
4	4	16 -91 33	Cuneus_R	19 -87 28	Cuneus_R	21 -81 28	Occipital_Sup_R
4	7	11 -94 7	Calcarine_R	13 -98 6	Calcarine_R	14 -101 2	Calcarine_R
4	8	18 -93 4	Cuneus_R	18 -103 4	Calcarine_R	22 -76 5	Lingual_R

Table 5.4: MNI coordinates of cortical projection points for each NIRS source-detector pair and corresponding anatomical regions as identified by AAL.

5.3 Results

5.3.1 Cortical projection points for NIRS probe

For all pilot participants, cortical surface projections suggest that our optode array primarily targets the cuneus (40%) and the calcarine fissure with surrounding cortex (40%), as well as the superior occipital gyrus (18.2%), see Table 5.4. These cortical regions contain visual areas V1/BA17, V2/BA18 and V5, which are targets for our neuroimaging pilot study (*cf.* Chapter 6).

5.3.2 NIRS probe sensitivity profiles

To evaluate if our NIRS probe was sensitive to absorption changes in the visual cortex, we calculated spatial sensitivity profiles for our three pilot participants. The total sensitivity of our probe is illustrated in Figure 5.5. Note that, to facilitate visualisation, AtlasViewer projects the volumetric sensitivity computed in the grey matter onto the surface of the pia mater by matching each volume element with its closest surface element. Absorption changes are assumed to be uniform in the GM voxels closest to a given pial surface element and are summed across these voxels.

For the surface region overlying our target areas in the occipital cortex, the sensitivity mostly falls into the range of 0.01–0.1 mm^{-1}. Assuming an absorption change of 0.001 mm^{-1} occurring over an area of 100 mm^2 as a likely upper limit for functional NIRS measurements, the probe is sensitive to optical density changes in the range of

	Peak electric field strength [V/m]		
Participant	**1.0 mA**	**1.5 mA**	**2.0 mA**
P01	0.338	0.507	0.676*
P02	0.474	0.701	0.948*
P03	0.696	1.039	1.385*
Mean±SD	*0.503±0.181*	*0.749±0.269*	*1.003±0.358*

Table 5.5: Peak electric field strength [V/m] for input currents of 1.0, 1.5 and 2.0 mA as modelled using SimNIBS. (Values marked with an asterisk were used to set the upper limit of the participant-specific E_{max} range in model visualisations).

0.001–0.01 (Aasted et al., 2015). In comparison, physiological noise due to the heartbeat typically generates an optical density change of approximately 0.01.

Importantly, the aggregate sensitivity of all channels is sufficiently uniform across our target areas. This is an advantage of the high channel density in our probe geometry — at the cost of a reduced but still adequate field of view.
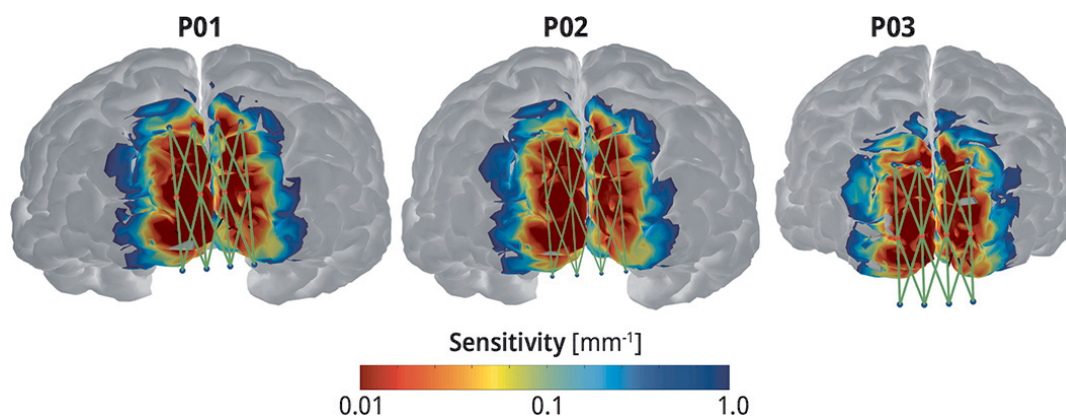
Figure 5.5: Distribution of aggregate sensitivity to optical density change in grey matter in three pilot participants. The Colin27 head model was scaled to each participant's head size.

5.3.3   tDCS-induced electric field strength

We estimated tDCS-induced electric field strength in three pilot participants. At all input current intensities, the highest peak electric field intensity (P03) in the sample is nearly twice the lowest peak intensity (P01), see Table 5.5. Notably, these correspond to the participants with the smallest (P03) and largest (P01) head size, respectively (Table 5.1). Furthermore, the results indicate a linear increase of peak field strength with input current intensity. Note that all figures presented here are scaled individually to each participant, but unified to the highest value occurring across all models of that participant (indicated in Table 5.5 with an asterisk).

The distribution of normalised electric field strength across the cortical surface is illustrated in Figure 5.7. For all participants and models, the region of highest field

intensity lies in the parieto-occipital cortex, with little to no changes seen in frontal-parietal regions. For the participant with the smallest head (P03), field intensity clearly extends more strongly towards the occipital pole. This is likely a result of a larger overall proportion of head surface being covered by the electrodes in this participant compared to the others.

For brain regions where the grey matter surface is tightly convoluted — such as early visual cortex — it is important to evaluate the induced electric fields not only at the most superficial reconstructions of the cortical surface, but also to consider deeper gyri and sulci. To better visualise these features, we used a sagittal cut slightly to the right of the midline, as well as two coronal and one transverse cut through the occipital pole of each participant (*cf.* Figure 5.6). Based on anatomical landmarks that can be reliably identified across all participants, coronal cuts were made at 1/3 and 2/3 of the total distance between the intersection of the calcarine fissure with the parieto-occipital sulcus and the occipital pole. The transversal cut was made at 2/3 of the total distance between the lower end of the occipital pole and the level of the intersection of the calcarine fissure with the parieto-occipital sulcus. For the transverse cut, the lateral extension from the midline was chosen to roughly reflect the region of highest NIRS sensitivity.
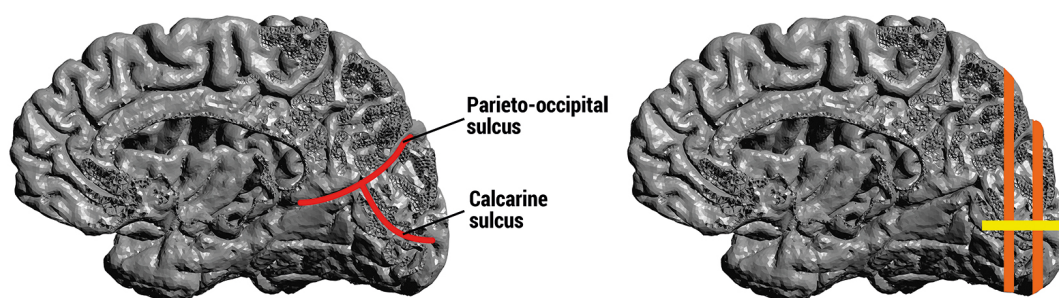
Figure 5.6: *Left:* Parieto-occipital and calcarine sulci. *Right:* Coronal cuts (orange) were made at 1/3 and 2/3 of the total distance between the intersection of the calcarine fissure with the parieto-occipital sulcus and the occipital pole. The transverse cut (yellow) was made at 2/3 of the total distance between the lower end of the occipital pole and the level of the intersection of the calcarine and parieto-occipital sulci.

Sagittal cuts through the whole brain (Figure 5.8) reveal that higher input currents lead to the induced electric field spreading into deeper-lying regions of the grey matter surface in the occipital cortex, including the calcarine fissure.

Similarly, transverse cuts of the occipital pole show that deeper cortical folds are more strongly polarised when larger input currents are used (Figure 5.9). Across all models, the field is clearly stronger in superficial regions of the grey matter around the occipital pole than in deeper areas. This relationship can also be seen when comparing the two coronal cuts — field intensity is generally lower at the deeper-lying cut at 2/3 of distance (Figure 5.11) than at the cut at only 1/3 of distance (Figure 5.10). The
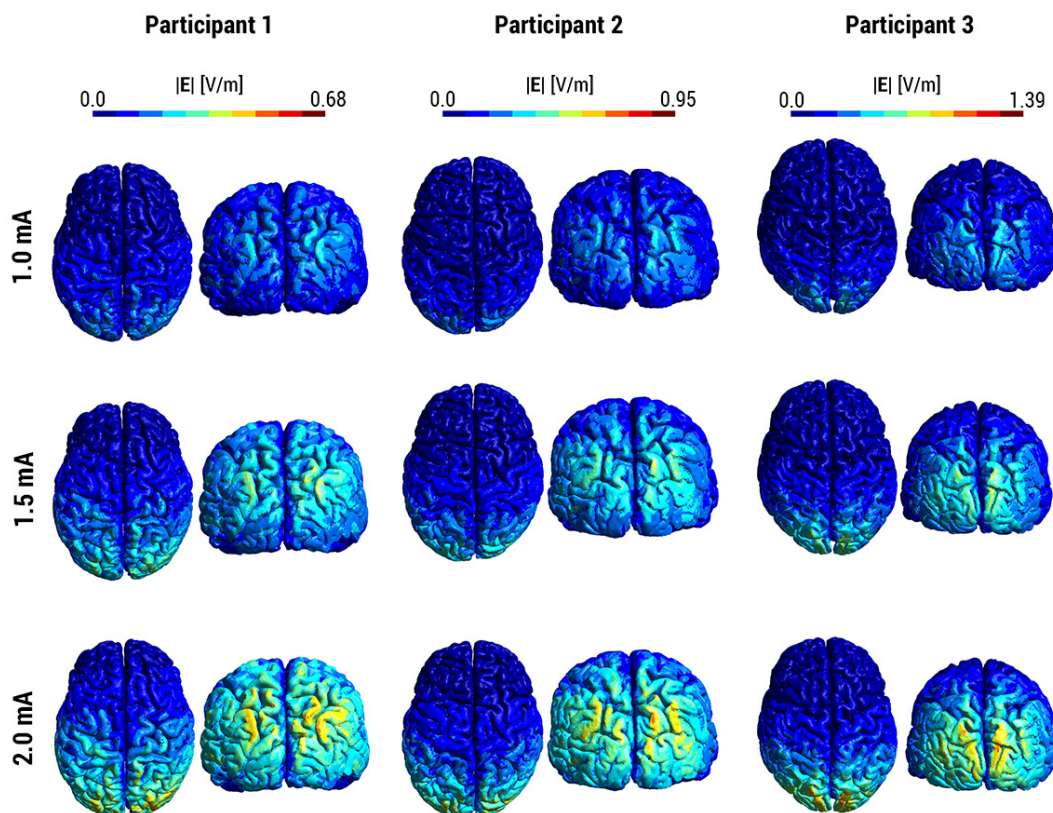
Figure 5.7: Superior and posterior views of tDCS-induced electric field magnitude [V/m] as modelled with SimNIBS for different current input levels (1.0, 1.5, 2.0 mA). Note that peak electric field magnitude differs between participants.

difference is particularly evident in Participant 03, for whom the electric field pattern spreads more towards the occipital pole. It is also interesting to note that coronal views demonstrate that field strength is low or zero for gyri of the calcarine fissure that are vertically oriented along the midline, but tends to be higher for horizontally oriented sulci and is comparatively strong at the bottom of these sulci.

For the participant closest to the sample means (P02), we also compared electric field strength for two Oz-Cz and PO7-PO8 electrode montages at 1.5 mA current input. Peak field intensity was 3.9% higher for the PO7-PO8 montage compared to the Oz-Cz montage (0.791 V/m for PO7-PO8 vs. 0.675 V/m for Oz-Cz). As illustrated by the posterior and sagittal views in Figure 5.12, the electric field is spread more towards frontal and parietal areas of the brain for the Oz-Cz montage commonly used in visual cortex tDCS experiments. Furthermore, transverse and coronal cuts show that the two montages have nearly opposite effects, i.e., areas with high intensity for one montage tend to show a low intensity for the other montage. Notably, cortical folds of the calcarine fissure generally appear to be more strongly polarised by the Oz-Cz montage.
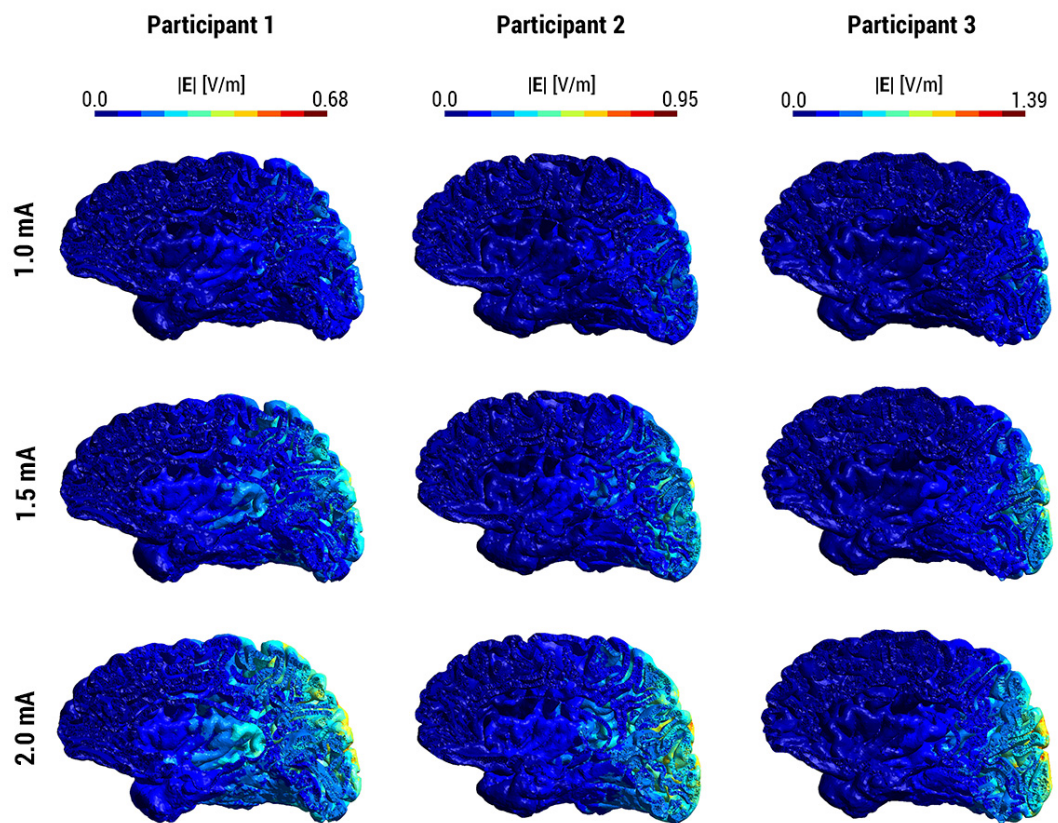
Figure 5.8: Sagittal view of right hemisphere, slightly lateral to the midline, of electric field magnitude [V/m] as modelled with SimNIBS for different current input levels (1.0, 1.5, 2.0 mA). Note that peak electric field magnitude differs between participants.
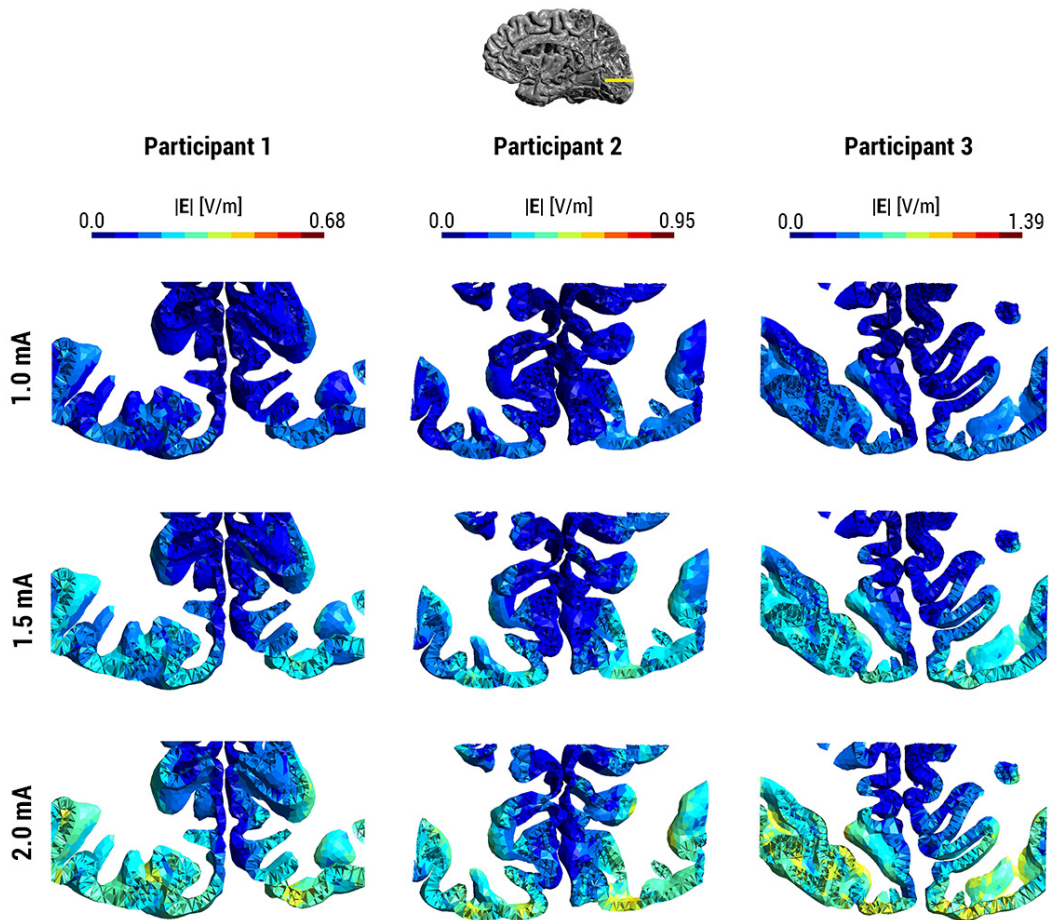
Figure 5.9: Transverse view of electric field magnitude [V/m] as modelled with SimNIBS for different current input levels (1.0, 1.5, 2.0 mA). Cut was made at 2/3 of the total distance between the lower end of the occipital pole and the level of the intersection of the calcarine and parieto-occipital sulci. Note that peak electric field magnitude differs between participants.
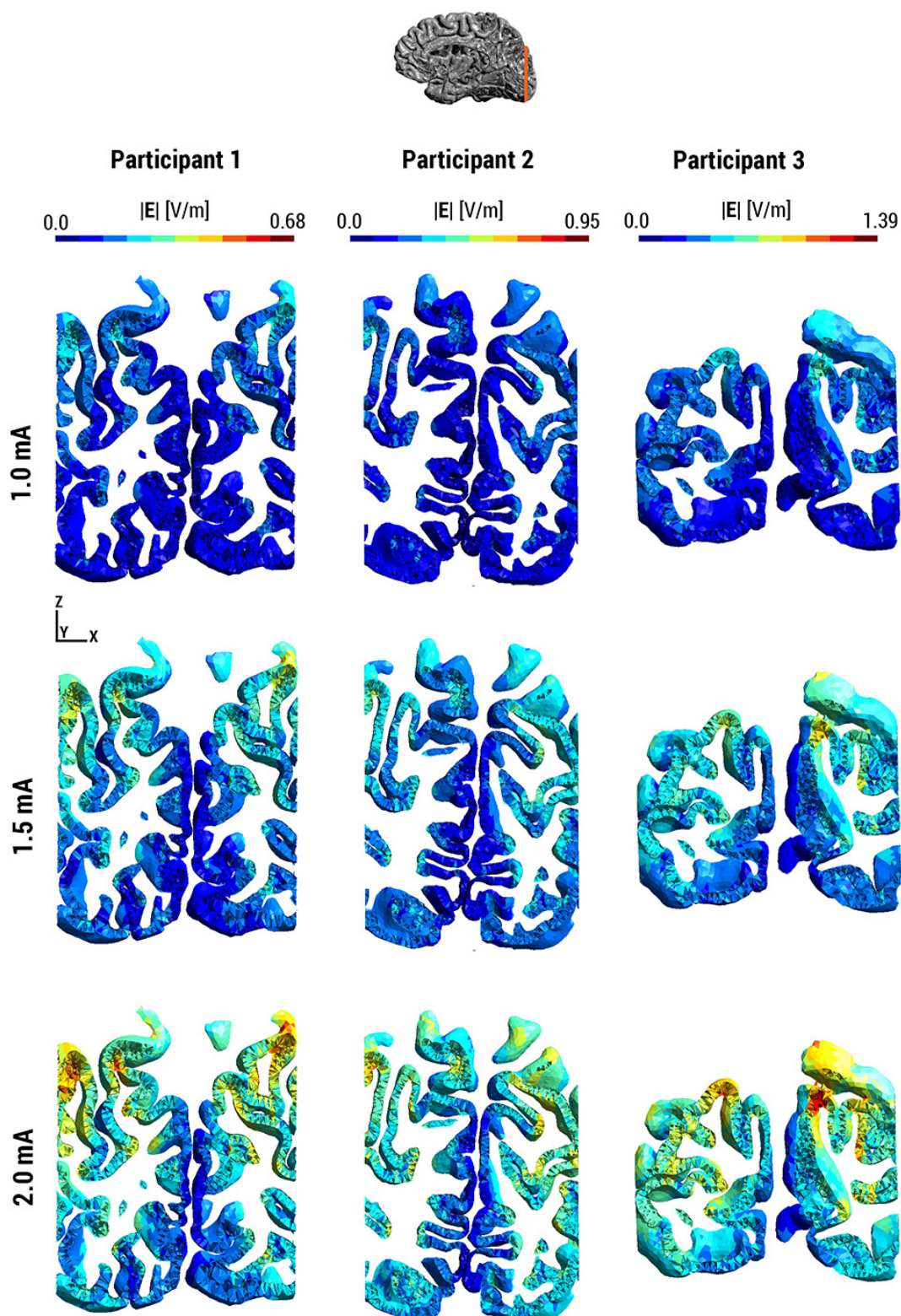
Figure 5.10: Coronal view of tDCS-induced electric field magnitude at different current input levels (1.0, 1.5, 2.0 mA). The cut was made at 1/3 of the total distance between the intersection of the calcarine fissure with the parieto-occipital sulcus and the occipital pole. Note that peak electric field magnitude differs between participants.
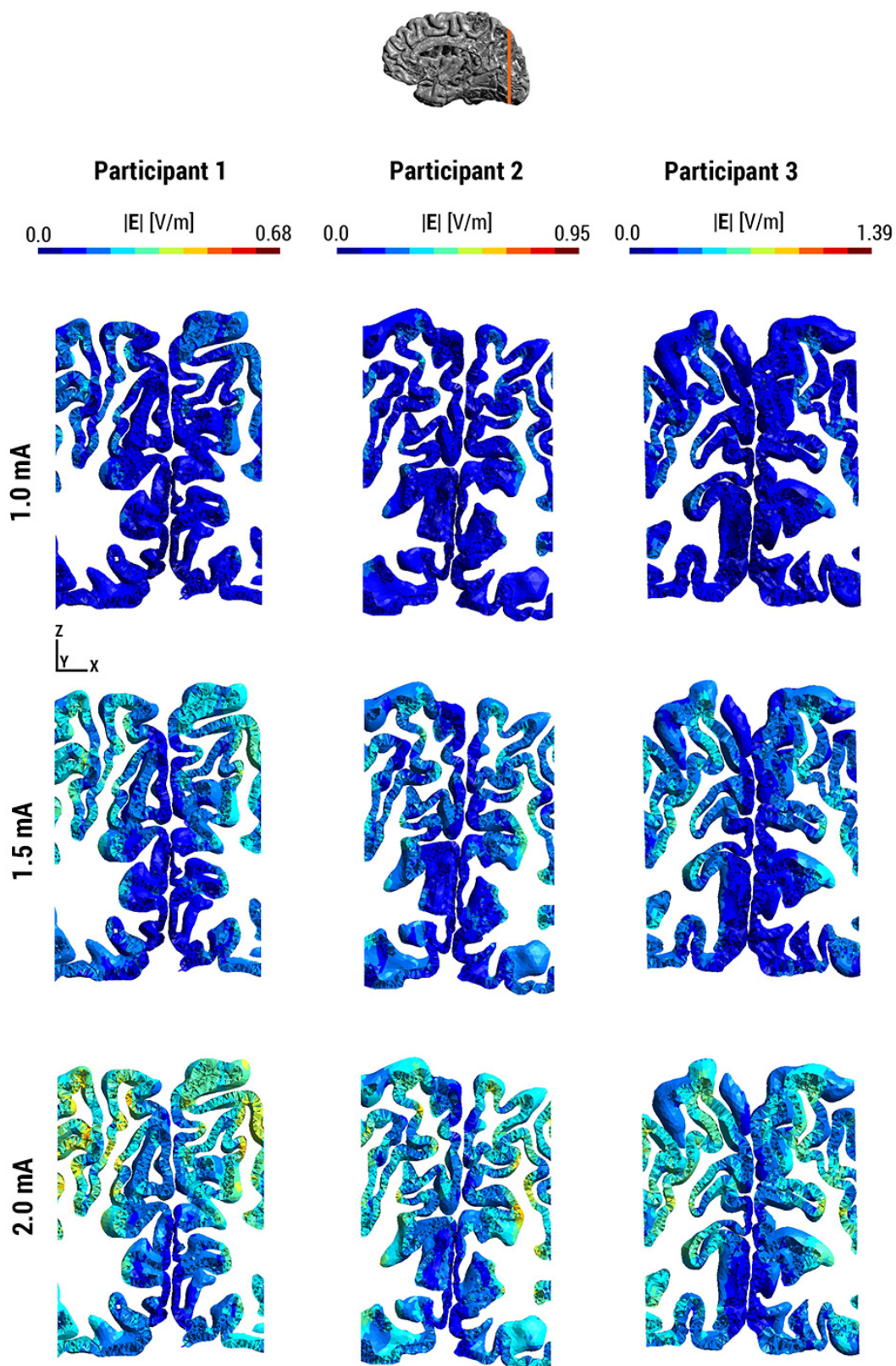
Figure 5.11: Coronal view of tDCS-induced electric field magnitude at different current input levels (1.0, 1.5, 2.0 mA). The cut was made at 2/3 of the total distance between the intersection of the calcarine fissure with the parieto-occipital sulcus and the occipital pole. Note that peak electric field magnitude differs between participants.
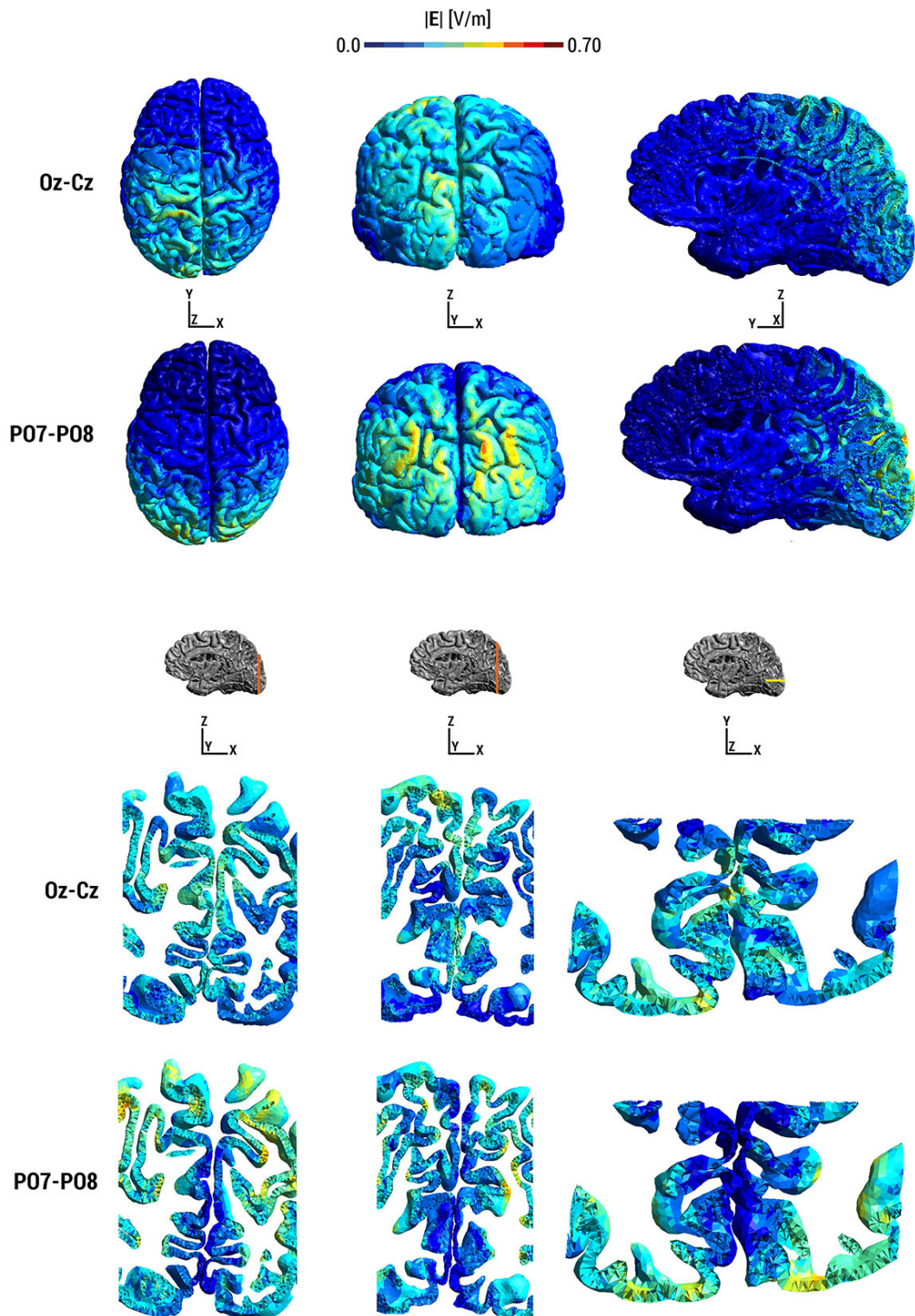
Figure 5.12: Comparison of electric field magnitude [V/m] for Oz-Cz and PO7-PO8 electrode montages at 1.5 mA current input for Participant 02.

5.4   Discussion

To evaluate electrode and optode placement for concurrent tDCS-NIRS of the visual cortex, we created finite-element-models of electric field distribution based on individual anatomical MRI scans. Models for three levels of input current intensity (1.0, 1.5, 2.0 mA) and two different electrode montages were assessed. Furthermore, we generated estimates of spatial sensitivity for a NIRS probe optimised for recording from the visual cortex. As a proof-of-principle, we applied this software pipeline to the brains of three pilot participants.

5.4.1   NIRS sensitivity

Results from photon migration models and anatomical labelling suggest that the specific spatial coverage afforded by our NIRS probe successfully targets occipital regions, including — crucially — regions of the primary and secondary visual cortex. In all participants, coverage is uniform across the cortical surface and sensitivity is sufficient to register optical density changes in visual NIRS recordings (*cf.* Aasted et al., 2015).

A limitation of our current approach is that volumetric information is projected onto a reconstruction of the pial surface to reduce computational load when creating sensitivity profiles, resulting in a loss of information. In addition, the AtlasViewer package currently does not allow the user to visualise or evaluate NIRS sensitivity along sulci — a particular shortcoming for a densely folded target area like the early visual cortex. Here, we rely on previous modelling work which has shown that sensitivity as a function of source-detector separation reaches an asymptote at 30-40 mm separation (e.g., Strangman et al., 2013). As all measurement channels in our probe geometry fall within this range, we are confident that depth sensitivity is unlikely to be further optimised by changes in probe geometry. The restricted field of view of the proposed probe could be extended by increasing the horizontal spacing within optode rows. This would, however, lead to a loss of effective resolution without further improving sensibility in our cortical target region — and, more practically, would interfere with the placement of tDCS electrodes to the sides of the probe.

This latter issue could potentially be overcome by using HD-tDCS, where multiple smaller scalp electrodes can be interleaved more flexibly with NIRS optodes (Villamar et al., 2013). However, our current aim was to apply tDCS while concurrently measuring NIRS and MEG. An HD-tDCS approach would require several more cables for delivering current to the scalp, thereby also greatly increasing the induced magnetic fields around the cables and — we would expect — increasing both the amplitude and incidence of MEG signal artefacts.

For issues specific to the use of NIRS, there are two unavoidable confounds in the sensitivity models constructed with AtlasViewer/TMCimg. First, hair is invisible to MRI and therefore not included in head models, but can both mechanically interfere with optode-scalp coupling and absorb light before it enters the scalp. Second, blood vessels are not captured in our head model. Specifically, the superior sagittal sinus — the largest dural venous sinus — runs along the midline and across our NIRS probe. This sinus is estimated to have a mean width of 9.9 mm in the midoccipital region (Andrews et al., 1989). However, near-infrared light travelling into blood vessels with diameters over 1 mm will be absorbed almost completely. Consequently, in practice, NIRS channels near to or crossing the occipital midline are likely to be far less sensitive to functional changes than our models suggest.

The anatomical accuracy of the sensitivity profiles generated with the approach presented here is further limited by the registration of individual head sizes to the Colin27 template, and our assumptions of an ellipsoid head shape. Our models are based on the segmentation of a single atlas brain. Any geometrical inaccuracies specific to the methods used to segment the Colin27 template are not assessed here. Furthermore, individual differences in scalp, skull or CSF thickness are not taken into account. For instance, skull thickness distribution differs for females and males (Law, 1993; Li et al., 2008) and brain tissues in older individuals may have different baseline optical properties (Duncan et al., 1996a). Similarly, it would be desirable to base photon migration models not on an idealised, "virtual" NIRS probe, but on digitised, participant- and session-specific optode positions. This would allow for a systematic assessment of the variance in probe placement and spatial sensitivity across a pool of participants. Both improvements incorporate participant-specific measurements from individual MRIs and are currently under development in AtlasViewer.

However, such a fully individualised approach poses a substantial additional demand on resources and may not be necessary in all cases. First, accurate segmentation of individual MRI scans is of key importance but constitutes a time-consuming step in the pipeline. Second, the digitisation of all NIRS optodes significantly extends the length of experimental sessions, especially for large optode arrays. Thus, the advantages of such an individualised approach must be weighed against the added burden for participant and experimenter.

5.4.2   tDCS-induced electric fields

Our evaluation of tDCS-induced electric field distributions suggests that a PO7-PO8 montage effectively focuses the field in occipital regions with no, or extremely low, polarisation in frontal brain areas, indicating that a frontal control montage is not a matter of high priority for visual tDCS experiments based on this configuration.

At the basis of FEM of tDCS lies the assumption that regional polarisation and, eventually, neuromodulatory effects of tDCS are predicted by local electric fields. This assumption suggests the concept of a coupling constant, defined as the amount of cell membrane compartment polarisation [mV] per unit uniform electric field [mV/mm] (Bikson et al., 2004). Based on this strongly simplified approach, an order-of-magnitude analysis of cellular tDCS effects can be attempted for our models. First, upon visual inspection of tDCS-induced electric fields, much of the cortex in the occipital region shows intensities in the range of 40–60% of peak field strength. If we assume an average field intensity of 50% of the mean peak field strength observed in our pilot participants, most cells in the occipital cortex would be exposed to fields at approximately 0.25 V/m (for 1.0 mA), 0.38 V/m (for 1.5 mA) and 0.5 V/m (for 2.0 mA). Second, experiments carried out *in-vitro* suggest that neuronal networks are sensitive to electric fields as low as 0.14 V/m (Francis et al., 2003). Following calculations outlined by Ruohonen & Karhu (2012), the estimated maximal polarisation of interlaminar astrocytes for an electric field strength of 0.5 V/m would be 0.08 mV. In comparison, the transmembrane potential of glial cells changes by approximately 2 mV when neurons are active (Massimini and Amzica, 2001). These considerations indicate that, on average, tDCS at all three input intensities is likely to effectively polarise a subset of neurons in the occipital cortex, but a significant polarisation of astrocytes can only be considered for the very highest peak intensity observed in our sample (E = 1.385 V/m, V = 0.22 mV). However, it is worth nothing that, even in absence of direct astrocytic polarisation, changes in rCBF may reflect more complex interactions of direct currents with the whole neurovascular unit, including downstream effects of neuronal activity.

Looking at field patterns across the whole brain, our results show that electric fields are stronger in superficial regions of the grey matter around the occipital pole compared to deeper-lying cortical areas. Higher input currents appear more likely to effectively stimulate deeper tissues in the occipital cortex, including the calcarine fissure. For the PO7-PO8 montage, field strength is low or null for vertically oriented calcarine gyri, but tends to be higher for horizontally oriented sulci and is comparatively strong at the bottom of these sulci. Thus, it appears that, while the PO7-PO8 montage leads to a well-focused field for the more superficially located higher visual areas, it may not lead to a strong polarisation for the primary visual cortex in the calcarine fissure. In contrast to current common practice in the literature, this view into deeper-lying cortical areas demonstrates that merely reporting the electric field spread through visualisation of the cortical surface is insufficient. More sophisticated evaluations of the electric field in an anatomically accurate and functionally relevant cortical ROI are necessary.

Furthermore, when comparing head sizes and electric field intensities, it is noteworthy that in our pilot sample the participant with the smallest head (P03) shows the

highest peak electric field intensity. Values for the participants with the second- and third-smallest heads indicate a trend towards increased peak intensity with decreasing head size. Moreover, the electric field is spread more towards the occipital pole for the participant with the smallest head. While these findings are based on a small preliminary sample, they support the prevalent idea that dose-dependent approaches for tDCS require participant-specific anatomical information (e.g., Berker et al., 2013).

In one participant, we also compared a widely used montage for visual cortex tDCS, where electrodes are placed at Oz and Cz, to our proposed tDCS-NIRS montage, where electrodes are placed over PO7 and PO8. Our analysis reveals similar peak electric field intensities and peak current densities for both montages. However, the montages differ significantly in the spatial distribution of the electric field. For the Oz-Cz montage, the electric field spreads more towards frontal and parietal areas of the brain compared to the PO7-PO8 montage. In addition, our results show that the two montages have nearly opposite effects on the electric field, i.e., areas with high intensity for one montage tend to show a low intensity for the other montage. Importantly, cortical folds of the calcarine fissure generally appear to be more strongly polarised by the Oz-Cz montage.

These differences in field intensity can be related to previous modelling efforts employing an inverse FEM approach to optimise electrode montages by Rampersand and colleagues (2013). Their analysis of several cortical target areas suggested that, to achieve maximal field intensity, electrodes are best placed on opposite sides close to the cortical target. In contrast, our own results show a lower field intensity for the calcarine fissure when electrodes are placed to the left and right of the target area in the PO7-PO8 montage compared to the orthogonal Oz-Cz montage. This disagreement may in part be explained by divergent definitions of the target area, warranting a more detailed, quantitative comparison beyond the scope of the present analysis.

In conclusion, our pilot analysis indicates that sufficient NIRS measurement sensitivity can be reached with the proposed optode array design while accommodating scalp electrodes for tDCS. Finite-element models of electric field distribution suggest that a bilateral electrode montage is likely to alter the transmembrane potential of at least a subset of neurons in the visual cortex, but may not induce sufficiently strong fields to directly modulate astrocytic activity. However, it is important to reiterate that estimates of electric field intensity are only one factor in the accurate prediction of tDCS effects. The excitability of neurons, or indeed other components of the NVU, depends on their morphology and electrophysiological properties as well as their position within and orientation relative to the induced electric field. Moreover, functional outcomes of electrical stimulation likely cannot be fully understood without considering network architecture and ongoing brain activity.

Chapter 6

On the feasibility of concurrent tDCS-NIRS-MEG

6.1 Introduction

The general rationale for the concurrent acquisition of NIRS-MEG data during tDCS has been introduced in Chapter 5. Here, we explore the technical feasibility of tDCS-NIRS-MEG in a pilot study. Beyond the question of electrode-optode montage selection for tDCS-NIRS, unique challenges in experimental design are posed by combining MEG and NIRS to probe tDCS effects on electrodynamic and hemodynamic stimulus-induced responses in the visual cortex.

MEG provides a measurement of the surface magnetic fields induced by cortical postsynaptic currents, i.e., the local field potential (Hansen et al., 2010). The neuro-chemical processes that occur during electrophysiological activity modulate local vascular responses, including cerebral blood flow (CBF), cerebral blood volume (CBV) and oxygen consumption (CMRO2) (Lecrux and Hamel, 2011; Muoio et al., 2014). These effects generate changes in the relative levels of oxy- and deoxyhemoglobin that can be measured with NIRS — the same processes at the site of neuronal activity which ultimately form the basis of the BOLD fMRI signal (*cf.* Figure 1.14; Lauritzen and Gold, 2003; Logothetis et al., 2001).

Both spatially and temporally, functional MRI has been shown to be highly correlated with NIRS across many sensory and cognitive tasks (e.g., Cui et al., 2011; Minati et al., 2011; Steinbrink et al., 2006; Toronov et al., 2007). A close association of electro- and hemodynamic responses is also likely, as it is widely accepted that neuronal, metabolic and vascular responses are highly correlated in space and time. Numerous studies have combined electrophysiology and fMRI to explore the coupling of oscillatory and hemodynamic signals; however, the details of their relationship remain controversial (Hall et al., 2014b; Hermes et al., 2017; Kayser et al., 2004; Ojemann et al., 2013).

In humans, cortical network activation in response to stimuli commonly co-occurs with an increase in the signal power of high-frequency oscillations, such as the gamma

band (Buzsáki and Wang, 2012; Jia and Kohn, 2011; Jia et al., 2011). Several previous findings point to a positive correlation of changes in gamma band power and BOLD response, although it remains unclear whether the BOLD response is best predicted by narrowband gamma (30—100 Hz) or broadband gamma (>100 Hz) (Hermes et al., 2017; Muthukumaraswamy and Singh, 2008; Niessing et al., 2005; Ojemann et al., 2013; Singh et al., 2002; Zumer et al., 2010). A rare combined NIRS-MEG study of the somatosensory cortex also found that power change in the beta and gamma bands was correlated with the hemodynamic response (Kikuchi et al., 2010).

However, electrodynamics evolve over a time scale of milliseconds, whereas it takes several seconds for the hemodynamic response function (HRF) to peak after stimulus onset — and similarly several seconds to return to baseline after stimulus offset. The literature of studies combining NIRS and MEG is sparse, but existing reports indicate that the onset of hemoglobin concentration changes lags 1–6 s behind the oscillatory response (Kikuchi et al., 2010; Sander et al., 2007).

Many fMRI studies and most NIRS studies of the visual cortex have used blocked experimental designs, where a visual stimulus is presented for approximately 15-30 s; signal changes are then compared to a baseline period without visual stimulation. For visual processing, both fMRI and NIRS studies have demonstrated that the strongest and most sustained hemodynamic changes are induced by pattern-reversing checkerboards (Kashou and Giacherio, 2016; Schroeter et al., 2004; Wijeakumar et al., 2012; Wylie et al., 2009). In particular, a reversal rate of around 7–8 Hz has been shown to elicit strong changes in hemoglobin concentrations measured by NIRS (Colier et al., 2001a; McIntosh et al., 2010; Rovati et al., 2007; Takahashi et al., 1999; Wylie et al., 2009).

Moreover, the strength of both oscillatory and hemodynamic responses is related to the visual contrast level of checkerboard stimuli. In a recent study investigating neurovascular coupling using fMRI and MEG, Stickland et al., 2019 characterised BOLD and gamma power changes in response to reversing checkerboard stimuli at five different visual contrasts (6.25%, 12.25%, 25%, 50%, 100%). In healthy controls, both peak gamma power change and BOLD change increased significantly with increasing visual contrast. These results are in line with previous reports of a linear increase of both visual evoked potential (VEP) amplitude and HbO/HbR concentration changes with checkerboard contrast (1%, 10%, 100%) from studies combining NIRS and EEG (Rovati et al., 2007; Si et al., 2016).

However, while the use of checkerboard stimuli ensures that any paradigms measuring evoked NIRS and MEG signals would have a high SNR, the very features that make this stimulus optimal for imaging studies may make it sub-optimal for brain

stimulation work. The checkerboard is a highly salient visual stimulus which, if presented with high contrast (around 100%), may drive cellular activity in the visual system to a theoretical maximum in both the metabolic and neurophysiological domains. This may mean that using such a stimulus in tDCS experiments which aim to increase or facilitate visual processing would fail, simply due to hitting this activity "ceiling". We therefore based our pilot study on black-and-white checkerboard stimuli with a maximum contrast of 50%, not 100%.

To date, few studies have investigated outcomes of electrical stimulation with NIRS (McKendrick et al., 2015). Previous tDCS-NIRS studies have explored stimulation effects in the motor cortex (Khan, 2013; Lei et al., 2016; Merzagora et al., 2010; Muthalib et al., 2013; Takai et al., 2016; Zheng et al., 2011), as well as in the sensorimotor and prefrontal cortices (Ishikuro et al., 2014; Jones et al., 2015), but — to the best of our knowledge — no previous NIRS study has investigated the effects of tDCS applied to the visual cortex.

As NIRS is an optical technique, the electric currents induced by tDCS do not perturb the measured signal. In contrast, the electromagnetic noise generated by tDCS is several orders of magnitude higher than the LFP measured by the superconducting quantum interference device magnetometers (SQUIDS) used in MEG. Consequently, electrical stimulation introduces substantial artefacts in concurrently recorded MEG signals.

The feasibility of recording MEG during tDCS in humans was first demonstrated for the motor cortex in a proof-of-principle experiment by Soekadar et al., 2013. Further evidence for the use of the two techniques in tandem was provided by Garcia-Cossio et al., 2015 in the motor cortex, and by Hanley et al., 2015 and Marshall et al., 2015 using online tDCS in the visual cortex.

Hanley et al., 2015 applied 1 mA of anodal tDCS during MEG and measured time-locked and induced responses in the motor beta (15-30 Hz) and visual gamma band (30-80 Hz) while participants performed a visuo-motor task before, during and after stimulation. They found a reduction of average power in the visual gamma band for anodal compared to sham tDCS; however, Hanley and colleagues employed both visual and motor cortex electrode montages in their study, yet this effect was not specifically associated with the visual cortex montage used. The magnitude of motor evoked responses was significantly enhanced during anodal stimulation, but no after-effects of tDCS were observed.

Marshall et al., 2015 used online tDCS at 2 mA to stimulate the visual cortex while participants viewed moving annulus stimuli known to produce strong modulations of alpha- and gamma-band activity. The presentation of visual stimuli produced the expected alpha power decrease (8-12 Hz) and gamma power increase (40-100 Hz), and this response pattern was observable both during active and sham tDCS. However,

neither anodal nor cathodal electrical stimulation produced systematic modulation of these oscillatory responses.

Collectively, these proof-of-principle studies suggest that tDCS-induced signal artefacts can be attenuated — but not completely removed — through the use of adaptive spatial filtering methods (beamforming). However, at present, there exists no comprehensive approach for tDCS artefact removal or a "ground truth" for the evaluation of artefact cleaning methods. In particular, the role of non-linear artefacts arising from systemic physiology and head movements remains a contested issue (Neuling et al., 2015; Noury and Siegel, 2017, 2018; Noury et al., 2016).

During tDCS, even very small changes in the distance between a current source and the magnetometers can lead to artefactual signal changes of a similar magnitude as the physiological signals of interest. Both non-rhythmic components, such as slow head drift, and rhythmic components, such as eye blinks, heartbeat and respiration, play a role. Artefacts induced by tDCS have been observed to be time-locked to the participant's heartbeat and respiration (Marshall et al., 2015; Noury et al., 2016), with peaks at the participant's heart rate and at the first harmonic of the respiration rate. It is therefore essential to monitor physiological signals, as well as eye and head movements during tDCS-MEG acquisition.

Such a multimodal approach, however, inevitably increases the burden on both resources and participants, and so the benefits of acquiring such data must be weighed carefully against any compromises in experimental design and data quality that ensue. In this pilot study, we therefore investigated the feasibility of acquiring concurrent NIRS-MEG data during online tDCS. Healthy participants viewed pattern-reversing checkerboard stimuli and performed a simple visual detection task while receiving active or sham tDCS to the occipital cortex. In a blocked experimental paradigm, we probed tDCS effects on oscillatory and hemodynamic responses in the early visual cortex by presenting the same checkerboard stimulus at three different levels of contrast. We used relative gamma power (30–90 Hz) and HbO/HbR concentration change as our primary empirical measures for MEG and NIRS, respectively. Based on previous findings in the literature, we expected these responses to increase with visual contrast. Electrocardiogram, respiration, eye movement and head motion were co-recorded for artefact removal. In addition, we acquired participant-specific MRI data to create finite-element models of electric field strength induced by tDCS via a PO7-PO8 electrode montage. Here, we discuss technical aspects and challenges of tDCS-NIRS-MEG data acquisition.

6.2 Methods

6.2.1 Study design and participants

Fifteen right-handed participants were recruited for this single-blind, sham-controlled pilot study. Ethical approval for the study was obtained from the School of Psychology Research and Audit Ethics Committee at Cardiff University. The study was carried out in accordance with the Declaration of Helsinki. Written informed consent was obtained prior to data collection. Participants received paid compensation.

All participants had normal or corrected-to-normal vision and reported to be free of systemic or neurological disease and medication affecting visual performance. No restrictions on hair type were made for inclusion in this pilot study.

Participants completed one experimental session to acquire structural MRI data and two sessions to acquire tDCS-NIRS-MEG data. Sessions in which tDCS was applied were counterbalanced for stimulation type (active vs. sham) and separated by at least 48 hours. Participants were not informed that the study included a sham condition.

Participant attrition

Of the 15 participants initially recruited for this pilot study, two male participants were excluded from data collection because their head circumference was too large to fit in the MEG dewar when additional NIRS and tDCS equipment was attached. Three female participants were excluded because their hair was too dense to establish sufficient mechanical optode-scalp coupling for NIRS acquisition from the occipital cortex. Therefore, only ten participants completed the experiment (8 male, M = 24.6$\pm$3.9 years).

For NIRS analysis, data from two participants was excluded due to signal saturation at multiple detector optodes. For MEG analysis, data from one participant was excluded because the CTF acquisition software failed to write an output file in one of the sessions. Data from five more participants was excluded due to issues with ECG recording, triggers and data epoching.

In total, NIRS data from eight participants and MEG data from four participants was analysed. Electric fields induced by tDCS were modelled in ten participants.

6.2.2 Visual stimulation & task

The experimental paradigm is illustrated in Figure 6.1. Stimuli were presented using a PROpixx LED projector (1920 x 1080 px resolution, 120 Hz refresh rate; VPixx Technologies Inc., Saint-Bruno, Canada) and Psychtoolbox (v3, Brainard, 1997; Kleiner et
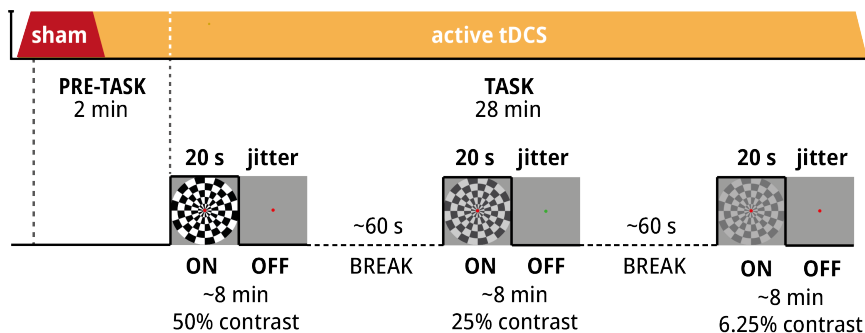
Figure 6.1: Schematic of the experimental paradigm. The order in which the three different checkerboard contrast levels (i.e., "runs") were presented was pseudo-randomised across participants and sessions. Each run consisted of 12 stimulus ON/OFF blocks.

al., 2007). Participants were seated in the MEG chair at a distance of 120 cm from the screen. Stimuli were viewed binocularly.

Full-field, black-and-white radial checkerboard stimuli with a pattern reversal rate of 7.5 Hz (i.e., 15 reversals per second) were used for visual stimulation. In "stimulus ON" periods, checkerboards were presented at one of three contrast levels (6.25%, 25% or 50%). Checkerboards were presented on a mean luminance background, which was also used as a baseline (i.e., in "stimulus OFF" periods). Checkerboards at each contrast level where presented in three separate data acquisition "runs" of approximately 7.5–8 minutes duration. The order of stimulus contrast levels was pseudo-randomised across participants and sessions. Each run consisted of 12 blocks of stimulus ON and OFF periods. Stimulus ON periods were 20 s in duration; the duration of stimulus OFF periods varied pseudo-randomly between 18.5 and 19.5 seconds. A short break of approximately 60 s was taken between runs.

A small red fixation dot was shown at the screen centre. To maintain a constant level of attention, participants were asked to maintain fixation and count the number of times the fixation dot changed colour from red to green. Counts were reported verbally during the breaks.

6.2.3 Transcranial direct current stimulation

Transcranial direct current stimulation was delivered using a battery-driven Neuro-Conn DC-STIMULATOR MR (NeuroCare Group GmbH, Ilmenau, Germany). In accordance with the modelling work described in Chapter 5, we applied current at 1.5 mA via two 5x5 cm^2 silicone-rubber electrodes placed at EEG 10-10 positions PO7 and PO8 (nominal current density: 0.06 mA/cm^2).

To minimise any potential magnetic field artefacts induced by the tDCS equipment, we placed the stimulator device outside the magnetically-shielded room (MSR) and
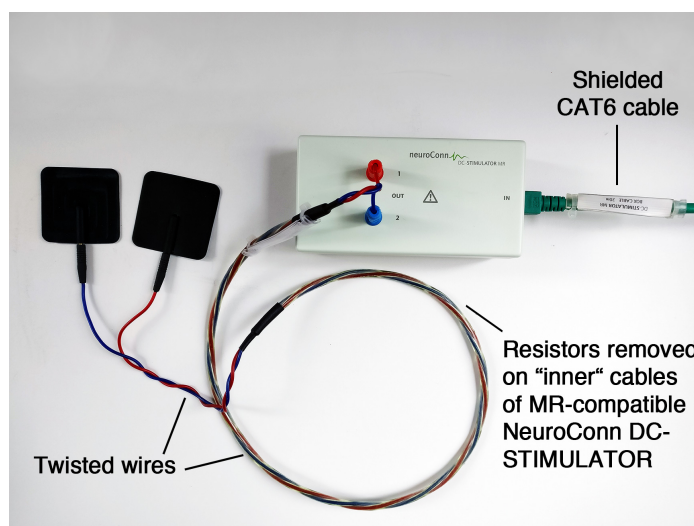
Figure 6.2: A shielded CAT6 cable and twisted "inner" cables were used to minimise current-induced magnetic fields while delivering current to the scalp electrodes. The stimulator device was placed outside the MSR.

used shielded cables to deliver current to the scalp electrodes (Figure 6.2). The NeuroConn MR-compatible stimulator cables were custom-modified by NeuroCare Group to remove two 5 kΩ resistors. This was necessary to allow the use of input currents above 1.0 mA without exceeding the device's safety impedance limit of 20 kΩ. The two "inner" cables — those within the MSR — ran together at the earliest possible location on the head and were twisted in order to minimise their magnetic fields.

The skin areas covered by electrodes were prepared with alcohol and Nuprep skin prep gel (Weaver and Company, Aurora, CO, USA). Electrodes were attached to the scalp with a layer of ten20 conductive paste (Weaver and Company, Aurora, CO, USA).

At the beginning of each tDCS session, a short impedance test protocol was executed (10 s linear current fade-in, 15 s DC stimulation at 1.5 mA, 10 s linear fade-out). Impedance levels were recorded at the 25 s mark. Test impedance was below 5.0 kΩ in all sessions.

Participants received 120 s of tDCS in the active tDCS condition and 60 s of tDCS in the sham condition before the task began. Current was faded in and out over 10 s. Total duration of stimulation in the active tDCS condition was 30 minutes (*cf.* Figure 6.1)

In contrast to the other experiments reported in this thesis, the experimental paradigm used in this chapter was single-blinded: participants were not explicitly made aware of the nature of the stimulation they received, but no effort was made to keep this from the experimenters. During data acquisition, the on- and offset of tDCS is clearly visible in the MEG channels. Therefore, double-blinding a concurrent tDCS-MEG experiment would require two experimenters to work independently — an "unblinded" experimenter to monitor the MEG acquisition and operate the stimulator, and a "blinded" experimenter to interact with participants. However, due to space constraints, such

an approach is not currently feasible in our MEG lab. At the end of the study, participants were asked to guess for each session whether they had received active or sham stimulation.

6.2.4   Eyetracking

To aid in offline artefact rejection, the participant's right pupil and corneal reflex was tracked using an EyeLink 1000 eyetracker (SR Research Ltd., Ottawa, Canada) with a sampling rate of 500 Hz. Gaze data was epoched into 30 s trials centered around stimulus onset. Trials in which participants had their eyes closed for more than 10 s were excluded from the MEG data analysis. The eyetracking output file from one experimental session was corrupted and could not be used for analysis.

6.2.5   MEG

Acquisition

Whole-head MEG data was acquired at a sampling rate of 1200 Hz using a 275-channel CTF system (CTF MEG International Services LP, Coquitlam, Canada). Four out of 275 channels were turned off due to excessive sensor noise. Twenty-nine additional reference channels were recorded for the purpose of noise rejection and the primary sensors were analysed as synthetic third-order gradiometers (Vrba and Robinson, 2001a). Participants were seated upright in the MEG system and were instructed not to move during the experiment. To minimise head motion, participants were stabilised using a neck brace and chin rest (Figure 6.3). All tDCS current-carrying wires were affixed to the MEG chair and neck brace to further reduce motion-related signal artefacts in the active tDCS condition.

Analysis

Analysis of MEG data was carried out using the FieldTrip toolbox (Oostenveld et al., 2011) and custom MATLAB scripts (v2015a, v2015b; The MathWorks Inc., Natick, MA, USA). Data was downsampled to 600 Hz for analysis.

Noise in the MEG signal during active and sham tDCS was characterised using the within-channel variance across time and the within-channel kurtosis. The metrics were calculated using sliding windows of 100 ms with 50 ms overlap to capture artefacts of short duration, averaged across channels and the maximal value across sliding windows was used to compare the two tDCS conditions.

For analysis, MEG data was cut into epochs containing 18 s of baseline followed by 20 s of visual stimulation. Data was band-pass filtered in the theta (6–9 Hz) and gamma

Figure 6.3: A participant seated in the MSR for tDCS-NIRS-MEG acquisition.

(30–90 Hz) bands. The time window used at further analysis steps was between 15 s pre-stimulus onset and 15 s post-stimulus onset.

The data was projected into source space using a Linearly Constrained Minimum Variance beamformer (LCMV, Van Veen et al., 1997) with a 6 mm isotropic grid in MNI space warped to each participant's MRI. Weights were calculated using the covariance matrix based on the entire time window (-15 s pre-stimulus onset to 15 s post-stimulus onset), which was combined with a single-shell forward model to obtain the spatial filter.

Source reconstruction was performed separately for the baseline (15 s pre-stimulus onset) and stimulus (15 s post-stimulus onset) time windows. These were used to identify the occipital voxel with the peak relative change from baseline in the theta and gamma bands, respectively. Virtual sensors were reconstructed at this location by multiplying the band-pass-filtered data with the beamformer weights. At this stage, single-trial virtual sensor timeseries were visualised and trials containing large artefacts were rejected. Trials marked as bad based on eyetracker data were also excluded (in total, an average of 2.25 ± 1.9 trials was excluded).

A time-frequency analysis was performed on the peak virtual sensor time course using the Hilbert transform between 2–96 Hz in steps of 0.5 Hz with a bandwidth of 4 Hz (theta) and 8 Hz (gamma). To compare conditions, the mean power over time and frequency was extracted for each stimulus contrast condition.

6.2.6   Head motion

Participants were fitted with fiducial coils at the nasion and preauricular points, which were localised relative to the MEG system at the beginning and end of each data acquisition run (10 Hz sampling rate). Head motion was calculated as the maximal difference between the end and start positions of the coils. Maximum displacement was 2 mm (M = 0.8±0.6) in the sham tDCS condition and 3 mm (M = 0.9±0.8) in the active tDCS condition (i.e., mean recorded head motion was within the measurement accuracy of the fiducial coils).

6.2.7   ECG

Electrocardiogram (ECG) was recorded with a sampling rate of 1200 Hz using two bipolar electrode pairs, with one electrode placed on the wrist and the reference electrode on the elbow bone on each arm. ECG data was downsampled to 600 Hz, standardised (z-scored) and trimmed to exclude missing or noisy data at the beginning and end of the recording based on visual inspection. A peak detection algorithm was applied using the *findpeaks* function in MATLAB (v2015a; The MathWorks Inc., Natick, MA, USA) to identify QRS complexes (Figure 6.4). No minimum peak threshold value was imposed, but peaks were required to be at least 0.5 s apart. Runs with excessive noise were excluded based on visual inspection; due to a hardware malfunction, these constituted 33% of acquired ECG data.

Heart rate was calculated by dividing the number of peaks detected within an epoch by the ECG epoch duration in minutes. This calculation was performed both for each run of continuous data (to compare the sham and active tDCS conditions), and for the baseline and stimulus time windows in each trial after epoching (to compare the stimulus ON and stimulus OFF conditions).

6.2.8   Respiration

An ML206 Gas Analyzer (ADInstruments Ltd, Oxford, United Kingdom) was used to monitor respiratory rate by recording end-tidal oxygen (O2) and end-tidal carbon dioxide (CO2) at a sampling rate of 1000 Hz. Respiration data from a single experimental session from a participant was excluded from analysis because the nasal cannula had partially slipped out of the participant's nose during the recording. CO2 traces were downsampled to 600 Hz and standardised. Peaks were identified using the same method as for ECG data. Peaks were required to exceed a z-score of 0.5 and to be at least 2.5 s apart; furthermore, spurious peaks were removed by requiring peaks and troughs to alternate (Figure 6.4).
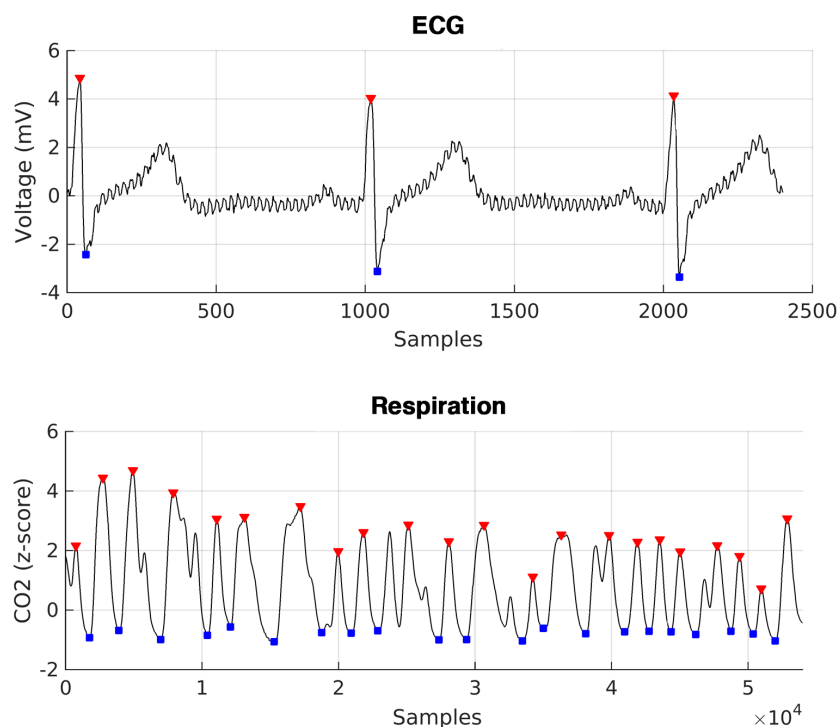
Figure 6.4: Examples of the peak detection algorithm applied to identify QRS complexes in the ECG signals (*top*) and peaks/troughs in the CO2 signal (*bottom*).

We calculated the respiration rate (number of peaks divided by epoch duration) and depth (mean peak-to-trough range) for the continuous data (active vs. sham tDCS). To check for stimulus-induced respiratory changes, we also cross-correlated the CO2 time course with a binary stimulus ON-OFF boxcar function. Cross-correlations were normalised and a maximum time lag of 1 s was used for physiological plausibility.

6.2.9 MRI

Similarly to the work discussed in Chapter 4, sequence parameters for the acquisition of structural MR images were based on the recommendations in Windhoff et al., 2013. Two T1-weighted and two T2-weighted contrasts were collected for each participant using a Siemens 3T Prisma scanner with a 64-channel head coil (Siemens Healthcare GmbH, Erlangen, Germany). Both T1- and T2-weighted images were collected to ensure good contrast between different brain and tissue compartments for subsequent segmentation. Both fat-suppressed and non-fat suppressed versions of the T1 and T2 scans were acquired. The T1 sequence was a 3D TurboFLASH sequence (sagittal acquisition; FOV 192 x 320 x 320; voxel size 1 mm isotropic) and the T2 sequence was a 3D Turbospin Echo (axial acquisition; FOV 256 x 256 x 96; voxel size 1 x 1 x 2mm, with a 1 mm gap to decrease the amount of fat shift in the slice selection direction).

6.2.10 Neuronavigation

Head locations were digitised based on individual structural MRI data using a Brainsight neuronavigation system (Rogue Research Inc., Montreal, Canada). Anatomical landmarks (Nz, LPA, RPA, tip of the nose), as well as the locations of the centre of each scalp electrode and NIRS optode were recorded.

6.2.11 NIRS

Acquisition

A Brainsight NIRS system (Rogue Research Inc., Montreal, Canada) was used to acquire NIRS data. The NIRS device was placed outside the MSR and 10 m fiberoptic cables were fed through the MSR waveguides to deliver near-infrared light. NIRS cables and optodes were free of ferromagnetic materials. Empty-room noise with and without the fiberoptic cables present in the MSR were recorded to verify that the NIRS equipment did not induce MEG signal artefacts.

The NIRS optode array was placed on the participant's head as described in Chapter 5. While the optodes of the Brainsight NIRS system have a comparatively low height of approximately 7 mm, the array must be expected to increase the distance between scalp and MEG sensors in the occipital area. Hair was parted to improve optode-scalp coupling. NIRS data was acquired using a sampling rate of 10 Hz. Light was emitted at 685 nm and 830 nm from a total of four source optodes and measured from eight photodiode detectors. To measure oxygenation changes in the blood vessels of the scalp, two additional "short separation" detectors were placed 10 mm to the left and right of the S1 and S4 optode, respectively.

A brief test recording was made before situating the participant in the MSR to ensure sufficient optode-scalp coupling and adjust session-specific NIRS acquisition parameters (i.e., laser power, detector gain and sensitivity). Optodes were covered with a dark cloth during this test to prevent stray light from entering the detectors. During data collection, signal interference from ambient light could be avoided, as participants were seated in the darkened MSR with the NIRS optode array fully inside the MEG dewar.

Analysis

NIRS data was analysed using the NIRS BrainAnalzIR toolbox (Santosa et al., 2018) and custom MATLAB scripts (v2015b, v2017b; The MathWorks Inc., Natick, MA, USA). Raw voltages were converted to oxygenated and deoxygenated hemoglobin concentrations using the Modified Beer-Lambert law with a partial pathlength factor (PPF) of 0.1 for both wavelengths.

A robust linear mixed effects model was constructed to evaluate the interaction between tDCS condition and stimulus contrast level. For each stimulus contrast level (i.e., 6.25%, 25%, 50%), the task-related hemodynamic response was modelled by convolving a boxcar function (Stimulus ON) with a canonical hemodynamic response function (HRF). A 3rd-order Legendre polynomial regressor was included in the design matrix to model slow signal drift. An autoregressive pre-whitening approach using iteratively re-weighted least-squares (AR-IRLS) was used to minimise serially correlated errors in the data resulting from physiological noise and heavy-tailed noise distributions due to motion artefacts (Barker et al., 2013). To account for signal noise from oxygenation changes in the blood vessels of the scalp, signals recorded by the two short separation channels were included as regressors.

Activation at the three different visual contrast levels for active vs. sham tDCS was compared using contrasts of estimated effects sizes, and evaluated using Student's t-tests. Multiple-comparisons were controlled for using a Benjamini–Hochberg FDR correction for the number of measurement channels (Benjamini and Hochberg, 1995).

6.2.12   Finite-element-modelling of tDCS

Electric fields induced by tDCS were simulated using ROAST v2.7.1. (Huang et al., 2019). Our approach was identical to the workflow described in Chapter 4 and outlined for ROAST in Figure 4.1.

Based on participant-specific MR scans, brain tissues (white matter, grey matter, CSF, skin, skull) were segmented automatically using the SPM12 toolbox (Penny et al., 2011) and touched up by morphological operations (Huang et al., 2013). The *cgalv2m* function in iso2mesh (Fang and Boas, 2009b) was used to generate a volumetric mesh for FEM. The digitised electrode locations recorded in the active tDCS session were simulated. Electrode thickness was set to the ROAST default value of 3 mm. Tissue conductivities were assigned based on the recommendations by Windhoff et al., 2013 (WM 0.126, GM 0.275, CSF 1.654, skull 0.010, skin 0.465, electrode 0.100, conductive gel 1.000 [S/m]). The finite-element models were solved for electric field distribution using GetDP (Geuzaine, 2007). We estimated mean electric field strength in the early visual cortex (V1, V2, V3v), as identified by the JuBrain Cytoarchitectonic Atlas (Amunts and Zilles, 2015; Amunts et al., 2007). As in Chapter 4, we rejected voxels in GM with field values greater than 0.8 V/m from further analysis. Across participants and ROIs, an average of 4.1±8.1% of voxels were omitted from analysis.

Electric field estimates were analysed using R v3.6.1/RStudio v1.1.463 (RStudio Team, 2016) and custom MATLAB scripts (v2017b; The MathWorks Inc., Natick, MA, USA).
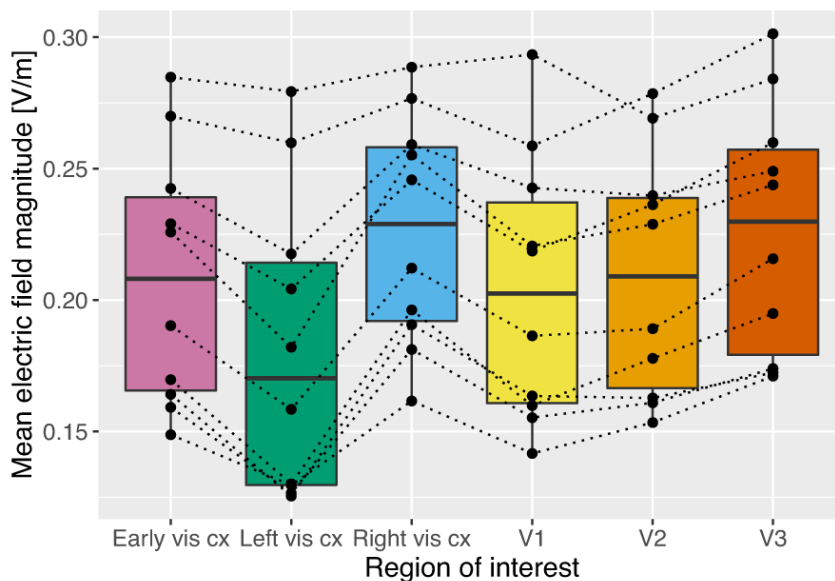
Figure 6.5: Mean electric field strength [V/m] in the visual regions-of-interest of ten pilot participants. Early visual cortex was defined as the combination of V1, V2 and V3v.

6.3 Results

6.3.1 tDCS-induced electric field magnitude

Structural MRI data from ten pilot participants was used for FEM of electric fields induced by tDCS. The distribution of mean electric field magnitude in our sample of pilot participants is shown in Figure 6.6. Mean electric field strength in the early visual cortex (V1, V2 and V3v) varied by up to 93% between participants (range: 0.15–0.29 V/m; Figure 6.5). The group average of mean electric field strength in the early visual cortex was 0.21 ± 0.05 V/m. Electric field magnitude was significantly higher in the right ($M = 0.23\pm0.06$) compared to the left hemisphere ($M = 0.18\pm0.04$), $t(9) = 6.74$, $p <$ .001, $r = 0.91$. This is likely due to the current entering via the anodal electrode at PO8 on the right side of the head.

6.3.2 ECG

Mean heart rate was 85.1 ± 6.4 bpm in the active tDCS condition and 79.0 ± 7.5 bpm in the sham condition. Mean heart rate was 80.8 ± 4.6 bpm during the stimulus OFF period and 80.2 ± 4.4 bpm during the stimulus ON period. Due to the small sample size ($N = 4$) and high data loss for ECG due to a hardware malfunction, no statistical tests were carried out. An examination of Figure 6.7 suggests that heart rate likely did not differ systematically across stimulation conditions.
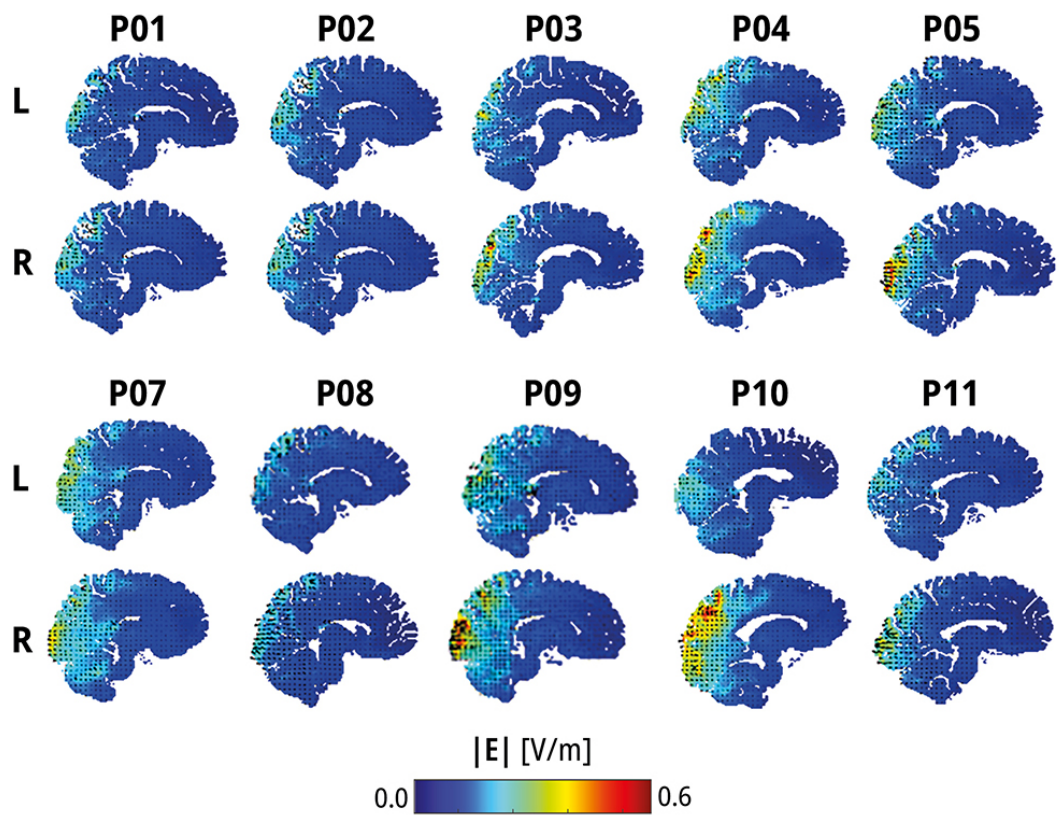
Figure 6.6: Distribution of mean electric field strength [V/m] induced by tDCS applied via electrodes at EEG positions PO7 (cathode) and PO8 (anode). Sagittal cuts slightly to the left (top) and right (bottom) the midline are shown for ten pilot participants.
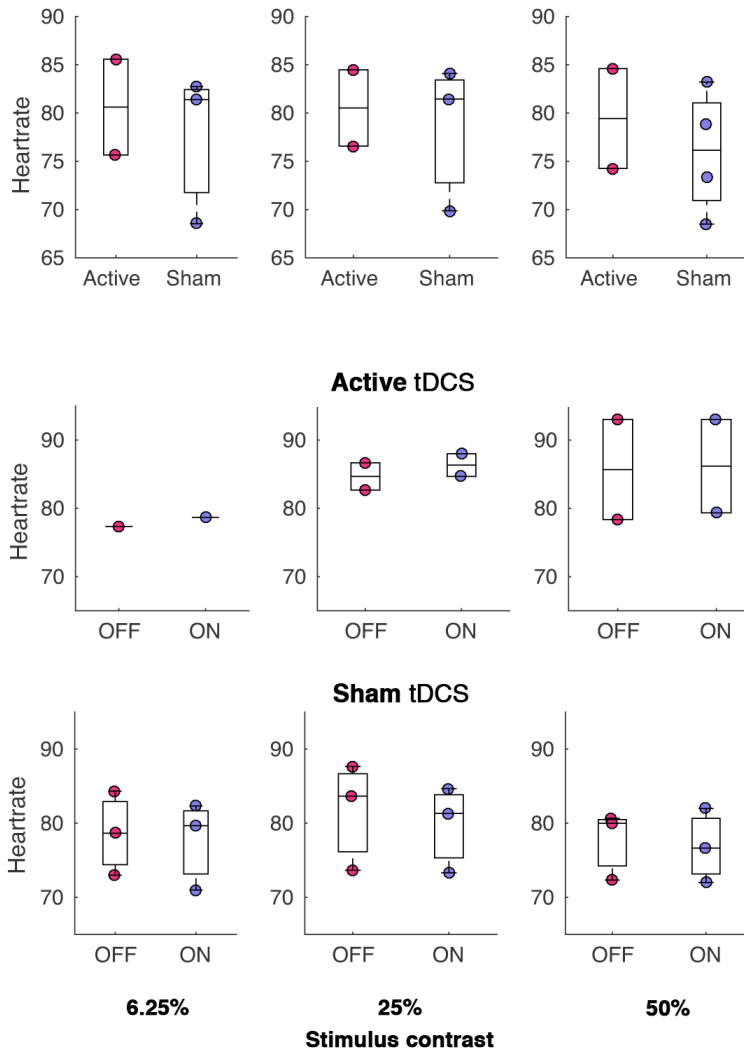
Figure 6.7: Heart rate [bpm] at different stimulus contrast levels for active vs. sham tDCS (top row) and for visual stimulus ON vs. OFF (bottom rows).
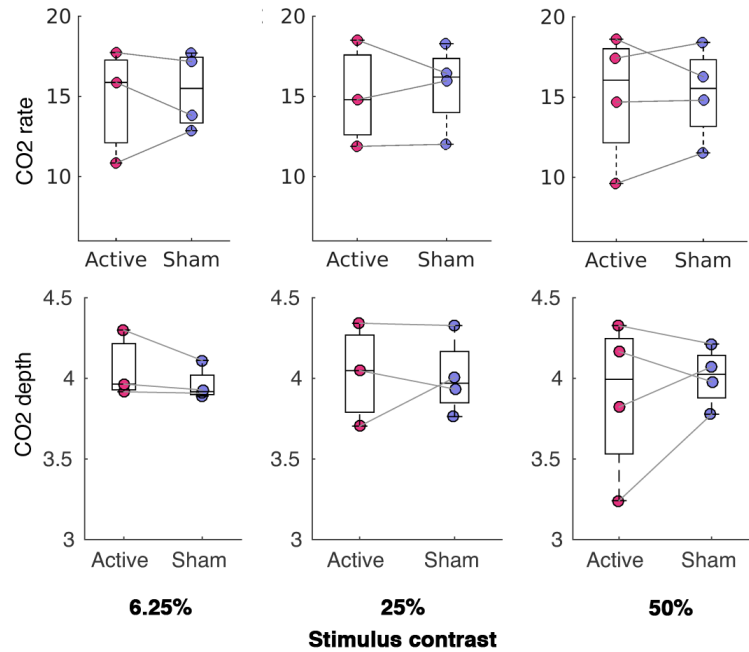
Figure 6.8: CO2 rate and depth during active vs. sham tDCS.

6.3.3 Respiration

Mean respiration rate was 15.0±3.3 in the active tDCS condition and 15.4±2.6 in the sham condition. Mean respiration depth was 3.5±1.1 in the active tDCS condition and 4.0±0.2 in the sham condition (Figure 6.8). Group average cross-correlation of the CO2 time series with a binary stimulus ON-OFF boxcar function was -0.002±0.011 for active tDCS and -0.004±0.011 for sham tDCS. These results indicate that respiration did not vary systematically for active and sham tDCS, and that stimulus onset did not modulate respiratory rate.

6.3.4 MEG: Noise during active and sham tDCS

Examinations of the within-channel variance and kurtosis indicated that noise was increased in the active tDCS condition (Figure 6.9). Initial sensor-level analysis of the MEG data showed prominent artefacts in occipital sensors during active but not sham tDCS (Figure 6.10). The topography of average variance within channels is consistent with current-carrying wires running from the scalp electrodes at EEG positions PO7 and PO8 to the back of the participant's neck and out of the MEG dewar. The artefacts visible at frontal sensors for P05 in both tDCS conditions are likely due to the participant's dental wire.
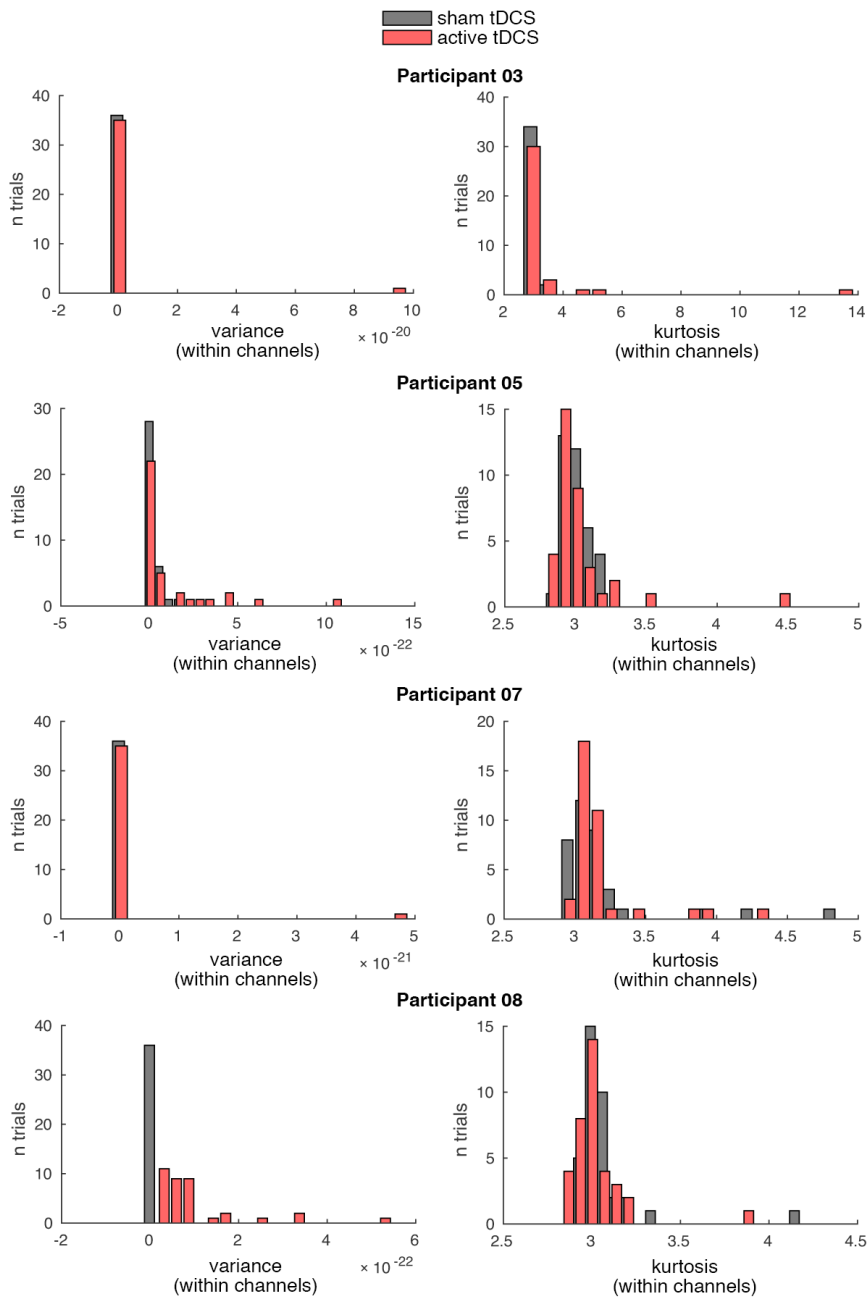
Figure 6.9: Variance and kurtosis within MEG channels for active vs. sham tDCS.
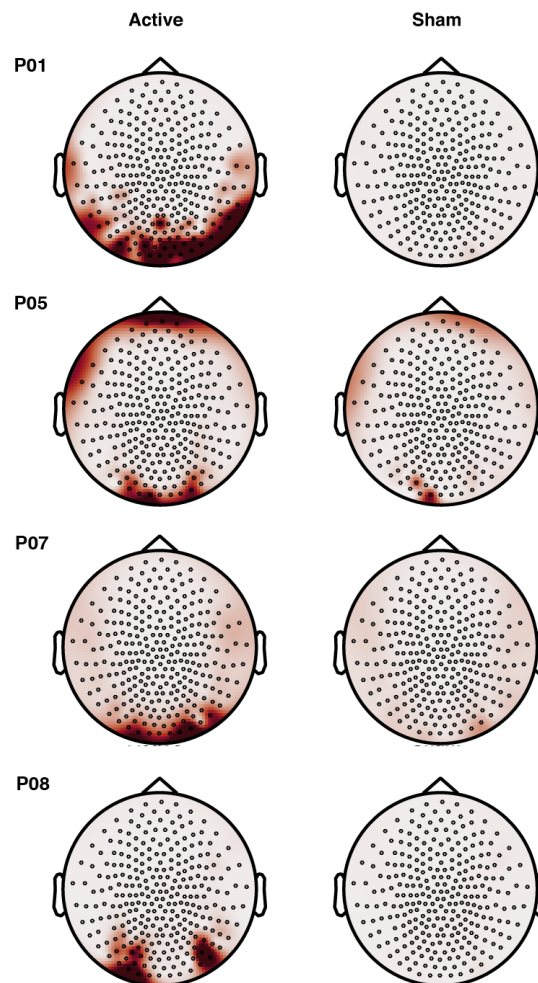
Figure 6.10: Topography of variance within channels during visual stimulation for active vs. sham tDCS. Note that Participant 05 was wearing a dental wire.

	tDCS	6.25%	25%	50%
HbO	active	2.03(1.43)	1.49(1.60)	2.25(2.50)
	sham	2.01(3.26)	0.43(3.55)	3.29(2.51)
HbR	active	-0.63(0.78)	-0.85(0.70)	-1.29(0.70)
	sham	-0.99(0.85)	-0.38(3.56)	-0.60(0.91)

Table 6.1: Mean(SD) of global mean beta for oxyhemoglobin (HbO) and deoxyhemoglobin (HbR) concentration for increasing visual stimulus contrast.

6.3.5 MEG: tDCS effects on theta and gamma power change

During sham tDCS, we observed a trend towards increased average theta and gamma power change in response to increasing stimulus contrast on the group level (Figures 6.11 and 6.12). For both frequency bands, oscillatory activity was focused in the occipital pole. Overall, this indicates that it is feasible to record MEG at occipital sensors despite the increased scalp-sensor distance caused by the NIRS optode array.

During active tDCS, a similar trend was observable for average gamma power change (Figure 6.12). However, the trend was less evident for the theta band (Figure 6.11), which may, in part, be due to the greater inter-individual variability in oscillatory response to increasing stimulus contrast — also evident during sham tDCS (Figure 6.13). Moreover, physiological noise is likely to more strongly affect frequency bands below 10 Hz.

As illustrated in Figures 6.11 and 6.12, average relative power change was decreased during active compared to sham tDCS for both frequency bands (theta: M_{active} = 12.36±8.5 vs. M_{sham} = 15.16±11.9; gamma: M_{active} = 9.25±6.71 vs. M_{sham} = 15.15±8.82). However, due to the extremely small sample size (N = 4), no statistical tests of significance were carried out.

6.3.6 NIRS: tDCS effects on oxy- and deoxyhemoglobin

We compared oxy- and deoxyhemoglobin concentration for active vs. sham tDCS at each stimulus contrast level (*cf.* Figure 6.14). Group averages of global mean beta (i.e., beta across all measurement channels) for both hemoglobin measures are given in Table 6.1.

Source-detector pairs with a significant change in activation for active compared to sham tDCS are listed in Table 6.2. However, after FDR correction for multiple comparisons, the only significant difference between the anodal and sham conditions was found for deoxyhemoglobin measured by source-detector pair 2–7 at the 25% contrast level, $t(42)$ = -3.78, p < .001.
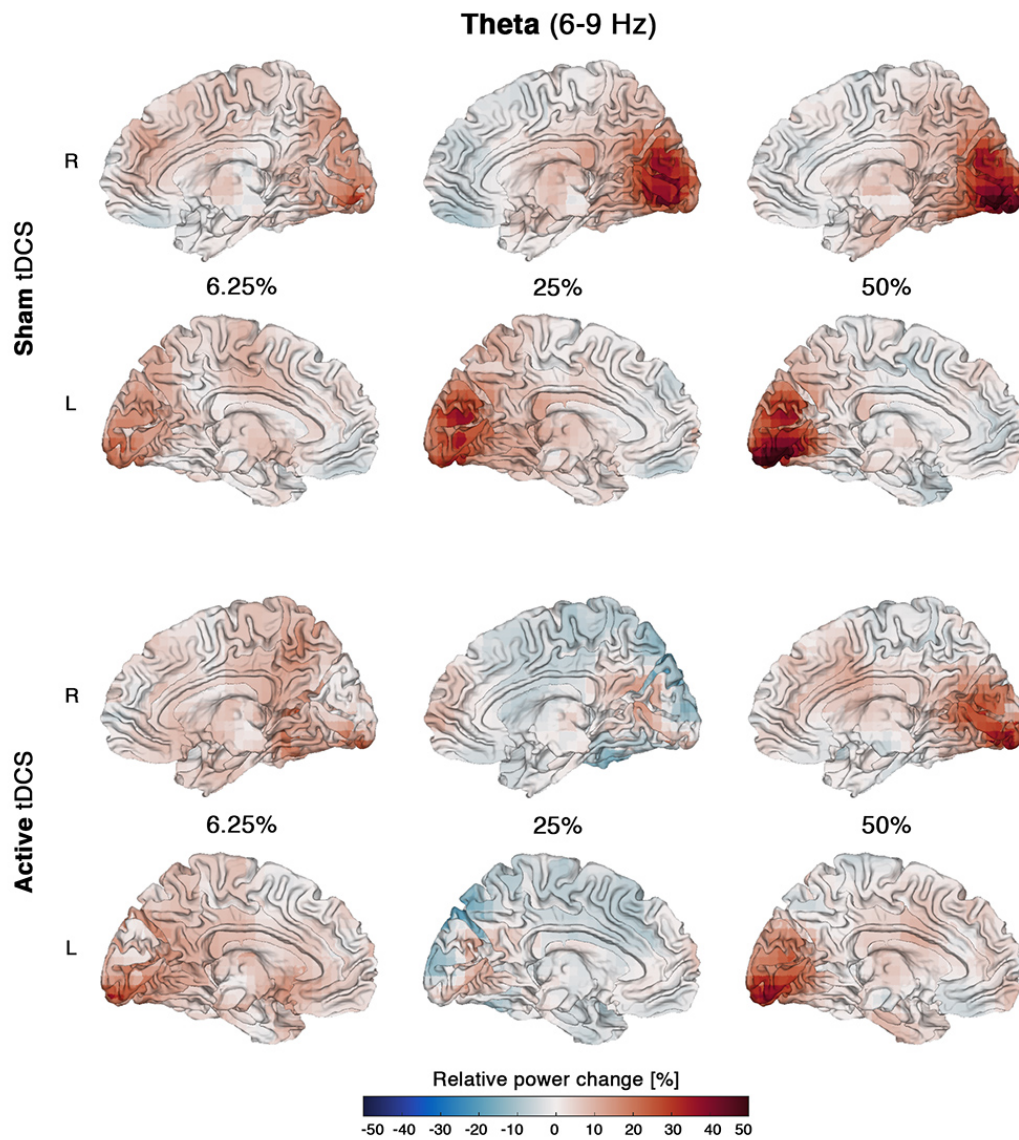
Figure 6.11: Group average of relative change in mean theta (6–9 Hz) power [%] in response to visual stimuli at increasing contrast levels (6.25%, 25%, 50%) during sham and active tDCS.

HbO/HbR	S–D	Contrast	t(42)	p
HbR	1–1	25%	-2.05	.046
HbR	3–6	6.25%	2.11	.040
HbO	1–6	50%	-2.30	.027
HbO	2–2	6.25%	2.85	.007
HbO	**2–7**	**25%**	**-3.78**	**.000**
HbO	2–7	50%	-2.42	.020
HbO	3–3	25%	3.24	.002
HbO	4–4	25%	2.19	.035
HbO	4–7	6.25%	-2.80	.008

Table 6.2: Channels (i.e., S-D pairs) with significant change in haemoglobin concentration for active vs. sham tDCS before FDR correction for multiple comparisons was applied. Only the channel highlighted in bold remained significant after Benjamini-Hochberg correction.
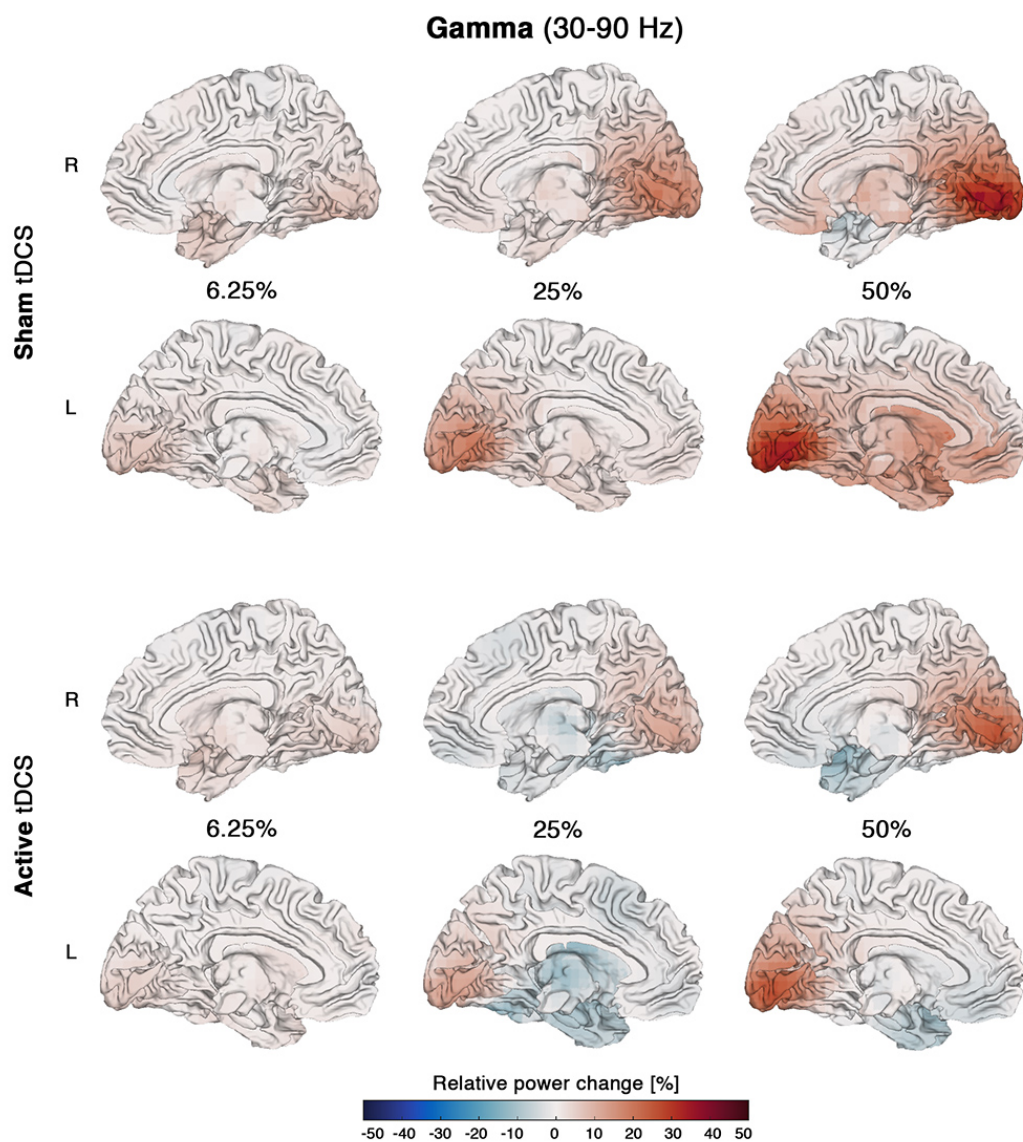
Figure 6.12: Group average of relative change in mean gamma (30–90 Hz) power [%] in response to visual stimuli at increasing contrast levels (6.25%, 25%, 50%) during sham and active tDCS.
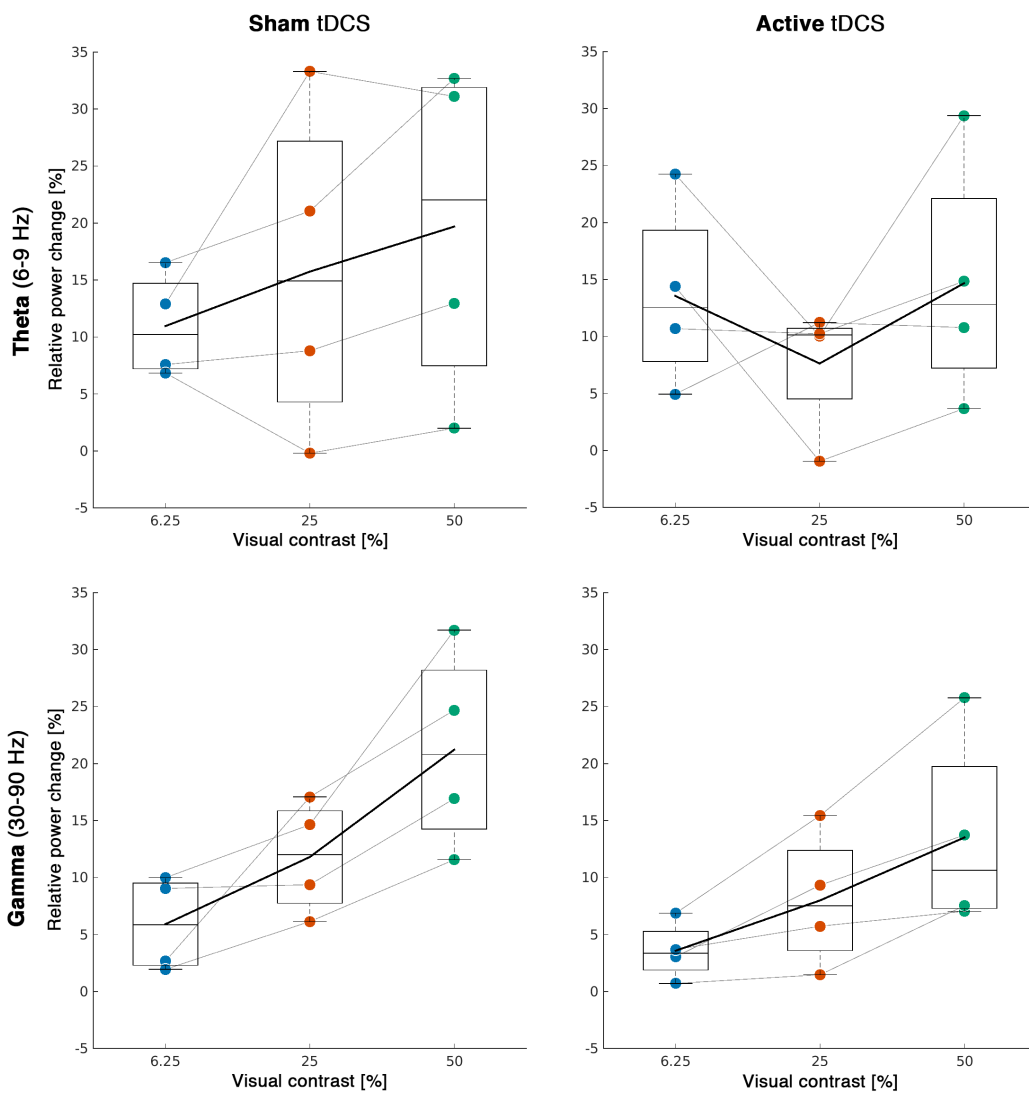
Figure 6.13: Inter-individual variability in average gamma (30–90 Hz) and theta (6–9 Hz) power change from baseline at increasing visual stimulus contrast.
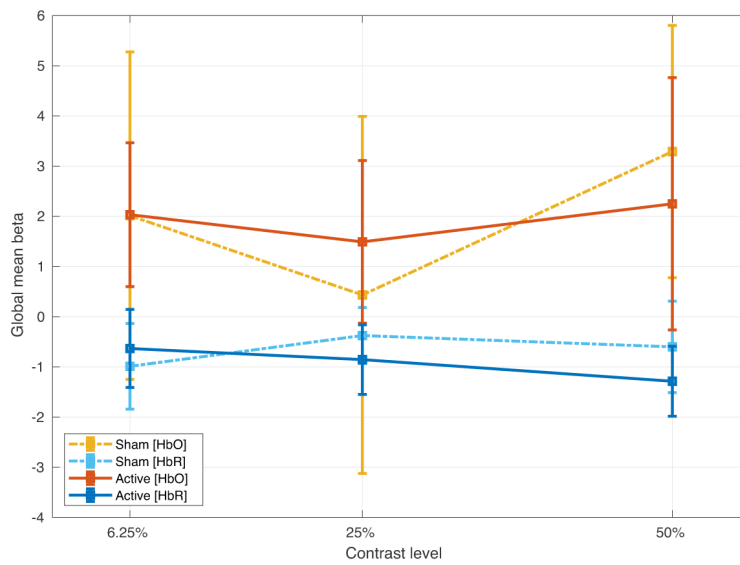
Figure 6.14: Group averages of relative oxy- and deoxyhemoglobin concentration changes across all measurement channels (global mean beta) at increasing stimulus contrast levels.
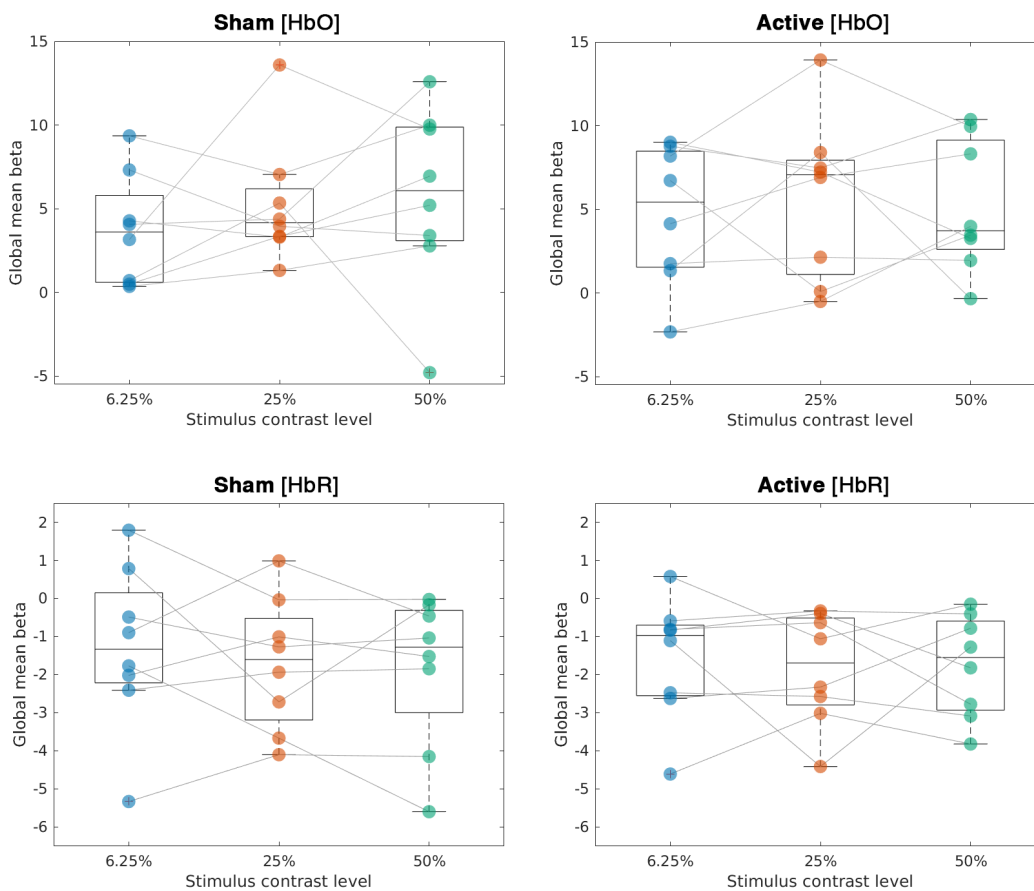
Figure 6.15: Inter-individual variability of oxy- and deoxyhemoglobin concentration changes (global mean beta) at increasing stimulus contrast levels.

6.4 Discussion

In this technical pilot study, we explored the feasibility of acquiring concurrent NIRS-MEG during tDCS of the visual cortex. We evaluated tDCS effects on oscillatory and hemodynamic responses to pattern-reversing checkerboard stimuli with different visual contrasts (6.25%, 25%, 50%). Direct current stimulation was applied to the occipital cortex via electrodes at PO7-PO8 and the induced electric field strengths were modelled for ten pilot participants.

Contrary to previous reports in the literature (Kashou and Giacherio, 2016; Schroeter et al., 2004; Wijeakumar et al., 2012), we found no evidence of increased stimulus-induced change in either oxy- or deoxyhemoglobin concentration with increasing stimulus contrast. In our sample of eight pilot participants, we also did not observe any significant effects of active tDCS on hemoglobin concentrations when compared to sham tDCS.

However, it is worth noting that we have taken a very conservative approach to multiple comparisons correction here; a follow-up data analysis could improve power by correcting comparisons for HbO and HbR at each stimulus contrast level separately. Furthermore, our current statistical model did not include the co-recorded ECG and respiration signals as regressors. It may also be worthwhile to evaluate concentration changes in the left and right hemispheres separately, as some previous studies have highlighted a response bias towards the left hemisphere for NIRS of the visual cortex (Colier et al., 2001b; Toronov et al., 2007; Wylie et al., 2009).

A further limitation of our NIRS data analysis is the lack of NIRS forward models based on participants' individual structural MR scans. As detailed in Chapter 5, we were forced to rely on scaling a template brain to the sizes of our three exemplar participants to subjectively explore the sensitivity of our proposed optode array. However, in the current chapter, we were also limited by the lack of availability of software tools to allow *inverse* modelling of the location and magnitudes of the generators of the NIRS signal in "brain-space". These kinds of analyses could not be performed on our data set due to unaddressed software issues in the AtlasViewer/NIRS Brain AnalyzIR toolboxes.

As we could not transform our NIRS data at the participant level from "channel space" to "brain space", we were also stymied in our ability to explicitly address the variability in our results. We were unable to combine our NIRS data across participants into a common anatomical space defined by a template brain — an approach that dominates group analyses of fMRI data — and thus we observed considerable inter-individual variability for stimulus-induced hemoglobin concentration changes. However, the relatively low SNR of NIRS compared to fMRI can result in modality-specific issues in power. Low inter- and intra-individual reliability has been reported

in previous NIRS studies of the visual cortex (Kashou and Giacherio, 2016; Minati et al., 2011), and it has been suggested that, to obtain equal power for a group comparison using parametric statistics, the sample size for NIRS must be doubled compared to fMRI experiments (Minati et al., 2011).

It is also worthwhile to mention that while we employed a fixation dot colour-change task to promote a constant level of attention throughout data collection and short breaks were taken between runs, several participants commented that they had difficulty remaining alert during data acquisition. A decreased level of alertness may have reduced stimulus response.

On a related note, participants did not receive explicit instructions regarding the consumption of caffeine prior to data acquisition. Caffeine may increase heart rate, metabolism and vasoconstriction — in turn, decreasing CBF and diminishing neurovascular coupling (Pelligrino et al., 2010). Under some circumstances, caffeine consumption could therefore increase the difficulty of obtaining reliable NIRS signals. Future studies may thus consider a restriction on caffeine ingestion.

In principle, it may be more effective to target the visual cortex with HD-tDCS during concurrent acquisition of NIRS. This would allow further optimisation of both the electrical stimulation and NIRS sensitivity by more flexibly interleaving electrodes and optodes. In particular, with respect to issues pertinent to NIRS, signal loss in channels crossing the superior sagittal sinus could then be avoided. However, if the goal is to combine tDCS-NIRS with simultaneous MEG, the additional current-carrying wires required for HD-tDCS would likely considerably increase signal artefacts for MEG.

In contrast to our NIRS findings, however, much of our MEG data replicated previous findings from the literature (e.g., Stickland et al., 2019). We did observe the expected trend towards an increase in stimulus-induced average theta and gamma power with visual contrast during sham tDCS. A similar relationship was evident for average gamma power during active tDCS, but less pronounced for the theta band. This may be explained by slow-frequency physiological and movement-related noise primarily affecting the lower frequency bands, in particular during active stimulation. Our results suggest that simultaneous NIRS-MEG of the visual cortex is feasible using the Brainsight NIRS system, particularly if no electrical stimulation is applied. Signal strength at occipital MEG sensors was sufficient to detect systematic activity changes in the visual cortex despite the increased source-sensor distance introduced by NIRS optodes.

Similarly to our exploration of empirical and modelling data in Chapter 4, we analysed finite-element models of tDCS-induced electric fields in ten of our pilot participants. The results suggest high inter-individual variance, with mean field strength in the early visual cortex varying by up to 93% between participants. Spatially, for all participants the electric field was largely focused in the parieto-occipital cortex,

but we observed a large range of mean field strength in our participants, with the lowest values perhaps suggesting that tDCS-induced polarisation may have been sub-threshold for modulating neuronal function. For 1.5 mA current input, models created with ROAST (v2.7.1, Huang et al., 2019) estimated the group average of mean electric field strength to be 0.21 V/m in our combined ROI of V1, V2 and V3v. In comparison, FEM constructed with SimNIBS (v2.0.1; Windhoff et al., 2013) in three pilot participants suggested a group average field strength of approximately 0.38 V/m for the occipital cortex (*cf.* Chapter 5). However, it is important to draw attention to key differences in how we defined the visual ROI in these two modelling pipelines. Furthermore, discrepancies between estimates calculated with ROAST v2.7.1 and SimNIBS v2.0.1 are likely partially due to divergent MRI segmentation approaches (see Huang et al., 2019 for detailed discussion)

Overall, the small sample size in this technical pilot study — in particular for MEG — limits our conclusions in regard to systematic changes in brain activity. We found that the experimental set-up posed a comparatively high burden on both participants and experimenters. The duration of a typical tDCS-NIRS-MEG acquisition session was 4–5 hours, with the participant present for 3–4 hours (excluding MRI data acquisition). Our multimodal data acquisition, which also encompassed the recording of separate signals for ECG, O2/CO2 rate, eyetracking and head motion, led to a relatively high rate of data loss. Experimenters aiming to use these co-recorded signals in a comprehensive artefact removal pipeline must consider that low-quality or missing data sets in any one modality will hamper analysis of other signals. For example, in the present pilot study, a large proportion of ECG traces was unusable due to hardware malfunction. This severely limited our ability to explore systematic changes in heart rate. For analysis of MEG signals, it is, however, crucial to ascertain that visual stimulation did not modulate participants' systemic physiological states (e.g., heart or respirator rate) — only then can one assume that tDCS-induced artefacts are comparable between periods of visual stimulation and baseline (Noury and Siegel, 2018).

Recorded head motion was minimal, suggesting that the use of a neck brace and chin rest was useful. In addition, the electrode-optode hardware likely further stabilised head motion by reducing the space between the head and the MEG dewar. Continuous head localisation throughout data acquisition would have been preferable to monitor head motion more closely for artefact removal. This was not feasible in this pilot study due to a malfunction of the CTF acquisition software, but would be recommended for future tDCS-NIRS-MEG studies.

In conclusion, we observed the expected activation changes with increasing visual contrast only for MEG but not NIRS signals. We found no significant effects of active compared to sham tDCS on either oscillatory or hemodynamic responses. However, the sample size of this technical pilot study was very small, limiting statistical analyses.

Our findings suggest that simultaneous NIRS-MEG of the visual cortex is feasible, but that NIRS data acquisition may be more vulnerable to inter-individual differences. For concurrent tDCS-NIRS-MEG, the co-recording and analysis of signals monitoring changes in physiology and movement is required to address open questions regarding the removal of tDCS-induced MEG artefacts. However, the complexity of the required hardware set-up, particularly the co-recording of physiological and movement signals, increases susceptibility to data loss, which should be taken into account when considering samples sizes in future tDCS-NIRS-MEG studies. Researchers interested in investigating the effects of *offline* tDCS could benefit from the use of concurrent MEG-NIRS without suffering a loss of data quality due to stimulation-related signal artefacts. Finally, it is worth reiterating that the difficulty of implementing double-blind study designs for concurrent tDCS-MEG poses constraints on the interpretation of future studies.

Chapter 7

General Discussion

The work presented in this thesis addressed a number of methodological challenges affecting studies investigating the neurophysiological basis of tDCS. Following on from early landmark studies in the motor system (Nitsche and Paulus, 2000, 2001; Priori et al., 1998), research in the field has been strongly biased towards the motor domain over the past two decades (Horvath et al., 2014; Jacobson et al., 2011).

Here, experiments focused on the visual system, based on the fact that vision has been extensively studied in neuroscience, and its structural and functional underpinnings are therefore comparatively well-characterised. In particular, the cellular correlates of stimulus detection and discrimination have been widely examined, with research in both humans and animals identifying the essential role of the primary visual cortex (e.g., Glickfeld et al., 2013; Lashley, 1943; Weiskrantz et al., 1974; Weiskrantz, 1996). Experimental tasks based on such low-level visual functions are relatively unaffected by top-down feedback from higher fronto-parietal areas, and the simplicity of these paradigms results in less cognitive confounds, such as working memory or task comprehension (Hanck et al., 2012). Accordingly, several previous double-blind, sham-controlled studies have investigated tDCS outcomes in the visual cortex, and have reported significant stimulation effects on contrast sensitivity (Antal et al., 2001; Behrens et al., 2017; Costa et al., 2015a; Kraft et al., 2010; Reinhart et al., 2016). Building on these previous approaches, work presented in this thesis aimed to bring together behavioural and neuroimaging data, as well as findings from participant-specific models of tDCS-induced electric fields, to further explore the use of tDCS for modulating visual function in healthy humans.

We first addressed the question of sham control for tDCS. Researchers in the field have increasingly adopted randomised, sham-controlled designs, and tDCS studies now typically compare experimental outcomes for verum (i.e., active) and sham (i.e., placebo) stimulation. In doing so, "active sham" stimulation protocols, in which tDCS is applied for a brief period to mimic verum stimulation, have become standard practice (Bikson et al., 2018; Brunoni et al., 2011; Gandiga et al., 2006; Woods et al., 2016). However, while such "FSF" sham protocols are now widely used, their efficacy is rarely

evaluated explicitly. Recent studies have cast doubt on the robustness of blinding participants with FSF protocols — at least, for certain stimulation parameters (Fonteneau et al., 2019). However, the factors influencing blinding robustness have not yet been fully identified.

In Chapter 2, we therefore compared two different current waveforms in the context of sham control for subsequent experimental work, where stimulation was applied to the occipital cortex at 1.5 mA. Our findings indicated that both a single-ramp/FSF protocol and a protocol with a second ramp at the end of the tDCS session — a "double ramp" — were successful at blinding experimenters. We found that the double ramp waveform was also effective for masking the stimulation condition from participants. In contrast, our results from the widely used "single ramp"/FSF sham protocol were somewhat more complex, with the significance of its efficacy dependent on our underlying assumptions about participants' chance level of guessing the tDCS condition. This highlights an important issue for placebo-controlled research, namely the current lack of standardised approaches for assessing blinding efficacy. In particular, studies employing within- or between-subjects designs with repeated-measures are faced with challenges in evaluating blinding strategies. Moreover, the nature of placebo — and nocebo — effects is a widely debated question that reaches far beyond tDCS to the wider clinical research community (Benedetti, 2014a; Burke et al., 2019; Finniss et al., 2010; Hróbjartsson and Gøtzsche, 2010).

For tDCS, as a non-pharmacological, device-based intervention, the concept of "differential placebo effects" (i.e., the notion that different types of placebos may lead to placebo effects of different strengths), may be particularly important (Boutron and Ravaud, 2011; Burke et al., 2019; Kaptchuk et al., 2000). At present, we cannot exclude the possibility that "active sham" protocols, such as investigated here, lead to particularly pronounced placebo effects, thereby confounding comparisons with verum tDCS. To address this, sham-versus-sham tDCS studies are needed.

Furthermore, current efforts to reorient tDCS research towards large cohort studies also mean that multi-center studies will likely become more common. To avoid difficulties in comparing results, it will therefore be essential to develop rigorous protocols for sham tDCS, including the detailed co-ordination of stimulation parameters, participant informed consent procedures and experimenter-participant interaction across research centres (Fonteneau et al., 2019).

Many questions remain to be addressed, including: the role — and indeed existence of — the Hawthorne effect (McCambridge et al., 2014); the robustness of sham control in single vs. multi-session tDCS studies; and the best strategy for blinding offline vs. online tDCS. But whichever of these issues ultimately turns out to be the most important, it seems obvious that the tDCS field would greatly benefit from the routine assessment of blinding efficacy in all studies. It is therefore perhaps incumbent upon

researchers to insist not only on the comprehensive reporting but also the explicit evaluation of sham protocols as part of the peer-review process.

In accordance with these arguments, we also assessed blinding robustness in the double-blind, sham-controlled experiments presented in Chapter 3, which concentrated on the use of different electrode montages for stimulating the visual cortex.

As noted above, our decision to use a simple *sensory* experiment as a "probe" of tDCS effects was motivated by the need to obtain more empirical data on tDCS's effectiveness beyond the motor cortex. From the beginnings of the modern era of tDCS (e.g. Nitsche and Paulus, 2000), new experimental approaches have tended to use changes in the amplitude of TMS-evoked MEPs to assess the efficacy of a given experimental paradigm. As the major source of efferent outputs from the brain, M1's main advantage is its link to a quantitative metric of its "excitability" — MEP amplitude. However, M1's uniqueness is also a distinct disadvantage — the outputs of the majority of other cortical areas in the mammalian brain are to other cortical areas, not to extra-cephalic targets. This means that using M1 as an index of the effects of tDCS on the brain in general is likely to lead to erroneous conclusions, and so for our empirical investigations we chose a simple sensory paradigm that would evoke observable behaviour from our participants.

Similarly to the small number of previous studies in this area, we assessed tDCS effects on contrast sensitivity at central and peripheral visual field locations. In two groups of healthy participants, we targeted the visual cortex either via electrodes placed at Oz-Cz or PO7-PO8. However, in contrast to previous reports, we failed to observe effects of tDCS on contrast detection thresholds regardless of electrode montage. As an alternative outcome measure, we also evaluated psychometric function slope and found that tDCS only modulated slopes when delivered via the Oz-Cz electrode montage. Furthermore, anodal verum stimulation via the Oz-Cz electrode montage and verum tDCS via the P07-PO8 montage both had a deleterious effect on participants' response times.

The lack of significant stimulation effects in our perimetry study may be due to a number of different factors. Firstly, the issue of the appropriate sample size for a given tDCS study is still a matter of disagreement between investigators and labs. Our sample size here was influenced by similar studies investigating tDCS effects in a superficially identical context, using automated perimetry to measure participants' contrast detection thresholds. However, like many other areas in psychology and neuroscience currently, tDCS studies are not immune to the "replication crisis" (Minarik et al., 2016), and due to publication bias, effect sizes in single studies carried out with small samples might be substantially overestimated. Yet, contrary to other widely-reported meta-analyses of the tDCS field (Horvath et al., 2014, 2015), Minarik and colleagues note that meta-analyses can suffer from similar biases if null-results

from studies with very small sample sizes are included.

Finally, putting aside issues arising from insufficient sample sizes or differences in analysis methodologies, it is currently an open question as to *when* to best apply tDCS in a given experiment. Early animal work on the effects of DC stimulation directly to the cortical surface in animals (e.g., Bindman et al., 1964) suggested that any modulation of neuronal activity thus caused would be long-lasting (persisting for 30 minutes at a minimum). As a consequence of these seminal studies, the idea of applying tDCS *before* a given experimental manipulation and relying on the longevity of its changes in neuronal function is still common across the tDCS literature. However, in parallel to this school of thought, the existence of associative learning and cellular mechanisms of plasticity that rely upon the pairing of modulation *and* stimulus processing has led many researchers to apply tDCS in tandem with their experimental paradigm. This was the approach that we used here, and it is currently unclear if adopting this "online" approach to tDCS is more or less effective for our particular paradigm than using an "offline" design. Perhaps more importantly, while accepting our caveats about the conclusions of the meta-analyses of Horvath and colleagues (Horvath et al., 2015), one of the least controversial conclusions of this work was that single-session tDCS seemed to be an under-powered approach to eliciting neuromodulation. It remains to be seen if our paradigm could be used as part of a perceptual learning experiment run with stronger effects in tDCS sessions over several days. Such an approach has proved effective in the motor system; however, it is an open question as to its utility for the rest of the brain.

The lack of significant results in our behavioural paradigm may, however, also be due to factors unrelated to our experimental design and sensory stimulation. Due to its anatomical morphology — on both a fine and gross scale — the visual cortex may be a particularly difficult brain region to target with tDCS, rendering individually-tailored stimulation approaches especially important for achieving reliable effects in visual experiments. Finite element modelling studies of tDCS have suggested that inter-individual differences in head anatomy likely confound group-comparisons of tDCS outcomes (e.g., Laakso et al., 2015; Opitz et al., 2015). However, to date, only a small number of studies have combined evidence from behavioural or neurophysiological experiments with results from modelling. Moreover, several different software pipelines for FEM of tDCS are currently available and their comparative accuracy in simulating induced electric fields has not yet been established.

In Chapter 4, we therefore presented work in which we simulated electric fields using two open-source FEM pipelines, SimNIBS and ROAST, and attempted to relate field estimates to the behavioural outcomes discussed in Chapter 3 (Experiment 1).

Although we created participant-specific head models for FEM, we found no correlation of estimated E-field strength in the early visual cortex and modulations in behavioural performance induced by anodal vs. sham tDCS. Our comparison of ROAST and SimNIBS pointed to a good overall agreement between their estimates of both E-field spread and strength, with the latter also broadly in line with previous findings from *in vivo* studies.

Two other studies recently combined electric field simulations with the measurement of MEPs and RMTs and, in contrast to our work, did find a significant relationship (Laakso et al., 2019; Mikkonen et al., 2018). However, their outcome measures, segmentation/FEM approaches and analysis strategies differed considerably from ours. Nonetheless, our collective findings point to numerous methodological and conceptual issues that need to be clarified in future tDCS-FEM studies. For example, currently some level of manual input is always required in the segmentation of MR images, and it is difficult to objectively assess segmentation accuracy, on the one hand, and to avoid subtle errors, on the other hand (Nielsen et al., 2018). Moreover, as noted previously, uncertainty remains in regard to the conductivity of different brain tissues, particularly for the skull. The impact of different parameters values for FEM still needs to be explored (but see Saturnino et al., 2019 for a recent effort in this regard.)

Above all, it remains a complex question as to exactly how strongly and which cells in the grey matter need to be polarised to reliably elicit behavioural effects in humans. Ultimately, estimates of electric field strength are only one factor in the accurate prediction of tDCS effects. The excitability of neurons, or indeed other components of the neuro-vascular unit depends on their morphology and electrophysiological properties, as well as their position within and orientation relative to the induced E-field. Most likely, neither electric field strength nor direction can fully explain the effects of tDCS on an individual level. Finite element models simulate the brain as a passive volume conductor, ignoring the complex excitable electrical properties of cells in brain tissue. Neuronal activity as an internal current source is not captured by current FEM approaches, but must be expected to interact dynamically with transcranially applied electrical fields. Thus, functional outcomes of tDCS likely cannot be fully understood without considering network architecture and ongoing brain activity. In this vein, Rahman et al., 2017 recently hypothesised that tDCS' lack of spatial specificity leads to the polarisation of afferent neurons in upstream cortical areas which can modulate activity in a target brain region.

This hypothesis — that a full appreciation of tDCS' effects requires the sampling of neuronal activity beyond the areas under each electrode — seems particularly suited to the application of functional neuroimaging in humans. In particular, acquisition of data from multiple imaging modalities within a single study — while imposing certain limitations on study design — can provide insight above and beyond a given method

in isolation. Consequently, in Chapters 5 and 6 we explored the concurrent use of NIRS and MEG during tDCS targeting the visual cortex. While MEG offers a highly time-resolved window into the brain's electrophysiological activity, NIRS has a unique advantage over other neuroimaging techniques: electrical stimulation does not introduce noise in its optical signal. However, experiments combining online tDCS with NIRS-MEG must overcome several technical challenges.

In a pilot analysis of three participants (Chapter 5), we assessed a potential electrode-optode layout for tDCS-NIRS. Modelling results suggested that sufficient NIRS measurement sensitivity could be achieved with our proposed NIRS optode array while accommodating scalp electrodes for tDCS. FEM of electric field distributions indicated that our bilateral electrode montage could be expected to effectively polarise at least a subset of neurons in visual cortex — but that this same montage may not have similar effects on glial cells.

We then investigated the technical feasibility of acquiring NIRS-MEG data during simultaneous application of tDCS (Chapter 6). Previous proof-of-principle studies suggested that tDCS-induced MEG signal artefacts can be attenuated through the use of beamforming (Garcia-Cossio et al., 2015; Hanley et al., 2015; Marshall et al., 2015; Soekadar et al., 2013), although at present there exists no consensus on the influence, evaluation and removal of non-linear artefacts induced by systemic physiology and head movements (Neuling et al., 2015; Noury and Siegel, 2017, 2018; Noury et al., 2016).

We recruited a pilot sample of 15 participants, but suffered a high rate of participant and data attrition due to the complexity of our experimental set-up, in particular caused by our requirement of co-recording participant physiological and head movement signals. However, our analyses of the remaining good quality data within our pilot cohort demonstrated that simultaneous NIRS-MEG of the visual cortex is indeed feasible. Although participant-specific FEM models suggested that our electrode montage successfully focused the electric field in the occipital cortex, we failed to find significant effects of tDCS on hemodynamic or oscillatory responses — a result that is perhaps not surprising given the small sample size as a result of participant attrition.

Our findings also indicated that NIRS signals were more affected by inter-individual variability — whether this was due to true neurophysiological effects or related to inter-individual factors influencing NIRS data quality remained unclear. The poor quality of co-recorded physiological signals severely hampered the analysis of MEG data acquired during active tDCS. Similarly, our NIRS data analysis was limited by the lack of availability of software tools to allow *inverse* modelling of the location and magnitudes of the generators of our NIRS signals. While frustrating, there is, at least, nothing *per se* that will prevent such analyses becoming commonplace in future years. In the context of the current pilot study, this would allow a direct comparison of the spatial distribution of NIRS signal changes with those derived from our MEG data and

our models of tDCS-induced E-fields. Access to such analysis tools would facilitate the beginnings of any explicit explorations of the links — or not! — between neuronal and hemodynamic responses to tDCS.

While our pilot study was limited in several regards, we were able to demonstrate that future studies aiming to investigate *offline* tDCS will be able to use concurrent MEG-NIRS without suffering a catastrophic loss of data quality in either domain. Furthermore, as the creation of forward models for both MEG and NIRS data analyses requires structural MRI data, future studies could also take advantage of acquired MR images to model tDCS-induced fields if appropriate acquisition sequences are selected (*cf.* Windhoff et al., 2013, for example). This will allow to explore potential links between inter-individual differences in functional changes and electric fields.

7.1 Concluding remarks

The human brain is a complex and self-organising dynamic system. Its response to a sustained external driving force, such as tDCS, likely includes some form of adaptive behaviour to ensure that it remains functional across a number of spatial and temporal scales. To understand and modulate the outcomes of tDCS in humans, we need to integrate insights spanning the entire gamut of neuroscientific knowledge, from microscopic to macroscopic levels of description. Any mechanistic explanation of tDCS must ultimately capture this complex interaction and must explain the interconnected, spatio-temporal features of electric fields in the brain. Future studies, building on work such as the studies presented in this thesis, will require multi-scale models that include both "static" simulations of induced electric fields — such as the ones presented here — as well as "dynamic" simulations of cellular activity — such as neural mass models (Coombes and Byrne, 2019).

At present, such large-scale models of tDCS are computationally intractable, and simulation studies to date have strongly simplified or simply neglected key factors. The ultimate result of this explanatory gap is that we currently lack models to predict task performance in humans undergoing tDCS. Consequently, researchers in the field have to navigate an enormous parameter space when designing and interpreting experiments. As highlighted by the work in this thesis, the interpretation of tDCS effects — or the lack thereof — on even the most elementary tasks quickly becomes a nigh-on impossible pursuit due to our gaps in understanding the relative importance of the many experimental and theoretical parameters involved in tDCS.

In tackling the herculean task of describing the brain's dynamic response to transcranial electrical stimulation, we can only truly make progress if experimental work is highly constrained by modelling efforts, and vice versa. To this end, it would be

greatly worthwhile for researchers in the field to routinely report individual data in addition to group-averaged data, to adopt more rigorous standards for methodological reporting in order to facilitate future replication efforts and to join efforts in collecting large data sets. In short, there remains much work to fruitfully employ future PhD researchers!

Bibliography

Aasted, C. M. et al. (2015). "Anatomical guidance for functional near-infrared spectroscopy: AtlasViewer tutorial". In: *Neurophotonics* 2.2, pp. 020801–17.

Aldini, G. (1804). *Essai theorique et experimental sur le galvanisme, avec une serie d'experiences faites en presence des commissaires de l'Institut national de France, et en divers amphitheatres anatomiques de Londres.* Paris: Fournier Fils.

Allen, N. J. and C. Eroglu (2017). "Cell Biology of Astrocyte-Synapse Interactions". In: *Neuron* 96.3, pp. 697–708.

Ambrus, G. G. et al. (2012). "The fade-in - Short stimulation - Fade out approach to sham tDCS – Reliable at 1 mA for naive and experienced subjects, but not investigators". In: *Brain Stimulation* 5.4, pp. 499–504.

Ammann, C., M. A. Lindquist, and P. A. Celnik (2017). "Response variability of different anodal transcranial direct current stimulation intensities across multiple sessions". In: *Brain Stimulation* 10.4, pp. 757–763.

Amunts, K. and K. Zilles (2015). "Architectonic mapping of the human brain beyond Brodmann". In: *Neuron* 88.6, pp. 1086–1107.

Amunts, K., A. Schleicher, and K. Zilles (2007). "Cytoarchitecture of the cerebral cortex — more than localization". In: *NeuroImage* 37.4, pp. 1061–1065.

Anderson, C. M. and M Nedergaard (2003). "Astrocyte-mediated control of cerebral microcirculation". In: *Trends in Neurosciences* 26.7, pp. 340–344.

Ando, S, N Kida, and S Oda (2001). "Central and peripheral visual reaction time of soccer players and nonathletes." In: *Perceptual and motor skills* 92.3 Pt 1, pp. 786–794.

Andrade, M. J. O. d. et al. (2018). "Daily variation of visual sensitivity to luminance contrast: Effects of time of measurement and circadian typology." In: *Chronobiology International* 52.2, pp. 1–12.

Andrews, B. T. et al. (1989). "Microsurgical anatomy of the venous drainage into the superior sagittal sinus." In: *Neurosurgery* 24.4, pp. 514–520.

Antal, A., M. A. Nitsche, and W. Paulus (2001). "External modulation of visual perception in humans." In: *NeuroReport* 12.16, pp. 3553–3555.

Antal, A. et al. (2003). "Manipulation of phosphene thresholds by transcranial direct current stimulation in man". In: *Experimental Brain Research* 150.3, pp. 375–378.

Antal, A. et al. (2004). "Excitability Changes Induced in the Human Primary Visual Cortex by Transcranial Direct Current Stimulation: Direct Electrophysiological Evidence". In: *Investigative Opthalmology & Visual Science* 45.2, pp. 702–6.

Antonenko, D. et al. (2019). "Towards precise brain stimulation: Is electric field simulation related to neuromodulation?" In: *Brain Stimulation* 12.5, pp. 1159–1168.

Arridge, S. R., M Cope, and D. T. Delpy (1992). "The theoretical basis for the determination of optical pathlengths in tissue: temporal and frequency analysis". In: *Physics in Medicine and Biology* 37.7, pp. 1531–1560.

Ashburner, J. and K. J. Friston (2005). "Unified segmentation". In: *NeuroImage* 26.3, pp. 839–851.

Attal, Y. and D. Schwartz (2013). "Assessment of subcortical source localization using deep brain activity imaging model with minimum norm operators: a MEG study". In: *PLoS One* 8.3, e59856.

Baczyk, M. and E. Jankowska (2014). "Presynaptic actions of transcranial and local direct current stimulation in the red nucleus". In: *The Journal of Physiology* 592.19, pp. 4313–4328.

Baillet, S. (2017). "Magnetoencephalography for brain electrophysiology and imaging". In: *Nature Neuroscience* 20.3, pp. 327–339.

Barker, J. W., A. Aarabi, and T. J. Huppert (2013). "Autoregressive model based algorithm for correcting motion and serially correlated errors in fNIRS". In: *Biomedical Optics Express* 4.8, pp. 1366–1379.

Barnes, G. R. et al. (2004). "Realistic spatial sampling for MEG beamformer images". In: *Human brain mapping* 23.2, pp. 120–127.

Bartheld, C. S. von, J. Bahney, and S. Herculano-Houzel (2016). "The search for true numbers of neurons and glial cells in the human brain: A review of 150 years of cell counting". In: *The Journal of Comparative Neurology* 524.18, pp. 3865–3895.

Bastani, A. and S. Jaberzadeh (2013). "Differential Modulation of Corticospinal Excitability by Different Current Densities of Anodal Transcranial Direct Current Stimulation". In: *PLoS ONE* 8.8, e72254.

Batsikadze, G et al. (2013). "Partially non-linear stimulation intensity-dependent effects of direct current stimulation on motor cortex excitability in humans". In: *The Journal of Physiology* 591.7, pp. 1987–2000.

Bebie, H., F. Fankhauser, and J. Spahr (1976). "Static perimetry: strategies". In: *Acta Ophthalmologica* 54.3, pp. 325–338.

Beer, A. (1852). "Bestimmung der Absorption des rothen Lichts in farbigen Flussigkeiten". In: *Annalen der Physik* 162, pp. 78–88.

Behrens, J. R. et al. (2017). "Long-Lasting Enhancement of Visual Perception with Repetitive Noninvasive Transcranial Direct Current Stimulation". In: *Frontiers in Cellular Neuroscience* 11, pp. 3553–10.

Benedetti, F. (2014a). *Placebo effects*. Oxford University Press.

— (2014b). "Placebo Effects: From the Neurobiological Paradigm to Translational Implications". In: *Neuron* 84.3, pp. 623–637.

Benedetti, F., E. Carlino, and A. Piedimonte (2016). "Increasing uncertainty in CNS clinical trials: the role of placebo, nocebo, and Hawthorne effects". In: *The Lancet Neurology* 15.7, pp. 736–747.

Benjamini, Y. and Y. Hochberg (1995). "Controlling the false discovery rate: a practical and powerful approach to multiple testing". In: *Journal of the Royal Statistical Society: Series B (Methodological)* 57.1, pp. 289–300.

Bergmann, T. O. et al. (2016). "Combining non-invasive transcranial brain stimulation with neuroimaging and electrophysiology: Current approaches and future perspectives". In: *NeuroImage* 140.C, pp. 4–19.

Berker, A. O. de, M. Bikson, and S. Bestmann (2013). "Predicting the behavioral impact of transcranial direct current stimulation: issues and limitations". In: *Frontiers in Human Neuroscience* 7, p. 613.

Bestmann, S. and N. Ward (2017). "Are current flow models for transcranial electrical stimulation fit for purpose?" In: *Brain Stimulation* 10.4, pp. 865–866.

Bestmann, S., A. O. de Berker, and J. Bonaiuto (2015). "Understanding the behavioural consequences of noninvasive brain stimulation". In: *Trends in Cognitive Sciences* 19.1, pp. 13–20.

Bikson, M. and A. Rahman (2013). "Origins of specificity during tDCS: anatomical, activity-selective, and input-bias mechanisms." In: *Frontiers in Human Neuroscience* 7, p. 688.

Bikson, M. et al. (2004). "Effects of uniform extracellular DC electric fields on excitability in rat hippocampal slices in vitro." In: *Journal of Physiology* 557.Pt 1, pp. 175–190.

Bikson, M. et al. (2018). "Rigor and reproducibility in research with transcranial electrical stimulation: An NIMH-sponsored workshop". In: *Brain Stimulation* 11.3, pp. 465–480.

Bindman, L. J., O. C. J. Lippold, and J. W. T. Redfearn (1962). "Long-lasting changes in the level of the electrical activity of the cerebral cortex produced by polarizing currents". In: *Nature* 196.4854, pp. 584–585.

— (1964). "The action of brief polarizing currents on the cerebral cortex of the rat (1) during current flow and (2) in the production of long-lasting after-effects". In: *The Journal of Physiology* 172.3, pp. 369–382.

Bjerrum, J (1889). "Om en Tilføjelse til den sædvanlige Synsfeltundersøgelse samt om Synsfeltet ved Glaukom". In: *Nord Ophthalmol Tidsskr* 2, pp. 141–185.

Bland, J. M. and D. G. Altman (1986). "Statistical methods for assessing agreement between two methods of clinical measurement". In: *The Lancet* 327.8476, pp. 307–310.

Bloch, F, W. W. Hansen, and M Packard (1946). "The Nuclear Induction Experiment". In: *Physical Review* 70 (7-8), pp. 474–485.

Boas, D. et al. (2002). "Three dimensional Monte Carlo code for photon migration through complex heterogeneous media including the adult human head." In: *Optics Express* 10.3, pp. 159–170.

Bolzoni, F., M. Bączyk, and E. Jankowska (2013). "Subcortical effects of transcranial direct current stimulation in the rat". In: *The Journal of Physiology* 591.16, pp. 4027–4042.

Bortoletto, M. et al. (2015). "The interaction with task-induced activity is more important than polarization: a tDCS study." In: *Brain Stimulation* 8.2, pp. 269–276.

Bouguer, P. (1729). *Essai d'optique sur la gradation de la lumière*. Chez Claude Jombert, ruë S. Jacques, au coin de la ruë des Mathurins, à l'Image Notre-Dame.

Boutron, I. and P. Ravaud (2011). "Blinding in Nonpharmacological Randomized Controlled Trials". In: *Randomized Clinical Trials of Nonpharmacological Treatments*. Ed. by I. Boutron, P. Ravaud, and D. Moher. 1st ed. New York: Chapman and Hall/CRC. Chap. 1, pp. 3–10.

Braak, H and E Braak (1976). "The pyramidal cells of Betz within the cingulate and precentral gigantopyramidal field in the human brain". In: *Cell and Tissue Research* 172.1, pp. 103–119.

Brainard, D. H. (1997). "The Psychophysics Toolbox". In: *Spatial Vision* 10, pp. 433–436.

Brem, A.-K. et al. (2014). "Is neuroenhancement by noninvasive brain stimulation a net zero-sum proposition?" In: *NeuroImage* 85.P3, pp. 1058–1068.

Brigadoi, S. and R. J. Cooper (2015). "How short is short? Optimum source–detector distance for short-separation channels in functional near-infrared spectroscopy". In: *Neurophotonics* 2.2, p. 025005.

Brückner, S. and T. Kammer (2016). "No Modulation of Visual Cortex Excitability by Transcranial Direct Current Stimulation". In: *PLoS ONE* 11.12, e0167697–14.

Brunoni, A. R. and F. Fregni (2011). "Clinical trial design in non-invasive brain stimulation psychiatric research". In: *International journal of methods in psychiatric research* 20.2, e19–e30.

Brunoni, A. R. et al. (2011). "A systematic review on reporting and assessment of adverse effects associated with transcranial direct current stimulation." In: *International Journal of Neuropsychopharmacology* 14.8, pp. 1133–1145.

Brunoni, A. R. et al. (2012). "Clinical research with transcranial direct current stimulation (tDCS): Challenges and future directions". In: *Brain Stimulation* 5.3, pp. 175–195.

Brunoni, A. R. et al. (2014). "Comparison of blinding effectiveness between sham tDCS and placebo sertraline in a 6-week major depression randomized clinical trial". In: *Clinical Neurophysiology* 125.2, pp. 298–305.

Burke, M. J., T. J. Kaptchuk, and A. Pascual-Leone (2019). "Challenges of differential placebo effects in contemporary medicine: The example of brain stimulation". In: *Annals of Neurology* 85.1, pp. 12–20.

Buzsáki, G. and X.-J. Wang (2012). "Mechanisms of gamma oscillations". In: *Annual Review of Neuroscience* 35, pp. 203–225.

Carney, M. W. P., M. D. Cashman, and B. F. Sheffield (1970). "Polarization in depression". In: *The British Journal of Psychiatry* 117.539, pp. 474–475.

Chaieb, L., A. Antal, and W. Paulus (2008). "Gender-specific modulation of short-term neuroplasticity in the visual cortex induced by transcranial direct current stimulation". In: *Visual Neuroscience* 25.01, pp. 77–81.

Chauhan, B. C. et al. (1993). "Characteristics of frequency-of-seeing curves in normal subjects, patients with suspected glaucoma, and patients with glaucoma." In: *Investigative Ophthalmology & Visual Science* 34.13, pp. 3534–3540.

Chauhan, M. et al. (2017). "Multishot echo-planar MREIT for fast imaging of conductivity, current density, and electric field distributions." In: *Magnetic Resonance in Medicine* 29, R1.

Chew, T., K.-A. Ho, and C. K. Loo (2015). "Inter- and Intra-individual Variability in Response to Transcranial Direct Current Stimulation (tDCS) at Varying Current Intensities." In: *Brain Stimulation* 8.6, pp. 1130–1137.

Clark, V. P. et al. (2011). "Transcranial direct current stimulation (tDCS) produces localized and specific alterations in neurochemistry: A 1H magnetic resonance spectroscopy study". In: *Neuroscience Letters* 500.1, pp. 67–71.

Claus, S. et al. (2012). "High frequency spectral components after secobarbital: the contribution of muscular origin—a study with MEG/EEG". In: *Epilepsy Research* 100.1-2, pp. 132–141.

Coffman, B. A., V. P. Clark, and R. Parasuraman (2014). "Battery powered thought: Enhancement of attention, learning, and memory in healthy adults using transcranial direct current stimulation". In: *NeuroImage* 85, pp. 895–908.

Cohen, D. (1968). "Magnetoencephalography: evidence of magnetic fields produced by alpha-rhythm currents". In: *Science* 161.3843, pp. 784–786.

Colier, W. N. et al. (2001a). "Simultaneous near-infrared spectroscopy monitoring of left and right occipital areas reveals contra-lateral hemodynamic changes upon hemi-field paradigm." In: *Vision Research* 41.1, pp. 97–102.

Colier, W. N. et al. (2001b). "Simultaneous near-infrared spectroscopy monitoring of left and right occipital areas reveals contra-lateral hemodynamic changes upon hemi-field paradigm". In: *Vision Research* 41.1, pp. 97–102.

Collins, D. L. et al. (1998). "Design and construction of a realistic digital brain phantom." In: *IEEE Transactions on Medical Imaging* 17.3, pp. 463–468.

Contini, D. et al. (2012). "Brain and muscle near infrared spectroscopy/imaging techniques". In: *Journal of Near Infrared Spectroscopy* 20.1, pp. 15–27.

Coombes, S. and Á. Byrne (2019). "Next generation neural mass models". In: *Nonlinear Dynamics in Computational Neuroscience.* Springer, pp. 1–16.

Cornwell, B. R. et al. (2008). "Evoked amygdala responses to negative faces revealed by adaptive MEG beamformers". In: *Brain Research* 1244, pp. 103–112.

Costa, T. L. et al. (2015a). "Contrasting effects of transcranial direct current stimulation on central and peripheral visual fields". In: *Experimental Brain Research* 233.5, pp. 1391–1397.

Costa, T. L. et al. (2015b). "Transcranial direct current stimulation as a tool in the study of sensory-perceptual processing." In: *Attention, Perception & Psychophysics* 77.6, pp. 1813–1840.

Costain, R, J. W. T. Redfearn, and O. C. J. Lippold (1964). "A controlled trial of the therapeutic effects of polarization of the brain in depressive illness". In: *The British Journal of Psychiatry* 110.469, pp. 786–799.

Cox, R. W. (1996). "AFNI: software for analysis and visualization of functional magnetic resonance neuroimages". In: *Computers and Biomedical research* 29.3, pp. 162–173.

Creutzfeldt, O. D., G. H. Fromm, and H Kapp (1962). "Influence of transcortical d-c currents on cortical neuronal activity." In: *Experimental Neurology* 5, pp. 436–452.

Cudeiro, J. and A. M. Sillito (2006). "Looking back: corticothalamic feedback and early visual processing". In: *Trends in Neurosciences* 29.6, pp. 298–306.

Cui, X. et al. (2011). "A quantitative comparison of NIRS and fMRI across multiple cognitive tasks". In: *NeuroImage* 54.4, pp. 2808–2821.

Da Silva, F. H. L. et al. (2010). *Electrophysiological basis of MEG signals.* London: Oxford University Press.

Dahnke, R., R. A. Yotter, and C. Gaser (2013). "Cortical thickness and central surface estimation". In: *NeuroImage* 65, pp. 336–348.

Daniel, P. and D Whitteridge (1961). "The representation of the visual field on the cerebral cortex in monkeys". In: *The Journal of Physiology* 159.2, pp. 203–221.

Dannhauer, M. et al. (2011). "Modeling of the human skull in EEG source analysis". In: *Human Brain Mapping* 32.9, pp. 1383–1399.

Dannhauer, M. et al. (2012). "A pipeline for the simulation of transcranial direct current stimulation for realistic human head models using SCIRun/BioMesh3D". In: *2012 Annual International Conference of the IEEE Engineering in Medicine and Biology Society.* IEEE, pp. 5486–5489.

Datta, A. et al. (2011). "Individualized model predicts brain current flow during transcranial direct-current stimulation treatment in responsive stroke patient". In: *Brain Stimulation* 4.3, pp. 169–174.

Datta, A. et al. (2012). "Inter-Individual Variation during Transcranial Direct Current Stimulation and Normalization of Dose Using MRI-Derived Computational Models." In: *Frontiers in Psychiatry* 3, p. 91.

David, M. C. M. M. et al. (2018). "Transcranial direct current stimulation in the modulation of neuropathic pain: a systematic review". In: *Neurological Research* 40.7, pp. 557–565.

De No, R. L. (1947). *A study of nerve physiology*. Vol. 131. Rockefeller Institute for Medical Research.

Dedoncker, J. et al. (2016). "A systematic review and meta-analysis of the effects of transcranial direct current stimulation (tDCS) over the dorsolateral prefrontal cortex in healthy and neuropsychiatric samples: influence of stimulation parameters". In: *Brain Stimulation* 9.4, pp. 501–517.

Delpy, D. T. et al. (1988). "Estimation of optical pathlength through tissue from direct time of flight measurement". In: *Physics in Medicine and Biology* 33.12, pp. 1433–1442.

Dougherty, E. T. and J. C. Turner (2016). "An Object-Oriented Framework for Versatile Finite Element Based Simulations of Neurostimulation". In: *Journal of Computational Medicine* 2016.2, pp. 1–15.

Dougherty, R. F. et al. (2003). "Visual field representations and locations of visual areas V1/2/3 in human visual cortex". In: *Journal of Vision* 3.10, pp. 1–13.

Duncan, A et al. (1996a). "Measurement of cranial optical path length as a function of age using phase resolved near infrared spectroscopy." In: *Pediatric Research* 39.5, pp. 889–894.

Duncan, A. et al. (1996b). "Measurement of cranial optical path length as a function of age using phase resolved near infrared spectroscopy". In: *Pediatric Research* 39.5, p. 889.

Durup, G. and H. Piéron (1932). "Recherches au sujet de l'interprétation du phénomène de Purkinje par des différences dans les courbes de sensation des récepteurs chromatiques". In: *L'Année psychologique* 33.1, pp. 57–83.

Dutta, A. (2015). "Bidirectional interactions between neuronal and hemodynamic responses to transcranial direct current stimulation (tDCS): challenges for brain-state dependent tDCS". In: *Frontiers in Systems Neuroscience* 9, pp. 795–7.

Dyke, K. et al. (2016a). "Intra-Subject Consistency and Reliability of Response Following 2 mA Transcranial Direct Current Stimulation". In: *Brain Stimulation*, pp. 1–7.

— (2016b). "Intra-Subject Consistency and Reliability of Response Following 2 mA Transcranial Direct Current Stimulation". In: *Brain Stimulation* 9.6, pp. 819–825.

Esmaeilpour, Z. et al. (2019). "Incomplete evidence that increasing current intensity of tDCS boosts outcomes". In: *Brain Stimulation* 11.2, pp. 310–321.

Fang, Q. and D. A. Boas (2009a). "Monte Carlo simulation of photon migration in 3D turbid media accelerated by graphics processing units". In: *Optics Express* 17.22, pp. 20178–20190.

— (2009b). "Tetrahedral mesh generation from volumetric binary and grayscale images". In: *2009 IEEE International Symposium on Biomedical Imaging: From Nano to Macro*. IEEE, pp. 1142–1145.

Fankhauser, F., J. Spahr, and H. Bebie (1977a). "Some aspects of the automation of perimetry". In: *Survey of Ophthalmology* 22.2, pp. 131–141.

— (1977b). "Three years of experience with the Octopus automatic perimeter". In: *Doc Ophthalmol Proc Ser* 14, pp. 7–15.

Faria, P. et al. (2012). "Feasibility of focal transcranial DC polarization with simultaneous EEG recording: preliminary assessment in healthy subjects and human epilepsy". In: *Epilepsy & Behavior* 25.3, pp. 417–425.

Fechner, G. T. (1860). *Elemente der Psychophysik I u. II*. Leipzig: Breitkopf & Härtlerl.

Fertonani, A., C. Ferrari, and C. Miniussi (2015). "What do you feel if I apply transcranial electric stimulation? Safety, sensations and secondary induced effects". In: *Clinical Neurophysiology* 126.11, pp. 2181–2188.

Fields, R. D. and B. Stevens-Graham (2002). "New insights into neuron-glia communication". In: *Science* 298.5593, pp. 556–562.

Filmer, H. L. et al. (2019). "Accounting for individual differences in the response to tDCS with baseline levels of neurochemical excitability". In: *Cortex* 115, pp. 324–334.

Finniss, D. G. et al. (2010). "Biological, clinical, and ethical advances of placebo effects". In: *The Lancet* 375.9715, pp. 686–695.

Fischl, B. (2012). "FreeSurfer." In: *NeuroImage* 62.2, pp. 774–781.

Fonteneau, C. et al. (2019). "Sham tDCS: A hidden source of variability? Reflections for further blinded, controlled trials". In: *Brain Stimulation*, pp. 1–6.

Francis, J. T., B. J. Gluckman, and S. J. Schiff (2003). "Sensitivity of neurons to weak electric fields." In: *The Journal of Neuroscience* 23.19, pp. 7255–7261.

Fritsch, B. et al. (2010). "Direct current stimulation promotes BDNF-dependent synaptic plasticity: potential implications for motor learning." In: *Neuron* 66.2, pp. 198–204.

Fritsch, G. T. and E. Hitzig (1870). "Über die elektrische Erregbarkeit des Grosshirns". In: *Archiv für Anatomie, Physiologie und Wissenschaftliche Medicin*, pp. 300–332.

Furuya, S. et al. (2014). "Ceiling effects prevent further improvement of transcranial stimulation in skilled musicians." In: *The Journal of Neuroscience* 34.41, pp. 13834–13839.

Galvani, L. (1791). *De viribus electricitatis in motu muscolari animalium*. Bologna.

— (1797). *Memorie sull 'elettricita' animale (lettera a L. Spallanzani)*. Bologna.

Gandiga, P. C., F. C. Hummel, and L. G. Cohen (2006). "Transcranial DC stimulation (tDCS): A tool for double-blind sham-controlled clinical studies in brain stimulation". In: *Clinical Neurophysiology* 117.4, pp. 845–850.

Garcia-Cossio, E. et al. (2015). "Simultaneous transcranial direct current stimulation (tDCS) and whole-head magnetoencephalography (MEG): assessing the impact of tDCS on slow cortical magnetic fields". In: *NeuroImage*, pp. 1–8.

Gebodh, N. et al. (2019). "Inherent physiological artifacts in EEG during tDCS". In: *NeuroImage* 185, pp. 408–424.

Gellner, A.-K., J. Reis, and B. Fritsch (2016). "Glia: a neglected player in non-invasive direct current brain stimulation". In: *Frontiers in Cellular Neuroscience* 10, p. 188.

Geuzaine, C. (2007). "GetDP: a general finite-element solver for the de Rham complex". In: *PAMM: Proceedings in Applied Mathematics and Mechanics*. Vol. 7. 1. Wiley Online Library, pp. 1010603–1010604.

Geuzaine, C. and J.-F. Remacle (2009). "Gmsh: A 3-D finite element mesh generator with built-in pre-and post-processing facilities". In: *International Journal for Numerical Methods in Engineering* 79.11, pp. 1309–1331.

Giordano, J. et al. (2017). "Mechanisms and Effects of Transcranial Direct Current Stimulation:" in: *Dose-Response* 15.1, p. 155932581668546.

Glickfeld, L. L., M. H. Histed, and J. H. R. Maunsell (2013). "Mouse primary visual cortex is used to detect both orientation and contrast changes." In: *The Journal of Neuroscience* 33.50, pp. 19416–19422.

Gloor, B. P. (2009). "Franz Fankhauser: the father of the automated perimeter". In: *Survey of Ophthalmology* 54.3, pp. 417–425.

Goldmann, H (1945). "Grundlagen exakter Perimetrie". In: *Ophtalmologica* 109.2-3, pp. 57–70.

— (1946). "Demonstration unseres neuen Projektionskugelperimeters samt theoretischen und klinischen Bemerkungen über Perimetrie". In: *Ophtalmologica* 111.2-3, pp. 187–192.

— (1999). "Fundamentals of exact perimetry". In: *Optometry and Vision Science* 76.8, pp. 599–604.

Gordon, G. R. J. et al. (2008). "Brain metabolism dictates the polarity of astrocyte control over arterioles." In: *Nature* 456.7223, pp. 745–749.

Graefe, A von (1856). "Ueber die Untersuchung des Gesichtsfeldes bei amblyopischen Affectionen". In: *Archiv für Ophthalmologie* 2.2, pp. 258–298.

Greinacher, R. et al. (2019). "The time course of ineffective sham-blinding during low-intensity (1 mA) transcranial direct current stimulation". In: *European Journal of Neuroscience* 10, pp. 1–9.

Grossman, P. et al. (2019). "Safety of Transcranial Direct Current Stimulation". In: *Practical Guide to Transcranial Direct Current Stimulation*. Springer, pp. 167–195.

Guillery, R. and S. M. Sherman (2002). "Thalamic relay functions and their role in corticocortical communication: generalizations from the visual system". In: *Neuron* 33.2, pp. 163–175.

Haag-Streit AG (2014). *[Brochure] Octopus 900, Flexibility and reliability*. Ophthalmological Instruments. Könitz, Switzerland.

Halassa, M. M. and P. G. Haydon (2010). "Integrated Brain Circuits: Astrocytic Networks Modulate Neuronal Activity and Behavior". In: *Annual Review of Physiology* 72.1, pp. 335–355.

Hall, C. N. et al. (2014a). "Capillary pericytes regulate cerebral blood flow in health and disease." In: *Nature* 508.7494, pp. 55–60.

Hall, E. L. et al. (2014b). "The relationship between MEG and fMRI". In: *NeuroImage* 102.P1, pp. 80–91.

Hall, K. M., R. A. Hicks, and H. K. Hopkins (1970). "The effects of low level DC scalp positive and negative current on the performance of various tasks". In: *The British Journal of Psychiatry* 117.541, pp. 689–691.

Hämäläinen, M. et al. (1993). "Magnetoencephalography — theory, instrumentation, and applications to noninvasive studies of the working human brain". In: *Reviews of Modern Physics* 65.2, p. 413.

Hampstead, B. M. et al. (2017). "Combined mnemonic strategy training and high-definition transcranial direct current stimulation for memory deficits in mild cognitive impairment". In: *Alzheimer's & Dementia: Translational Research & Clinical Interventions* 3.3, pp. 459–470.

Hanck, J et al. (2012). "Using detection or identification paradigms when assessing visual development: Is a shift in paradigm necessary?" In: *Journal of Vision* 12.6, pp. 4–4.

Hanley, C. J., K. D. Singh, and D. J. McGonigle (2015). "Transcranial modulation of brain oscillatory responses: A concurrent tDCS-MEG investigation". In: *NeuroImage,* pp. 1–13.

Hansen, P., M. Kringelbach, and R. Salmelin (2010). *MEG: An Introduction to Methods*. New York: Oxford University Press.

Hashemirad, F. et al. (2016). "The effect of anodal transcranial direct current stimulation on motor sequence learning in healthy individuals: a systematic review and meta-analysis". In: *Brain and Cognition* 102, pp. 1–12.

He, Q. et al. (2019). "No effects of anodal transcranial direct current stimulation on contrast sensitivity function". In: *Restorative Neurology and Neuroscience* 37.2, pp. 109–118.

Heijl, A and C. Krakau (1975). "An automatic static perimeter, design and pilot study". In: *Acta Ophthalmologica* 53.3, pp. 293–310.

Herbart, J. F. (1824). *Psychologie als Wissenschaft, neu gegründet auf Erfahrung, Metaphysik und Mathematik*. Königsberg: Unzer.

Herjanic, M. and B. Moss-Herjanic (1967). "Clinical report on a new therapeutic technique: polarization." In: *The Canadian Psychiatric Association Journal* 12.4, pp. 423–424.

Hermes, D., M. Nguyen, and J. Winawer (2017). "Neuronal synchrony and the relation between the blood-oxygen-level dependent response and the local field potential". In: *PLoS Biology* 15.7, e2001461–42.

Herold, F. et al. (2018). "Applications of Functional Near-Infrared Spectroscopy (fNIRS) Neuroimaging in Exercise–Cognition Science: A Systematic, Methodology-Focused Review". In: *Journal of Clinical Medicine* 7.12, pp. 466–43.

Hill, A. T., P. B. Fitzgerald, and K. E. Hoy (2016). "Effects of anodal transcranial direct current stimulation on working memory: a systematic review and meta-analysis of findings from healthy and neuropsychiatric populations". In: *Brain stimulation* 9.2, pp. 197–208.

Hill, N. J. (2001). "Testing hypotheses about psychometric functions". PhD thesis. University of Oxford.

Hillebrand, A and G. R. Barnes (2002). "A quantitative assessment of the sensitivity of whole-head MEG to activity in the adult human cortex". In: *NeuroImage* 16.3, pp. 638–650.

Hillebrand, A. and G. R. Barnes (2005). "Beamformer analysis of MEG data". In: *International Review of Neurobiology* 68, pp. 149–171.

— (2011). "Practical constraints on estimation of source extent with MEG beamformers". In: *Neuroimage* 54.4, pp. 2732–2740.

Hitzig, E. (1867). "Über die Anwendung unpolarisirbarer Electroden in der Electrotherapie". In: *Berliner klinische Wochenschrift* (4), pp. 404–406.

— (1870). "Physiologisches und Therapeutisches über einige electrische Reizmethoden". In: *Berliner klinische Wochenschrift* (7), pp. 137–138.

Hoddes, E et al. (1973). "Quantification of sleepiness: a new approach." In: *Psychophysiology* 10.4, pp. 431–436.

Horvath, J. C., J. D. Forte, and O. Carter (2014). "Evidence that transcranial direct current stimulation (tDCS) generates little-to-no reliable neurophysiologic effect beyond MEP amplitude modulation in healthy human subjects: A systematic review". In: *Neuropsychologia,* pp. 1–24.

— (2015). "Quantitative Review Finds No Evidence of Cognitive Effects in Healthy Populations From Single-session Transcranial Direct Current Stimulation (tDCS)". In: *Brain Stimulation* 8.3, pp. 535–550.

Hróbjartsson, A. and P. C. Gøtzsche (2010). "Placebo interventions for all clinical conditions". In: *Cochrane Database of Systematic Reviews* 43.supplement, pp. 820–312.

Hsu, T.-Y. et al. (2014). "Transcranial direct current stimulation over right posterior parietal cortex changes prestimulus alpha oscillation in visual short-term memory task." In: *NeuroImage* 98, pp. 306–313.

Huang, Y. et al. (2013). "Automated MRI segmentation for individualized modeling of current flow in the human head". In: *Journal of Neural Engineering* 10.6, p. 066004.

Huang, Y. et al. (2017). "Measurements and models of electric fields in the *in vivo* human brain during transcranial electric stimulation". In: *eLife* 6, pp. 1–56.

Huang, Y. et al. (2019). "Realistic vOlumetric-Approach to Simulate Transcranial Electric Stimulation — ROAST — a fully automated open-source pipeline". In: *Journal of Neural Engineering* 16.5.

Hubel, D. H. and T. N. Wiesel (1962). "Receptive fields, binocular interaction and functional architecture in the cat's visual cortex". In: *The Journal of Physiology* 160.1, pp. 106–154.

Indahlastari, A. and R. J. Sadleir (2015). "A comparison between block and smooth modeling in finite element simulations of tDCS". In: *37th Annual International Conference of the IEEE Engineering in Medicine and Biology Society (EMBC)*. IEEE, pp. 3403–3406.

Irimia, A., M. J. Erhart, and T. T. Brown (2014). "Variability of magnetoencephalographic sensor sensitivity measures as a function of age, brain volume and cortical area". In: *Clinical Neurophysiology* 125.10, pp. 1973–1984.

Ishikuro, K. et al. (2014). "Cerebral functional imaging using near-infrared spectroscopy during repeated performances of motor rehabilitation tasks tested on healthy subjects". In: *Frontiers in Human Neuroscience* 8, p. 292.

Iuculano, T and R Cohen Kadosh (2013). "The Mental Cost of Cognitive Enhancement". In: *Journal of Neuroscience* 33.10, pp. 4482–4486.

Jacobson, L., M. Koslowsky, and M. Lavidor (2011). "tDCS polarity effects in motor and cognitive domains: a meta-analytical review". In: *Experimental Brain Research* 216.1, pp. 1–10.

Jefferys, J. (1981). "Influence of electric fields on the excitability of granule cells in guinea-pig hippocampal slices." In: *The Journal of Physiology* 319.1, pp. 143–152.

Jia, X. and A. Kohn (2011). "Gamma rhythms in the brain". In: *PLoS Biology* 9.4, e1001045.

Jia, X., M. A. Smith, and A. Kohn (2011). "Stimulus selectivity and spatial coherence of gamma components of the local field potential". In: *Journal of Neuroscience* 31.25, pp. 9390–9403.

Jöbsis, F. F. (1977). "Noninvasive, infrared monitoring of cerebral and myocardial oxygen sufficiency and circulatory parameters." In: *Science* 198.4323, pp. 1264–1267.

Johnson, C. A., J. L. Keltner, and F Balestrery (1978). "Effects of target size and eccentricity on visual detection and resolution." In: *Vision Research* 18.9, pp. 1217–1222.

Johnson, C. A., M. Wall, and H. S. Thompson (2011). "A history of perimetry and visual field testing". In: *Optometry and Vision Science* 88.1, E8–E15.

Jones, K. T., F. Gözenman, and M. E. Berryhill (2015). "The strategy and motivational influences on the beneficial effect of neurostimulation: A tDCS and fNIRS study". In: *NeuroImage* 105.C, pp. 238–247.

Jonson, C. A., J. L. Keltner, and F. Balestrery (1978). "Effects of target size and eccentricity on visual detection and resolution". In: *Vision Research* 18.9, pp. 1217–1222.

Jung, Y.-J., J.-H. Kim, and C.-H. Im (2013). "COMETS: A MATLAB toolbox for simulating local electric fields generated by transcranial direct current stimulation (tDCS)". In: *Biomedical Engineering Letters* 3.1, pp. 39–46.

Kandel, E. R. et al. (2013). *Principles of Neural Science*. Vol. 5. New York: McGraw-Hill.

Kaptchuk, T. J. et al. (2000). "Do medical devices have enhanced placebo effects?" In: *Journal of Clinical Epidemiology* 53.8, pp. 786–792.

Kashou, N. H. and B. M. Giacherio (2016). "Stimulus and optode placement effects on functional near-infrared spectroscopy of visual cortex". In: *Neurophotonics* 3.2, pp. 025005–10.

Kastner, S., K. A. Schneider, and K. Wunderlich (2006). "Beyond a relay nucleus: neuroimaging views on the human LGN". In: *Progress in Brain Research* 155, pp. 125–143.

Kayser, C. et al. (2004). "A comparison of hemodynamic and neural responses in cat visual cortex using complex stimuli". In: *Cerebral Cortex* 14.8, pp. 881–891.

Kessler, S. K. et al. (2012). "Differences in the experience of active and sham transcranial direct current stimulation". In: *Brain Stimulation* 5.2, pp. 155–162.

Khan, B. (2013). "Functional near-infrared spectroscopy maps cortical plasticity underlying altered motor performance induced by transcranial direct current stimulation". In: *Journal of Biomedical Optics* 18.11, pp. 116003–12.

Kidgell, D. J. et al. (2013). "Different current intensities of anodal transcranial direct current stimulation do not differentially modulate motor cortex plasticity." In: *Neural Plasticity* 2013.3, pp. 603502–9.

Kikuchi, M. et al. (2010). "Neurovascular coupling in the human somatosensory cortex". In: *NeuroReport* 21.17, pp. 1106–1110.

Kim, J.-H. et al. (2014). "Inconsistent outcomes of transcranial direct current stimulation may originate from anatomical differences among individuals: Electric field simulation using individual MRI data". In: *Neuroscience Letters* 564, pp. 1–6.

Kirilina, E et al. (2012). "The physiological origin of task-evoked systemic artefacts in functional near infrared spectroscopy". In: *NeuroImage* 61.1, pp. 70–81.

Kleiner, M., D. Brainard, and D. Pelli (2007). "What's new in Psychtoolbox-3?" In: *Perception* 37.14, pp. 1–16.

Koehler, R. C., R. J. Roman, and D. R. Harder (2009). "Astrocytes and the regulation of cerebral blood flow". In: *Trends in Neurosciences* 32.3, pp. 160–169.

Koessler, L. et al. (2017). "In-vivo measurements of human brain tissue conductivity using focal electrical current injection through intracerebral multicontact electrodes." In: *Human Brain Mapping* 38.2, pp. 974–986.

Kraft, A. et al. (2010). "Transcranial direct current stimulation affects visual perception measured by threshold perimetry". In: *Experimental Brain Research* 207.3-4, pp. 283–290.

Krause, B., J. Márquez-Ruiz, and R. Cohen Kadosh (2013). "The effect of transcranial direct current stimulation: a role for cortical excitation/inhibition balance?" In: *Frontiers in Human Neuroscience* 7, p. 602.

Kuo, M. F. and M. A. Nitsche (2012). "Effects of Transcranial Electrical Stimulation on Cognition". In: *Clinical EEG and Neuroscience* 43.3, pp. 192–199.

Laakso, I. et al. (2015). "Inter-subject Variability in Electric Fields of Motor Cortical tDCS". In: *Brain Stimulation* 8.5, pp. 906–913.

Laakso, I. et al. (2019). "Can electric fields explain inter- individual variability in transcranial direct current stimulation of the motor cortex?" In: *Scientific Reports*, pp. 1–10.

Lafon, B. et al. (2017). "Direct-Current Stimulation-Alters Neuronal Input/Output Function". In: *Brain Stimulation* 10.1, pp. 36–45.

Lambert, J.-H. (1760). *Photometria, sive de Mensura et gradibus luminis, colorum et umbrae*. Sumptibus viduae E. Klett.

Lang, N. et al. (2005). "How does transcranial DC stimulation of the primary motor cortex alter regional neuronal activity in the human brain?" In: *European Journal of Neuroscience* 22.2, pp. 495–504.

Lange, F. and I. Tachtsidis (2019). "Clinical Brain Monitoring with Time Domain NIRS: A Review and Future Perspectives". In: *Applied Sciences* 9.8, p. 1612.

Lascaratos, J. and S. Marketos (1988). "A historical outline of Greek ophthalmology from the Hellenistic period up to the establishment of the first universities". In: *History of Ophthalmology 1*. Springer, pp. 157–169.

Lashley, K. S. (1943). "Studies of cerebral function in learning XII. Loss of the maze habit after occipital lesions in blind rats". In: *Journal of Comparative Neurology* 79.3, pp. 431–462.

Lauritzen, M. and L. Gold (2003). "Brain function and neurophysiological correlates of signals used in functional neuroimaging". In: *Journal of Neuroscience* 23.10, pp. 3972–3980.

Lauterbur, P. C. (1973). "Image Formation by Induced Local Interactions: Examples Employing Nuclear Magnetic Resonance". In: *Nature* 242.5394, pp. 190–191.

Law, S. K. (1993). "Thickness and resistivity variations over the upper surface of the human skull." In: *Brain Topography* 6.2, pp. 99–109.

Learmonth, G. et al. (2017). "No Interaction between tDCS Current Strength and Baseline Performance: A Conceptual Replication". In: *Frontiers in Neuroscience* 11, pp. 846–13.

Lecrux, C and E Hamel (2011). "The neurovascular unit in brain function and disease". In: *Acta Physiologica* 203.1, pp. 47–59.

Lee, C. et al. (2017). "COMETS2: An advanced MATLAB toolbox for the numerical analysis of electric fields generated by transcranial direct current stimulation". In: *Journal of Neuroscience Methods* 277, pp. 56–62.

Lei, T., D. Ma, and F. Jiang (2016). "Mapping the Cortical Activation Changes Induced by Transcranial Direct Current Stimulation: A fNIRS-tDCS Study". In: *Proceedings of the 6th International Asia Conference on Industrial Engineering and Management Innovation*. Paris: Atlantis Press, pp. 355–361.

Leibowitz, J. (1957). "Electroshock therapy in Ibn Sina's Canon". In: *Journal of Historical Medicine* 12, pp. 71–72.

Li, H. et al. (2008). "Investigation of the critical geometric characteristics of living human skulls utilising medical image analysis techniques". In: *International Journal of Vehicle Safety* 2.4, p. 345.

Li, L. M., K. Uehara, and T. Hanakawa (2015). "The contribution of interindividual factors to variability of response in transcranial direct current stimulation studies." In: *Frontiers in Cellular Neuroscience* 9.180, pp. 181–19.

Liebetanz, D. et al. (2002). "Pharmacological approach to the mechanisms of transcranial DC-stimulation-induced after-effects of human motor cortex excitability." In: *Brain* 125.Pt 10, pp. 2238–2247.

Lisman, J. E. (2001). "Three Ca2+ levels affect plasticity differently: the LTP zone, the LTD zone and no man's land." In: *Journal of Physiology* 532.Pt 2, p. 285.

Logothetis, N. K. et al. (2001). "Neurophysiological investigation of the basis of the fMRI signal". In: *Nature* 412.6843, p. 150.

Logothetis, N. K., C. Kayser, and A. Oeltermann (2007). "In vivo measurement of cortical impedance spectrum in monkeys: implications for signal propagation". In: *Neuron* 55.5, pp. 809–823.

Lolas, F (1977). "Brain polarization: behavioral and therapeutic effects." In: *Biological Psychiatry* 12.1, pp. 37–47.

López-Alonso, V. et al. (2014). "Inter-individual Variability in Response to Non-invasive Brain Stimulation Paradigms". In: *Brain Stimulation* 7.3, pp. 372–380.

López-Alonso, V. et al. (2015). "Intra-individual variability in the response to anodal transcranial direct current stimulation." In: *Clinical neurophysiology* 126.12, pp. 2342–2347.

Luber, B. (2014). "Neuroenhancement by noninvasive brain stimulation is not a net zero-sum proposition". In: *Frontiers in Systems Neuroscience* 8, p. 127.

Luft, C. D. B. et al. (2014). "Best of both worlds: promise of combining brain stimulation and brain connectome". In: *Frontiers in Systems Neuroscience* 8.804, p. 248701.

Lynn, J. R. (1969). "Examination of the visual field in glaucoma". In: *Investigative Ophthalmology & Visual Science* 8.1, pp. 76–84.

Mancuso, L. E. et al. (2016). "Does transcranial direct current stimulation improve healthy working memory?: a meta-analytic review". In: *Journal of Cognitive Neuroscience* 28.8, pp. 1063–1089.

Marquez, J. et al. (2015). "Transcranial direct current stimulation (tDCS): does it have merit in stroke rehabilitation? A systematic review". In: *International Journal of Stroke* 10.3, pp. 306–316.

Márquez-Ruiz, J. et al. (2012). "Transcranial direct-current stimulation modulates synaptic mechanisms involved in associative learning in behaving rabbits". In: *Proceedings of the National Academy of Sciences* 109.17, pp. 6710–6715.

Marshall, T. R. et al. (2015). "On the relationship between cortical excitability and visual oscillatory responses — A concurrent tDCS-MEG study". In: *NeuroImage*, pp. 1–9.

Martin, D. M. et al. (2014). "Use of transcranial direct current stimulation (tDCS) to enhance cognitive training: effect of timing of stimulation". In: *Experimental Brain Research* 232.10, pp. 3345–3351.

Martin, P. R. et al. (1997). "Evidence that blue-on cells are part of the third geniculo-cortical pathway in primates". In: *European Journal of Neuroscience* 9.7, pp. 1536–1541.

Massimini, M and F Amzica (2001). "Extracellular calcium fluctuations and intracellular potentials in the cortex during the slow sleep oscillation." In: *Journal of Neurophysiology* 85.3, pp. 1346–1350.

Maxwell, J. C. (1861). "On physical lines of force". In: *A dynamical theory of the electromagnetic field*, pp. 1875–89.

McCambridge, J., J. Witton, and D. R. Elbourne (2014). "Systematic review of the Hawthorne effect: New concepts are needed to study research participation effects". In: *Journal of Clinical Epidemiology* 67.3, pp. 267–277.

McGinnis, J. (2010). *Avicenna.* New York: Oxford University Press.

McIntosh, M. A. et al. (2010). "Absolute Quantification of Oxygenated Hemoglobin within the Visual Cortex with Functional Near Infrared Spectroscopy (fNIRS)". In: *Investigative Opthalmology & Visual Science* 51.9, pp. 4856–5.

McKendrick, R., R. Parasuraman, and H. Ayaz (2015). "Wearable functional near infrared spectroscopy (fNIRS) and transcranial direct current stimulation (tDCS): expanding vistas for neurocognitive augmentation". In: *Frontiers in Systems Neuroscience* 9, pp. 1394–14.

Medina, J. and S. Cason (2017). "No evidential value in samples of transcranial direct current stimulation (tDCS) studies of cognition and working memory in healthy populations". In: *Cortex* 94, pp. 131–141.

Merzagora, A. C. et al. (2010). "Prefrontal hemodynamic changes produced by anodal direct current stimulation". In: *NeuroImage* 49.3, pp. 2304–2310.

Metea, M. R. and E. A. Newman (2006). "Glial cells dilate and constrict blood vessels: a mechanism of neurovascular coupling." In: *The Journal of Neuroscience* 26.11, pp. 2862–2870.

Meyer, G (1987). "Forms and spatial arrangement of neurons in the primary motor cortex of man." In: *The Journal of Comparative Neurology* 262.3, pp. 402–428.

Mikkonen, M. et al. (2018). "TMS Motor Thresholds Correlate With TDCS Electric Field Strengths in Hand Motor Area". In: *Frontiers in Neuroscience* 12, pp. 151–10.

Minarik, T. et al. (2016). "The Importance of Sample Size for Reproducibility of tDCS Effects". In: *Frontiers in Human Neuroscience* 10.81, pp. 365–5.

Minati, L. et al. (2011). "Variability comparison of simultaneous brain near-infrared spectroscopy and functional magnetic resonance imaging during visual stimulation". In: *Journal of Medical Engineering & Technology* 35.6-7, pp. 370–376.

Miniussi, C., J. A. Harris, and M. Ruzzoli (2013). "Modelling non-invasive brain stimulation in cognitive neuroscience." In: *Neuroscience and Biobehavioral Reviews* 37.8, pp. 1702–1712.

Miranda, P. C., M. Lomarev, and M. Hallett (2006). "Modeling the current distribution during transcranial direct current stimulation". In: *Clinical neurophysiology* 117.7, pp. 1623–1629.

Monai, H. et al. (2016). "Calcium imaging reveals glial involvement in transcranial direct current stimulation-induced plasticity in mouse brain". In: *Nature Communications* 7, pp. 1–10.

Monte-Silva, K. et al. (2013). "Induction of Late LTP-Like Plasticity in the Human Motor Cortex by Repeated Non-Invasive Brain Stimulation". In: *Brain Stimulation* 6.3, pp. 424–432.

Muoio, V, P. B. Persson, and M. M. Sendeski (2014). "The neurovascular unit - concept review". In: *Acta Physiologica* 210.4, pp. 790–798.

Murakami, S. and Y. Okada (2006). "Contributions of principal neocortical neurons to magnetoencephalography and electroencephalography signals". In: *The Journal of Physiology* 575.3, pp. 925–936.

Muthalib, M. et al. (2013). "Effects of Transcranial Direct Current Stimulation of the Motor Cortex on Prefrontal Cortex Activation During a Neuromuscular Fatigue Task: An fNIRS Study". In: *Oxygen Transport to Tissue XXXV*. New York, NY: Springer New York, pp. 73–79.

Muthukumaraswamy, S. D. and K. D. Singh (2008). "Spatiotemporal frequency tuning of BOLD and gamma band MEG responses compared in primary visual cortex". In: *NeuroImage* 40.4, pp. 1552–1560.

Neuling, T. et al. (2015). "Friends, not foes: Magnetoencephalography as a tool to uncover brain dynamics during transcranial alternating current stimulation". In: *NeuroImage* 118.C, pp. 406–413.

Nias, D. K. (1976). "Therapeutic effects of low-level direct electrical currents." In: *Psychological Bulletin* 83.5, pp. 766–773.

NICE (2017). *Glaucoma: diagnosis and management*. National Institute for Health and Care Excellence. URL: ***https://www.nice.org.uk/guidance/ng81***.

Nichols, A. L. and J. K. Maner (2008). "The Good-Subject Effect: Investigating Participant Demand Characteristics". In: *The Journal of General Psychology* 135.2, pp. 151–166.

Nielsen, J. D. et al. (2018). "Automatic skull segmentation from MR images for realistic volume conductor models of the head: Assessment of the state-of-the-art". In: *NeuroImage* 174, pp. 587–598.

Niessing, J. et al. (2005). "Hemodynamic signals correlate tightly with synchronized gamma oscillations". In: *Ccience* 309.5736, pp. 948–951.

Nitsche, M. A. and W. Paulus (2000). "Excitability changes induced in the human motor cortex by weak transcranial direct current stimulation." In: *Journal of Physiology* 527 Pt 3, pp. 633–639.

— (2001). "Sustained excitability elevations induced by transcranial DC motor cortex stimulation in humans". In: *Neurology* 57.10, pp. 1899–1901.

Nitsche, M. A. et al. (2007). "Timing-dependent modulation of associative plasticity by general network excitability in the human motor cortex." In: *The Journal of Neuroscience* 27.14, pp. 3807–3812.

Nitsche, M. A. et al. (2008). "Transcranial direct current stimulation: State of the art 2008". In: *Brain Stimulation* 1.3, pp. 206–223.

Noury, N. and M. Siegel (2017). "Phase properties of transcranial electrical stimulation artifacts in electrophysiological recordings". In: *NeuroImage* 158, pp. 406–416.

— (2018). "Analyzing EEG and MEG signals recorded during tES, a reply". In: *NeuroImage* 167, pp. 53–61.

Noury, N., J. F. Hipp, and M. Siegel (2016). "Physiological processes non-linearly affect electrophysiological recordings during transcranial electric stimulation". In: *NeuroImage*, pp. 1–11.

O'Connell, N. E. et al. (2012). "Rethinking Clinical Trials of Transcranial Direct Current Stimulation: Participant and Assessor Blinding Is Inadequate at Intensities of 2mA". In: *PLoS ONE* 7.10, e47514–5.

Ohn, S. H. et al. (2008). "Time-dependent effect of transcranial direct current stimulation on the enhancement of working memory." In: *NeuroReport* 19.1, pp. 43–47.

Ojemann, G. A., N. F. Ramsey, and J. Ojemann (2013). "Relation between functional magnetic resonance imaging (fMRI) and single neuron, local field potential (LFP) and electrocorticography (ECoG) activity in human cortex". In: *Frontiers in Human Neuroscience* 7, p. 34.

Oostenveld, R. et al. (2011). "FieldTrip: open source software for advanced analysis of MEG, EEG, and invasive electrophysiological data". In: *Computational Intelligence and Neuroscience* 2011, 1:1–1:9.

Opitz, A. et al. (2015). "Determinants of the electric field during transcranial direct current stimulation." In: *NeuroImage* 109, pp. 140–150.

Opitz, A. et al. (2016). "Spatiotemporal structure of intracranial electric fields induced by transcranial electric stimulation in humans and nonhuman primates". In: *Scientific Reports* 6, p. 31236.

Opitz, A. et al. (2017). "Limitations of ex vivo measurements for in vivo neuroscience". In: *Proceedings of the National Academy of Sciences* 114.20, pp. 5243–5246.

Palm, U. et al. (2013). "Evaluation of Sham Transcranial Direct Current Stimulation for Randomized, Placebo-Controlled Clinical Trials". In: *Brain Stimulation* 6.4, pp. 690–695.

Palm, U. et al. (2016). "tDCS for the treatment of depression: a comprehensive review". In: *European Archives of Psychiatry and Clinical Neuroscience* 266.8, pp. 681–694.

Peirce, J. and M. MacAskill (2018). *Building experiments in PsychoPy*. SAGE Publications Ltd.

Pellegrini, M., M. Zoghi, and S. Jaberzadeh (2018). "Cluster analysis and subgrouping to investigate inter-individual variability to non-invasive brain stimulation: a systematic review." In: *Reviews in the Neurosciences* 29.6, pp. 675–697.

Pelligrino, D. A., H.-L. Xu, and F. Vetri (2010). "Caffeine and the Control of Cerebral Hemodynamics". In: *Journal of Alzheimer's Disease* 20.s1, S51–S62.

Penny, W. D. et al. (2011). *Statistical parametric mapping: the analysis of functional brain images*. London, UK: Elsevier.

Perea, G., M. Sur, and A. Araque (2014). "Neuron-glia networks: integral gear of brain function". In: *Frontiers in Cellular Neuroscience* 8, p. 378.

Perutz, M (1995). "Hoppe-Seyler, Stokes and haemoglobin." In: *Biological Chemistry* 376.8, pp. 449–450.

Plonsey, R. and D. B. Heppner (1967). "Considerations of quasi-stationarity in electrophysiological systems". In: *The Bulletin of Mathematical Biophysics* 29.4, pp. 657–664.

Pöppel, E and L. O. Harvey (1973). "Light-difference threshold and subjective brightness in the periphery of the visual field." In: *Psychologische Forschung* 36.2, pp. 145–161.

Portney, G. L. and M. A. Krohn (1978). "Automated perimetry: Background, instruments and methods". In: *Survey of Ophthalmology* 22.4, pp. 271–278.

Price, A. R. et al. (2015). "A meta-analysis of transcranial direct current stimulation studies examining the reliability of effects on language measures". In: *Brain Stimulation* 8.6, pp. 1093–1100.

Prins, N (2012). "The psychometric function: The lapse rate revisited". In: *Journal of Vision* 12.6, pp. 25–25.

Prins, N. and F. A. A. Kingdom (2016). *Psychophysics: A practical introduction.* Academic Press.

Priori, A. (2003). "Brain polarization in humans: a reappraisal of an old tool for prolonged non-invasive modulation of brain excitability". In: *Clinical Neurophysiology* 114.4, pp. 589–595.

Priori, A. et al. (1998). "Polarization of the human motor cortex through the scalp". In: *Neuroreport* 9.10, pp. 2257–2260.

Pulgar, V. M. (2015). "Direct electric stimulation to increase cerebrovascular function". In: *Frontiers in Systems Neuroscience* 9.159, pp. 379–5.

Purcell, E. M., H. C. Torrey, and R. V. Pound (1946). "Resonance Absorption by Nuclear Magnetic Moments in a Solid". In: *Physical Review* 69 (1-2), pp. 37–38.

Purpura, D. P. and J. G. McMurtry (1965). "Intracellular activities and evoked potential changes during polarization of motor cortex." In: *Journal of Neurophysiology* 28.1, pp. 166–185.

Radman, T. et al. (2009). "Role of cortical cell type and morphology in subthreshold and suprathreshold uniform electric field stimulation in vitro." In: *Brain Stimulation* 2.4, pp. 215–228.

Rahman, A. et al. (2013). "Cellular effects of acute direct current stimulation: somatic and synaptic terminal effects". In: *The Journal of Physiology* 591.10, pp. 2563–2578.

Rahman, A. et al. (2017). "Direct current stimulation boosts synaptic gain and cooperativity in vitro". In: *The Journal of Physiology* 595.11, pp. 3535–3547.

Rains, J. D. (1963). "Signal luminance and position effects in human reaction time". In: *Vision Research* 61, pp. 239–251.

Rampersad, S, D Stegeman, and T Oostendorp (2013). "OP 11. Optimized tDCS electrode configurations for five targets determined via an inverse FE modeling approach". In: *Clinical Neurophysiology* 124.10, e61–e62.

Rampersad, S. M. et al. (2014). "Simulating Transcranial Direct Current Stimulation With a Detailed Anisotropic Human Head Model". In: *IEEE Transactions on Neural Systems and Rehabilitation Engineering* 22.3, pp. 441–452.

Ramsay, J. and G. Schlagenauf (1966). "Treatment of depression with low voltage direct current". In: *Southern Medical Journal* 59.8, pp. 932–934.

Ranck, J. B. (1975). "Which elements are excited in electrical stimulation of mammalian central nervous system: a review." In: *Brain Research* 98.3, pp. 417–440.

Reato, D et al. (2010). "Low-Intensity Electrical Stimulation Affects Network Dynamics by Modulating Population Rate and Spike Timing". In: *Journal of Neuroscience* 30.45, pp. 15067–15079.

Redfearn, J. W. T., O. C. J. Lippold, and R Costain (1964). "A preliminary account of the clinical effects of polarizing the brain in certain psychiatric disorders". In: *The British Journal of Psychiatry* 110.469, pp. 773–785.

Reinhart, R. M. G. et al. (2016). "Electrical Stimulation of Visual Cortex Can Immediately Improve Spatial Vision". In: *Current Biology* 26.14, pp. 1867–1872.

Remak, R. (1844). "Neurologische Erläuterungen". In: *Archiv für Anatomie, Physiologie und Wissenschaftliche Medicin* 12, pp. 463–472.

Remington, L. A. (2012). "Visual pathway". In: *Clinical anatomy and physiology of the visual system*, pp. 233–252.

Rivara, C.-B. et al. (2003). "Stereologic characterization and spatial distribution patterns of Betz cells in the human primary motor cortex". In: *The Anatomical Record Part A: Discoveries in Molecular, Cellular, and Evolutionary Biology* 270.2, pp. 137–151.

Roland, P. E. and K. Zilles (1998). "Structural divisions and functional fields in the human cerebral cortex". In: *Brain Research Reviews* 26.2-3, pp. 87–105.

Rountree, L. (2018). "Optimisation of perimetric stimuli for mapping changes in spatial summation in glaucoma". PhD thesis. Cardiff University.

Rountree, L. et al. (2018). "Optimising the glaucoma signal/noise ratio by mapping changes in spatial summation with area-modulated perimetric stimuli." In: *Scientific Reports* 8.1, p. 2172.

Rovati, L. et al. (2007). "Optical and electrical recording of neural activity evoked by graded contrast visual stimulus". In: *BioMedical Engineering OnLine* 6.1, p. 28.

RStudio Team (2016). *RStudio: Integrated Development Environment for R*. RStudio, Inc. Boston, MA. URL: *http://www.rstudio.com/*.

Ruffini, G. et al. (2013). "Transcranial Current Brain Stimulation (tCS): Models and Technologies". In: *IEEE Transactions on Neural Systems and Rehabilitation Engineering* 21.3, pp. 333–345.

Ruohonen, J. and J. Karhu (2012). "tDCS possibly stimulates glial cells". In: *Clinical Neurophysiology* 123.10, pp. 2006–2009.

Rush, S and D. A. Driscoll (1968). "Current distribution in the brain from surface electrodes." In: *Anesthesia and Analgesia* 47.6, pp. 717–723.

Russo, R. et al. (2013). "Perception of Comfort During Active and Sham Transcranial Direct Current Stimulation: A Double Blind Study". In: *Brain Stimulation* 6.6, pp. 946–951.

Salvador, R. et al. (2019). "Role of Computational Modeling for Dose Determination". In: *Practical Guide to Transcranial Direct Current Stimulation*. Springer, pp. 233–262.

Sander, T. H. et al. (2007). "Cross-correlation analysis of the correspondence between magnetoencephalographic and near-infrared cortical signals." In: *Methods of Information in Medicine* 46.2, pp. 164–168.

Santarnecchi, E. et al. (2015). "Enhancing cognition using transcranial electrical stimulation". In: *Current Opinion in Behavioral Sciences* 4, pp. 171–178.

Santosa, H. et al. (2018). "The NIRS Brain AnalyzIR Toolbox". In: *Algorithms* 11.5, p. 73.

Sarvas, J. (1987). "Basic mathematical and electromagnetic concepts of the biomagnetic inverse problem". In: *Physics in Medicine & Biology* 32.1, p. 11.

Saturnino, G. B., A. Antunes, and A. Thielscher (2015). "On the importance of electrode parameters for shaping electric field patterns generated by tDCS". In: *NeuroImage* 120.C, pp. 25–35.

Saturnino, G. B. et al. (2018). "SimNIBS 2.1: A Comprehensive Pipeline for Individualized Electric Field Modelling for Transcranial Brain Stimulation". In: *bioRxiv*, p. 500314.

Saturnino, G. B. et al. (2019). "A principled approach to conductivity uncertainty analysis in electric field calculations". In: *NeuroImage* 188, pp. 821–834.

Scholkmann, F. and M. Wolf (2013). "General equation for the differential pathlength factor of the frontal human head depending on wavelength and age". In: *Journal of Biomedical Optics* 18.10, p. 105004.

Scholkmann, F. et al. (2014). "A review on continuous wave functional near-infrared spectroscopy and imaging instrumentation and methodology". In: *NeuroImage* 85.P1, pp. 6–27.

Schroeter, M. L. et al. (2004). "Towards a standard analysis for functional near-infrared imaging". In: *NeuroImage* 21.1, pp. 283–290.

Schutt, H. H. et al. (2016). "Painfree and accurate Bayesian estimation of psychometric functions for (potentially) overdispersed data". In: *Vision Research* 122, pp. 105–123.

Schwan, H. P. and C. F. Kay (1957). "Capacitive properties of body tissues". In: *Circulation Research* 5.4, pp. 439–443.

Schwann, T. (1839). *Mikroskopische Untersuchungen uber die Uebereinstimmung in der Struktur und dem Wachsthum der Thiere und Pflanzen*. Verlag der Sander'schen Buchhandlung (GE Reimer).

Scribonius Largus (1529). "De compositione medicamentorum". In: *De compositionibus medicamentorum. Liber unus*. Ed. by J. Ruellius. Basel: Cratander, Andreas, 350–16] 318 p., 1] l.

Sheffield, L. J. and R. M. Mowbray (1968). "The effects of polarization on normal subjects". In: *The British Journal of Psychiatry* 114.507, pp. 225–232.

Si, J. et al. (2016). "Correlation between electrical and hemodynamic responses during visual stimulation with graded contrasts". In: *Journal of Biomedical Optics* 21.9, pp. 091315–11.

Singh, K. D. (2006). "Magnetoencephalography". In: *Methods in Mind*. New York: MIT Press, pp. 291—326.

Singh, K. D. et al. (2002). "Task-related changes in cortical synchronization are spatially coincident with the hemodynamic response". In: *NeuroImage* 16.1, pp. 103–114.

Smith, S. M. et al. (2005). "Variability in fMRI: A re-examination of inter-session differences". In: *Human Brain Mapping* 24.3, pp. 248–257.

Soekadar, S. R. et al. (2013). "In vivo assessment of human brain oscillations during application of transcranial electric currents." In: *Nature Communications* 4, p. 2032.

Sriraman, A., T. Oishi, and S. Madhavan (2014). "Timing-dependent priming effects of tDCS on ankle motor skill learning". In: *Brain Research* 1581, pp. 23–29.

Stagg, C. J. et al. (2009). "Polarity-Sensitive Modulation of Cortical Neurotransmitters by Transcranial Stimulation". In: *Journal of Neuroscience* 29.16, pp. 5202–5206.

Stagg, C. J. et al. (2011a). "Polarity and timing-dependent effects of transcranial direct current stimulation in explicit motor learning". In: *Neuropsychologia* 49.5, pp. 800–804.

Stagg, C. J. and H. Johansen-Berg (2013). "Studying the effects of transcranial direct-current stimulation in stroke recovery using magnetic resonance imaging." In: *Frontiers in Human Neuroscience* 7, p. 857.

Stagg, C. J. and M. A. Nitsche (2011). "Physiological Basis of Transcranial Direct Current Stimulation". In: *The Neuroscientist* 17.1, pp. 37–53.

Stagg, C. J., V. Bachtiar, and H. Johansen-Berg (2011b). "The role of GABA in human motor learning." In: *Current biology* 21.6, pp. 480–484.

Stagg, C. J. et al. (2013). "Widespread modulation of cerebral perfusion induced during and after transcranial direct current stimulation applied to the left dorsolateral prefrontal cortex." In: *The Journal of Neuroscience* 33.28, pp. 11425–11431.

Stagg, C. J., A. Antal, and M. A. Nitsche (2018). "Physiology of transcranial direct current stimulation". In: *The Journal of ECT* 34.3, pp. 144–152.

Steinbrink, J. et al. (2006). "Illuminating the BOLD signal: combined fMRI–fNIRS studies". In: *Magnetic Resonance Imaging* 24.4, pp. 495–505.

Stevens, S. S. (1936). "A scale for the measurement of a psychological magnitude: Loudness". In: *Psychological Review* 43, pp. 405–416.

Stevens, S., A. Carton, and G. Shickman (1958). "A scale of apparent intensity of electric shock." In: *Journal of Experimental Psychology* 56.4, p. 328.

Stevens, S. S. (1960). "The psychophysics of sensory function". In: *American Scientist* 48.2, pp. 226–253.

Stickland, R. et al. (2019). "Neurovascular coupling during visual stimulation in multiple sclerosis: a MEG-fMRI study". In: *Neuroscience* 403, pp. 54–69.

Stogsdill, J. A. and C. Eroglu (2017). "The interplay between neurons and glia in synapse development and plasticity". In: *Current Opinion in Neurobiology* 42, pp. 1–8.

Strangman, G. E., Z. Li, and Q. Zhang (2013). "Depth sensitivity and source-detector separations for near infrared spectroscopy based on the Colin27 brain template". In: *PloS ONE* 8.8, e66319.

Strangman, G. E., Q. Zhang, and Z. Li (2014). "Scalp and skull influence on near infrared photon propagation in the Colin27 brain template". In: *NeuroImage* 85, pp. 136–149.

Strasburger, H. (2001). "Converting between measures of slope of the psychometric function". In: *Perception & Psychophysics* 63.8, pp. 1348–1355.

Strasburger, H., I. Rentschler, and M. Jüttner (2011). "Peripheral vision and pattern recognition: A review". In: *Journal of Vision* 11.5, pp. 13–13.

Strube, W. et al. (2015). "Efficacy and interindividual variability in motor-cortex plasticity following anodal tDCS and paired-associative stimulation". In: *Neural Plasticity* 2015.

Takahashi, K et al. (1999). "Hemodynamic changes in visual cortex were dependant on flash-frequency". In: *NeuroImage* 9, S891–S891.

Takai, H. et al. (2016). "Effect of Transcranial Direct Current Stimulation over the Primary Motor Cortex on Cerebral Blood Flow: A Time Course Study Using Near-infrared Spectroscopy". In: *Oxygen Transport to Tissue XXXVII*. New York, NY: Springer New York, pp. 335–341.

Tanzi, M. C., S. Farè, and G. Candiani (2019). *Foundations of Biomaterials Engineering*. Academic Press.

Terzuolo, C. A. and T. H. Bullock (1956). "Measurement of imposed voltage gradient adequate to modulate neuronal firing". In: *Proceedings of the National Academy of Sciences of the United States of America* 42.9, p. 687.

Thielscher, A., A. Antunes, and G. B. Saturnino (2015). "Field modeling for transcranial magnetic stimulation: A useful tool to understand the physiological effects of TMS?" In: *Conference proceedings: Annual International Conference of the IEEE Engineering in Medicine and Biology Society.* 2015, pp. 222–225.

Tierney, T. M. et al. (2019). "Optically pumped magnetometers: From quantum origins to multi-channel magnetoencephalography". In: *NeuroImage* 199, pp. 598–608.

Toronov, V. Y., X. Zhang, and A. G. Webb (2007). "A spatial and temporal comparison of hemodynamic signals measured using optical and functional magnetic resonance imaging during activation in the human primary visual cortex". In: *NeuroImage* 34.3, pp. 1136–1148.

Tremblay, S. et al. (2016). "Systematic assessment of duration and intensity of anodal transcranial direct current stimulation on primary motor cortex excitability". In: *European Journal of Neuroscience* 44.5, pp. 2184–2190.

Treutwein, B and H Strasburger (1999). "Fitting the psychometric function." In: *Perception & Psychophysics* 61.1, pp. 87–106.

Trivedi, D. P., K. J. Hallock, and P. R. Bergethon (2013). "Electric fields caused by blood flow modulate vascular endothelial electrophysiology and nitric oxide production." In: *Bioelectromagnetics* 34.1, pp. 22–30.

Truong, D. Q. et al. (2013). "Computational modeling of transcranial direct current stimulation (tDCS) in obesity: Impact of head fat and dose guidelines". In: *NeuroImage* 2, pp. 759–766.

Tseng, P. et al. (2012). "Unleashing potential: transcranial direct current stimulation over the right posterior parietal cortex improves change detection in low-performing individuals." In: *The Journal of Neuroscience* 32.31, pp. 10554–10561.

Tsuzuki, D. et al. (2007). "Virtual spatial registration of stand-alone fNIRS data to MNI space". In: *NeuroImage* 34.4, pp. 1506–1518.

Tsuzuki, D. et al. (2012). "Stable and convenient spatial registration of stand-alone NIRS data through anchor-based probabilistic registration." In: *Neuroscience Research* 72.2, pp. 163–171.

Turi, Z., W. Paulus, and A. Antal (2012). "Functional neuroimaging and transcranial electrical stimulation." In: *Clinical EEG and Neuroscience* 43.3, pp. 200–208.

Turi, Z. et al. (2014). "When size matters: large electrodes induce greater stimulation-related cutaneous discomfort than smaller electrodes at equivalent current density." In: *Brain Stimulation* 7.3, pp. 460–467.

Turi, Z. et al. (2019). "Blinding is compromised for transcranial direct current stimulation at 1 mA for 20 min in young healthy adults". In: *European Journal of Neuroscience* 00, p. 1.

Turpin, A., D. Jankovic, and A. McKendrick (2010). "Identifying steep psychometric function slope quickly in clinical applications". In: *Vision Research* 50.23, pp. 2476–2485.

Tyler, W. J. et al. (2015). "Transdermal neuromodulation of noradrenergic activity suppresses psychophysiological and biochemical stress responses in humans". In: *Scientific Reports*, pp. 1–17.

Tzourio-Mazoyer, N et al. (2002). "Automated anatomical labeling of activations in SPM using a macroscopic anatomical parcellation of the MNI MRI single-subject brain." In: *NeuroImage* 15.1, pp. 273–289.

Underwood, E. (2016). "Cadaver study challenges brain stimulation methods". In: *Science* 352.6284, pp. 397–397.

Van der Zee, P et al. (1992). "Experimentally measured optical pathlengths for the adult head, calf and forearm and the head of the newborn infant as a function of inter optode spacing". In: *Oxygen Transport to Tissue XIII*. Springer, pp. 143–153.

Van Veen, B. D. et al. (1997). "Localization of brain electrical activity via linearly constrained minimum variance spatial filtering". In: *IEEE Transactions on Biomedical Engineering* 44.9, pp. 867–880.

Vaseghi, B., M. Zoghi, and S. Jaberzadeh (2014). "Does anodal transcranial direct current stimulation modulate sensory perception and pain? A meta-analysis study". In: *Clinical Neurophysiology* 125.9, pp. 1847–1858.

Villamar, M. F. et al. (2013). "Technique and considerations in the use of 4x1 ring high-definition transcranial direct current stimulation (HD-tDCS)". In: *JoVE (Journal of Visualized Experiments)* 77, e50309.

Virchow, R. L. K. (1860). *Cellular Pathology*. John Churchill.

Voie, A. et al. (2014). "Parametric mapping and quantitative analysis of the human calvarium." In: *Computerized Medical Imaging and Graphics* 38.8, pp. 675–682.

Volta, A. (1918). *Le opere di Alessandro Volta, I Vol.* Milan: Hoepli.

— (1923). *Le opere di Alessandro Volta, II Vol.* Milan: Hoepli.

Volterra, A. and J. Meldolesi (2005). "Astrocytes, from brain glue to communication elements: the revolution continues". In: *Nature Reviews Neuroscience* 6.8, p. 626.

Vrba, J. and S. E. Robinson (2001a). "Signal processing in magnetoencephalography". In: *Methods* 25.2, pp. 249–271.

— (2001b). "Signal processing in magnetoencephalography". In: *Methods* 25.2, pp. 249–271.

Wall, M., K. E. Kutzko, and B. C. Chauhan (2002). "The relationship of visual threshold and reaction time to visual field eccentricity with conventional automated perimetry." In: *Vision Research* 42.6, pp. 781–787.

Wallace, D. et al. (2016). "Perceived Comfort and Blinding Efficacy in Randomised Sham-Controlled Transcranial Direct Current Stimulation (tDCS) Trials at 2 mA in Young and Older Healthy Adults". In: *PLoS ONE* 11.2, e0149703–16.

Walsh, J and S Seignette (1773). "Of the Electric Property of the Torpedo. In a Letter from John Walsh, Esq; FRS to Benjamin Franklin, Esq; LL. D., FRS, Ac. R. Par. Soc. Ext., &c." In: *Philosophical Transactions (1683-1775)*.

Wang, B et al. (2013). "Visual field maps of the human visual cortex for central and peripheral vision". In: *Neuroscience and Biomedical Engineering* 1.2, pp. 102–110.

Weber, E. H. (1834). *De pulsu, resorptione, auditu et tactu: Annotationes anatomicae et physiologicae*. Leipzig: Koehlor.

Weiskrantz, L et al. (1974). "Visual capacity in the hemianopic field following a restricted occipital ablation." In: *Brain* 97.4, pp. 709–728.

Weiskrantz, L. (1996). "Blindsight revisited". In: *Current Opinion in Neurobiology* 6.2, pp. 215–220.

Wichmann, F. A. and N. J. Hill (2001). "The psychometric function: I. Fitting, sampling, and goodness of fit." In: *Perception & Psychophysics* 63.8, pp. 1293–1313.

Wiethoff, S., M. Hamada, and J. C. Rothwell (2014). "Variability in response to transcranial direct current stimulation of the motor cortex". In: *Brain Stimulation* 7.3, pp. 468–475.

Wijeakumar, S. et al. (2012). "Localization of Hemodynamic Responses to Simple Visual Stimulation: An fNIRS Study". In: *Investigative Opthalmology & Visual Science* 53.4, pp. 2266–8.

Windhoff, M., A. Opitz, and A. Thielscher (2013). "Electric field calculations in brain stimulation based on finite elements: An optimized processing pipeline for the generation and usage of accurate individual head models". In: *Human Brain Mapping* 34.4, pp. 923–935.

Woods, A. J. et al. (2016). "A technical guide to tDCS, and related non-invasive brain stimulation tools". In: *Clinical Neurophysiology* 127.2, pp. 1031–1048.

Wylie, G. R. et al. (2009). "Using co-variations in the Hb signal to detect visual activation: a near infrared spectroscopic imaging study". In: *NeuroImage* 47.2, pp. 473–481.

Zaidi, F. H. et al. (2007). "Short-wavelength light sensitivity of circadian, pupillary, and visual awareness in humans lacking an outer retina". In: *Current Biology* 17.24, pp. 2122–2128.

Zarghooni, K. et al. (2016). "Occipital bone thickness: Implications on occipital-cervical fusion. A cadaveric study". In: *Acta Orthopaedica Et Traumatologica Turcica* 50.6, pp. 606–609.

Zeiss (2014a). *Humphrey Field Analyzer 3 from Zeiss: The best just got better [Brochure]*. Carl Zeiss Meditec AG. Jena, Germany.

— (2014b). *Humphrey visual field analyzers, innovation and connectivity [Brochure]*. Carl Zeiss Meditec AG. Jena, Germany.

Zhao, Z. et al. (2012). "Directing migration of endothelial progenitor cells with applied DC electric fields". In: *Stem Cell Research* 8.1, pp. 38–48.

Zheng, X., D. C. Alsop, and G. Schlaug (2011). "Effects of transcranial direct current stimulation (tDCS) on human regional cerebral blood flow". In: *NeuroImage* 58.1, pp. 26–33.

Zimmerman, J. E., P. Thiene, and J. T. Harding (1970). "Design and operation of stable rf-biased superconducting point-contact quantum devices, and a note on the properties of perfectly clean metal contacts". In: *Journal of Applied Physics* 41.4, pp. 1572–1580.

Zonta, M. et al. (2003). "Neuron-to-astrocyte signaling is central to the dynamic control of brain microcirculation." In: *Nature Neuroscience* 6.1, pp. 43–50.

Zumer, J. M. et al. (2010). "Relating BOLD fMRI and neural oscillations through convolution and optimal linear weighting". In: *Neuroimage* 49.2, pp. 1479–1489.